ISSN-0366-6913

Cerâmica

ÓRGÃO OFICIAL DA ASSOCIAÇÃO BRASILEIRA DE CERÂMICA - ANO LXVI - VOL. 66, 378 - ABR/MAI/JUN 2020

ASSOCIAÇÃO BRASILEIRA

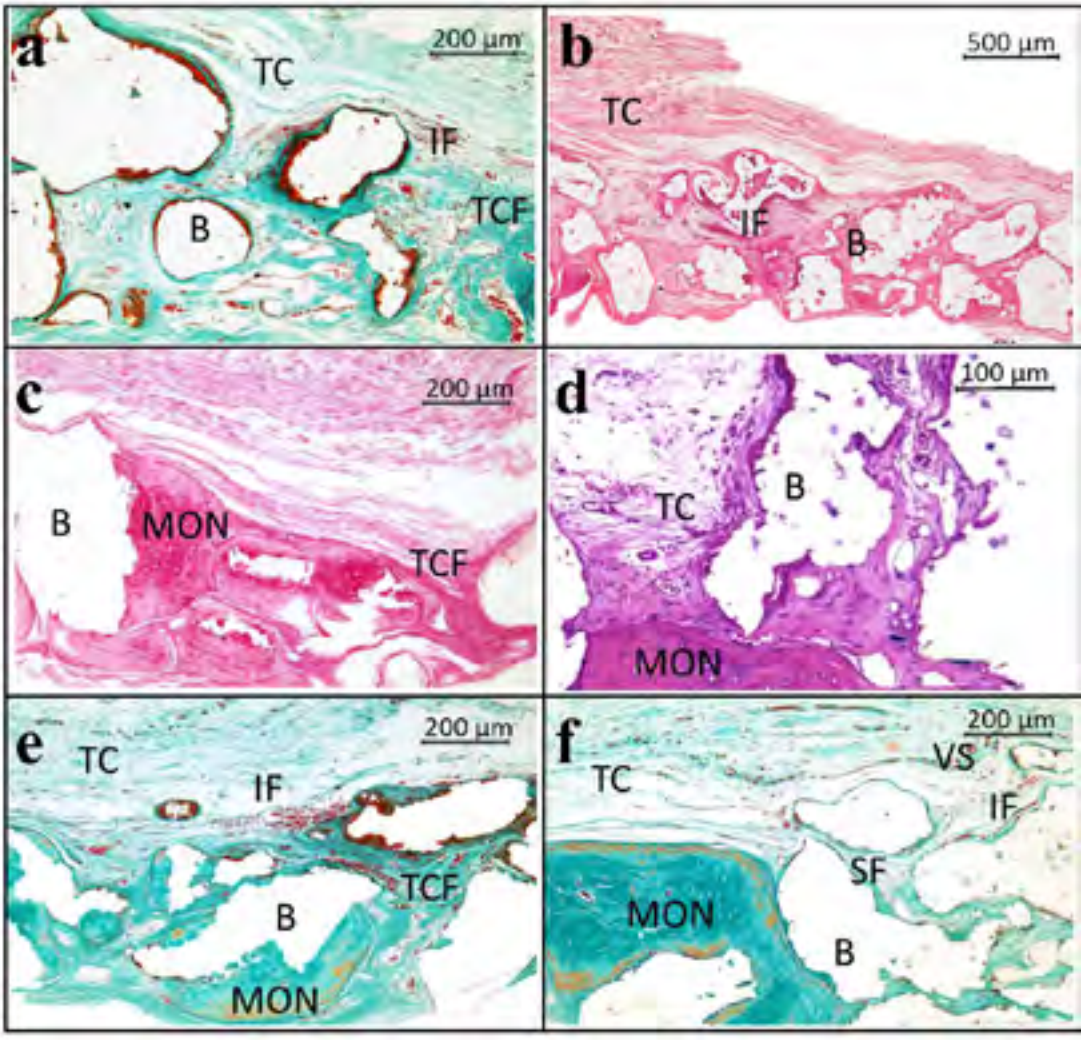

DE CERÂMICA

Cerâmica

A revista Cerâmica, órgão oficial da Associação Brasileira de Cerâmica (ABCeram), publica contribuições originais (e artigos revisão) de interesse na área de cerâmica, compreendendo arte cerâmica, abrasivos, biocerâmicas, cerâmicas avançadas, cerâmica branca, cerâmica de mesa, cerâmica eletroeletrônica, cerâmica estrutural, cerâmica magnética, cerâmica nuclear, cerâmica óptica, cerâmica química, cerâmica termomecânica, cerâmica vermelha, cimento, compósitos de matriz cerâmica, materiais refratários, materiais de revestimento, matérias-primas, vidrados, vidros e vitrocerâmicas, análise microestrutural, instrumentação, processos de fabricação, síntese de pós, técnicas de caracterização, etc. Todas as contribuições são submetidas independentemente a análise por relatores, pertencente ou não ao Conselho de Editores. Cerâmica é publicada trimestralmente. Os artigos publicados podem ser acessados por meio de: www.scielo.br/ce. Cópias impressas são distribuídas aos sócios da ABCeram e a bibliotecas do Brasil e de outros países.

Cerâmica, the official journal of the Brazilian Ceramic Society, accepts original (and review) articles in the entire field of ceramic science and technology, including ceramic art, bioceramics, advanced ceramics, electro-electronic ceramics, magnetic ceramics, optical ceramics, nuclear ceramics, structural ceramics, ceramic raw materials, cements, sanitaryware and porcelain, thermal insulators, ceramic tiles, refractories, glazes and ceramic pigments, glasses and glass-ceramics, ceramic matrix composites, characterization techniques, ceramic equipments, microstructural analysis, manufacturing processes, powder synthesis, etc. All contributions are independently refereed. Cerâmica is published every three months. Published papers can be accessed by: www.scielo.br/ce. Printed copies are distributed to members of the Brazilian Ceramic Society and to libraries worldwide.

Editor Principal (*Principal Editor*)

H. N. Yoshimura
CECS - UFABC
Av. dos Estados, 5001
Santo André, SP 09210-580
humberto.yoshimura@ufabc.edu.br
ceram.abc@gmail.com

Editores Associados (*Associate Editors*)

D. Z. de Florio
CECS - UFABC
Av. dos Estados, 5001
Santo André, SP 09210-580
daniel.florio@ufabc.edu.br

R. Salomão
SMM - EESC - USP
Av. João Dagnone, 1100
São Carlos, SP 13563-120
rsalomao@sc.usp.br

F. M. B. Marques
DEMaC - Univ. Aveiro
Aveiro 3810-193
Portugal
fmarques@ua.pt

A. M. Segadães
DEMaC - Univ. Aveiro
Aveiro 3810-193
Portugal
segadaes@ua.pt

A. E. Martinelli
DEMat - CT - UFRN
Campus Lagoa Nova s/n
Natal, RN 59072-970
martinelli.ufrn@gmail.com

Conselho de Editores (*Editorial Board*)

Acchar W. - UFRN - RN
Berg E.A.T. - PR
Bergmann C.P. - UFRGS - RS
Bezerra U.T. - IFPB - PB
Bressiani A.H.A. - IPEN - SP
Holanda J.N.F. - UENF - RJ
Hotza D. - UFSC - SC
Kiminami R.H.G.A. - UFSCar - SP
Lameiras F.A. - CDTN - MG
Longo E. - UNESP - SP
Melo D.M.A. - UFRN - RN
Muccillo E.N.S. - IPEN - SP
Muccillo R. - IPEN - SP
Nascimento R.M. - UFRN - RN
Pandolfelli V.C. - UFSCar - SP
Pianaro S.A. - UEPG - PR
Pulcinelli S.H. - UNESP - SP
Resende W.S. - IBAR - SP
Riella H.G. - UFSC - SC
Rodrigues J.A. - UFSCar - SP
Santilli C.V. - UNESP - SP
Santos I.M.G. UFPB - PB
Silva C.R.M. - UNB - DF
Vasconcelos W.L. - UFMG - MG
Vieira C.M.F. - UENF - RJ
Zanotto E.D. - UFSCar - SP

Baptista J.L. - Univ. Aveiro - Portugal
Carda J.B. - Univ. Castellón - Spain
Castro M.S. - Univ. Mar del Plata - Argentina
Castro R.H.R. - Univ. California, Davis - USA
Clemens F.J. - EMPA - Switzerland
Esposito V. - DTU - Denmark
Fernandez J.F. - ICV-CSIC - Spain
Greil P. - F-Alexander-U. Erlangen - Germany
Prado F.D. - Univ. Nacional del Sur - Argentina
Sakka Y. - NIMS - Japan
Sin A. - Pirelli Labs - Italy
Steil M.C. - Univ. Grenoble Alpes - France
Studart A.R. - ETH Zürich - Switzerland
Traversa E. - Univ. Roma "Tor Vergata" - Italy
Velez M. - Univ. Missouri-Rolla - USA
Watari K. - AIST - Japan
Yoshimura M. - NCKU - Taiwan; TIT - Japan

Editores Principais Anteriores (*Previous Principal Editors*): P. S. Santos (*in memoriam*); R. Muccillo (1997-2015)

Cerâmica – Revista trimestral editada pela Associação Brasileira de Cerâmica – ABCERAM, ISSN 0366-6913, registro nº 1004/P209/73 no DPF, fundada em 09/09/1953 - CFMO 0255 - CNPJ: 61.615.977/0001-08.
Associação Brasileira de Cerâmica - IPT - prédio 36 - 2. Andar,
Av. Prof. Almeida Prado 532, Cidade Universitária, S. Paulo, 05508-901, Brasil.
tel: 11-3768-4284, fax: 11-3768-7101
abceram@abceram.org.br, http://www.abceram.org.br

Projeto Gráfico: TWA Studio Gráfico - contato@twastudio.com.br
http://www.twastudio.com.br

- Toda correspondência destinada à revista Cerâmica deve ser endereçada ao Editor Principal.
- Os trabalhos técnicos publicados pela revista Cerâmica são de total responsabilidade dos autores. Artigos assinados não expressam necessariamente a opinião da publicação ou da ABCERAM.

- Any correspondence to Cerâmica should be addressed to the Principal Editor.
- The Brazilian Ceramic Society and the Editors assume no responsibility for the contents of the technical papers and for the statements and opinions advanced by the contributors.

Cerâmica, ISSN-0366-6913, é indexada em (is indexed in): Web of Science (isiknowledge.com), Scopus, Ceramic Abstracts, British Ceramic Abstracts, Chemical Abstracts, Engineered Materials Abstracts, INIS Atomindex, Chemical Engineering and Biotechnology Abstracts (CEABA-VtB), Directory of Open Access Journals (DOAJ), Scimago Journal & Country Rank (SJR), SciELO (www.scielo.br/ce).

CAPA: Fotomicrografias do reparo de ensaio in vivo de regeneração de defeito ósseo crítico em rato Wistar nos grupos em que houve implantação dos biomateriais (B): a,c,e) grânulos de fosfato de cálcio bifásico (β-TCP + $Ca_2P_2O_7$); b,d,f) grânulos de fosfato de cálcio bifásico+5% vidro bioativo fosfatado (P_2O_5-CaO-CaF_2). Coloração: a,e,f) tricrômico de Masson-Goldner; b) picrosirius-red; c,d) hematoxilina-eosina. V. artigo de R. S. Almeida, M. H. Prado da Silva, D. Navarro da Rocha, I. I. A. Ribeiro, A. A. Barbosa Júnior, F. B. Miguel, F. P. Rosa, p. 119.

COVER: *Photomicrographs of the repair of in vivo test of bone regeneration in critical bone defect in Wistar rats in the groups in which the biomaterials (B) were implanted: a,c,e) granules of biphasic calcium phosphate (β-TCP/$Ca_2P_2O_7$); b,d,f) granules of biphasic calcium phosphate +5% bioactive glass (P_2O_5-CaO-CaF_2). Staining: a,e,f) Masson-Goldner trichrome; b) picrosirius-red; c,d) hematoxylin-eosin. See article by R. S. Almeida, M. H. Prado da Silva, D. Navarro da Rocha, I. I. A. Ribeiro, A. A. Barbosa Júnior, F. B. Miguel, F. P. Rosa, p. 119.*

PATROCINADOR

CONFEA

CAPES

CNPq

FAPESP

Associação Brasileira de Cerâmica

Tel: 11 3768 4284
Fax: 11 3768 7101
abceram@abceram.org.br
http://www.abceram.org.br

DIRETORIA

Presidente
Antonio Carlos de Camargo
Escola Superior de Engenharia e Gestão

Vice-Presidente
Edmilson Ricelli dos Passos
Elfusa Geral de Eletrofusão Ltda.

Diretor Administrativo-Financeiro
Ulisses Soares do Prado
Lining Representação, Consultoria e Projetos Ltda.

Diretora de Publicações
Juliana Marchi
Universidade Federal do ABC
Diretor de Comissões Técnicas
Samuel Marcio Toffoli
Escola Politécnica da USP
Diretor de Assuntos Especiais
Edgar Dutra Zanotto
Universidade Federal de São Carlos
Diretor de Assuntos Empresariais
Túlio Lissandro Melo de Morais
Imerys Fused Minerals Salto Ltda.
Diretor de Comunicações
Leandro César Ribeiro
Elfusa Geral Eletrofusão Ltda.
Diretor de Eventos
Mauro Akerman
Akerman Desenvolvimento Profissional Ltda.

CONSELHO
Presidente do Conselho
Luís Leonardo Horne Curimbaba Ferreira
Mineração Curimbaba Ltda.

Categorias Patrocinador / Coletivo
Ecio Rodrigues de Araujo
ELFUSA Geral Eletrofusão Ltda.
Nelson Touron Martinez Junior
Mineração Curimbaba Ltda.

Categorias Individual, Júnior e Instituição
Dolores Ribeiro Ricci Lazar
Instituto de Pesquisas Energéticas e Nucleares - IPEN
Fernando dos Santos Ortega
Centro Universitário FEI
Gelmires de Araújo Neves
Universidade Federal de Campina Grande - UFCG
Humberto Naoyuki Yoshimura
Universidade Federal do ABC - UFABC
Luiz Fernando Grespan Setz
Universidade Federal do ABC - UFABC
Marcelo Rodrigues Sampaio
Associação Nacional das Entidades de Produtores de Agregados para Construção - ANEPAC
Renata Ayres Rocha
Universidade Federal do ABC - UFABC
Ruth Herta Goldschmidt Aliaga Kiminami
Universidade Federal de São Carlos - UFSCar
Sonia Regina Homem de Mello Castanho
Instituto de Pesquisas Energéticas e Nucleares - IPEN
Válquiria de Fátima Justo
Consultora

Editorial

Este número da revista Cerâmica, 378, apresenta 15 artigos, 11 escritos em inglês e 4 em português, com autoria de 56 autores. Considerando a localização da instituição do autor correspondente, 4 artigos são provenientes de países do exterior (Arábia Saudita, Índia, Iraque e Síria) e 11 artigos são de diferentes estados brasileiros: 1 da Bahia, 2 de Minas Gerais, 1 da Paraíba, 1 de Pernambuco, 2 do Piauí, 2 do Rio de Janeiro, 1 do Rio Grande do Norte e 1 de Santa Catarina.

Aproveitamos para parabenizar os pesquisadores Mariana A.L. Braulio (4Cast), J.R. Cunha (Alcoa Alumar, Brasil), D. Whiteman (Alcoa, Austrália) e V.C. Pandolfelli (UFSCar-DEMa) pelo prêmio TMS Light Metals (The Minerals, Metals and Materials Society, Estados Unidos) ao trabalho "Improving the reliability of fluidized bed calciners by suitable refractory lining selection" publicado na Light Metals em 2019, decorrente de um projeto UFSCar-DEMa-Empresa. O Prof. Dr. Victor C. Pandolfelli, coordenador do projeto, é membro do Conselho de Editores da revista Cerâmica.

Convidamos os leitores a participarem do 64º Congresso Brasileiro de Cerâmica, que será realizado no Centro de Convenções do Hotel Majestic, na cidade de Águas de Lindóia, SP, entre 25 e 28 de maio de 2020.

Humberto N. Yoshimura
Editor

PATROCINADOR

Intercalation experiments for morphological alteration of kaolinite present in iron ore tailings

(Experimentos de intercalação para alteração morfológica da caulinita presente em rejeitos de mineração de ferro)

M. V. B. Gonçalves[1]*, A. V. Cardoso[2], F. V. Parreira[3]

[1]Federal University of Ouro Preto, REDEMAT, Pç. Tiradentes 20, 35400-000, Ouro Preto, MG, Brazil

[2]University of the State of Minas Gerais, School of Design-REDEMAT, 31270-010, Belo Horizonte, MG, Brazil

[3]Vale S.A., Ferrous Technology Center, 34006-270, Nova Lima, MG, Brazil

Abstract

The main aim of this work was to evaluate the use of kaolinite present in iron ore tailings (IOT) in the synthesis of halloysite-like structures. The segregation of kaolinite was performed by acid leaching of the IOT. Three steps were strictly controlled for the efficacy of the synthesis procedure: i) pre-intercalation of the clay mineral using dimethyl sulfoxide; ii) obtaining the methoxy-modified kaolinite; iii) intercalation of the methoxy-kaolinite with suitable organic molecules. The synthesis procedure was performed in one-step and two-step. X-ray diffraction result showed that the product obtained from the IOT was composed essentially of kaolinite. The leaching was efficient in concentrating the kaolinite, considerably increasing the percentage of this clay mineral in the segregated product. Apparently, the contamination of Fe^{3+} ions did not interfere in the synthesis process. FESEM images indicated the morphological transformation of plate-like kaolinite for kaolinite nanotubes with a halloysite-like structure.
Keywords: iron ore tailings, kaolinite, intercalation, nanotubes, halloysite.

Resumo

O principal objetivo deste trabalho foi avaliar o uso da caulinita presente no rejeito de mineração de ferro (RMF) na síntese de estruturas semelhantes à haloisita. A segregação da caulinita foi realizada por meio da lixiviação ácida do RMF. Três etapas foram rigorosamente controladas para eficácia do procedimento de síntese: i) pré-intercalação do argilomineral usando dimetilsulfóxido; ii) obtenção da caulinita metoxi-modificada; iii) intercalação da metoxi-caulinita com moléculas orgânicas adequadas. O procedimento de síntese foi realizado em uma etapa e duas etapas. O resultado de difração de raios X mostrou que o produto obtido do RMF foi composto essencialmente por caulinita. A lixiviação foi eficiente para concentrar a caulinita, aumentando consideravelmente o percentual deste argilomineral no produto segregado. Aparentemente, a contaminação por íons de Fe^{3+} não interferiu no processo de síntese. Imagens de MEVFEG indicaram a transformação morfológica das placas de caulinita para nanotubos de caulinita com estrutura semelhante à haloisita.
***Palavras-chave**: rejeito de mineração de ferro, caulinita, intercalação, nanotubos, haloisita.*

INTRODUCTION

In recent years, an increase in iron ore production has been observed, making interactions between this technique and the environment important. One of the main aspects related to iron production is the large volume of tailings generated in the beneficiation stage, the treatment given to the ore to maximize the use of the material of interest. Recently, due to the high demand for iron ore, rocks with low levels of iron are now feasible, implying an increase in the volume of tailings generated [1]. To maximize yield in the process of obtaining iron and exploiting the unrecovered materials of interest that are released together with the tailings, mining companies have been striving to improve mineral processing techniques to minimize the losses in the beneficiation stage and reprocessing the tailings generated, and also developing technologies to develop new applications and/or products using, for example, the clay minerals contained in iron ore tailings. In general, the minerals identified in iron ore tailings (IOT) are hematite, goethite, gibbsite, muscovite, quartz, and kaolinite. Kaolinite [$Al_2(OH)_4Si_2O_5$] is a clay mineral belonging to the kaolin group and occurs in the plate-like shape. The kaolinite can be subjected to the intercalation process that is used as a strategy to expand the interlayer space of clay minerals. Nanosized tubular halloysite, also called halloysite nanotube (HNT), is the most common occurrence of clay mineral halloysite that belongs to the kaolin group and, similar to kaolinite, is a phyllosilicate where each layer is formed by an octahedral alumina sheet and a silica tetrahedral sheet in a 1:1 stoichiometric ratio. HNT vary in length from the submicron scale up to ca. 30 μm. Generally, internal

**m.vitorbg@gmail.com*

https://orcid.org/0000-0002-2047-0777

diameters range from ca. 10 to 100 nm and internal diameter from ca. 20 to 190 nm [2, 3]. In the HNT, the outer surface is formed by siloxane (Si-O-Si) groups (tetrahedral sheet) and a gibbsite matrix composed of aluminol (Al-OH) groups (octahedral sheet) is present at the inner surface [4, 5]. Chemically, halloysite and kaolinite are similar, except that the halloysite layers are separated by a monolayer of water molecules; thus, the halloysite has the structural formula $Al_2(OH)_4Si_2O_5.nH_2O$. When hydrated (n=2), it is called 'halloysite 10 Å', and 10 Å indicates the d_{001} value of the layers. The dehydrated structure (n=0) is called 'halloysite 7 Å'.

The tubular structure of halloysite results from the wrapping of the 1:1 clay mineral layers under favorable geological conditions and is driven by the mismatch between the tetrahedral and octahedral sheets. In order to understand the rolling mechanism of the 1:1 layer of tetrahedral and octahedral sheets, several models have been proposed [6]. Increasing demand for HNT is observed, although it is not as common as kaolinite [7-9]. In recent years, several studies have broadened the field of application of HNT to highly technological applications such as catalytic supports and other functional materials due to their particular morphology and specific properties [8, 10]. In addition, the nanoparticles are also capable of adsorbing and storing a large number of hydrogen molecules [11] and drugs for controlled release [12-14], forming antibacterial biological membranes [15] and polymer-based composites [16-18], among other technological uses. Obtain a halloysite-like structure, based on the rolling of the kaolinite layers, has attracted the attention of several researchers [9, 19-26]. According to [9, 22], HNT has noble applications in nanotechnology; however, deposits of this clay mineral with attractive quality are rare worldwide. Besides, the presence of associated impurities and the morphology of HNT found in nature may not be uniform; therefore, the synthesis of nanotubes from intercalated and delaminated kaolinite is an important issue to be treated.

Although kaolinite occurs naturally in the plate-like shape, it has been shown to be susceptible to transform into nanotubes through intercalation/deintercalation methods. According to [6], kaolinite layers curl to compensate for the lateral misfit between the tetrahedral and octahedral sheets when the hydrogen bonds between the layers are sufficiently weakened. When water molecules occur between the 1:1 layers, similar to the halloysite structure, the interlayer force is weakened; therefore, the octahedral and tetrahedral sheets are free to approach their normal dimensions, which lead to a curvature of kaolinite layers [27]. In platy kaolinite, the structural stress generated by the mismatch between the tetrahedral and octahedral sheets is compensated by the formation of intense hydrogen bonds between the basal oxygen of the tetrahedral sheets and the inner-surface hydroxyl of the adjacent layer [28]. Gardolinsky and Lagaly [21], citing [6], stated that kaolinite layers curl to compensate the lateral misfit between larger tetrahedral sheets and smaller octahedral sheets when the interlayer hydrogen bonds are sufficiently weakened. In non-hydrated 1:1 platy particles, the tendency to make shorter interlayer hydrogen bonds provides an additional driving force to tetrahedral rotation [6]. Thus, tetrahedral rotation corrects the misfit of a non-hydrated structure, a result that cannot be accomplished by a rolling mechanism. The rolling mechanism is energetically more favorable than tetrahedral rotation but can only occur in sufficiently thin particles and weakened interlayer hydrogen bonds. The large basal space of the intercalation compounds prevents the reestablishment of hydrogen bonds between the layers of kaolinite, causing the rolling mechanism to occur to stabilize the clay mineral structure [21].

The layer delamination and curl procedure can be performed in one-step, where intercalation and swelling occur at the same time, or two-step, where intercalation and swelling occur separately. Three steps were strictly controlled for the efficacy of the synthesis procedure: i) pre-intercalation of the clay mineral; ii) obtaining the methoxy-modified kaolinite; iii) intercalation of the methoxy-kaolinite with suitable organic molecules [22, 25]. When the synthesis process occurs in two steps, an additional deintercalation step becomes necessary. Thus, the objective of this study was to segregate kaolinite from the other mineral components present in the IOT, to use it as a raw material for the synthesis of halloysite-like nanotubes to compare its performance with high-purity products.

EXPERIMENTAL

Materials and methods: iron ore tailings (IOT), collected from the thickener underflow of an iron ore industry (Vale S.A., Minas Gerais, Brazil), were selected for their kaolinite content and one sample with relatively high kaolinite content (~9.7%) was selected for this study. Two samples of high purity kaolinite (Standard Amazon, Amazon Basin, Brazil, and Sigma-Aldrich) were also used as received without further purification. The chemical composition of Amazon kaolinite (K-A) and Sigma-Aldrich kaolinite (K-SA) was determined by chemical analysis, and the results were expressed in the respective oxide form; iron content was determined using a wet method; the other elements were analyzed using

Table I - Results of chemical analysis (wt%) of the samples K-A and K-SA.
[Tabela I - Resultados de análise química (% em massa) das amostras K-A e K-SA.]

Sample	Fe_2O_3	SiO_2	Al_2O_3	P_2O_5	MnO	CaO	MgO	TiO_2	Na_2O	K_2O	LOI
K-A	1.66	44.77	38.20	0.20	0.00129	0.0150	0.021	0.963	0.239	0.009	14.09
K-SA	0.44	49.14	35.21	0.38	0.00052	0.0093	0.133	0.336	-	-	11.97

LOI - loss on ignition.

inductively coupled plasma optical emission spectroscopy (ICP-OES). The iron content of the samples was determined by the titanium (III) chloride reduction method, according to ABNT NBR ISO 2597-2 [29], in which the titration is based on an oxy-reduction reaction between the titrate (Fe^{2+}) and the titrant ($K_2Cr_2O_7$). Approximately 0.400 g of each sample was dissolved in hot HCl, reduced, oxidized, and finally titrated with a standard potassium dichromate solution to determine iron content. For ICP-OES analysis, approximately 0.200 g of each sample was weighed in platinum crucibles, fused with sodium tetraborate and sodium carbonate, and then solubilized with 25% (v/v) HCl solution and diluted to 100 mL with distilled water. The results of the chemical analysis of K-A and K-SA are shown in Table I.

Hydrochloric acid (HCl, Fmaia), dimethyl sulfoxide (DMSO, Fmaia), methanol (MeOH, Fmaia), cetyltrimethylammonium chloride (CTMACl, Sigma-Aldrich), cetyltrimethylammonium bromide (CTAB, Sigma-Aldrich), isopropanol (Fmaia), 1,4-dioxane (Fmaia), ethanol (Fmaia) and hexylamine (C6N, Fmaia) of analytical grade purity (>99.0%) were used as received. To segregate the kaolinite from the IOT, acid leaching was performed using a hydrochloric acid solution and distilled water, 70% (v/v). To this solution, a certain amount of iron ore tailings (solid:liquid=1:6) was added at 120 °C for 2 h. After cooling, the acid-insoluble residue was separated by vacuum filtration, dried in air and stored for further characterization and synthesis studies. To prepare DMSO-intercalated kaolinite (kaolinite-DMSO), 10 g of kaolinite (high-purity and IOT segregated) was added into a mixture of 60 mL DMSO and 10 mL distilled water, stirred and refluxed at 150 °C for 7 h. The solid in the mixture was separated by centrifugation and washed 3 times using 1,4-dioxane and isopropanol to eliminate the excess DMSO. The product was dried at 60 °C for 24 h [25]. To prepare methoxy-modified kaolinite (kaolinite-MeOH), 5 g of kaolinite-DMSO was added into 100 mL of methanol (MeOH) and stirred for 7 days at room temperature. The solid in the mixture was separated by centrifugation and used while wet for the synthesis process [25]. To prepare halloysite-like nanotubes in a one-step route, approximately 1 g of wet kaolinite-MeOH was added into a 40 mL MeOH solution of CTMACl 1 M and 40 mL MeOH solution of CTAB 1 M and both stirred at 80 °C for 24 h. The solid in the mixture was separated by centrifugation, washed 6 times with ethanol to remove the agent (CTMACl and CTAB) excess, and then dried at room temperature. To prepare halloysite-like nanotubes in a two-step route, approximately 0.5 g of wet kaolinite-MeOH was added into 15 mL of C6N. The intercalation compounds were redispersed in 1,4-dioxane (20 mL) and sonicated for 10 min for the swelling. The process was repeated 3 times.

Instrumental techniques: powder X-ray diffraction (XRD) patterns were obtained using a PANalytical Empyrean with CoKα radiation (λ=1.78896 nm) operating at 40 kV and 40 mA. The diffractograms were obtained in the range 5-80° (2θ) with a step size of 0.013°. Mössbauer spectra were collected at room temperature (298 K) with a spectrometer operating in constant acceleration mode with triangular reference signals using a ^{57}Co source diffused on an Rh sheet. The data accumulation was done with a multichannel analyzer with 1024 channels and a speed range of -11 to +11 mm/s. The calibration of the spectrometer was done by collecting the spectra of the metallic iron at room temperature. The spectrum adjustment was performed using Lorentzian lines. The numerical results of the adjustments are reported as the hyperfine parameters, which are the magnetic hyperfine field (B_{hf}) given in T, relative subspectral area (RA) in %, quadrupole splitting ($2\varepsilon_Q$) and isomer shift (δ) given in mm/s. Isomer shifts are given with reference to metallic iron (α-Fe) at room temperature. The samples (high-purity and IOT segregated kaolinites) were previously sprayed. Samples for field emission gun scanning electron microscopy (FESEM) were analyzed with a FEI Quanta FEG 3D microscope. The clay mineral powder was ultrasonically dispersed in ethanol for 10 min, rested on a silicon base, and then dried at room temperature; the samples were carbon-coated for FESEM. The equipment used for chemical analysis was the Varian 715-ES ICP-OES; the methodology used for sample preparation was described before.

RESULTS AND DISCUSSION

Initially, the characterization of the high-purity products was carried out to verify the chemical and morphological quality of the product segregated from IOT.

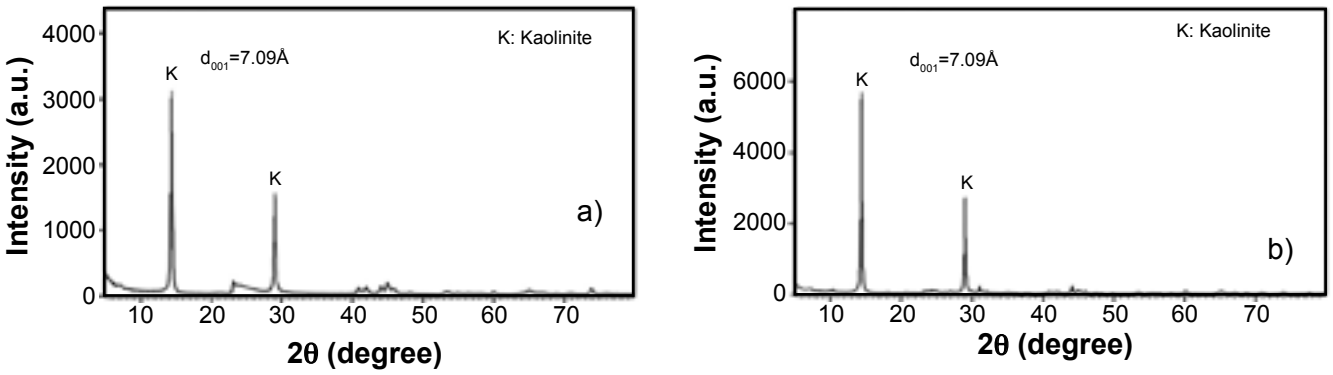

Figure 1: XRD patterns of high-purity kaolinite: a) K-A; and b) K-SA.
[Figura 1: Padrões de DRX de caulinita de elevada pureza: a) K-A; e b) K-SA.]

Amazon kaolinite and Sigma-Aldrich kaolinite

XRD: the X-ray diffractograms of K-A and K-SA are shown in Figs. 1a and 1b, respectively. Both kaolinite samples showed a typical diffraction pattern and were predominantly composed of clay mineral kaolinite, presenting a typical pattern of diffraction of a kaolin with a high degree of purity, that is, presented a well-defined and intense peak for kaolinite in its characteristic angle (~14° 2θ, CoKα), which refers to the distance between planes (001) of the monoclinic structure, with characteristic basal reflection of 7.09 Å (d_{001}).

Mössbauer spectroscopy: the Mössbauer spectrum of the K-A (Fig. 2a) shows two components with very different isomer shifts (δ) and quadrupole splittings ($2\varepsilon_Q$): i) a doublet of Fe^{3+} with $2\varepsilon_Q$ of 0.65 mm/s and δ of 0.25 mm/s; ii) a doublet of Fe^{2+} with $2\varepsilon_Q$ of 2.52 mm/s and δ of 1.31 mm/s. The relative subspectral area (RA) of the Fe^{3+} doublet is 71%, while that of the doublet Fe^{2+} is 29%. The Mössbauer spectrum of the K-SA (Fig. 2b) show: i) a doublet of Fe^{3+} with $2\varepsilon_Q$ of 0.43 mm/s and δ of 0.26 mm/s. According to [30-32], it is possible to predict that both samples have iron in the kaolinite structure. The Fe^{3+} doublet, identified in the two samples, indicated the presence of Fe^{3+} in an octahedral position of kaolinite, replacing Al. The Fe^{2+} doublet, identified in the K-A, indicated the presence of Fe^{2+} in the octahedral position, assumed to be structural, substituting trioctahedral Al. However, according to the predicted values in the literature, it is not possible to discard the possibility that iron was present in the muscovite structure. As the RA of the doublet is proportional to the amount of the structural iron in kaolinite, the structural octahedral Fe^{3+} content in the kaolinite was higher than the Fe^{2+} content.

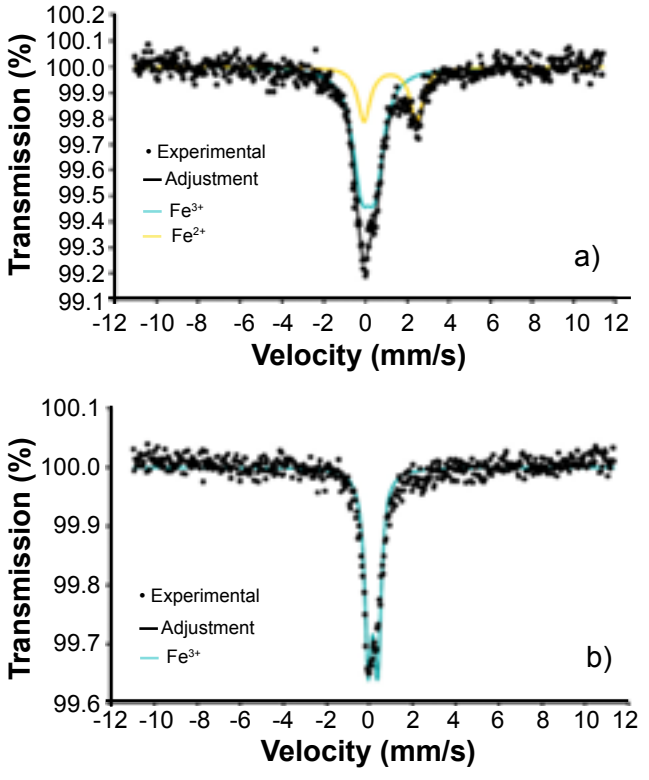

Figure 2: Mössbauer spectrum of the high-purity K-A (a) and K-SA (b).

[Figura 2: Espectro Mössbauer de caulinita de elevada pureza K-A (a) e K-SA (b).]

FESEM: as indicated by the FESEM images of K-A and K-SA (Fig. 3), the platy-like kaolinite particles were characterized by euhedral to subhedral crystals, the latter due to particles with irregular shapes, in plate-like shape with a predominantly hexagonal profile that reflected the well-defined pseudo-hexagonal character of the structure of this clay mineral. Sigma-Aldrich high-purity kaolinite (K-SA) had a complex basal surface, showing large particles with a high occurrence of micro-islands with very small dimensions, also presenting broken and irregular edges. Although we cannot claim that there is a correlation between grain morphology and crystal structure only by SEM images, Zbick and Smart [33] and Du et al. [34] correlate complex characteristics and lamellar size with the degree of crystallinity of the clay mineral. This complex basal surface was similar to a poorly crystallized kaolinite described in [34]. Amazon kaolinite (K-A) presented a characteristic morphology of kaolinite derived from residual weathering, which is the incidence of this sample. Most crystals were small particles and had well-defined edges and angles, exhibiting typical kaolinite morphology with a pseudo-hexagonal plate showing low stacking levels. According to [33], these characteristics corresponded to well-crystallized kaolinite. However, small rounded crystal aggregates with smaller particle size coexisted.

According to [35], the presence of iron in the kaolinite structure contributes to the reduction of the structural order of clay mineral. According to the results of Mössbauer spectroscopy, both samples had structural Fe^{3+} ions. The results indicated that the presence of this ion did not directly affect regularity and the presence of surface defects of the clay mineral crystals. However, only in the structure of the K-A Fe^{2+} ions were identified. The Fe^{2+}, that replaces trioctahedral Al, was responsible for the reduction of the structural order of the clay mineral, inducing the roundness of the crystals. This phenomenon was possibly due to an electrical deficiency; in this case, Fe^{2+} ions did not replace trioctahedral Al^{3+} ions at a ratio of $3Fe^{2+}$:$2Al^{3+}$ to maintain charge neutrality [36, 37]. It is well established that the Si tetrahedral sheet is larger than the Al octahedral sheet. This mismatch induces structural stress on the clay mineral that can be compensated by various types of structural distortion. One is the rotation of the tetrahedron from the ideal hexagonal arrangement to ditrigonal shape. The second is the slope of the tetrahedron, just as the basal oxygen does not occur in the same plane. The inclination of the tetrahedron takes the apical Si-O bond to polarize from the perpendicular direction of the plane (001). However, distortions in the tetrahedron and octahedron cannot totally release stress, possibly due to interlayer hydrogen bonds. This accumulated stress is possibly the reason that large crystallites occur in the form of booklets, such as that shown in Sigma-Aldrich kaolinite.

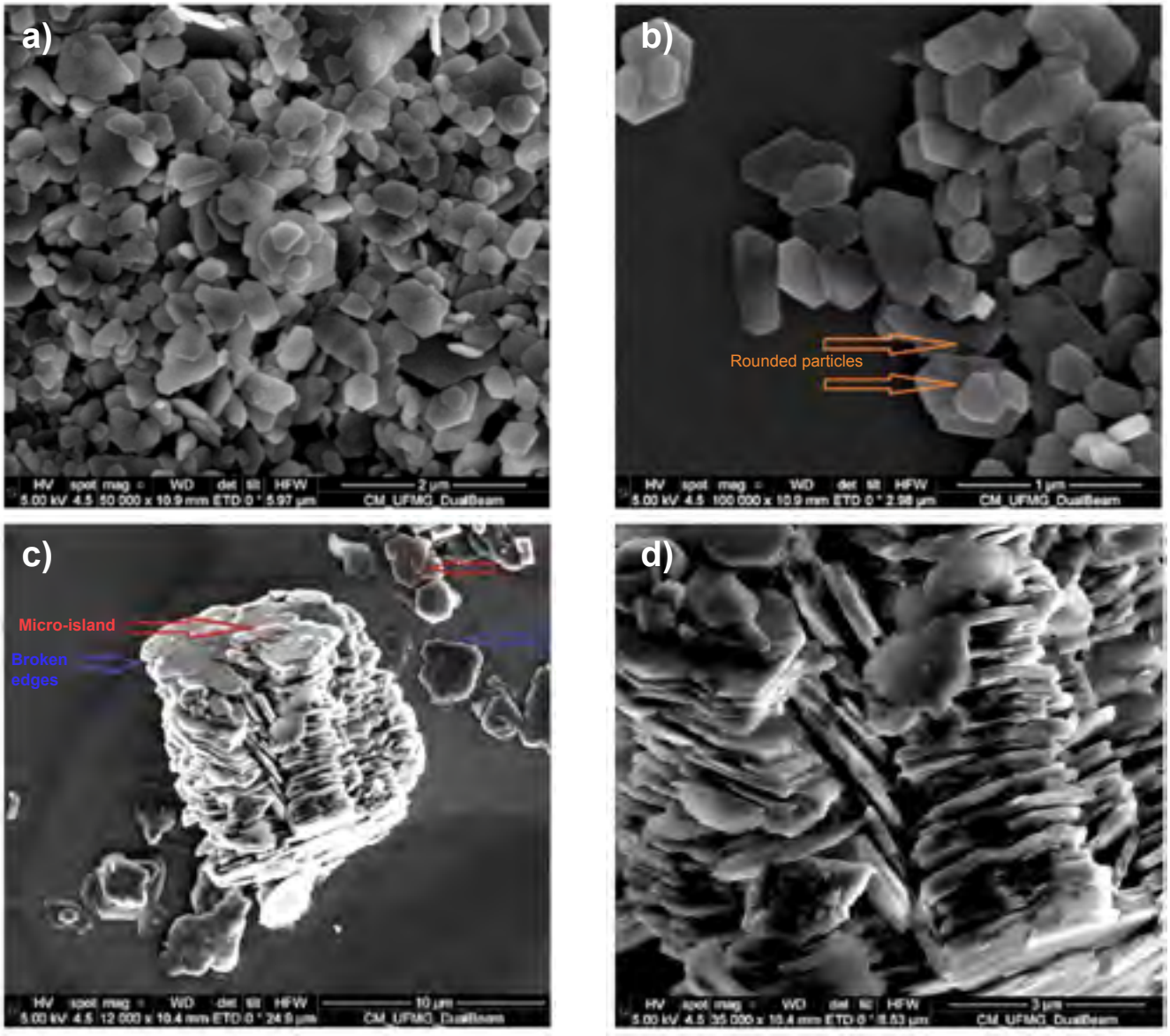

Figure 3: FESEM images of K-A (a,b) and K-SA (c,d).
[Figura 3: Imagens de MEVFEG de K-A (a,b) e K-SA (c,d).]

Iron ore tailings and acid-insoluble residue

The chemical composition of the selected IOT (Table II) showed that iron oxide, silica, and alumina were the major constituents. Silica and alumina were the major constituents of acid-insoluble residue (AIR) with minor amounts of iron oxide. The value of loss on ignition (LOI) of IOT was due to the presence of a substantial amount of moisture and structural water (loss by dehydroxylation of goethite and kaolinite).

XRD: the XRD patterns in Figs. 4a and 4b show the IOT before and after acid leaching, respectively. The solid product obtained after acid leaching is the AIR. Unlike IOT, which had hematite, goethite, quartz, and kaolinite as major phases, in AIR, the major mineralogical phases identified were muscovite, quartz, and kaolinite. It was possible to verify that the intensity of the characteristic peak of kaolinite was higher than the other mineralogical phases, indicating the majority presence of the crystalline phase of this clay mineral. A quantitative analysis of the mineralogical composition of AIR was performed through the application of the Rietveld method. Comparing the final results of the quantification of the phases (56% kaolinite, 2% hematite, 40% quartz, and 2% muscovite) with initial composition of IOT (9.7% kaolinite, 23.8% hematite, 57.3% goethite, 8% quartz, and magnetite, gibbsite, and mica <1%), it is stated that there was a significant concentration of kaolinite. The presence of quartz was significant (40%) because HCl used in leaching did not solubilize quartz. The quantitative value of kaolinite identified by applying the Rietveld method exceeded the value of a simple rational calculation. Considering that 18.33 wt% of the alumina in AIR corresponded to kaolinite (excluding impurities such as alumina of gibbsite and muscovite), a maximum of 46.4%

Table II - Results of chemical analysis (wt%) of the IOT and AIR.
[Tabela II - Resultados de análise química (% em massa) do IOT e AIR.]

Sample	Fe_2O_3	FeO	SiO_2	Al_2O_3	P_2O_5	MnO	CaO	MgO	TiO_2	LOI
IOT	72.26	0.148	12.77	6.28	0.36	0.36	0.011	0.136	0.216	7.80
AIR	0.32	-	73.63	18.33	0.11	<0.005	0.006	0.103	0.748	6.94

IOT - iron ore tailings; AIR - acid-insoluble residue; LOI - loss on ignition.

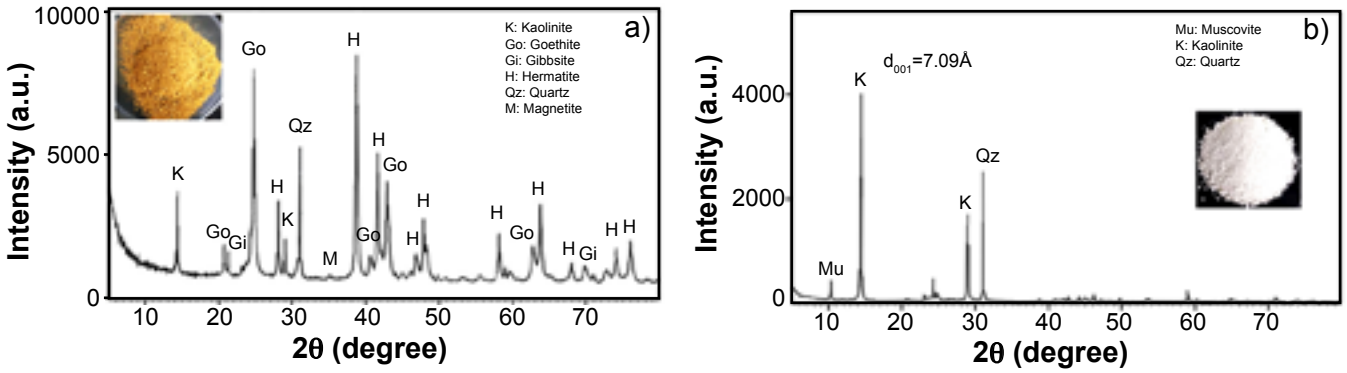

Figure 4: XRD patterns of IOT (a) and AIR (b); the inset shows the image of the sample.
[Figura 4: Padrões de DRX de IOT (a) e AIR (b); o inserto mostra imagem da amostra.]

of kaolinite should be obtained. The 56% kaolinite value obtained by the Rietveld method, therefore, exceeded an experimental margin of error, overestimating the result.

Comparing the AIR and IOT diffractograms, it is possible to affirm that the acid leaching procedure was adequate to concentrate the kaolinite present in the IOT, although the content of impurities such as quartz was high. The remaining ferrous phase, hematite, was present in very low quantity, practically undetectable by X-ray diffraction. It is emphasized that the mineralogical composition of the AIR resembled the mineralogical composition of K-SA, except for low amounts of remaining ferrous phases that could be eliminated by a low additional leaching time of the IOT. In addition, the $FeCl_3$-rich liquor generated after the acid leaching of IOT can be used for the synthesis of alternative nanomaterials at a low cost, such as hematite nanoparticles [38], magnetite nanoparticles [39, 40], among others. Synthesis using this liquor minimizes the impact caused by this step of the kaolinite segregation process.

Mössbauer spectroscopy: the Mössbauer spectrum of the AIR (Fig. 5) shows three components: i) an external sextet due to hematite with a magnetic hyperfine field (B_{hf}) of 51.6 T, isomer shift (δ) of 0.37 mm/s, and quadrupole splitting ($2\varepsilon_Q$) of 2.52 mm/s. These parameters were similar to standard hematite with high crystallinity and low (or no) isomorphic substitution [41]; ii) an internal sextet due to goethite with B_{hf} of 38.0 T, δ of 0.36 mm/s, and $2\varepsilon_Q$ of -0.26 mm/s [41]; iii) a doublet of Fe^{3+} with $2\varepsilon_Q$ of 0.37 mm/s and δ of 0.23 mm/s. It is suggested that this doublet is relative to the iron present in the clay mineral structure. The relative subspectral area (RA) of the hematite was 62%, goethite was 28%, and Fe^{3+} was 10%. The low RA of this ion indicated a low presence of structural iron atoms (Fe^{3+}) in the clay mineral.

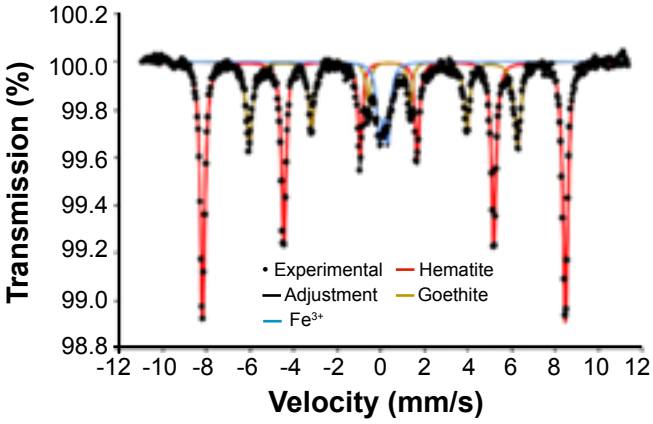

Figure 5: Mössbauer spectrum of AIR.
[Figura 5: Espectro Mössbauer do AIR.]

FESEM: the FESEM images of AIR (Fig. 6) show that the obtained kaolinite presented similar morphology of K-A and K-SA. Similar to K-SA, the segregated product presented large crystallites, which justified the identification of booklet stacking, possibly due to high levels of structural stress [42]. However, there was a low occurrence of micro-islands and fewer occurrences of defects in the edges of the clay mineral, presenting a surface of lower complexity. These characteristics indicated well-crystallized kaolinite and confirmed that the presence of the structural Fe^{3+} ion does not directly affect the surface characteristics and crystallite size [33, 34].

DMSO-intercalated kaolinite

The pre-intercalation of kaolinite is the first step

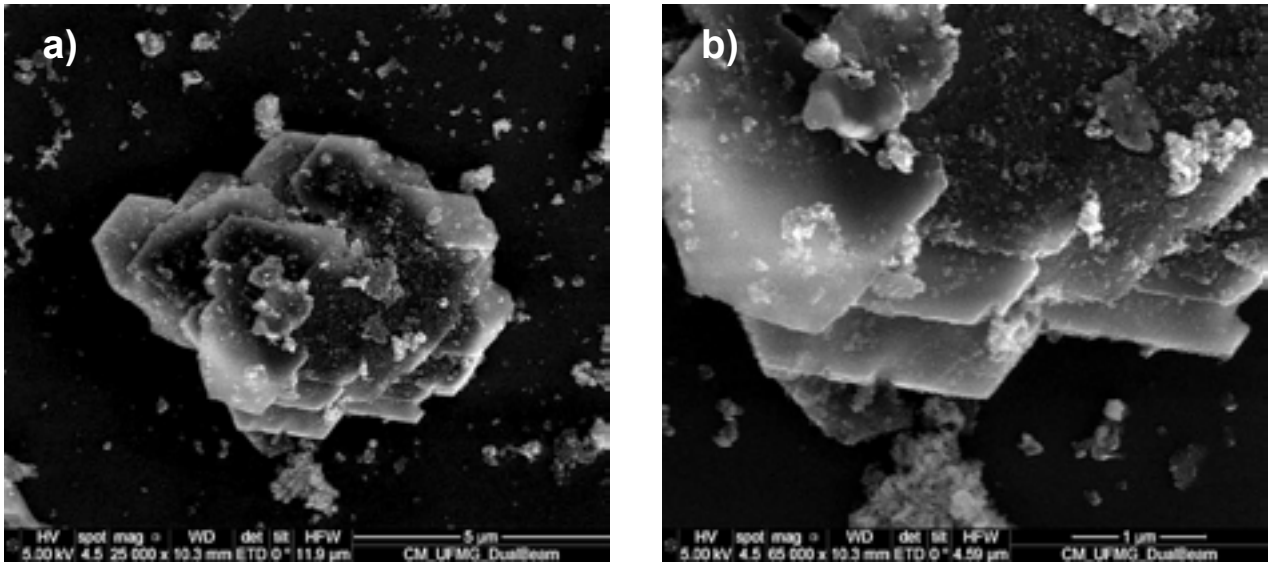

Figure 6: FESEM images of kaolinite present in AIR from IOT.
[Figura 6: Imagens de MEVFEG da caulinita presente no AIR obtido do IOT.]

responsible for increasing the distance between the kaolinite layers, and this procedure was performed with DMSO. The obtained kaolinite-DMSO exhibited XRD pattern similar to that of DMSO-intercalated kaolinite previously reported [25, 26, 43-45]. The diffraction pattern showed a significant change of the characteristic kaolinite peak from ~14° 2θ (d_{001}=7.09 Å) to ~9° 2θ (d_{001}=11.40 Å, Fig. 7). This change is characteristic of the intercalation of a DMSO monolayer giving rise to a 4.31 Å increase in the basal space. In the three samples of kaolinite (high-purity and present in AIR), there was intercalation with DMSO with variation in the degree of intercalation. In the interlayer space of kaolinite, the oxygen of S=O group of DMSO forms hydrogen bonds with inner surface hydroxyls of the gibbsite sheet of the kaolinite layer (O-H---O bonds) and one methyl group of DMSO is trapped into the ditrigonal hole in the tetrahedral sheet (C-H---O bonds) with the other S-C bond nearly parallel to this sheet [25].

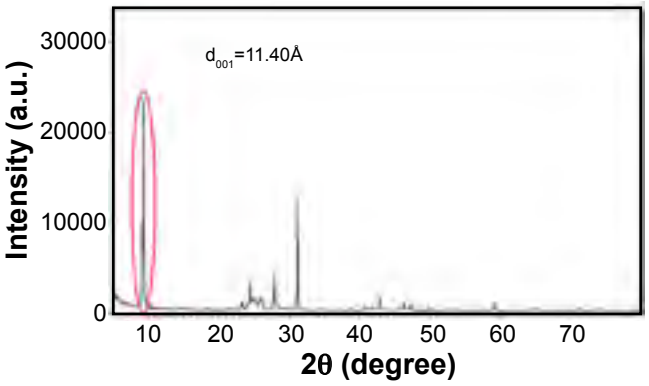

Figure 7: XRD pattern of the kaolinite-DMSO present in the AIR from IOT, highlighting the region that indicates DMSO-intercalated kaolinite.
[Figura 7: Padrão de DRX da caulinita-DMSO presente no AIR obtido do IOT, com destaque para a região que indica caulinita intercalada com DMSO.]

Differences in the degree of intercalation may be related to the crystallinity of kaolinite, the accumulated structural stress level (due to the mismatch between tetrahedral and octahedral sheets), the particle size of the crystallite, and the distribution of the defects of the clay mineral [23, 42, 46, 47]. The highest degree of intercalation was achieved for K-SA and kaolinite present in AIR, both close to approximately 100% of intercalation (calculated by Eq. A), and it was lower for the K-A with approximately 76.7% of intercalation. These results indicated that the presence of Fe^{2+} ion, responsible for a decrease in the particle size of the crystallite, directly affected the intercalation rate.

$$\%\text{intercaltion} = \frac{I(001)_{complex}}{I(001)_{complex} + I(001)_{kaolinite}} \qquad (A)$$

where $I(001)_{complex}$ and $I(001)_{kaolinite}$ are the intensities of (001) diffractions of DMSO-intercalated kaolinite and kaolinite, respectively [48]. K-SA and kaolinite in AIR had a larger crystallite particle size when compared to K-A, and was present in the form of booklets, possibly because they presented higher structural stress. The higher the stress, the faster and higher are the indexes of intercalation [42].

Methoxy-modified kaolinite

The synthesis of methoxy-kaolinite was performed to obtain an organic/inorganic hybrid with high reactivity and a hydrophobic interlayer able to inhabit the intercalating region (alkylamine or quaternary ammonium salt). In the three kaolinite samples, methoxy-modified kaolinite (kaolinite-MeOH) exhibited (001) diffractions with a d_{001} value of 10.80 Å (Fig. 8), with variations in the degree of intercalation, according to the DMSO intercalation. Kaolinite presents in the AIR from IOT had approximately 100% of intercalation

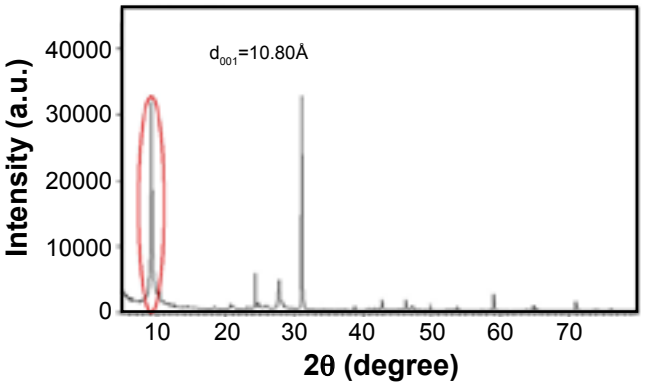

Figure 8: XRD pattern of methoxy-modified kaolinite present in AIR from IOT, highlighting the region that indicates kaolinite-MeOH.
[Figura 8: Padrão de DRX da caulinita metoxi-modificada presente no AIR obtido do IOT, com destaque para a região que indica caulinita-MeOH.]

(similar to kaolinite-DMSO). This configuration indicated a typical interlayer structure of methoxy-modified kaolinite before drying, which was composed of monolayer methanol molecules between unmodified siloxane surface and the methoxy-modified inner surface in which the aluminol (AlOH) groups in the interlayer space were converted to AlOMe groups, accompanied by the loss of hydrogen from methanol (MeOH). Besides, a small number of water molecules may have been generated by the combination of the hydrogen loss of MeOH and the hydroxyl groups of kaolinite [25, 44].

When intercalated with methanol, after having been pre-intercalated with a suitable organic agent, the basal interplanar distance (d_{001}) of methoxy-modified kaolinite was ~11 Å, before drying. According to [49], when the methoxy-kaolinite is dried, the value of d_{001} is close to 8.6 Å; when this product undergoes heating to 150 °C, the value of d_{001} decreases to values close to 8.2 Å without loss of methoxy groups. Thus, the dry methoxy-kaolinite is partially hydrated and a number of MeOH or water molecules are possibly present in the interlayer region of kaolinite. The reduction of basal distance is attributed mainly to the escape of methanol molecules from the interlayer region during the drying process [25]. The value of Δd_{001} between pure kaolinite (K-A, K-SA, and present in AIR; 7.09 Å) and synthesized methoxy-modified kaolinite (10.80 Å) was 3.71 Å, which is equal to the diameter of the methanol molecule, indicating that there were methanol molecules in the interlayer region of clay mineral [49, 50]. The d_{001} value for the kaolinite-MeOH (10.80 Å) measured after drying under ambient conditions was larger than those previously reported (8.2-8.6 Å). Due to insufficient reaction time, methyl groups away from the aluminol surface were not fully embedded into SiO_6 macrorings of the adjacent silicate surface, that is, methanol molecules that remained 'loose' in the interlayer region of kaolinite even after the mild drying condition contributed to the larger basal space. The coexistence of grafted methanol molecules and unsubstituted DMSO molecules were not confirmed. If the characteristic peak of kaolinite-DMSO were detected, it would be possible to attribute the largest space in the interlayer region of kaolinite due to the coexistence of these molecules [26].

Kaolinite nanotubes

In the one-step route, the key to the morphology change is the intercalation of quaternary ammonium salts in the interlayer region of kaolinite, which results in the reduction of structural stiffness and weakening of the interlayer hydrogen bonds [3]. Otherwise, in the two-step route, the deintercalation of the alkylamine promotes morphological change [23]. The efficiency of the formation of nanotubes depends mainly on the type of guest species. In the one-step route, the following factors are determinant: the group type present at the end of the quaternary ammonium salt (typically called the 'head group' of the ammonium salt), the carbon chain length, and the equilibrium anion of charge (Br^-, Cl^-). Another important parameter for the rolling of the layers is the poor interaction between the organic cation (a head group of the intercalating agent) and the methoxy-modified octahedral sheet. Guest species containing trimethylammonium groups [$(CH_3)_3N^+H$] are commonly used because of the interactions between the guest species and the interlayer surface of the methoxy-modified kaolinite are relatively weak, allowing a flexible matrix of interlayer guest species and resulting in simultaneous intercalation and rolling [22]. The organic compounds used were cetyltrimethylammonium bromide [CTAB-$CH_3(CH_2)_{15}N(Br)(CH_3)_3$] and cetyltrimethylammonium chloride [CTMACl-$CH_3(CH_2)_{15}N(Cl)(CH_3)_3$].

The FESEM images of methoxy-modified K-SA reacted with CTAB are shown in Fig. 9. When the methoxy-modified K-SA reacted with CTAB, the layers of the clay mineral began to roll and a number of nanotube structures were formed. However, the images also showed the presence of platy or partially curled kaolinite layers. These structures are the result of incomplete delamination and rolling of kaolinite layers. Even though the procedure was carried out at elevated temperature (80 °C), which facilitated the diffusion of organic molecules in the interlayer region of the kaolinite, possibly the concentration of the intercalating and the reaction time was insufficient to promote efficient delamination and rolling. On the other hand, according to [23, 51], the formation of nanotube structures depends on the efficiency of the interlayer modification steps, the structural order, and the particle size of the starting clay mineral. According to the X-ray diffraction and FESEM images, K-SA had high purity, but was poorly crystallized, due to the identified microdefects; however, it presented crystals with relatively large particle sizes that favor the processes of intercalation [42, 44]. These factors may explain the formation of nanotube structures, but with low occurrence. It was possible to observe that the length of the nanotube structures formed was smaller than the lateral dimension of the kaolinite matrix. This result indicated that some

kaolinite layers were fragmented during the intercalation process, indicating possible aggressiveness of CTAB to kaolinite [22, 25]. Fig. 9 suggests that the formation of nanotubes was initiated by the delamination of the surface layers. As a result, nanotube structures remained bound to the platy kaolinite, suggesting that successive intercalation steps would possibly increase the number of rolled layers, affecting deeper layers within the kaolinite particles [23].

Due to the surface characteristics and low presence of microdefects in the kaolinite present in the AIR from IOT, it is possible to affirm that it was a well-crystallized clay mineral, better than K-SA [33, 34]. The particle sizes of the crystallites of the two kaolinites were similar. The variation of the synthesized products was possibly related to the ammonium salt used and the characteristics of the starting clay minerals. According to [51], the number of rolled layers is proportional to the structural order of kaolinite. The products synthesized using CTMACl and kaolinite from IOT (Fig. 10) were formed by fully rolled plate, showing that the delamination and rolling processes were more intense and the combination between a kaolinite with better structural order and CTMACl was more effective in promoting delamination and rolling of the kaolinite layers, when compared to the procedure using CTAB. The intercalation procedures are more effective in better crystallized raw materials [23, 42]. The results also indicated that CTMACl was less aggressive to kaolinite since no fragmented plate was observed and the CTMACl head group had weaker interaction with the methoxy-modified layer when compared to the CTAB. In addition, the intercalating agents used had carbonic chains of the same size, varying only the volume of the counterion, Br^- or Cl^-. When bromine, which has a higher atomic radius in relation to chlorine, is present in the ammonium salt, the appropriate carbon chain has a lower number of carbons, which may justify more aggressive intercalation when using CTAB [22]. By increasing the

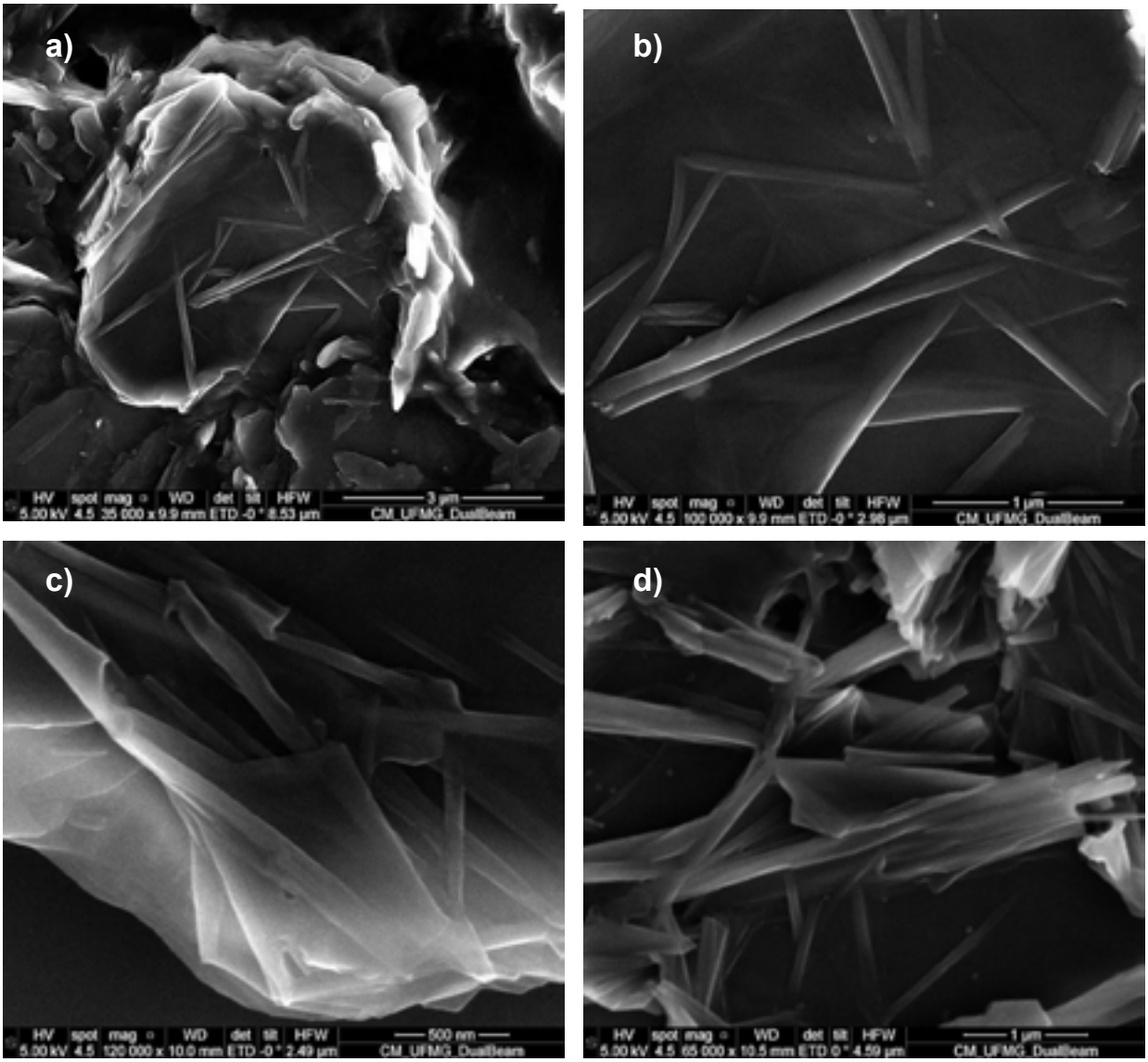

Figure 9: FESEM images of methoxy-modified K-SA reacted with CTAB.
[Figura 9: Imagens de MEVFEG da K-SA metoxi-modificada após reação com CTAB.]

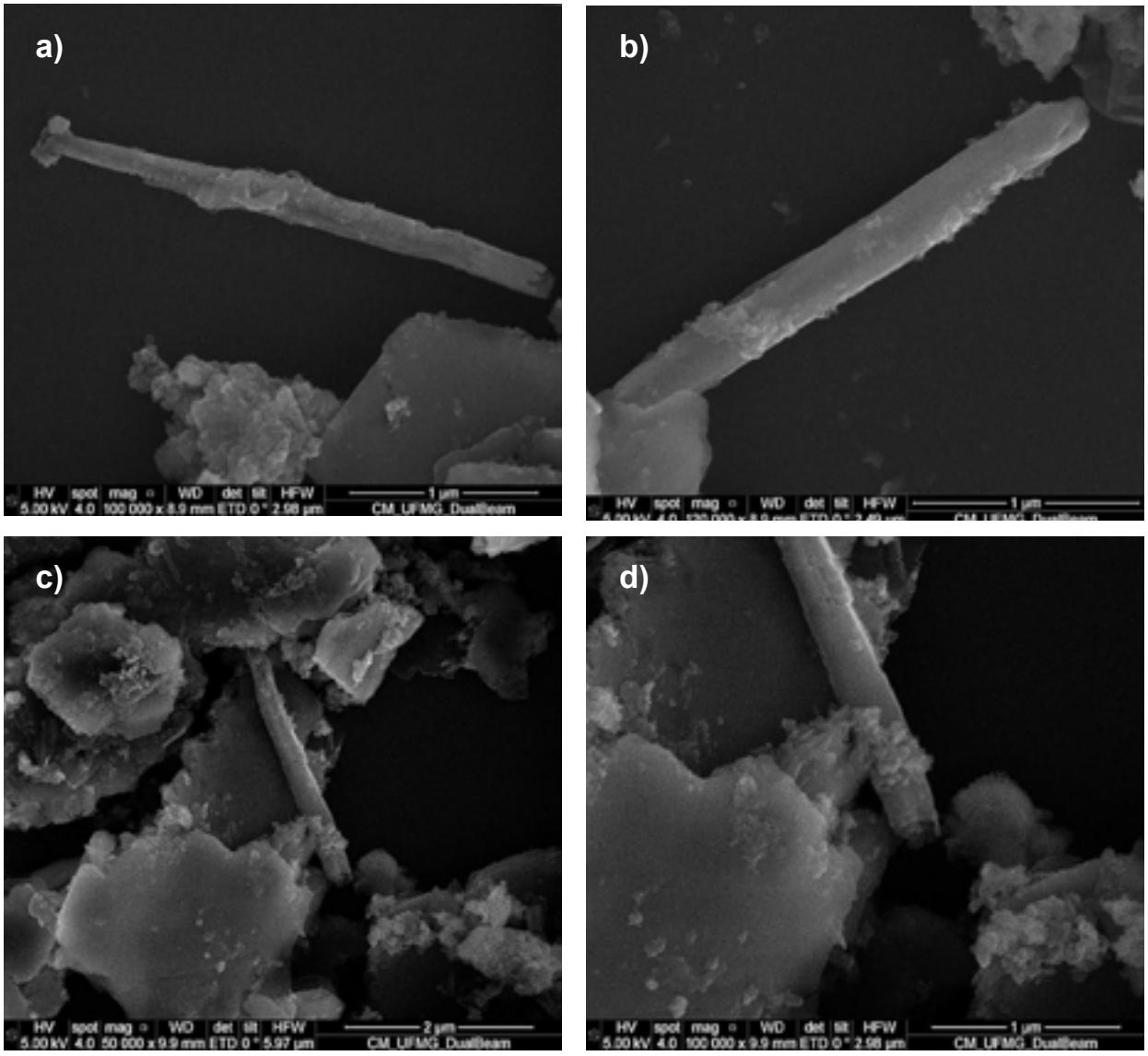

Figure 10: FESEM images of methoxy-modified kaolinite present in the AIR from IOT, reacted with CTMACl.
[Figura 10: Imagens de MEVFEG da caulinita metoxi-modificada presente no AIR obtido do IOT, após reação com CTMACl.]

concentration of the intercalating agent (CTMACl) or by performing repeated procedures, the synthesis yield may be increased, and the concentration of nanotubes in the sample may increase. As observed in the XRD pattern of the AIR sample (Fig. 4b), muscovite and quartz mineralogical phases were identified. These mineralogical phases apparently influenced the yield of the synthesis process. Additional AIR purification steps can eliminate these phases and increase the concentration amount of nanotube. According to [22, 25, 26], the length of the kaolinite nanotubes synthesized using the same intercalating agent (CTMACl) was 100-850, 150-700, and 300-2000 nm, respectively. The product synthesized in this study had an average size of 2990 nm. This increase may be due to the lateral dimension of the kaolinite layers being larger than those used in the cited studies. These results were in agreement with Matusik et al. [23], who affirm that the length of the nanotubes depends on the lateral dimension of the plate of the delaminate clay minerals.

In the two-step procedure, a strong interaction of the amino group with the methoxy-modified kaolinite leads to the formation of nanotube structures because the guest species form a rigid matrix of interlayer intercalated species. Moreover, the adjustment of the interaction between the intercalating agent and the deintercalation promoting solvent must be controlled to achieve a satisfactory degree of delamination and rolling [22]. Another important parameter is the flexibility of the guest molecules. As shown in [22], when larger and more flexible molecules are used to intercalate the methoxy-kaolinite, such as octadecylamine (C18N) there is no formation of nanotubes, whereas when smaller molecules such as hexylamine (C6N) are used the formation of nanotube structures is observed. In the two-step procedure, hexylamine [C6N-$CH_3(CH_2)_5NH_2$] was used as the intercalating and 1,4-dioxane as the deintercalating solvent. In the product synthesized from the two-step procedure (K-SA reacted with C6N, Fig. 11), it was possible to observe superficial nanotube

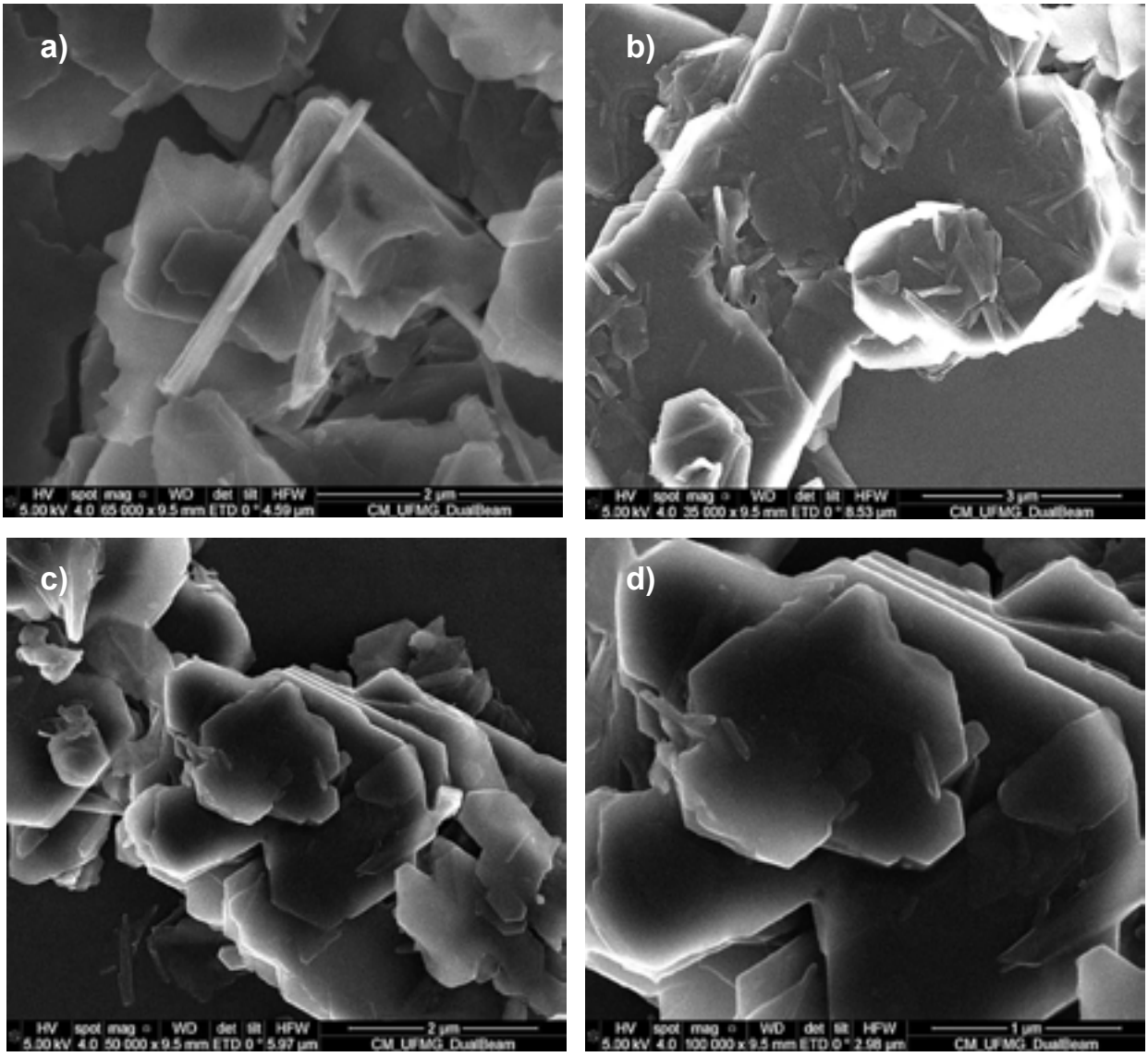

Figure 11: FESEM images of methoxy-modified Sigma-Aldrich kaolinite reacted with C6N.
[Figura 11: Imagens de MEVFEG da caulinita Sigma-Aldrich metoxi-modificada após reação com C6N.]

structures, formed by the delamination of surface clay mineral layers, adhered to the platy kaolinite particles, similar to the product synthesized using CTAB. This fact may be associated with the low concentration of intercalating/deintercalating agents, insufficient intercalation/deintercalation steps, and the use of poorly crystallized kaolinite. Another factor that diminishes the reaction yield is a possible low interaction between the C6N and the 1,4-dioxane, which implies a low deintercalation. In Figs. 11c and 11d, it is possible to observe a kaolinite plate with high basal interplanar distance indicating that the intercalation of alkylamine occurred efficiently. However, due to the low interaction with the deintercalating solvent, the formation of nanotube structures was low. By adjusting the interaction between the intercalation compound and the deintercalation solvent, the efficient delamination and rolling can be achieved [22].

No nanotube structures were obtained using the K-A as raw material, regardless of the intercalating agent used. Although the platy kaolinite was well-defined and presented high structural order, according to [42, 52], the particle size strongly interferes with the kaolinite intercalation processes, being more determinant than the crystallinity of the clay mineral. The K-A, similar to the K-SA and the kaolinite obtained from the IOT, presented the Fe^{3+} ion in its structure; however, only the Amazon kaolinite presented structural Fe^{2+}, resulting in smaller particle size. This may justify a lower yield in the intercalation with dimethyl sulfoxide (76.7%), consequently inefficiency in the formation of the methoxy-kaolinite, and the intercalation with the intercalating agents possibly did not occur, or there was not enough time for the intercalation reaction occur, not resulting in morphological alteration.

CONCLUSIONS

Although at the initial stages, the results achieved

were encouraging. Even in very low quantities, nanotubes were observed regardless of the intercalating agent used (cetyltrimethylammonium bromide - CTAB, cetyltrimethylammonium chloride - CTMACl, and hexylamine - C6N). The methods used to concentrate the kaolinite present in the iron ore tailings were efficient, considering the exploratory and scientific character of this experiment. The impurity phases identified in the acid-insoluble residue possibly can be removed by further steps. Although a quantitative analysis was not performed, it was possible to observe the formation of nanotubes from the segregated kaolinite. The segregated kaolinite, even with the Fe^{3+} ion in its structure, was highly intercalated with dimethyl sulfoxide (DMSO). Methoxy-modified kaolinite was synthesized because, as shown by FESEM, nanotube structures were obtained after the reaction of the methoxy-modified product with CTMACl. The reaction yield using the acid-insoluble residue as a raw material possibly may be increased when synthesis is carried out after the remaining impurities are completely eliminated, that is, using an acid-insoluble residue with a higher percentage of kaolinite; additionally, increasing the concentration of the intercalating agent or performing repeated intercalation procedures. Tubular structures were not observed using Amazon kaolinite (K-A) as raw material, possibly due to the presence of structural Fe^{2+} ions. It is important to emphasize that the presence of Fe^{3+} ions in the kaolinite structure did not interfere in the efficiency of the intercalation with DMSO, methoxy-modification, intercalation, and synthesis of nanotube structures. A comparative analysis of the structure of synthesized products and natural halloysite nanotubes is the object of study of the next stages of the project.

ACKNOWLEDGMENTS

Financial support from the Brazilian Mining Company Vale S.A. and the technological support from CM-UFMG are gratefully acknowledged.

REFERENCES

[1] L.C.R. de Andrade, "Caracterização de rejeitos de mineração de ferro, in natura e segregados, para aplicação como material de construção civil", Doct. Thesis, Fed. Un. Viçosa, Brazil (2014).
[2] D. Janacek, L. Kvitek, M. Karlikova, K. Pospiskova, I. Safarik. Appl. Clay Sci. **162** (2018) 10.
[3] P. Yuan, A. Thill, F. Bergaya, *Nanosized tubular clay minerals, halloysite and imogolite*, Elsevier (2016).
[4] C.E.Y. Erpek, G. Ozkoc, U. Yilmazer, Polym. Compos. **38**, 11 (2017) 2337.
[5] P. Yuan, P.D. Southon, Z. Liu, M.E.R. Green, J.M. Hook, S.J. Antill, C.J. Kepert. J. Phys. Chem. C **112**, 40 (2008) 15742.
[6] B. Singh, Clay Clay Miner. **44**, 2 (1996) 191.
[7] C. Detellier, R.A. Schoonheydt, Elements **10**, 3 (2014) 201.
[8] A. El Haddar, E. Gharibi, A. Azdimousa, N. Fagel, I.-E. El Amrani El Hassani, M. El Ouahabi, Clay Miner. **53**, 1 (2018) 65.
[9] X. Li, D. Wang, Q. Liu, S. Komarneni, Appl. Clay Sci. **168** (2019) 421.
[10] V.M. Abbasov, H.C. Ibrahimov, G.S. Mukhtarova, E. Abdullayev, Fuel **184** (2016) 555.
[11] J. Jin, Y. Zhang, J. Ouyang, H. Yang, Phys. Chem. Miner. **41**, 5 (2014) 323.
[12] M.R. Dzamukova, E.A. Naumenko, Y.M. Lvov, R.F. Fakhrullin, Sci. Rep. **5** (2015) 10560.
[13] Y.M. Lvov, M.M. Devilliers, R.F. Fakhrullin, Expert Opin. Drug Deliv. **13**, 7 (2016) 977.
[14] M. Massaro, A. Campofelice, C.G. Colletti, G. Lazzara, R. Noto, S. Riela, Appl. Clay Sci. **160** (2018) 186.
[15] Y. Chen, Y. Zhang, J. Liu, H. Zhang, K. Wang, J. Chem. Eng. **210** (2012) 298.
[16] E. Abdullayev, V. Abbasov, A. Tursunbayeva, V. Portnov, H. Ibrahimov, G. Mukhtarova, Y. Lvov, CS Appl. Mater. Interfaces **5**, 10 (2013) 4464.
[17] P.C. Ferrari, F.F. Araujo, S.A. Pianaro, Cerâmica **63**, 368 (2017) 423.
[18] M. Liu, Z. Jia, D. Jia, C. Zhou, Prog. Polym. Sci. **39**, 8 (2014) 1498.
[19] R.L. Frost, X. Li, Q. Liu, H. Cheng, S. Zhang, J. Colloid Interf. Sci. **444** (2015) 74.
[20] J.E.F.C. Gardolinski, G. Lagaly, Clay Miner. **40**, 4 (2005) 537.
[21] J.E.F.C. Gardolinski, G. Lagaly, Clay Miner. **40**, 4 (2005) 547.
[22] Y. Kuroda, K. Ito, K. Itabashi, K. Kuroda, Langmuir **27**, 5 (2011) 2028.
[23] J. Matusik, A. Gaweł, E. Bielanska, W. Osuch, K. Bahranowski, Clay Clay Miner. **57**, 4 (2009) 452.
[24] B. Singh, D.R. Mackinnon, Clay Clay Miner. **44**, 6 (1996) 825.
[25] P. Yuan, D. Tan, F. Annabi-Bergaya, W. Yan, D. Liu, Z. Liu, Appl. Clay Sci. **83-84** (2013) 68.
[26] H. Xu, X. Jin, P. Chen, G. Shao, H. Wang, D. Chen, H. Lu, R. Zhang, Ceram. Int. **41**, 5 (2015) 6463.
[27] T.F. Bates, F.A. Hildebrand, A. Swinedford, Am. Mineral. **35** (1950) 463.
[28] P. Yuan, D. Tan, F. Annabi-Bergaya, Appl. Clay Sci. **112-113** (2015) 75.
[29] NBR ISO 2597-2, "Iron ores: determination of total iron content, Part 2, titrimetric methods after titanium (III) chloride reduction", Ass. Bras. Norm. Téc., S. Paulo (2013).
[30] O. Castelein, L. Aldon, J. Olivier-Fourcade, J.C. Jumas, J.P. Bonnet, P. Blanchart, J. Eur. Ceram. Soc. **22**, 11 (2002) 1767.
[31] C.A.S. Pérez, D. Gobbi, J.L.N. Marcos, C. Paduani, J.D. Ardisson, Cerâmica **50** (2004) 115.
[32] S. Petit, A. Decarreau, Clay Miner. **25**, 2 (1990) 181.
[33] M. Zbik, R.S.C. Smart, Clay Clay Miner. **46**, 2 (1998) 153.
[34] J. Du, G. Morris, R.A. Pushkarova, R.S.C. Smart, Langmuir. **26**, 16 (2010) 13227.

[35] J.C. Araujo, J.T. Assis, V.I. Monine, L.C. Bertolino, Rev. Matér. **11**, 3 (2006) 361.
[36] A.H. Cuttler, Clay Miner. **15**, 4 (1980) 429.
[37] J.T. Kloprogge, *Spectroscopic methods in the study of kaolin minerals and their modifications*, Springer (2019) 434.
[38] L.A. Silva, "Síntese e caracterização de nanopartículas de hematita e de ferro zerovalente sintetizadas a partir de cloreto férrico", Doct. Thesis, Fed. Un. Santa Catarina, Brazil (2015).
[39] S.K. Giri, N.N. Das, G.C. Pradhan, Powder Technol. **214**, 3 (2011) 513.
[40] R. Sakthivel, R. Kumar, R. Behura, B.K. Mishra, D. Das, J. Alloys Compd. **645** (2015) 398.
[41] R.M. Cornell, U. Shwertmann, *The iron oxides: structure, properties, reactions, occurrences and uses*, 2nd ed., Wiley-VCH (2003) 664.
[42] Y. Deng, G. Norman White, J.B. Dixon, J. Colloid Interf. Sci. **250**, 2 (2002) 379.
[43] D.L. Guerra, J.A. Sousa, C. Airoldi, R.R. Viana, Cerâmica **54**, 331 (2008) 273.
[44] Q. Liu, S. Zhang, H. Cheng, F. Gao, C. Liu, B.J. Teppen, Appl. Clay Sci. **151** (2018) 46.
[45] J.A. Mbey, F. Thomas, C.J. Ngally Sabouang, Liboum, D. Njopwouo, Appl. Clay Sci. **83-84** (2013) 327.
[46] G. Lagaly, M. Ogawa, I. Dékány, in "Handbook of clay science" **1**, F. Bergaya, B.K.G. Theng, G. Lagaly (Eds.), Elsevier (2006) 309.
[47] P.J.R. Uwins, I.D.R. Mackinnon, J.G. Thompson, A.J.E. Yago, Clay Clay Miner. **41**, 6 (1993) 707.
[48] G.J. Churchman, J.S. Whitton, G.G.C. Claridge, B.K.G. Theng, Clay Clay Miner. **32**, 4 (1984) 241.
[49] Y. Komori, H. Enoto, R. Takenawa, S. Hayashi, Y. Sugahara, K. Kuroda, Langmuir **16**, 12 (2000) 5506.
[50] L. Zhang, C. Wang, Z. Yan, X. Wu, Y. Wang, D. Meng, H. Xie, Appl. Clay Sci. **86** (2013) 106.
[51] J. Matusik, E. Wisła-Walsh, A. Gaweł, E. Bielanska, K. Bahranoowski, Clay Clay Miner. **59**, 2 (2011) 116.
[52] P.J.R. Uwins, I.D.R. Mackinnon, J.G. Thompson, in 28th Ann. Meet., Lunar Planet. Inst., Houston (1991) 154.
(Rec. 19/06/2019, Rev. 10/09/2019, 28/10/2019, Ac. 30/10/2019)

CC BY-NC

Reuso de resíduo de lama de papel na produção de suporte cerâmico poroso de baixo custo

(Reuse of paper sludge waste in the production of low-cost porous ceramic support)

R. A. Bou-Issa[1], R. L. Loiola[1], J. N. F. Holanda[1]*

[1]Universidade Estadual do Norte Fluminense Darcy Ribeiro, LAMAV-CCT, Grupo de Materiais Cerâmicos, Av. Alberto Lamego 2000, 28013-602, Campos dos Goytacazes, RJ, Brasil

Resumo

A indústria de papel gera enorme volume de resíduo de lama de papel. Neste trabalho foi desenvolvido um novo suporte cerâmico poroso usando resíduo de lama de papel como matéria-prima alternativa. Os suportes cerâmicos foram produzidos por prensagem e sinterizados entre 1000 e 1200 ºC. A influência da incorporação do resíduo de lama de papel nas propriedades físicas e microestrutura sinterizada foi investigada. Os resultados indicaram que o resíduo de lama de papel atua como um agente formador de poro. Os suportes cerâmicos produzidos apresentaram massa específica aparente de 1,16 a 2,01 g/cm^3, porosidade aparente de 14,6% a 46,7% e tensão de ruptura à flexão de 15,4 a 39,9 MPa. Análise microestrutural indicou que os suportes cerâmicos apresentaram estrutura morfológica altamente porosa. Tais resultados indicaram que suportes cerâmicos contendo até 30% em massa de resíduo de lama de papel têm potencial para serem empregados na fabricação de membranas de filtração.
Palavras-chaves: suporte cerâmico, resíduo de lama de papel, valorização, propriedades, microestrutura.

Abstract

The paper industry generates a huge volume of paper sludge waste. In this study, a new porous ceramic support using paper sludge waste as an alternative raw material was developed. The ceramic supports were produced by pressing and sintered between 1000 and 1200 °C. The influence of the incorporation of the paper sludge waste on the physical properties and sintered microstructure was investigated. The results indicated that the paper sludge waste acts as a pore-forming agent. The produced ceramic supports showed an apparent specific mass of 1.16 to 2.01 g/cm^3, apparent porosity of 14.6% to 46.7%, and flexural strength of 15.4 to 39.9 MPa. Microstructural analysis indicated that the ceramic supports had a highly porous morphological structure. Such results indicated that porous ceramic supports containing up to 30 wt% of paper sludge waste have the potential to be employed in the manufacture of filtration membranes.
***Keywords**: ceramic support, paper sludge waste, valorization, properties, microstructure.*

INTRODUÇÃO

Na atualidade existe um interesse cada vez maior no reuso e valorização de resíduos poluentes como matérias-primas alternativas e renováveis aplicadas no desenvolvimento de materiais cerâmicos. Tal fato se deve principalmente à possibilidade de matérias-primas tradicionais serem substituídas parcial ou totalmente nas formulações cerâmicas por resíduos poluentes, que contribui para preservação das fontes de matérias-primas naturais com consideráveis benefícios econômicos e ambientais. O Brasil detém uma expressiva indústria de produção de papel. Em 2018, por exemplo, a produção brasileira de papel foi de 10,443 milhões de toneladas [1]. Tal volume de produção de papel gera riqueza e milhares de empregos diretos e indiretos. Por outro lado, a fabricação industrial de papel também gera uma quantidade significativa de resíduo poluente na forma de lama, que é o produto final do processo após o tratamento de águas residuais em estação de tratamento de efluente [2-4]. Este resíduo apresenta-se na forma de uma lama de papel fibrosa de coloração acinzentada, a qual constitui uma mistura compósita formada principalmente de fibras de celulose, caulim, calcita, substâncias químicas usadas no tratamento e água [3, 4]. Do ponto de vista de potencial poluidor, é classificado de acordo com a norma ABNT NBR 10004 como um resíduo não perigoso, mas não inerte (classe IIA) [5]. Em geral a indústria do papel descarta este resíduo principalmente em aterro sanitário que apresenta custo elevado, além de ser problemático em termos de sustentabilidade ambiental [4, 6]. Esta situação reforça a necessidade na busca de novas alternativas tecnológicas e viáveis para o descarte final sustentável deste abundante resíduo poluente.

As membranas cerâmicas são largamente empregadas em processos de microfiltração e ultrafiltração com largo

**bou_issa@hotmail.com*
https://orcid.org/0000-0002-8718-7562

campo de aplicação em processos industriais [7-10]. O suporte poroso é considerado parte fundamental da membrana cerâmica, pois é o responsável pela resistência mecânica e transporte de fluxo [11]. Os suportes cerâmicos comerciais são em regra caros devido ao alto custo das matérias-primas sintéticas usadas como, por exemplo, alumina, cordierita, óxido de titânio e mulita, além da alta temperatura de sinterização empregada [9, 11, 12]. Por este motivo, nos últimos anos têm sido estimuladas pesquisas voltadas para o desenvolvimento de novos suportes cerâmicos porosos usando matérias-primas convencionais baratas tais como argilas e caulins [8, 9, 12, 13]. Verifica-se também que a literatura disponível é escassa em relação ao reuso e valorização de resíduos poluentes no processamento de suporte poroso de membrana cerâmica [13, 14]. Em particular, o uso de resíduo de lama proveniente da indústria do papel ainda não tem sido investigado na produção de suporte cerâmico poroso de baixo custo para emprego em membrana. O objetivo principal deste trabalho é o desenvolvimento de um novo suporte cerâmico poroso de baixo custo para potencial aplicação em membrana cerâmica usando o resíduo de lama produzido na indústria de papel como um agente formador de poro.

MATERIAIS E MÉTODOS

As matérias-primas de partida utilizadas para processamento de suporte cerâmico poroso foram caulim comercial (Armil Mineração do Nordeste, Brasil) e resíduo de lama de papel fornecido pela Copapa (Rio de Janeiro, Brasil), que fabrica papel *tissue* (papéis usados como lenços, guardanapos, papel higiênico, etc.). O caulim foi fornecido na granulometria <325 mesh (<45 μm ASTM). O resíduo lama de papel coletado na forma *in natura* foi submetido a processo de secagem, desagregado e passado na peneira de 100 mesh (<149 μm ASTM). Após o beneficiamento foram estabelecidas as composições das massas cerâmicas, conforme mostrado na Tabela I. A massa cerâmica RB1 correspondeu à massa cerâmica de referência isenta de resíduo de lama de papel (isto é, 100% de caulim).

As análises químicas das matérias-primas foram realizadas por combinação das técnicas de espectrometria de fluorescência de raios X e espectrometria de absorção atômica. A perda ao fogo (PF) foi determinada a partir da expressão PF(%)=[(Ms–Mc)/Ms].100, onde Ms é a massa da amostra seca (g) a 110 ºC e Mc é a massa da amostra calcinada (g) a 1000 ºC por 2 h. A morfologia das partículas das matérias-primas foi observada por microscopia eletrônica de varredura (MEV) via imagens de elétrons secundários (Shimadzu, SSX-550). As análises térmicas (análise térmica diferencial, ATD, e análise termogravimétrica, ATG) das matérias-primas e massas cerâmicas foram realizadas em um analisador simultâneo ATG-ATD (Netzsch, STA 409E) da temperatura ambiente até 1100 ºC com taxa de aquecimento de 10 ºC/min.

Tabela I - Composição das formulações cerâmicas usadas (% em massa).
[Table I - Composition of the ceramic formulations used (mass %).]

Formulação	Caulim	Resíduo de lama de papel
RB1	100	0
RB2	90	10
RB3	80	20
RB4	70	30

As massas cerâmicas, com as proporções de caulim e resíduo de lama de papel (Tabela I) foram misturadas e homogeneizadas usando um misturador cilíndrico de laboratório durante 30 min. Após mistura, as massas cerâmicas foram umedecidas com água (7% em massa). Os suportes cerâmicos foram preparados por prensagem uniaxial em uma prensa hidráulica (Schwing Siwa, PHMA) usando pressão de compactação de aproximadamente 60 MPa e matriz de aço cilíndrica (diâmetro de 25 mm). Os suportes cerâmicos compactados foram secados a 110 ºC por 24 h e depois sinterizados em um forno mufla (Nova Instruments, NI1384) em atmosfera oxidante em patamar de 1000, 1050, 1100, 1150 e 1200 ºC por 2 h.

Os suportes cerâmicos preparados foram caracterizados em termos de absorção de água (AA), massa específica aparente (MEA), porosidade aparente (PA), retração linear, perda de massa, resistência mecânica e análise microestrutural. AA, PA e MEA foram determinadas de acordo com a norma ASTM C373. A retração linear foi determinada a partir das medidas do diâmetro das amostras cilíndricas após secagem e sinterização. A perda de massa das amostras foi determinada a partir das medidas de massa das amostras após secagem e sinterização usando uma balança analítica de precisão ±0,01 g. Devido à geometria das amostras sinterizadas (disco), a tensão de ruptura à flexão (σ_f) foi determinada a partir da expressão σ_f=2,7.σ_t (MPa) [9], onde σ_t=2.P/(π.d.h) é a resistência à tração determinada pelo método de compressão diametral (P é a carga de ruptura, d é o diâmetro da amostra e h é a espessura da amostra). A carga de ruptura (P) foi determinada usando uma máquina de ensaios universal (Instron, mod. 5582) com velocidade de carregamento de 0,5 mm/min. A microestrutura sinterizada foi avaliada por microscopia eletrônica de varredura via imagens de elétrons retroespalhados, após metalização com uma fina camada de paládio.

RESULTADOS E DISCUSSÃO

A Tabela II apresenta as composições químicas do caulim e do resíduo de lama de papel em termos de óxidos constituintes mais a perda ao fogo. Como esperado, o caulim usado foi composto essencialmente de SiO_2 (46,92% em massa), Al_2O_3 (38,94% em massa) e pequenas quantidades de impurezas (óxidos de Ca, Mg, Fe, K, Na, Mn, Ti e P). O caulim apresentou razão SiO_2/Al_2O_3=1,21. Este resultado indicou que o caulim foi constituído predominantemente

pelo argilomineral caulinita [15]. De fato, a perda ao fogo do caulim foi de 12,88% em massa, que foi próxima do valor teórico da caulinita (13,95%). Os resultados da Tabela II também mostram que o resíduo de lama de papel foi principalmente composto de CaO (25,17% em massa) e quantidades menores de SiO_2 (4,38% em massa) e Al_2O_3 (4,35% em massa). Tais resultados foram em acordo com dados de composição química do resíduo de lama de papel reportados na literatura [5]. Em particular, a alta quantidade de CaO se deve fundamentalmente à presença de material carbonáceo na forma de calcita ($CaCO_3$). Os componentes SiO_2 e Al_2O_3 estavam na forma combinada formando a estrutura da caulinita, o que indicou que o resíduo de lama de papel continha caulim [4]. Constatou-se ainda que o resíduo de lama de papel apresentou alta perda ao fogo (65,23% em massa), associada principalmente à combustão de fibra de celulose e decomposição de calcita [4]. Isto significou que o resíduo de lama de papel por apresentar alta perda ao fogo pode desempenhar a função de um agente formador de poro. Do ponto de vista de processamento de um suporte cerâmico poroso, isto é positivo, em princípio.

Os aspectos morfológicos das partículas de caulim e resíduo de lama de papel podem ser observados na Fig. 1. O pó de caulim (Fig. 1a) foi composto essencialmente de partículas com morfologia em forma de placas. Tais placas são típicas do argilomineral caulinita que é o constituinte majoritário de caulins comerciais. A amostra de resíduo de lama de papel no estado seco (Fig. 1b) foi composta por aglomerados com morfologia irregular e textura altamente porosa. Tais aglomerados são constituídos principalmente de misturas de fibra de celulose, caulinita e calcita.

Tabela II - Composição química das matérias-primas (% em massa).
[Table II - Chemical composition of the raw materials (mass %).]

Óxido	Caulim	Resíduo de lama de papel
SiO_2	46,92	4,38
Al_2O_3	38,94	4,35
CaO	0,05	25,17
MgO	0,05	0,25
Fe_2O_3	0,27	0,28
K_2O	0,64	0,06
Na_2O	0,06	0,05
MnO	0,05	0,05
TiO_2	0,05	0,09
P_2O_5	0,09	0,09
Perda ao fogo	12,88	65,23

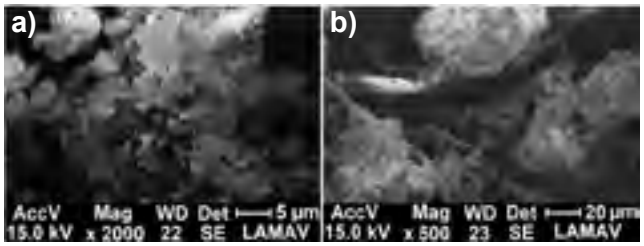

Figura 1: Micrografias de MEV: a) caulim; e b) resíduo de lama de papel.
[Figure 1: SEM micrographs: a) kaolin; and b) paper sludge waste.]

A Fig. 2 apresenta os resultados das análises térmicas (ATD/ATG) das matérias-primas e formulações cerâmicas estudadas. O comportamento térmico da amostra de caulim (Fig. 2a) pode ser descrito como: i) um pequeno evento endotérmico ocorreu entre ~25 e 200 ºC relacionado à liberação de água fisicamente adsorvida sobre a superfície das partículas, com perda de massa de 0,63%; ii) um expressivo evento endotérmico a 555,8 ºC relacionado à desidroxilação das partículas de caulinita para formação da metacaulinita amorfa, com perda de massa de 10,54%; e iii) um evento exotérmico a 1002,0 ºC relacionado à decomposição da metacaulinita e concomitante formação de novas fases cristalinas, como estrutura espinélio (Al-Si) e/ou a nucleação de mulita primária [16]. A perda de massa total obtida da curva ATG de 11,17% foi próxima do valor da perda ao fogo de 12,88% (Tabela II). O comportamento térmico do resíduo de lama de papel (Fig. 2b) pode ser descrito como: i) um evento endotérmico entre 24,9 e 199,7 ºC relacionado à liberação de água fisicamente adsorvida acompanhada de perda de massa de 3,94%; ii) um evento exotérmico entre 199,7 e 390,0 ºC relacionado à decomposição de celulose e hemicelulose (isto é, perda de material volátil leve) [17], com alta perda de massa de 35,31%; iii) um evento exotérmico entre 390,0 e 639,2 ºC relacionado à decomposição de lignina (isto é, perda de material volátil mais pesado) [17], com perda de massa de 10,55%. Ressalta-se que nesta faixa de temperatura, devido à presença de caulim no resíduo de lama de papel, o evento endotérmico relacionado à desidroxilação da caulinita provavelmente foi sobreposto; e iv) um evento endotérmico entre 639,2 e 889,1 ºC relacionado à decomposição da calcita acompanhado de perda de massa de 17,90%. Observou-se também que a perda de massa total do resíduo de lama de papel obtida da curva ATG foi cerca de 67,70%, que foi em acordo com o valor da perda ao fogo de 65,23% (Tabela II). Os comportamentos térmicos das formulações RB2 (Fig. 2c) e RB4 (Fig. 2d) foram em acordo com aqueles das matérias-primas individuais. Além disso, ambas as formulações apresentaram um evento exotérmico em aproximadamente 1000 ºC, o qual pode ser provavelmente atribuído à formação de fases de silicato e aluminossilicato de cálcio [4, 18]. As perdas de massas totais das formulações RB2 e RB4 foram 17,67% e 25,98%, respectivamente.

As Figs. 3 e 4 mostram micrografias da superfície de fratura dos suportes cerâmicos das formulações RB1 e RB4, respectivamente, obtidas por microscopia eletrônica de varredura via imagens de elétrons retroespalhados. Tais micrografias mostraram a sequência típica do

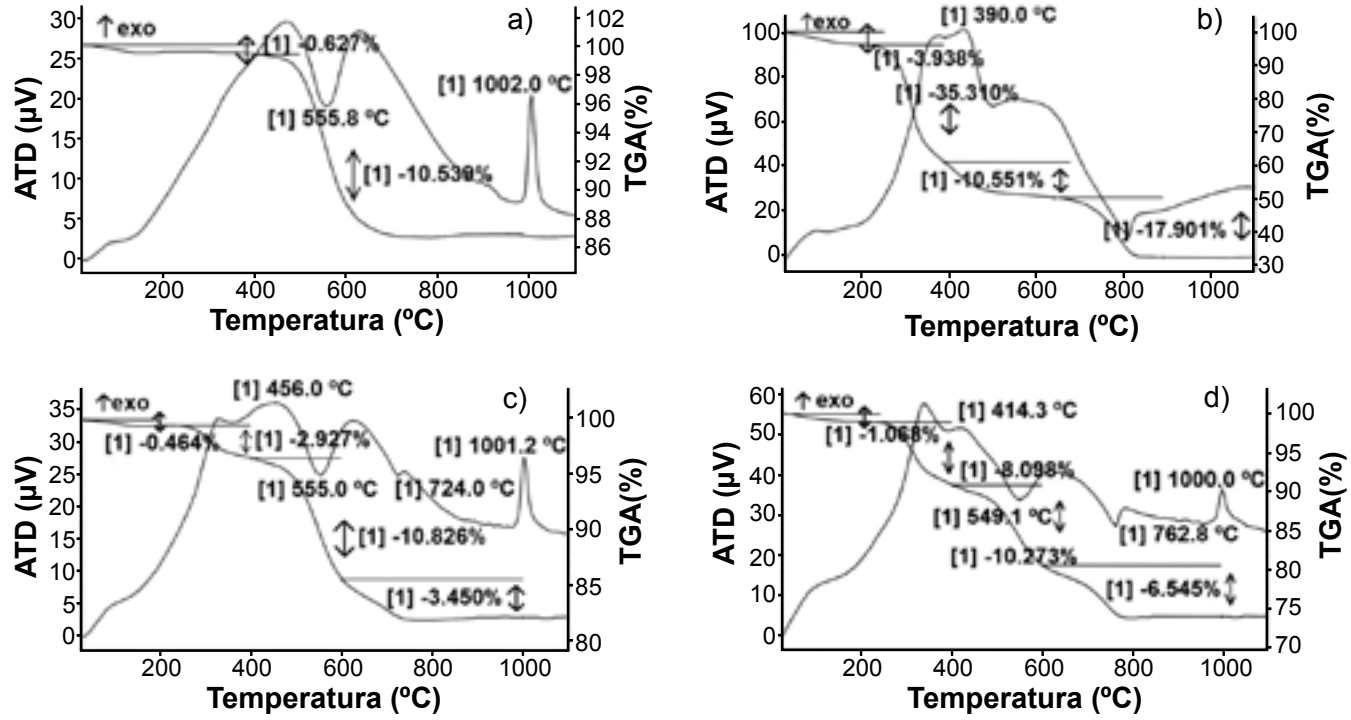

Figura 2: Curvas de ATD/ATG de: a) caulim; b) resíduo de lama de papel; c) formulação RB2; e d) formulação RB4.
[Figure 2: DTA/TG curves of: a) kaolin; b) paper sludge waste; c) RB2 formulation; and d) RB4 formulation.]

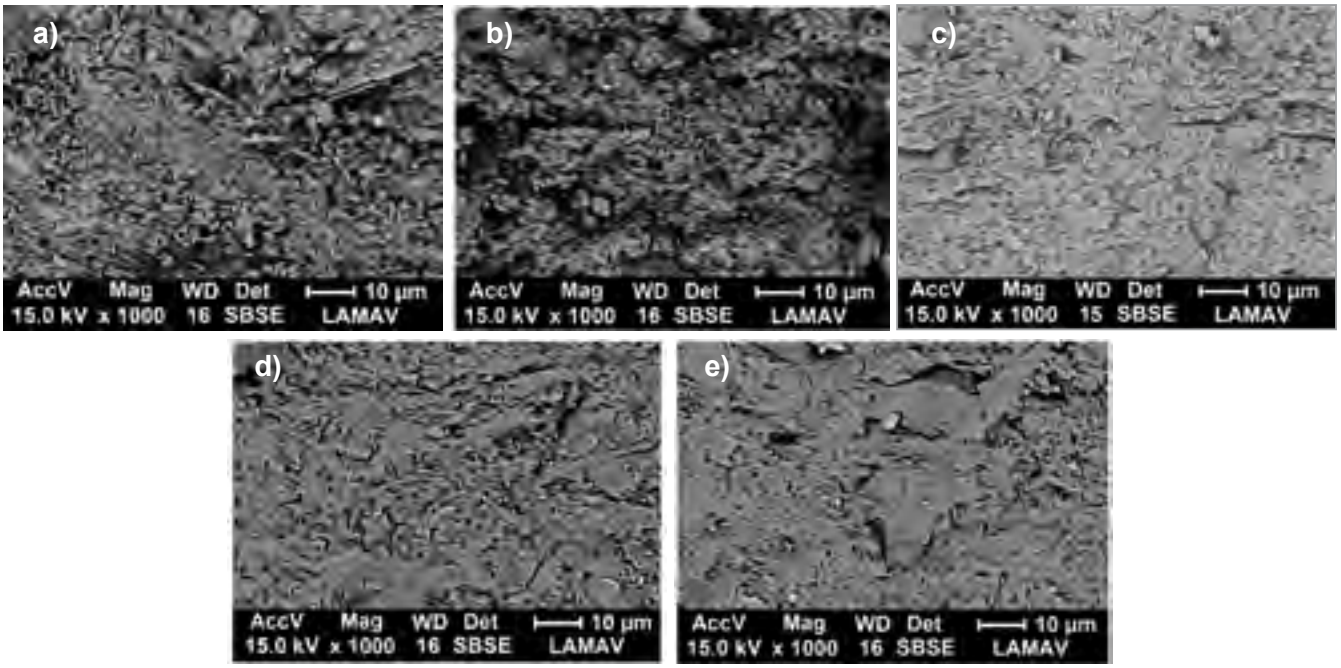

Figura 3: Micrografias de MEV das superfícies de fratura da formulação RB1 em diferentes temperaturas de sinterização: a) 1000 ºC; b) 1050 ºC; c) 1100 ºC; d) 1150 ºC; e e) 1200 ºC.
[Figure 3: SEM micrographs of the fracture surfaces of the RB1 formulation at different sintering temperatures: a) 1000 ºC; b) 1050 ºC; c) 1100 ºC; d) 1150 ºC; and e) 1200 ºC.]

comportamento da microestrutura dos suportes cerâmicos com o aumento da temperatura de sinterização. Como esperado, o efeito da temperatura de sinterização foi o de aumentar o grau de sinterização com concomitante redução da porosidade aberta em todos os suportes cerâmicos. Por outro lado, a análise comparativa entre as superfícies de fratura das formulações RB1 (Fig. 3) e RB4 (Fig. 4) indicou claramente que a incorporação de resíduo de lama de papel atuou como um agente formador de poros, o qual resultou em estruturas sinterizadas altamente porosas (Fig. 4). De fato, o suporte cerâmico produzido com o resíduo de lama de papel apresentou maior quantidade de poros

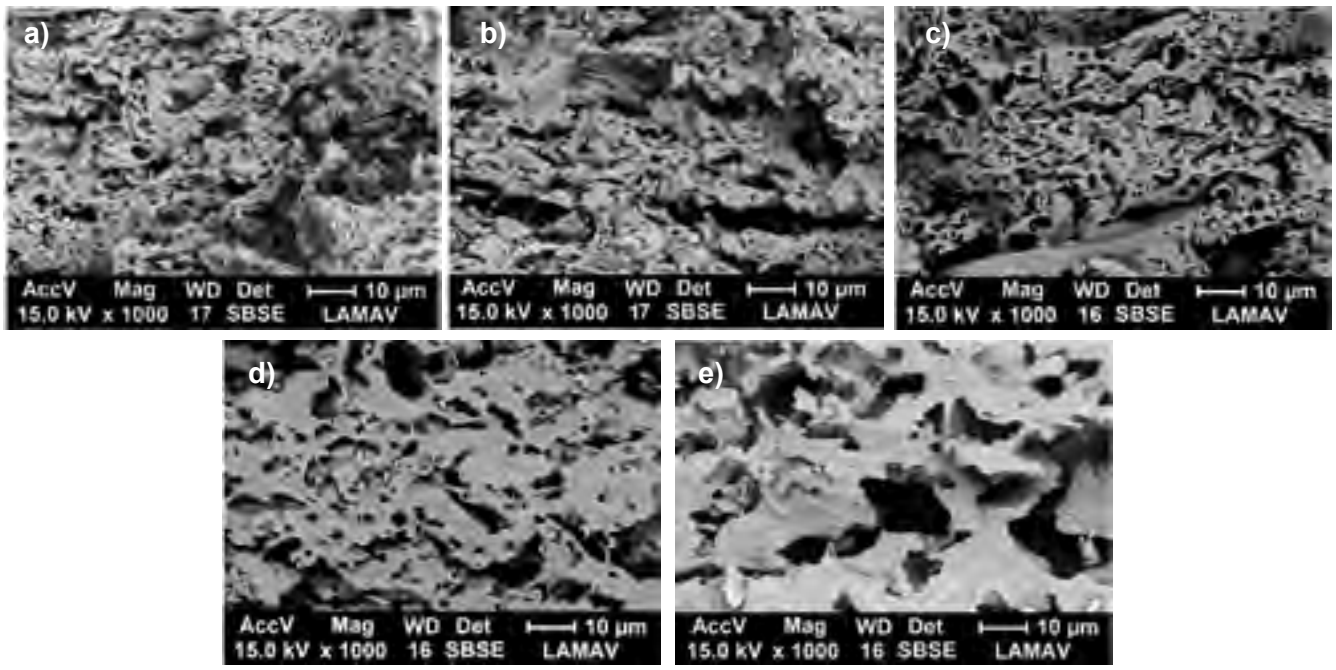

Figura 4: Micrografias de MEV das superfícies de fratura da formulação RB4 em diferentes temperaturas de sinterização: a) 1000 ºC; b) 1050 ºC; c) 1100 ºC; d) 1150 ºC; e e) 1200 ºC.
[Figure 4: SEM micrographs of the fracture surfaces of the RB4 formulation at different sintering temperatures: a) 1000 ºC; b) 1050 ºC; c) 1100 ºC; d) 1150 ºC; and e) 1200 ºC.]

observáveis de diferentes tamanhos e bem distribuídos. Isto foi em acordo com a destruição térmica do resíduo de lama de papel durante o processo de sinterização, conforme os comportamentos térmicos observados na Fig. 2. A inspeção das superfícies de fratura constatou ainda ausência de trincas e defeitos superficiais nos suportes cerâmicos.

A evolução das propriedades físicas dos suportes cerâmicos em função da temperatura de sinterização e quantidade de resíduo de lama de papel é mostrada na Fig. 5. A correlação entre as propriedades físicas foi estabelecida. A Fig. 5a mostra o comportamento da retração linear (variação do diâmetro) dos suportes cerâmicos em função da temperatura de sinterização e quantidade de resíduo de lama de papel adicionado. A retração linear é fundamentalmente associada ao grau de sinterização da amostra. O efeito da temperatura de sinterização foi aumentar a retração linear dos suportes. Tal efeito está relacionado à maior sinterabilidade que promove uma aproximação entre as partículas, o qual resulta no aumento da retração. Deve-se notar, no entanto, que a adição de 30% em massa de resíduo de lama de papel (formulação RB4) praticamente não alterou a retração linear dos suportes na faixa de temperatura de sinterização empregada. Pode-se observar também na Fig. 5a que o comportamento de sinterização dos suportes foi influenciado pela quantidade de resíduo adicionado. Notou-se que acima de 1000 ºC ocorreu uma tendência de menor valor de retração linear com a incorporação do resíduo. Este comportamento se deve basicamente à composição do resíduo de lama de papel que continha quantidades apreciáveis de compostos como fibra de celulose e carbonato de cálcio. Tais compostos se decompuseram durante o processo de sinterização com concomitante liberação de voláteis para fora da estrutura do suporte cerâmico. A perda de massa dos suportes cerâmicos durante o processo de sinterização é mostrada na Fig. 5b. Como esperado, os suportes cerâmicos contendo resíduo de lama de papel apresentaram altos valores de perda de massa (20,7% a 36,2%). Os suportes cerâmicos apresentaram um intenso processo de transferência de massa, no qual ocorreram reações químicas complexas associadas ao caulim (desidroxilação da caulinita: $Al_2O_3.2SiO_2.2H_2O \rightarrow Al_2O_3.2SiO_2+H_2O\uparrow$) e resíduo de lama de papel (combustão da fibra de celulose e decomposição da calcita: $CaCO_3 \rightarrow CaO+CO_2\uparrow$). Este resultado foi em acordo com os resultados das análises térmicas (ATD/ATG) mostrados na Fig. 2. Observou-se também que em qualquer temperatura de sinterização o efeito do resíduo de lama de papel foi o de elevar substancialmente a perda de massa dos suportes cerâmicos. No entanto, para as formulações RB3 e RB4 queimadas a 1200 ºC ocorreu um aumento súbito de perda de massa em relação a 1150 ºC. Não se encontrou uma explicação plausível para essa perda de massa, pois aparentemente as reações de perda de massa envolvidas foram aquelas descritas pelas curvas de ATG, de forma que é necessária mais investigação para elucidar tal elevação da perda de massa, a qual será objeto de trabalho futuro.

O comportamento da massa específica aparente dos suportes cerâmicos em função da temperatura de sinterização e quantidade de resíduo é mostrado na Fig. 5c. A massa específica aparente dos suportes cerâmicos sinterizados contendo resíduo de lama de papel foi na faixa de 1,16 a 2,01 g/cm^3. O comportamento de densificação

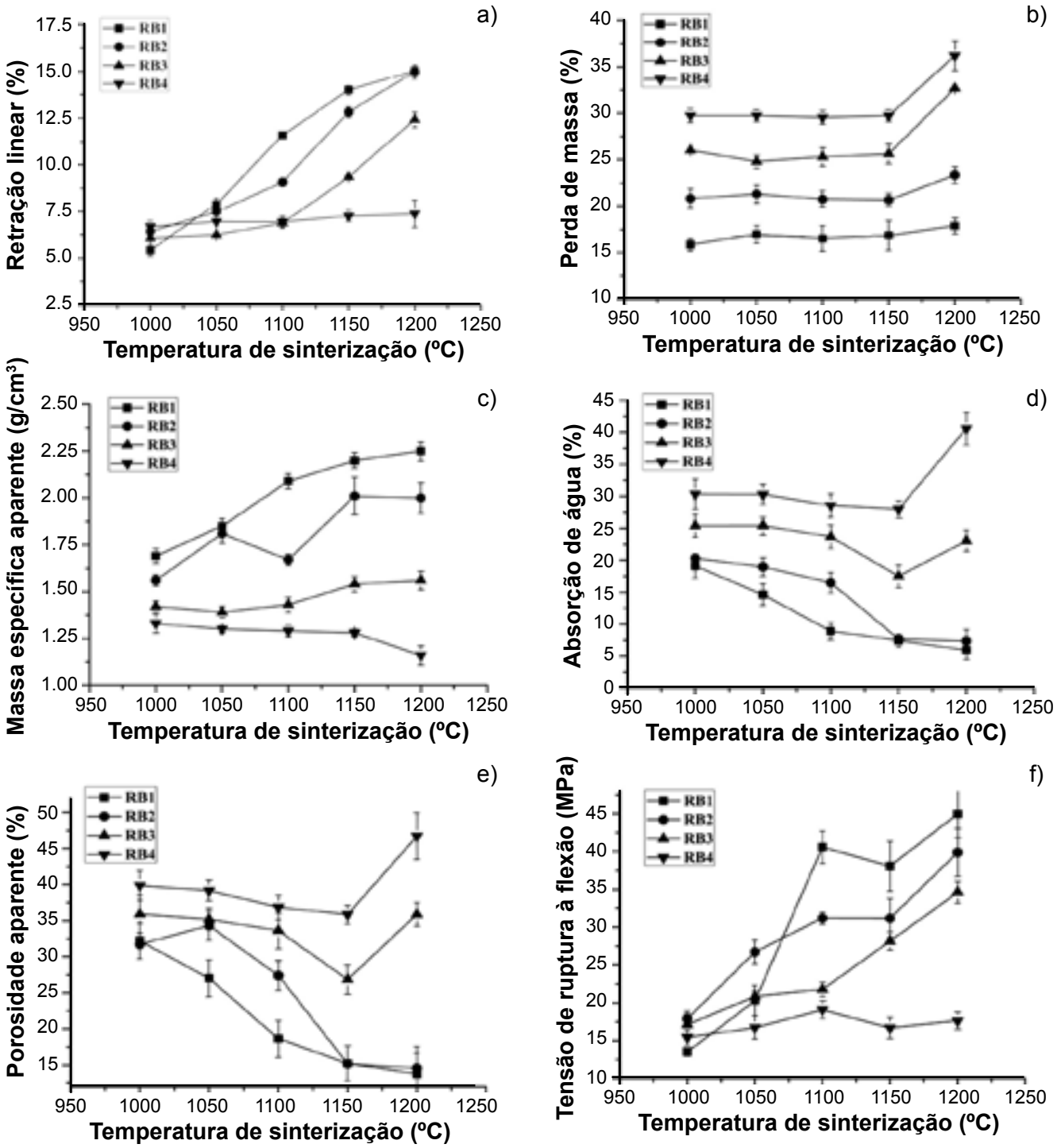

Figura 5: Resultados de retração linear (a), perda de massa (b), massa específica aparente (c), absorção de água (d), porosidade aparente (e) e tensão de ruptura a flexão (f) dos suportes cerâmicos.
[Figure 5: Results of linear shrinkage (a), mass loss (b), apparent specific mass (c), water absorption (d), apparent porosity (e), and flexural strength (f) of the ceramic supports.]

dos suportes cerâmicos foi associado a dois fatores opostos simultâneos influenciando a densificação, quais sejam: i) sinterização devido ao crescimento de pescoço interpartícula dominada principalmente por sinterização de estado sólido; e ii) desgaseificação relacionada à liberação de voláteis oriundos principalmente da combustão da fibra de celulose e decomposição de calcita. No entanto, a perda de massa oriunda da desgaseificação foi o parâmetro predominante na densificação dos suportes cerâmicos. De fato, em todas as temperaturas de sinterização a incorporação de maior quantidade de resíduo de lama de papel resultou em menor taxa de densificação, formação de porosidade e expansão

da estrutura. Este comportamento foi consistente com as microestruturas (Fig. 4), retração linear (Fig. 5a) e perda de massa (Fig. 5b). A Fig. 5d mostra os valores de absorção de água dos suportes cerâmicos. Como esperado, a substituição do caulim com resíduo de lama de papel resultou em maior absorção de água para todas as temperaturas de sinterização. Este aumento de absorção de água foi essencialmente em linha com a composição do resíduo de lama de papel e perda de massa (Fig. 5b) que tendeu a originar porosidade aberta e retardar a densificação dos suportes cerâmicos.

A Fig. 5e mostra a evolução da porosidade aparente dos suportes cerâmicos a diferentes temperaturas de sinterização. Como esperado, os suportes cerâmicos incorporados com resíduo de lama de papel tenderam a apresentar maior porosidade do que aqueles isentos de resíduo. Tal efeito foi em acordo com a perda de massa (Fig. 5b), massa específica aparente (Fig. 5c) e absorção de água (Fig. 5d). Quanto maior foi a quantidade de resíduo de lama de papel incorporado, maior foi a quantidade de porosidade formada na estrutura do suporte cerâmico. Isto é interessante devido à formação de maior porosidade aumentar a permeabilidade do suporte cerâmico, que é de alto interesse para aplicação em membranas. O mecanismo de formação de porosidade neste novo suporte cerâmico foi intimamente relacionado aos processos de destruição térmica da fibra de celulose e calcita presentes no resíduo de lama de papel, que ocorreram em distintas regiões de temperatura durante a etapa de sinterização. Neste trabalho os suportes cerâmicos incorporados com resíduo de lama de papel apresentaram os seguintes valores de porosidade aparente conforme a formulação: RB2 14,6% a 34,3%; RB3 26,9% a 35,9%; e RB4 35,9% a 46,7%. Tais resultados indicaram que as formulações contendo resíduo de lama de papel apresentam potencial em termos de produção de suporte cerâmico poroso aplicado em membranas de filtração de baixo custo [19], principalmente a formulação RB4. A tensão de ruptura à flexão dos suportes cerâmicos é mostrada na Fig. 5f. O comportamento mecânico apresentou boa correlação com todas as outras propriedades estudadas e microestrutura sinterizada. Observou-se que a incorporação de maior quantidade de resíduo de lama de papel diminuiu a resistência mecânica do suporte cerâmico. Isto foi consequência direta do aumento da porosidade, como mostrado na Fig. 5e. As formulações contendo resíduo de lama de papel apresentaram os seguintes valores de tensão de ruptura à flexão conforme a formulação: RB2 17,9 a 39,9 MPa; RB3 17,1 a 34,6 MPa; e RB4 15,4 a 19,1 MPa, de forma que os suportes cerâmicos apresentaram resistência mecânica adequada para aplicação em membranas de filtração [20].

CONCLUSÕES

O resíduo de lama de papel gerado na indústria de papel pode ser usado como uma matéria-prima renovável barata que apresenta potencial para substituir parcialmente o caulim natural em formulações para fabricação de suporte cerâmico poroso. O resíduo de lama de papel foi composto principalmente de carbonato de cálcio na forma de calcita e fibras de celulose, cuja perda de massa total obtida da curva ATG foi de 67,70%. A incorporação do resíduo de lama de papel causou importantes mudanças nas propriedades técnicas (retração linear, massa específica aparente, absorção de água, porosidade aparente e tensão de ruptura à flexão) e microestrutura sinterizada dos suportes cerâmicos. O resíduo de lama de papel atuou positivamente como um agente formador de poros durante o processo de sinterização do suporte cerâmico. Os resultados também indicaram que suportes cerâmicos porosos contendo 30% em massa de resíduo de lama de papel têm potencial para serem usados em membranas de filtração. Esta se constitui uma alternativa tecnológica viável de reuso e valorização de resíduo poluente produzido na indústria de papel, atual e de grande importância econômica e ambiental.

AGRADECIMENTOS

Os autores agradecem ao CNPq (Processo 305928/2016-3) e FAPERJ (Processo E-26/ 203.013/2016) pelo apoio financeiro a este trabalho. Os autores também gostariam de agradecer à empresa COPAPA (Companhia Paduana de Papéis) pelo fornecimento do resíduo de lama de papel.

REFERÊNCIAS

[1] IBÁ, "Estatísticas da indústria brasileira de árvores", Boletim **57** (2019) 1.
[2] M. Sutcu, S. Akkurt, Ceram. Int. **35** (2009) 2625.
[3] M.C. Monte, E. Fuente, A. Blanco, C. Negro, Waste Manag. **29** (2009) 293.
[4] J.A. Cusidó, L.V. Cremades, S. Soriano, M. Devant, Appl. Clay Sci. **108** (2015) 191.
[5] R.M. Pinheiro, "Reciclagem de lodo primário da estação de tratamento de efluentes da indústria de papel em cerâmica argilosa", Diss. Mestr., UENF, Campos dos Goytacazes (2008).
[6] S.K. Ding, S. Kulkarni, V. Kumar, P. Vashistha, J. Clean. Prod. **204** (2018) 321.
[7] J.M. Benito, A. Conesa, F. Rubio, M.A. Rodriguez, J. Eur. Ceram. Soc. **25** (2005) 1895.
[8] S. Sarker, S. Bamdyopadhyay, A. Larbot, S. Cerneaux, J. Membr. Sci. **392-393** (2012) 130.
[9] A. Harabi, F. Zenikheri, B. Boudaira, F. Bouzeraba, A. Guechi, L. Foughali, J. Eur. Ceram. Soc. **34** (2014) 1329.
[10] B. Das, B. Chakrabarty, P. Barkakati, Ceram. Int. **42** (2016) 14326.
[11] G. Chen, H. Qi, W. Xing, N. Xu, J. Membr. Sci. **318** (2008) 38.
[12] I. Hedfi, N. Hamdi, M.A. Rodriguez, E. Srasra, Ceram. Int. **42** (2016) 5089.
[13] V.J. Silva, M.F. Silva, W.P. Gonçalves, R.R. Menezes, G.A. Neves, H.L. Lira, L.N.L. Santana, Ceram. Int. **42** (2016) 15471.
[14] J. Liu, Y. Dong, X. Dong, S. Hampshire, L. Zhur, Z. Zhur, L. Li, J. Eur. Ceram. Soc. **36** (2016) 1059.

[15] G.P. Souza, S.J.G. Sousa, L.A.H. Terrones, J.N.F. Holanda, Cerâmica **51**, 320 (2005) 381.
[16] G.P. Souza, R. Sánchez, J.N.F. Holanda, J. Therm. Anal. Calor. **79** (2003) 293.
[17] M.R.C. Silva, A.S. Gurgel, S.L.F. Andersen, in Anais XI Congr. Bras. Eng. Quím. Inic. Cient., Campinas (2015).
[18] M.M. Jordam, M.B. Almendro-Candel, M. Romero, J.M. Rincón, Appl. Clay Sci. **30** (2005) 219.
[19] R.C.O. Lima, H.L. Lira, G.A. Neves, M.C. Silva, S.D. Silva, Rev. Eletron. Mater. Process. **63** (2011) 163.
[20] N. Kouras, A. Harabi, F. Bouzerara, L. Fouguali, A. Policicchio, S. Stelitano, F. Galiano, A. Figoli, J. Eur. Ceram. Soc. **37** (2017) 3159.
(Rec. 10/05/2019, Rev. 09/08/2019, 09/10/2019, Ac. 01/11/2019)

BY-NC

Structural transition and magnetic properties of high Cr-doped $BiFeO_3$ ceramic

(Transição estrutural e propriedades magnéticas da cerâmica $BiFeO_3$ dopada com Cr)

S. S. Arafat[1,2]*

[1]King Faisal University, Faculty of Science, Physics Department, Saudi Arabia

[2]Fayoum University, Faculty of Science, Physics Department, Egypt

Abstract

Magnetic properties of $BiFe_{1-x}Cr_xO_3$ perovskite-type solids reaction synthesized at high pressure were investigated and a magnetic phase diagram was established. X-ray diffraction data revealed a crystal structure transformation from rhombohedral to monoclinic as Cr^{3+} ions substituted Fe ions in the samples. Néel temperature T_N and spin-reorientation temperature T_{SR} were determined from dM/dT by measuring the temperature dependence of magnetization (M-T). The magnetization results indicated that T_N and T_{SR} were strongly dependent on Cr^{3+} ion doping; both T_N and T_{SR} decreased with the increase of Cr^{3+} doping. The magnetic hysteresis loops investigated at room temperature reflected an antiferromagnetic behavior from x= 0.4 to 0.6 and weak ferromagnetic at x=1.0. Besides, the remnant magnetization M_r and maximum magnetization M_{max} increased with increasing x from 0.4 up to 1.0. The Cr doping was found to be helpful in reducing coercivity H_c for the magnetic samples from x= 0.4 to 0.8 and their applications as magnetic sensors are possible.

Keywords: perovskite-type structure, high-pressure solid-state synthesis, X-ray diffraction, magnetic properties.

Resumo

Propriedades magnéticas de $BiFe_{1-x}Cr_xO_3$ do tipo perovskita sintetizado por reação no estado sólido a alta pressão foram investigadas e um diagrama de fase magnética foi estabelecido. Os dados de difração de raios X revelaram a transformação da estrutura cristalina de romboédrica para monoclínica conforme íons de Cr^{3+} substituíram íons de Fe nas amostras. As temperaturas de Néel T_N e de reorientação de spin T_{SR} foram determinadas a partir de dM/dT por meio da medição da magnetização em função da temperatura (M-T). Os resultados da magnetização indicaram que T_N e T_{SR} foram fortemente dependentes da dopagem de íon Cr^{3+}; T_N e T_{SR} diminuíram com o aumento da dopagem de Cr^{3+}. Os laços de histerese magnética investigados à temperatura ambiente refletiram um comportamento antiferromagnético de x= 0,4 a 0,6 e ferromagnético fraco em x=1,0. Além disso, a magnetização remanescente M_r e a magnetização máxima M_{max} aumentaram com o aumento de x de 0,4 até 1,0. A dopagem de Cr foi útil na redução da coercividade H_c para amostras magnéticas de x= 0,4 a 0,8 e suas aplicações como sensores magnéticos são possíveis.

***Palavras-chave**: estrutura perovskita, síntese em estado sólido de alta pressão, difração de raios X, propriedades magnéticas.*

INTRODUCTION

Multiferroics materials possessing coupling of two or more types of ordering like ferromagnetic and ferroelasticity in a single-phase have exposed a lot of interest in physics and opens many possibilities of practical applications in modern technologies. These kinds of materials have been investigated for a new type of memory applications using a combination of ferromagnetic and ferroelectric properties [1-4]. This class of materials has found its applications in the field of electro-optic transducer controlled by magnetism and microwave devices [5]. Moreover, the ferroelectro-magnetic phenomena have long aroused intense interest for researchers in the solid-state and material sciences.

Among the multiferroic materials, $BiFeO_3$ belonging to ABO_3 family with a rhombohedrally distorted simple perovskite structure with a space group R3c has been of much interest due to its relatively high antiferromagnetic-paramagnetic Néel temperature T_N=653-643 K [6, 7] and its ferroelectric-paraelectric Curie temperature, T_C=1103 K [8]. Several studies have been performed to determine the crystal structures and magnetic properties of $BiFeO_3$, encouraged to a great extent by its potential magneto-electric properties [9]. $BiFeO_3$ exhibits antiferromagnetic and ferroelectric order concurrently. The antiferromagnetic order originates from unpaired electrons in the d orbitals of Fe^{3+} ions at the B positions of the perovskite crystal structure [10, 11], while the ferroelectric order is caused by the free electron pair in an s-p hybrid orbital of Bi^{3+} occupying the A site. This antiferromagnetic order can be changed in different ways, one of them by cationic substitution,

**ssoliman@kfu.edu.sa, samia.arafat@yahoo.com*

https://orcid.org/0000-0001-6811-8142

thus leading to a ferromagnetic response [12]. Another perovskite multiferroic material is $BiCrO_3$ which was first synthesized in 1968 by firing under very high pressure. It has a monoclinic C2 structure at room temperature, exhibits a parasitic ferromagnetic ordering at 123 K, and undergoes a structural phase transition at 440 K [13].

The doping process is recognized to be a suitable method to change the specific physical properties of a material [14-19]. The nature of the doping effect has been studied by doping $BiFeO_3$ with Cr. $BiFe_{1-x}Cr_xO_3$ (x=0.4-1.0), where a portion of Fe^{3+} ions is substituted by Cr^{3+} ions, are studied. High-pressure synthesis is a powerful technique to explore new materials. $BiFe_{1-x}Cr_xO_3$ with perovskite-type structure was reported to be synthesized under high pressure of 7 GPa. In this study, the performance of X-ray powder diffraction at room temperature, magnetization characteristics with temperature, and their hysteresis loops at room temperature are conducted.

EXPERIMENTAL

The polycrystalline ceramics samples of $BiFe_{1-x}Cr_xO_3$ (x= 0.4, 0.5, 0.6, 0.8, and 1.0) were prepared by a solid-state reaction technique under a high pressure of 7 GPa. Mixed powders of Bi_2O_3 (99.9%), Fe_2O_3 (99.9%), and Cr_2O_3 (99.9%) with stoichiometric proportion (1:1 molar ratio) were mixed in an agate mortar for 0.5 h. Afterward, these were packed into gold capsules (~4x6 mm^2) and was calcined in a cubic anvil-type apparatus under 7 GPa at 1000 °C for 1 h [20].

X-ray diffraction experiments were carried out using a diffractometer with CuKα source. The X-ray pattern was recorded at an interval of 0.010° at room temperature. The structural parameters were refined by Rietveld analysis of diffraction data in the 2θ range of 20°-65°. The magnetic properties were measured using a superconducting quantum interference device magnetometer (SQUID, Quantum Design). The data were collected under zero-field cooling and field cooling at 1 kOe from 5 to 400 K, below and above the Néel and spin-reorientation temperatures.

RESULTS AND DISCUSSION

Structural analysis: Fig. 1a shows the X-ray powder diffraction (XRD) patterns for $BiFe_{1-x}Cr_xO_3$ where x= 0.4, 0.5, 0.6, 0.8, and 1.0 at room temperature (RT). The patterns revealed that the peaks were sharp and strong indicated a good crystallization aspect of the samples. There were some impurity phases of $BiFeO_9$, Bi_2O_3, and $Bi_{25}FeO_{40}$ formed along with the $BiFeO_3$ phase in the solid-state reaction process, as reported by several authors [21-24]. The percentage of the impurity phases determined by calculating the ratio of the

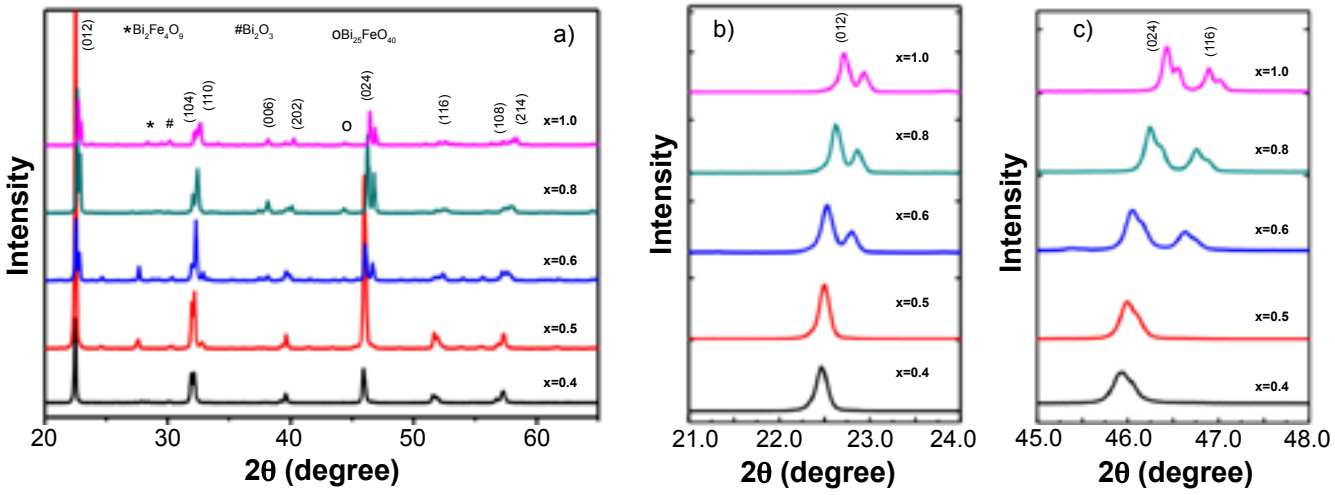

Figure 1: X-ray diffraction patterns of $BF_{1-x}C_xO_3$, x=0.4-1.0, at RT.
[Figura 1: Padrões de difração de raios X de $BF_{1-x}C_xO_3$, x=0,4-1,0, à temperatura ambiente.]

Table I - Crystal structures and lattice parameters of $BiFe_{1-x}Cr_xO_3$, x=0.4-1.0.
[Tabela I - Estruturas cristalinas e parâmetros de rede de $BiFe_{1-x}Cr_xO_3$, x=0,4-1,0.]

Sample	Structure	a (Å)	b (Å)	c (Å)	β	Cell volume (Å^3)
x=0.4	Rhombohedral	5.563	5.563	13.773	-	369.1
x=0.5	Rhombohedral	5.559	5.559	13.749	-	367.9
x=0.6	Monoclinic	9.530	5.925	9.935	107.52	535.0
x=0.8	Monoclinic	9.468	5.884	9.932	108.26	525.5
x=1.0	Monoclinic	9.435	5.891	10.070	108.19	531.7

area under the peak using Origin Pro 8 gave the value range of 2%-8% for x=0.4-1.0, respectively. For x= 0.4 and 0.5, the materials displayed a typical rhombohedral structure with R3c space group, distorted perovskite structure, and was indexed as a hexagonal unit cell. However, for x= 0.6 to 1.0, the structure changed to a monoclinic (m) C2/c symmetry. Figs. 1b and 1c show the magnified patterns at 2θ around 22.5° and 45° of the samples. The single peaks at 2θ= 22.5° and 45° of a rhombohedral structure in x=0.4 were shifted to higher 2θ giving a decrease of lattice parameter, and split gradually into two peaks, indicating that the crystal structure transformed from rhombohedral symmetry to a monoclinic symmetry when x=1 ($BiCr_{1.0}O_3$) [13]. It was clear that the material was controlled by a new structural phase for heavily doped samples. The transitional point of the structure change was identified at x=0.6 ($BiFe_{0.4}Cr_{0.6}O_3$)

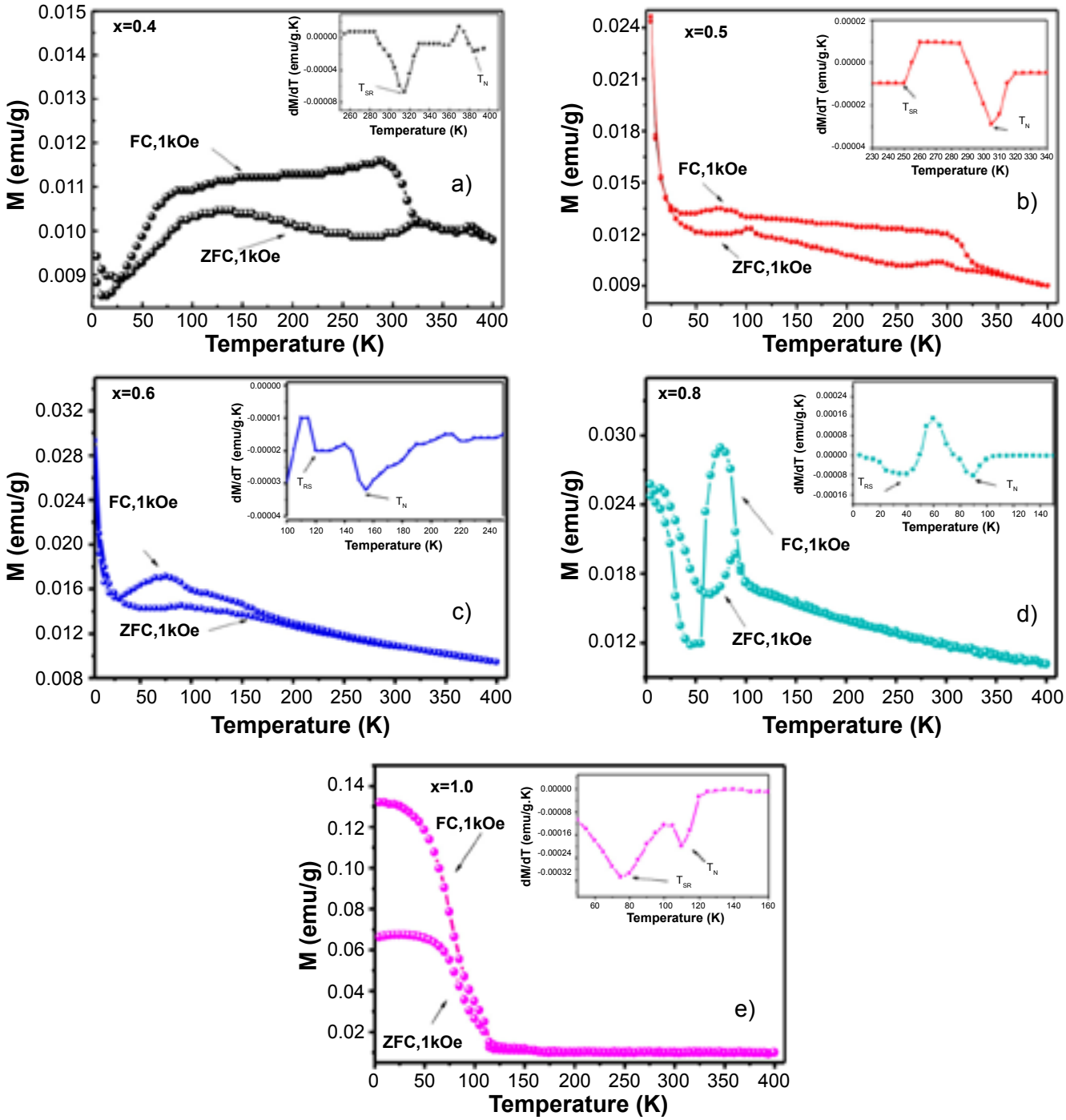

Figure 2: Variation of the magnetization (M) with temperature (T) for $BiFe_{1-x}Cr_xO_3$, x=0.4-1.0; the inset shows the plot of dM/dT curve as a function of temperature.

[Figura 2: Variação da magnetização (M) com a temperatura (T) para $BiFe_{1-x}Cr_xO_3$, x=0,4-1,0; o inserto mostra o gráfico da curva dM/dT em função da temperatura.]

Table II - Magnetic parameters of $BiFe_{1-x}Cr_xO_3$, x=0.4-1.0.
[Tabela II - Parâmetros magnéticos de $BiFe_{1-x}Cr_xO_3$, x=0,4-1,0.]

Sample	T_{SR} (K)	T_N (K)	M_{max} (emu/g)	M_r (emu/g)	H_c (kOe)
x=0.4	315	370	0.1007	0.0023	0.20
x=0.5	250	305	0.1030	0.0016	0.10
x=0.6	120	155	0.1065	0.0008	0.01
x=0.8	35	90	0.1120	0.0001	0.02
x=1.0	75	110	0.1100	0.0080	0.50

when two phases appeared. However, nearly single-phase was obtained in other samples. Also, the data showed a decrease in lattice parameters with increasing of x (Cr ions). The variation of lattice parameters with the concentration of x is illustrated in Table I.

Magnetic properties: Figs. 2a to 2e and insets show the temperature dependence of the zero-field cooled (ZFC) and field cooled (FC) magnetization (M-T) measured under a field of 1 kOe. The derivative dM/dT inset curves for BF1-xCxO3, x= 0.4, 0.5, 0.6, 0.8, and 1.0 from 230 up to 400 K are indicated. The magnetization showed Curie-Weiss like behavior above the transition temperatures. All samples revealed two magnetic transitions. The first one is the Néel temperature T_N in which the paramagnetic phase changes to the antiferromagnetic phase, and the second one has been recognized as spin-reorientation transition T_{SR} from antiferromagnetic to weak ferromagnetic ordering. The T_N and T_{SR} values were confirmed from peak positions of the FC-dM/dT plot versus T at 1 kOe, as observed in [25]. Also, by increasing Cr^{3+} ion doping, the Néel temperature T_N and spin-reorientation temperature T_{SR} shifted towards lower temperatures. The change in T_N and T_{SR} as a function of Cr concentration (x) is shown in Table II. This significant decrease in T_N and T_{SR} was probably due to the transformation of relatively heavy Fe^{3+} ions (0.645 Å) to lighter Cr^{3+} ions (0.615 Å) leading to a reduction in the concentration of Fe^{3+} ions and sublattice moments which are slightly canted along the c-axis [26, 27]. In addition, the magnitudes of magnetization increased as Cr^{3+} ion doping increased in the samples when going from heavier to lighter ions.

Room temperature magnetization hysteresis (M-H) loops of $BiFe_{1-x}Cr_xO_3$ with x= 0.4, 0.5, 0.6, 0.8, and 1.0 are shown in Fig. 3 with the inset in the field range of ±1.0 kOe. The combined plots for all the samples demonstrated a relative effect of the Cr^{3+} ion doping concentration on the magnetic properties of these samples. It is clearly seen that none of the samples exhibited saturation magnetization. This could be due to the antiferromagnetic nature of the samples. Similar behavior has been reported by several authors [28-30]. Besides, the nonzero remnant magnetization M_r and tiny magnetic hysteresis, along with the antiferromagnetic behavior as demonstrated in the inset, indicated the existence of weak ferromagnetic behavior.

The remnant magnetization M_r, maximum magnetization M_{max}, and coercivity H_c for the $BiFe_{1-x}Cr_xO_3$, x= 0.4, 0.5, 0.6, 0.8, and 1.0 samples are listed in Table II. It was seen that the magnetization increased with the increase of Cr^{3+} ion doping in the sample. Besides, the Cr^{3+} ion doping effect was responsible for efficient ferromagnetic properties. The enhancement in magnetic properties showed by adding of Cr^{3+} ions replacing Fe^{3+} ions may be attributed to two major reasons. The first reason can be explained by the existence of the uncompensated spins in the two sublattices as a result of the different magnetic moment of Cr^{3+} ions ($\mu=3.87.\mu_B$) with regard to Fe^{3+} ions ($\mu=5.92.\mu_B$) in octahedral sites. The antiferromagnetic arrangement is associated with the direction of electron spin, where the number of spin-up is equal to the number of spin-down in the sublattices, related to the mechanism of compensation [10]. While Fe^{3+} ions were substituted by Cr^{3+} ions, the spins in the sublattices of $BiFeO_3$ were uncompensated, where the number of spin-up was not the same as the number of spin-down, resulting in a weak ferromagnetic arrangement. The second reason, the improvement of magnetic behavior with increasing the Cr^{3+} ion doping concentration in the sample may be related to the variation in the B-O-B bond angle. The substitution of Fe^{3+} ions by Cr^{3+} ions led to an increase in the canting of spins and thus enhanced the magnetization in $BiFe_{1-x}Cr_xO_3$ samples.

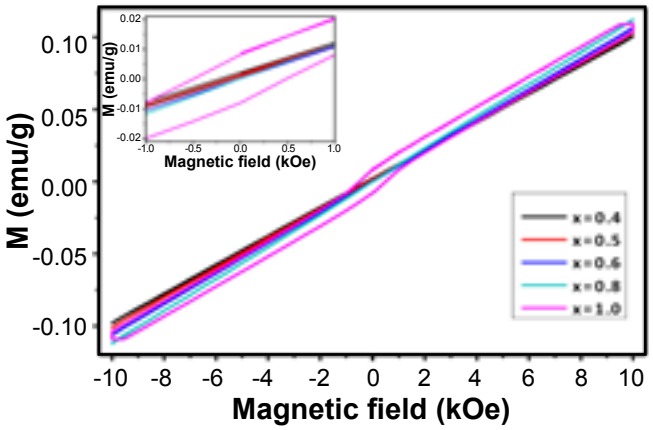

Figure 3: Magnetic hysteresis loops for $BiFe_{1-x}Cr_xO_3$, x=0.4-1.0.
[Figura 3: Laços de histerese magnética para $BiFe_{1-x}Cr_xO_3$, x=0,4-1,0.]

CONCLUSIONS

The effects of the Cr ions substitution for Fe ions of

$BiFe_{1-x}Cr_xO_3$, with x= 0.4, 0.5, 0.6, 0.8, and 1.0 on the structural and magnetic properties were studied. The structure changed from rhombohedral when x= 0.4 and 0.5 to monoclinic when x= 0.6, 0.8, and 1.0. Replacement of Fe^{3+} ions by Cr^{3+} ions significantly changed the magnetic properties of $BiFe_{1-x}Cr_xO_3$. The helical spin structure of $BiFe_{1-x}Cr_xO_3$ was improved towards a ferromagnetic structure beyond $BiCrO_3$. In addition, the Néel temperature T_N and spin-reorientation transition temperature T_{SR} shifted towards lower values with increasing x (Cr ion) from 315 K for $BiFe_{0.4}Cr_{0.6}O_3$ to 75 K for $BiCrO_3$. In conclusion, the process of substituting Cr^{3+} ions for Fe^{3+} ions of $BiFe_{1-x}Cr_xO_3$ changes the crystal structure and brings the magnetic transition temperatures T_{SR} and T_N to lower values. The M-H hysteresis loops at room temperature revealed that the doped samples $BiFe_{1-x}Cr_xO_3$ (x=0.4, 0.5, 0.6, 0.8) were antiferromagnetic while the pure $BiCrO_3$ (x=1.0) was weak ferromagnetic. The remnant magnetization and coercivity decreased starting from x= 0.4 to 0.8 and then increased in the pure $BiCrO_3$ (x=1.0) sample with enhancement in magnetic behavior with the increase of Cr doping.

ACKNOWLEDGMENTS

The author would like to express her thanks and deep gratitude to King Faisal University, College of Science, Physics Department, and the Deanship of Scientific Research for their kind support. This study was funded by the Deanship of Scientific Research (King Faisal University): proposal No. 186057.

REFERENCES

[1] M. Fiebig, Th. Lottermoser, D. Frohlich, A.V. Goltsev, R.V. Pisarev, Nature **419** (2002) 818.
[2] N. Hur, S. Park, P.A. Sharma, J.S. Ahm, S. Guha, S.W. Cheong, Nature **429** (2004) 392.
[3] T. Kimura, S. Kawamoto, I. Yamade, M. Azuma, M. Takano, Y. Tokura, Phys. Rev. B **67** (2003) 180401.
[4] S.T. Wang, H. Song, J. Mater. Sci. Mater. Electron. **29** (2018) 5566.
[5] C. Michel, K.M. Moreau, G.D. Achenbach, R. Gerson, W.J. James, Solid State Commun. **7** (1969) 701.
[6] N.A. Hill, J. Phys. Chem. B **104** (2000) 6694.
[7] B. Dhanalakshmi, K. Pratap, B. Parvatheeswara Rao, P.S.V. Subba Rao, J. Alloys Compd. **676** (2016) 193.
[8] F. Kubel, H. Schmid, Acta Crystallogr. B **46** (1990) 698.
[9] P. Fischer, M. Polemska, I. Sosnowska, M. Szymaski, J. Phys. C Solid State Phys. **13** (1980) 1931.
[10] L.G. Betancourt-Cantera, A.M. Bolarín-Miró, C.A. Cortés-Escobedo, L.E. Hernández-Cruz, F. Sánchez-De Jesús, J. Magn. Magn. Mater. **456** (2018) 381.
[11] J.T. Heron, D.G. Schlom, R. Ramesh, Appl. Phys. Rev. **1** (2014) 21303.
[12] G. Dhir, P. Uniyal, N.K. Verma, Phys. Status Solidi C **14** (2017) 1610.
[13] S. Niitaka, M. Azuma, M. Takano, E. Nishibori, M. Takata, M. Sakata, Solid State Ion. **72** (2004) 557.
[14] I. Sosnawska, W. Schafer, W. Kockelmam, K.H. Andersen, O. Troyanochuk, Appl. Phys. A **74** (2002) 1040.
[15] H. Uchida, R. Ueno, H. Nakaki, H. Funakubo, S. Koda, Jap. Appl. Phys. **44** (2005) L561.
[16] X. Qi, J. Dho, R. Tomov, M.G. Blamire, J.I. Macmanus-Driscoll, Appl. Phys. Lett. **86** (2005) 63903.
[17] S.R. Das, P. Bhattacharya, R.N.P. Choudhary, R.S. Katiyar, J. Appl. Phys. **99** (2006) 66107.
[18] R. Mazumder, A. Sen, J. Alloys Compd. **475** (2009) 577.
[19] A.J. Jorcobson, B.E.F. Fender, J. Phys. C Solid State Phys. **8** (1975) 844.
[20] S.S. Arafat, Chin. Phys. B **23** (2014) 66101.
[21] Q. Zhang, H. Zhu, H. Xu, B. Gao, J. Xiao, Y. Liang, L. Zhu, G. Zhu, Q. Xiao, J. Alloys Compd. **546** (2013) 57.
[22] F. Chang, N. Zhang, F. Yang, S. Wang, G. Song, J. Phys. D Appl. Phys. **40** (2007) 7799.
[23] V.N. Minh, N.G. Quan, J. Alloys Compd. **509** (2011) 2663.
[24] X. Qi, X. Zhang, J. Qi, H. Xu, H. Wang, Key Eng. Mater. **512-515** (2012) 1240.
[25] A.A. Belik, Sci. Technol. Adv. Mater. **16** (2015) 26003.
[26] S. Chihaoui, M. Koubaa, W. Cheilkhrouhou-Koubaa, A. Cheilkhrouhou, H. Guermazi, J. Alloys Compd. **771** (2019) 327.
[27] A. Pal, C.D. Sekhar, A. Venimadhav, P. Murugavel, J. Phys. Condens. Matter **29** (2017) 1.
[28] M.N. Hossain, M.A. Matin, M.A. Hakim, M.F. Islam, Mater. Sci. Eng. **438** (2018) 12016.
[29] A. Kumar, K. Yadav, Mater. Sci. Eng. B **176** (2011) 227.
[30] B. Wang, X. Tian, X. Song, L. Ma, S. Yu, C. Hao, K. Chen, Q. Lie, Colloid Surf. A **461** (2014) 184.
(Rec. 01/06/2019, Rev. 13/08/2019, 26/10/2019, Ac. 02/11/2019)

BY-NC

Regeneração de defeito ósseo crítico após implantação de fosfato de cálcio bifásico (β-fosfato tricálcico/pirofosfato de cálcio) e vidro bioativo fosfatado

(Regeneration of a critical bone defect after implantation of biphasic calcium phosphate - β-tricalcium phosphate/calcium pyrophosphate - and phosphate bioactive glass)

R. S. Almeida[1]*, M. H. Prado da Silva[2], D. Navarro da Rocha[2], I. I. A. Ribeiro[1], A. A. Barbosa Júnior[3], F. B. Miguel[4], F. P. Rosa[1]

[1]Universidade Federal da Bahia, Instituto de Ciências da Saúde, Laboratório de Bioengenharia Tecidual e Biomateriais, Av. Reitor Miguel Calmon s/n, 40110-100, Salvador, BA, Brasil

[2]Instituto Militar de Engenharia, Seção de Engenharia Mecânica e de Materiais, Rio de Janeiro, RJ, Brasil

[3]Fundação Oswaldo Cruz, Instituto Gonçalo Moniz, Salvador, BA, Brasil

[4]Universidade Federal do Recôncavo da Bahia, Centro de Ciências da Saúde, Santo Antônio de Jesus, BA, Brasil

Resumo

Objetivou-se avaliar novos biomateriais fosfatados para regeneração de defeito ósseo crítico. Distribuíram-se 45 ratos Wistar em três grupos: CON (sem implantação de biomaterial), FCB (grânulos de fosfato de cálcio bifásico: fosfato tricálcico tipo β, β-TCP/ pirofosfato de cálcio) e FCB/BV (FCB/vidro bioativo fosfatado), avaliados aos 15, 45 e 120 dias de pós-operatório. No grupo CON, observaram-se neoformação óssea restrita às bordas ósseas e preenchimento do defeito por delgado tecido conjuntivo fibroso. Em FCB e FCB/BV, os grânulos preencheram toda a extensão do defeito e apresentaram maior fragmentação em FCB/BV. A neoformação óssea foi mais evidente no FCB. De permeio às partículas dos biomateriais formou-se um tecido conjuntivo frouxo, que evoluiu para fibroso em FCB. Os biomateriais desencadearam discreta reação inflamatória crônica granulomatosa, que se tornou inconspícua. Conclui-se que os materiais foram biocompatíveis, atuaram como arcabouços tridimensionais, apresentaram potencial osteocondutor e favoreceram a regeneração óssea, principalmente FCB. A adição do vidro bioativo aumentou a biodegradabilidade de FCB/BV.
Palavras-chave: biomateriais, implantes experimentais, fosfatos de cálcio, regeneração óssea.

Abstract

The objective was to evaluate new phosphate biomaterials for the regeneration of a critical bone defect. 45 Wistar rats were distributed in three groups: CON (without biomaterial implantation), FCB (biphasic calcium phosphate granules: β-tricalcium phosphate, β-TCP/calcium pyrophosphate) and FCB/BV (FCB/bioactive glass granules), evaluated at 15, 45, and 120 postoperative days. In the CON group, bone neoformation restricted to bone edges and filling of the defect by thin fibrous connective tissue were observed. In FCB and FCB/BV, the granules filled the entire extent of the defect and showed greater fragmentation in FCB/BV. Bone neoformation was more evident in FCB. From the biomaterial particles, a loose connective tissue was formed, which evolved to fibrous in FCB. Biomaterials triggered a discrete chronic inflammatory granulomatous reaction, which became inconspicuous. It was concluded that materials were biocompatible, acted as three-dimensional scaffolds, presented osteoconductive potential, and favored bone regeneration, especially FCB. The addition of bioactive glass increased the biodegradability of FCB/BV.
***Keywords**: biomaterials, experimental implants, calcium phosphates, bone regeneration.*

INTRODUÇÃO

Situações em que ocorrem grandes perdas ósseas, por exemplo após as ressecções de tumores e fraturas extensas, o reparo tecidual ocorre de forma limitada, demandando o uso de enxertos [1]. Como alternativa, a bioengenharia tecidual tem desenvolvido biomateriais para atuar como substitutos ósseos e proporcionar o restabelecimento funcional e estético, para reinserção social e laboral destes indivíduos [2]. Há um consenso que o termo biomaterial refere-se a materiais que podem interagir com sistemas biológicos para avaliar, tratar, aumentar ou substituir qualquer tecido, *órgão ou função do corpo* [3]. De maneira clássica, em relação à sua composição química, estes materiais podem ter origem metálica, cerâmica, polimérica ou compósitos - uma

**renata.almeidabio@gmail.com*
https://orcid.org/0000-0001-8359-6345

combinação destes [4]. Porém, recentemente esta definição vem sendo refutada e discutida de forma mais abrangente, considerando-se os biomateriais como substâncias desenvolvidas de forma que, sozinha ou como parte de um sistema complexo, podem ser usadas para direcionar, pelo controle de interações com componentes de sistemas vivos, qualquer procedimento terapêutico ou diagnóstico, em humanos ou medicina veterinária, podendo incluir tecidos engenheirados, células, órgãos e até vírus [4].

Os biomateriais cerâmicos são amplamente utilizados por exibirem ângulos de contato de 60-85° com a água e, portanto, não induz mudanças conformacionais nas proteínas plasmáticas adsorvidas, o que promove a migração e adesão celular [2]. Dentre estes o β-fosfato tricálcico (β-TCP) é utilizado nas técnicas regenerativas como componente de cimentos biológicos ou como reforço de arcabouços poliméricos [5], devido à sua semelhança com componentes inorgânicos do tecido ósseo, não apresentar risco de transmissão de doenças, ter boa biocompatibilidade e participar do equilíbrio cálcio/fósforo do organismo [6]. Além do β-TCP, o pirofosfato de cálcio ($Ca_2P_2O_7$) também vem sendo utilizado como um substituto ósseo reabsorvível, biocompatível e não tóxico [7, 8]. Ao apresentar uma razão molar Ca/P de 1,0, o $Ca_2P_2O_7$ exibe uma maior taxa de reabsorção do que a do β-TCP (Ca/P=1,5) e vem sendo indicado como uma possível alternativa às fases hidroxiapatita e β-TCP para a regeneração óssea [9]. Já os vidros bioativos são promissores devido à sua capacidade de ligar-se quimicamente ao tecido ósseo, sem formar tecido de interposição, o que estimula a neoformação tecidual e a regeneração [10]. São compostos principalmente por sílica, cálcio, sódio e fósforo, sendo os vidros bioativos fosfatados mais fácies de fundir e quimicamente mais instáveis que os silicatos, o que favorece sua biodegradação e bioabsorção [11]. Quando em contato com fluidos biológicos, os vidros bioativos formam um hidroxicarbonato de apatita semelhante à hidroxiapatita do tecido ósseo [12], que tem afinidade por fatores de crescimento que interagem com macrófagos e estes exibem forte gradiente químico para células progenitoras de osteoblastos [10].

Estas cerâmicas exibem excelentes propriedades de biorreabsorção, osteocondução, osteoindução e osteogênese. Quando utilizadas de forma isolada são geralmente projetadas para preenchimento ósseo ou como revestimento bioativo em implantes metálicos [13]; desta forma, espera-se que a incorporação de 5% de vidro bioativo ao β-TCP e ao pirofosfato de cálcio proporcione a vantagem adicional da bioatividade aumentada em conjunto com a estabilidade mecânica melhorada [14]. Outro fator de grande relevância é que os biomateriais devem ser fabricados com propriedades adequadas ao tecido que se pretende reparar, juntamente com suas exigências geométricas [1]. Sendo assim, os grânulos são muito favoráveis, por formarem um arcabouço que permite a adesão e a migração celular, por serem de fácil manuseio e capazes de preencher o defeito [15]. Além disso, as propriedades dos biomateriais devem ser sempre avaliadas e os testes *in vivo* permitem estudar as interações teciduais previamente à sua aplicação clínica, visto que o método de fabricação, a composição química e o formato podem interferir no comportamento celular e na interface biomaterial/tecido. Diante do exposto, este trabalho avaliou a biocompatibilidade e a biofuncionalidade de grânulos de biomateriais de fosfato de cálcio bifásico (β-fosfato tricálcico/pirofosfato de cálcio) e vidro bioativo fosfatado, como novas composições para regeneração de defeito ósseo crítico.

MATERIAL E MÉTODOS

Este estudo foi previamente aprovado pela Comissão de Ética no Uso de Animais (protocolo 38/2012) do Instituto de Ciências da Saúde da Universidade Federal da Bahia e seguiu as Normas Éticas de Pesquisas em Animais (Lei nº 11794 de 2008), bem como as diretrizes do Instituto Nacional de Saúde para o cuidado e uso de animais de laboratório (NIH Publicação nº 85-23 Rev. 1985). Os biomateriais utilizados foram produzidos e caracterizados seguindo protocolo descrito na literatura [16, 17]. Os biomateriais foram produzidos pelo método de deposição química, onde esponjas poliméricas de poliuretano foram imersas em uma solução rica em íons de cálcio (Ca^{2+}) e fosfato (PO_4^{3-}), com razão molar Ca/P=1,67, a 80 °C, com trocas durante três dias até a completa deposição de monetita ($CaHPO_4$). Após a deposição, foi realizada a etapa de conversão alcalina, onde as esponjas recobertas pela monetita foram imersas em solução 0,1 mol/L de hidróxido de potássio (KOH, Merck, Alemanha) a 60 °C por 24 h. As amostras foram levadas ao forno (LF914, Jung, Brasil) e aquecidas até 900 °C, onde a esponja polimérica foi volatizada, dando origem ao arcabouço cerâmico poroso de fosfato de cálcio bifásico [fosfato tricálcico do tipo β (β-TCP) + pirofosfato de cálcio ($Ca_2P_2O_7$)].

O vidro bioativo fosfatado (P_2O_5-CaO-CaF_2) foi projetado para ter a seguinte composição (em mol): 60% de pentóxido de fósforo (P_2O_5) + 20% de óxido de cálcio (CaO) + 20% de fluoreto de cálcio (CaF_2). A fonte do P_2O_5 utilizada foi o ácido ortofosfórico (H_3PO_4, Merck, Alemanha), enquanto a fonte de CaO foi o carbonato de cálcio ($CaCO_3$, Sigma Aldrich, Alemanha), e para o fluoreto de cálcio utilizou-se um reagente analítico (CaF_2, Sigma Aldrich, Alemanha). Estes reagentes foram misturados e homogeneizados em uma placa com agitação magnética (Q261M12, Quimis, Brasil) por 24 h, seguido de secagem em estufa a 60 ºC por 6 h. A mistura foi fundida em um forno a 1400 °C, usando um cadinho de platina, com patamar de 2 h e taxa de aquecimento de 5 °C/min. O fundido foi retirado rapidamente do forno e vertido para um recipiente contendo água destilada, para formação de partículas de vidro (frita), que em seguida foram trituradas em um moinho de bola (MA 350, Marconi, Brasil). Estas partículas de vidro bioativo fosfatado foram classificadas em um sistema de peneiras da série Tyler, para então se selecionar uma distribuição de tamanhos inferiores a 20 μm (500 mesh). As partículas foram peneiradas em fluxo contínuo de álcool etílico (Vetec,

Brasil) para facilitar a passagem do material pela peneira. Posteriormente, à metade dos arcabouços cerâmicos porosos de fosfato de cálcio bifásico (β-TCP + $Ca_2P_2O_7$) foram adicionados 5% do vidro bioativo fosfatado. Por fim, todos os arcabouços cerâmicos porosos foram sinterizados a 1200 °C para consolidação da estrutura cerâmica. Os arcabouços formados foram fragmentados e classificados utilizando-se peneiras com aberturas na faixa de 0,5 a 0,7 mm. Em seguida os grânulos de fosfato de cálcio bifásico (grupo FCB) e de fosfato de cálcio bifásico/vidro bioativo (grupo FCB/BV) foram acondicionados em *eppendorfs* e esterilizados com 15 kGy de radiação gama.

Caracterização dos materiais: para a identificação das fases cristalinas dos arcabouços porosos, utilizou-se um difratômetro da PANalytical, X'Pert PRO MPD. A varredura foi realizada no intervalo 10°<2θ<80° com uma fenda incidente de 1° e divergente de 1/2°, tempo por passo de 100 s e passo de coleta de 0,02° com uma fonte de cobre e potência de 40 kV e 40 mA. A análise quantitativa de fases, através do refinamento pelo método de Rietveld, foi realizada utilizando o programa X'Pert HighScore Plus (PANalytical) e foram obtidas as frações de fases cristalinas dos arcabouços porosos antes e após a etapa de conversão alcalina, bem como dos grânulos sinterizados com (grupo FCB/BV) e sem vidro bioativo (grupo FCB). A análise da morfologia superficial dos arcabouços porosos e grânulos obtidos foi realizada em um microscópio eletrônico de varredura (MEV, JSM 5800LV, Jeol).

Ensaio in vivo: para implantação dos biomateriais utilizaram-se 45 *Rattus novergicus* Wistar, machos adultos, com massa corpórea entre 350 e 400 g distribuídos aleatoriamente para composição de três grupos: CON (defeito vazio, preenchimento apenas com o coágulo sanguíneo); FCB (grânulos de fosfato de cálcio bifásico) e FCB/BV (grânulos de fosfato de cálcio bifásico/vidro bioativo). O procedimento cirúrgico para confecção do defeito ósseo crítico foi o mesmo descrito em outros trabalhos do grupo [18-20]. Após remoção do fragmento ósseo os biomateriais foram implantados de acordo com seus respectivos grupos experimentais, exceto para o grupo controle. Ao final, o retalho cutâneo foi reposicionado e suturado com pontos simples (Fig. 1). Aos 15, 45 e 120 dias de pós-cirúrgico, os animais foram eutanasiados com dose letal do anestésico para remoção da calvária. Os espécimes foram fixados em formaldeído tamponado a 4% (Aldrich, Reino Unido) por no mínimo 72 h e descalcificados com ácido nítrico a 7% (Aldrich, Reino Unido) durante 7 dias para o processamento histológico. Após a inclusão em parafina, foram realizados cortes transversais de forma seriada com 7 μm de espessura e corados com hematoxilina-eosina (HE), picrosirius-red (PIFG) e tricrômico de Masson-Goldner (TMG) [20]. A análise histomorfométrica foi realizada por microscopia óptica utilizando microscópio MM6B (Leica, Alemanha) acoplado a uma câmera digital DFC7000T (Leica, Alemanha) e o sistema de análise de processamento de imagens LAS Core (Leica, Alemanha). Foram realizadas as medidas de extensão linear do defeito (em mm), porcentagem de preenchimento linear do defeito por matriz óssea neoformada mineralizada e área seccional neomineralizada em relação à área seccional total do defeito [20].

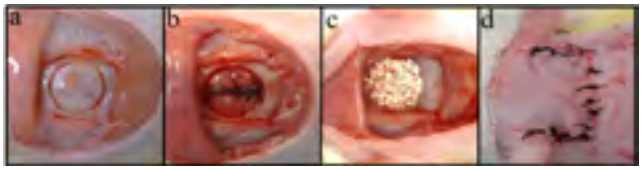

Figura 1: Fotos das etapas do procedimento cirúrgico evidenciando a demarcação do defeito (a) e remoção do fragmento ósseo (b) para implantação dos biomateriais (c), seguido de reposicionamento do retalho e sutura (d).

[Figure 1: Pictures of the steps of the surgical procedure showing the demarcation of the defect (a) and removal of the bone fragment (b) for implantation of biomaterials (c), followed by flap repositioning and suture (d).]

RESULTADOS E DISCUSSÃO

De acordo com os resultados obtidos por difração de raios X (DRX), a técnica de deposição química produziu um recobrimento de monetita (JCPDS 01-070-1425) sobre as esponjas poliméricas (Fig. 2), que se apresenta como a fase termodinamicamente mais estável em condições ácidas, como a encontrada na solução precursora (pH 3,8) utilizada neste trabalho [13, 21]. Durante a etapa de conversão alcalina, parte da fase monetita depositada foi transformada em hidroxiapatita (JCPDS 09-0432), 23,6%, conforme a quantificação de fases obtida através do refinamento pelo método de Rietveld. Assim, majoritariamente o recobrimento sobre as esponjas poliméricas apresentou 76,4% da fase monetita. Após a volatilização das esponjas poliméricas a 900 ºC e posterior fragmentação dos arcabouços porosos, os grânulos produzidos se apresentaram como um fosfato de cálcio bifásico, devido à identificação dos picos referentes às fases β-TCP (JCPDS 09-0169) e pirofosfato de cálcio (JCPDS 01-071-2123) nos difratogramas das amostras (Figs. 2c e 2d). A análise quantitativa de fases indicou 53,1% de pirofosfato de cálcio e 46,9% de β-TCP para os grânulos do grupo FCB. Para o grupo FCB/BV, a adição do vidro bioativo fosfatado aumentou a quantidade da fase β-TCP para 55,2%, enquanto houve uma diminuição no teor de pirofosfato de cálcio para 46,8%. É estabelecida na literatura a transformação da fase monetita para o pirofosfato de cálcio após o tratamento térmico acima de 800 ºC [22, 23]. Recentes estudos vêm utilizando clinicamente o pirofosfato de cálcio e o fosfato tricálcico (β e α) devido ao maior potencial bioativo, quando em comparação à fase hidroxiapatita [24, 25]. A bioatividade é uma propriedade que está diretamente relacionada com a dissolução dos fosfatos de cálcio [21]. Por isso, atualmente é verificada uma crescente demanda na produção de fosfatos de cálcio com maior capacidade osteocondutora e bioatividade, consequência de uma adequada biorreabsorção em meio fisiológico.

Na Fig. 3a é possível observar que a superfície da monetita depositada sobre as esponjas poliméricas se apresentou

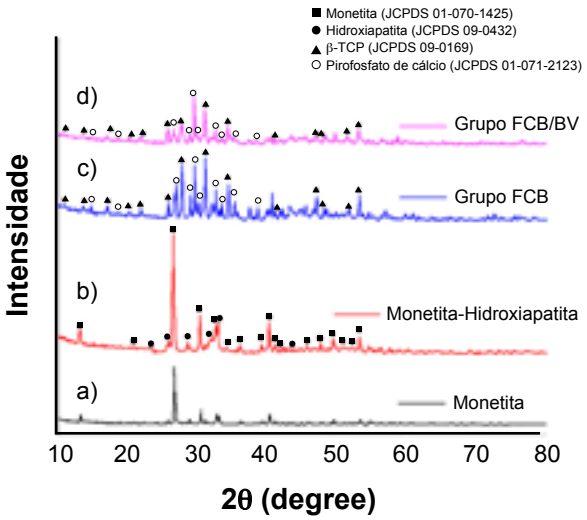

Figura 2: Difratogramas de raios X das amostras: a) monetita; b) monetita-hidroxiapatita; c) grupo FCB; e d) grupo FCB/BV.
[Figure 2: X-ray diffraction patterns of the samples: a) monetite; b) monetite-hydroxyapatite; c) FCB group; and d) FCB/BV group.]

em morfologia de placas, em dimensão micrométrica, característica dessa fase ácida de fosfato de cálcio [13]. Após a etapa de conversão alcalina, uma precipitação parcial e superficial de hidroxiapatita confirmou os resultados obtidos por DRX (Fig. 3b). O estudo cinético e morfológico da etapa de conversão em meio alcalino, também utilizada no presente estudo, sugeriu que o processo de precipitação da hidroxiapatita ocorreu pela dissolução superficial da fase precursora com uma posterior nucleação e crescimento da hidroxiapatita [26]. Além disso, as análises por MEV demostraram uma maior densificação dos grânulos do grupo FCB/BV (Fig. 3d), quando comparado ao grupo FCB (Fig. 3c). Este resultado foi compatível com uma sinterização em

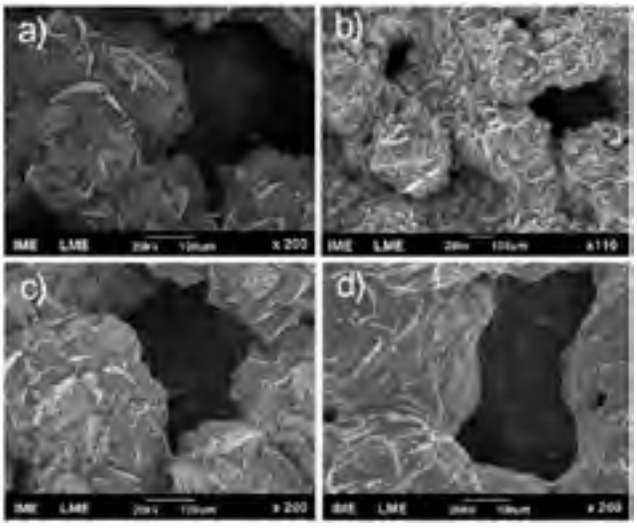

Figura 3: Micrografias de MEV das superfícies de: a) monetita; b) monetita-hidroxiapatita; c) grupo FCB; e d) grupo FCB/BV.
[Figure 3: SEM micrographs of the surfaces of: a) monetite; b) monetite-hydroxyapatite; c) FCB group; and d) FCB/BV group.]

fase líquida, também observada em trabalhos anteriores [17].

Em estudos experimentais, a perda tecidual extensa pode ser observada com a confecção de defeito ósseo crítico, sem implantação de um arcabouço e nem aplicação de outra terapia regenerativa [18], como pode ser observado no grupo CON (defeito vazio). Em razão das especificidades dessa resposta e pela ausência de um suporte estrutural, neste grupo aos 15 dias a região de extensão do defeito foi preenchida por tecido conjuntivo fibroso bem vascularizado e com espessura inferior ao osso remanescente (Fig. 4a), que se tornou mais denso e com pouca vascularização aos 45 dias e com espessura mais delgada aos 120 dias (Fig. 4b) [18, 19]. Esse tipo de reparo decorre da lesão tecidual causada pelo procedimento cirúrgico, em que há liberação de fatores de crescimento que atraem células fusiformes mesenquimais e induzem a diferenciação de fibroblastos para síntese do tecido conjuntivo [18]. Nestas situações, a regeneração óssea também é caracterizada por um processo reparativo e reacional à lesão tecidual, onde células osteoprogenitoras presentes no periósteo e no endósteo do osso adjacente são estimuladas a se proliferar e diferenciar em osteoblasto para produzir nova matriz óssea [12]. No grupo CON a neoformação óssea foi restrita às bordas do defeito, apresentando maior extensão aos 45 dias (Fig. 4c) e sem expansão aos 120 dias (Fig. 4d). Em contrapartida, nos grupos em que houve implantação dos biomateriais, FCB (grânulos de fosfato de cálcio bifásico) e FCB/BV (grânulos de fosfato de cálcio bifásico/vidro bioativo fosfatado), notou-se aos 15 dias evidente neoformação óssea nas regiões de bordas e por condução entre as partículas do biomaterial, em direção radial, com maior expansão em FCB que preencheu aproximadamente 30% do defeito (Figs. 4e e 4g) e mais limitada em FCB/BV (~15%, Figs. 4f e 4h). Após 45 dias esta matriz osteoide tornou-se mais evidente, encontrando-se em alguns animais desconectada das bordas e ocupando aproximadamente 60% do defeito em FCB (Fig. 5a) e 40% em FCB/BV (Fig. 5b). Já aos 120 dias houve regeneração em extensão de aproximadamente 80-90% do defeito em FCB (Fig. 5c) e 60% em FCB/BV (Fig. 5d). No presente trabalho, a maior quantidade da fase pirofosfato de cálcio no grupo FCB resultou em maior capacidade regenerativa de defeitos ósseos críticos, como observado no resultado da Fig. 5c. Esta extensão da neoformação óssea observada nos grupos em que houve implantação dos biomateriais (FCB e FCB/BV) está associada à propriedade de osteocondução, decorrente da presença de um suporte estrutural (partículas do biomaterial). As áreas de mineralização estavam em regiões próximas à dura-máter, fonte primária de células osteogênicas e de fatores osteoindutivos [27]. O biomaterial composto apenas por fosfato de cálcio bifásico (FCB) parece ter estimulado uma melhor atuação dos osteoblastos para síntese de nova matriz osteoide, o que está em consonância com outros autores que utilizaram estes biomateriais isolados [28-30] ou em conjunto [31, 32] e obtiveram ótimos resultados para regeneração de defeitos críticos.

No grupo FCB aos 15 dias, a região de extensão do defeito foi preenchida pelos grânulos do biomaterial

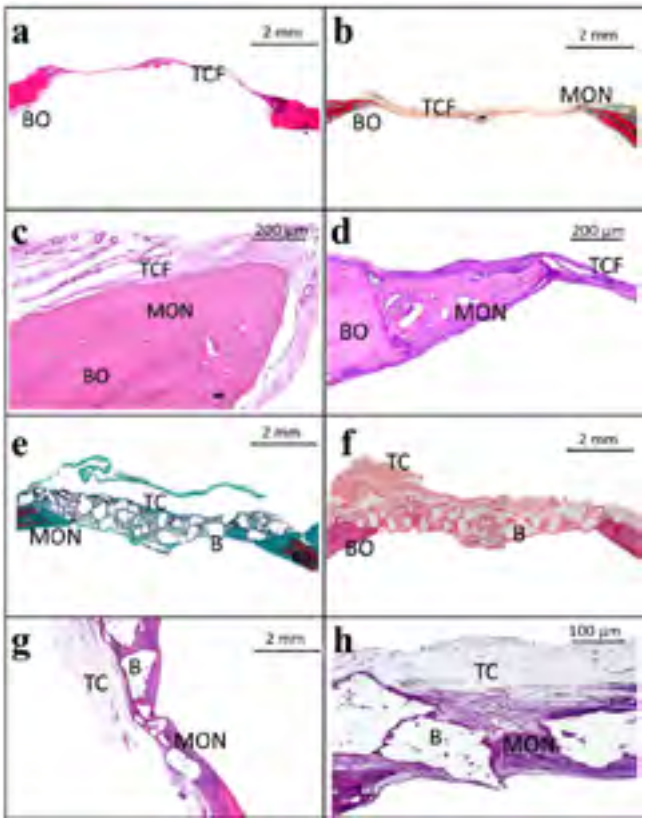

Figura 4: Fotomicrografias da região do defeito: a) CON em HE; b) CON em TMG; c) CON em HE; d) CON em HE; e) FCB em TMG; f) FCB/BV em PIFG; g) FCB em HE; h) FCB/BV em HE. Grupo CON: preenchimento do defeito por delgado tecido conjuntivo fibroso (TCF) aos 15 dias (a), que se tornou mais denso aos 120 dias (b); a neoformação óssea permaneceu restrita às bordas do defeito dos 15 dias (c) aos 120 dias (d). Grupos em que houve a implantação dos biomateriais: aos 15 dias notou-se evidente deposição de matriz osteoide (MON) nas regiões de bordas ósseas (BO) e por condução entre as partículas do biomaterial (e-h), com maior expansão em FCB (g); o preenchimento da região de extensão se deu pela organização tridimensional das partículas dos biomateriais (B) e por deposição de tecido conjuntivo (TC) bem vascularizado, principalmente próximo à veia central.

[Figure 4: Photomicrographs of the defect region: a) CON in HE; b) CON in TMG; c) CON in HE; d) CON in HE; e) FCB in TMG; f) FCB/BV in PIFG; g) FCB in HE; h) FCB/BV in HE. CON group: defect was filled by thin fibrous connective tissue (TCF) at 15 days (a), which became denser after 120 days (b); bone neoformation remained restricted to the edges of the defect from 15 days (c) to 120 days (d). Groups in which the biomaterials were implanted: at 15 days, osteoid matrix (MON) deposition was evident in the bone edge regions (BO) and by conduction between the biomaterial particles (e-h), with greater expansion in FCB (g); the extension region was filled by the three-dimensional organization of the biomaterial particles (B) and by the deposition of well-vascularized connective tissue (CT), especially near the central vein.]

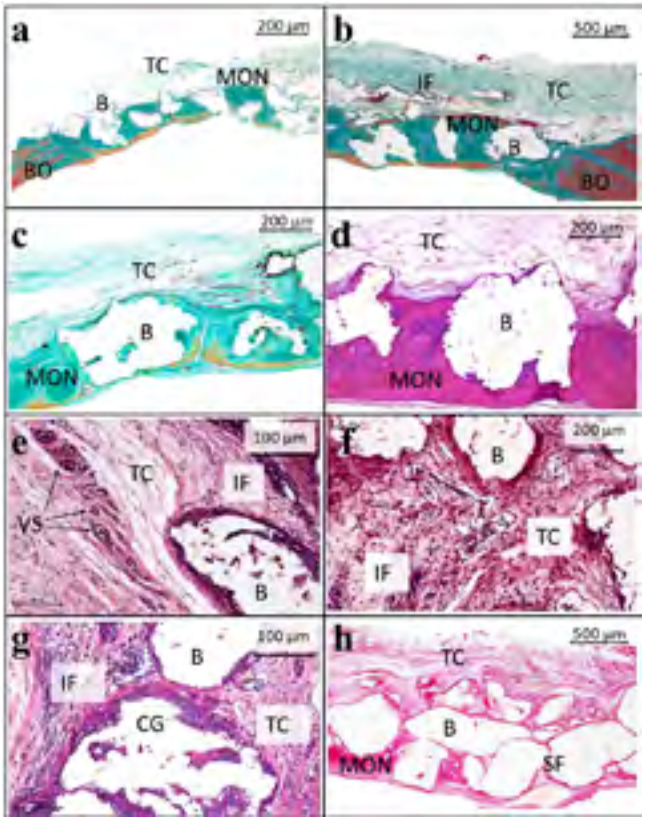

Figura 5: Fotomicrografias do reparo nos grupos em que houve implantação dos biomateriais (B): a) FCB em TMG; b) FCB/BV em TMG; c) FCB em TMG; d) FCB/BV em HE; e) FCB em HE; f) FCB/BV em HE; g) FCB em HE; h) FCB/BV em PIFG. A neoformação de matriz osteoide (MON) a partir das bordas ósseas (BO) tornou-se mais evidente aos 45 dias (a,b), regenerando de 60-90% do defeito aos 120 dias (c,d), juntamente com intensa degradação das partículas. Aos 15 dias, de permeio às partículas, formou-se um tecido conjuntivo frouxo (TC) edemaciado, bem vascularizado e com presença de discreto a moderado infiltrado inflamatório mononuclear e discreta reação granulomatosa (IF) (e,f), com abundante presença de células gigantes multinucleadas (CG) (g). Aos 45 dias, este tecido conjuntivo tornou-se fibroso (TCF) em algumas regiões, com projeção de septos fibrosos (SF) circuncidando as partículas (h).

[Figure 5: Photomicrographs of the repair in the groups in which the biomaterials were implanted (B): a) FCB in TMG; b) FCB/BV in TMG; c) FCB in TMG; d) FCB/BV in HE; e) FCB in HE; f) FCB/BV in HE; g) FCB in HE; h) FCB/BV in PIFG. The osteoid matrix neoformation (MON) from bone edges (BO) became more evident at 45 days (a,b), regenerating 60-90% of the defect after 120 days (c,d), together with intense particle degradation. At 15 days, permeating the particles, a loose, well-vascularized loose connective tissue (CT) was formed, with the presence of mild to moderate mononuclear inflammatory infiltrate and slight granulomatous reaction (IF) (e,f), with an abundant presence of multinucleated giant cells (CG) (g). After 45 days, this connective tissue became fibrous (TCF) in some regions, with a projection of fibrous septa (SF) circumcising the particles (h).]

(perdidos durante o processamento histológico, restando apenas espaços vazios com alguns resíduos), que possuíam formatos diversos e se organizaram de duas a quatro camadas (Fig. 4e). Em FCB/BV os espaços deixados foram mais homogêneos e demonstraram que as partículas se organizaram de duas a três camadas, com espessura similar às bordas ósseas (Fig. 4f). No entanto, a permanência das partículas na região de implante durante todo o estudo e a perda do material durante o processamento histológico

(corte) são indicadores da dureza dos grânulos, que pode ter sido decorrente do processo de sinterização a 1200 °C em que os biomateriais foram submetidos [33]. Entretanto, foi possível observar que a adição do vidro bioativo fosfatado influenciou na estabilidade química dos grânulos do grupo FCB/BV. A literatura ainda não possui um consenso sobre o mecanismo de dissolução dos vidros bioativos [34]. Dos 45 aos 120 dias, observou-se que as partículas sofreram intensa degradação, apresentando maior fragmentação e tamanhos muito reduzidos em FCB/BV (Fig. 5b) em comparação ao grupo FCB (Fig. 5a). Apesar da maior biodegradabilidade *in vivo* do grupo FCB/BV, um maior processo regenerativo não foi observado. Aos 45 dias, o tecido conjuntivo apresentou muita fibrose intersticial, com formação de septos fibrosos circuncidando as partículas, principalmente em FCB (Fig. 5h). Ainda foi possível observar a permanência de discreta inflamação mononuclear linfocitária e moderada reação inflamatória granulomatosa em FCB (Fig. 6a), entretanto em FCB/BV notou-se maior declínio da reação inflamatória com presença de poucas células mononucleares (Fig. 6b). Já aos 120 dias, o tecido conjuntivo ainda apresentava-se edemaciado (Figs. 6c e 6d) e tornou-se fibroso em FCB (Figs. 6c e 6e). Em ambos os grupos a reação inflamatória foi escassa, porém ainda com discreta reação crônica granulomatosa ao redor das partículas (Figs. 6e e 6f). No grupo CON, aos 15 dias foi possível visualizar discreto infiltrado inflamatório mononuclear distribuído de forma difusa, que se apresentou inconspícuo aos 45 dias e ausente aso 120 dias (Figs. 4a a 4c).

A faixa de tamanho dos grânulos (0,5 a 0,7 mm) evitou que as partículas muito pequenas ocupassem os espaços entre as maiores, o que poderia reduzir o interstício e o potencial regenerativo devido à obstrução do espaço necessário para a migração celular e formação vascular [35]. A organização dos biomateriais com o tecido de preenchimento forneceu suporte estrutural para a proliferação de células e para o mecanismo de reparo, desenvolvendo espessura similar ao osso pré-existente em contraste ao grupo controle. Esses dados estão em consonância com diversos estudos que utilizaram biomateriais para regenerar defeito ósseo crítico [18-20]. A evolução do tecido conjuntivo frouxo para fibroso em FCB sugeriu que o biomaterial pode ser adequado para preenchimento de sulcos, partes moles, dentre outros sítios. O processo inflamatório observado em todos os grupos foi devido à liberação de citocinas e mediadores químicos após a lesão tecidual e vascular, que desencadeou uma cascata de reação inflamatória [18, 36, 37]. Nos grupos em que houve a implantação de biomateriais notou-se inflamação crônica granulomatosa do tipo corpo estranho, com a presença de células gigantes multinucleadas em torno das partículas em uma tentativa de degradar o biomaterial [36, 38]. A intensidade dessa resposta inflamatória foi relacionada com as características morfológicas e físico-químicas dos biomateriais, sendo a fase crônica essencial para determinar a biocompatibilidade e o tipo de reparo tecidual [35, 36]. Desta forma, ambos os biomateriais utilizados em nosso estudo foram biocompatíveis. Nossos achados contribuem

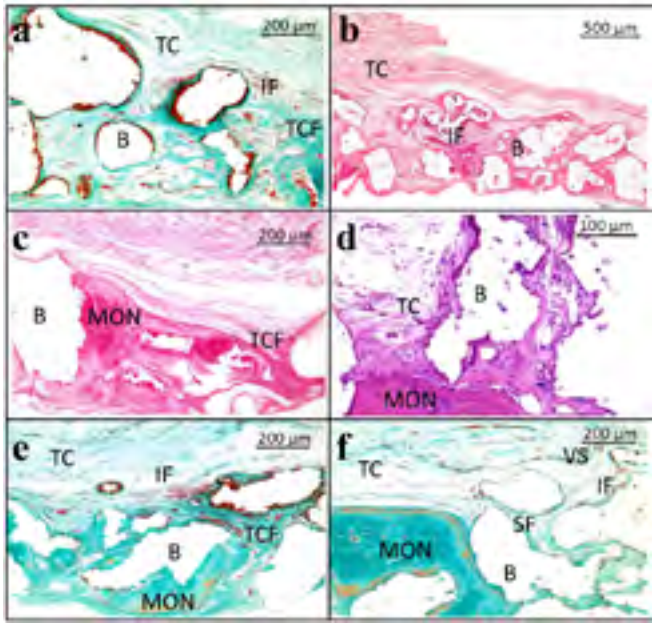

Figura 6: Fotomicrografias do reparo nos grupos em que houve implantação dos biomateriais (B): a) FCB em TMG; b) FCB/BV em PIFG; c) FCB em HE; d) FCB/BV em HE; e) FCB em TMG; f) FCB/BV em TMG. Imagens mostram a organização do tecido conjuntivo (TC), onde é possível observar discreta reação inflamatória (IF) aos 45 dias (a,b). Aos 120 dias esta inflamação apresentava-se diminuta ou quase inexistente, porém o tecido conjuntivo ainda se encontrava edemaciado (c-f) e tornou-se fibroso (TCF) em FCB (c,e). No decorrer do tempo, as partículas dos biomateriais (B) que se encontravam envolvidas por septos de tecido fibroso (SF) foram substituídas por matriz osteoide neoformada (MON).

[Figure 6: Photomicrographs of the repair in the groups in which the biomaterials were implanted (B): a) FCB in TMG; b) FCB/BV in PIFG; c) FCB in HE; d) FCB/BV in HE; e) FCB in TMG; f) FCB/BV in TMG. The images show the connective tissue organization (TC), where it is possible to observe a slight inflammatory reaction (IF) after 45 days (a,b). After 120 days, this inflammation was small or almost nonexistent, but the connective tissue was still swollen (c-f), and became fibrous (TCF) in FCB (c,e). Over time, the particles of biomaterials (B) that were surrounded by fibrous tissue septa (SF) were replaced by a neoformed osteoid matrix (MON).]

para o entendimento do processo de reparo ósseo após implantação dos biomateriais à base de β-fosfato tricálcico/pirofosfato de cálcio e vidro bioativo fosfatado, uma vez que possibilitou identificar a biocompatibilidade, capacidade dos biomateriais para promover a angiogênese, direcionar a adesão, migração e proliferação celular, além de avaliar sua biodegradação e bioabsorção, características essenciais para regeneração óssea.

CONCLUSÕES

Os materiais avaliados neste estudo foram biocompatíveis, atuaram como arcabouços tridimensionais, apresentaram potencial osteocondutor e favoreceram a regeneração óssea, principalmente os grânulos de fosfato

de cálcio bifásico. A adição do vidro bioativo fosfatado aumentou a biodegradabilidade dos grânulos de fosfato de cálcio bifásico/vidro bioativo, todavia não favoreceu uma maior regeneração óssea. Ambas as composições testadas são propícias para utilização como substitutos ósseos.

AGRADECIMENTOS

Ao Instituto Militar de Engenharia por ceder os biomateriais utilizados; à Universidade Estadual de Feira de Santana por disponibilizar o biotério para realização dos experimentos; ao Instituto de Patologia Geral e Cutânea por viabilizar o processamento das amostras e à Fundação de Amparo à Pesquisa do Estado da Bahia pela bolsa de estudos e financiamento deste trabalho.

REFERÊNCIAS

[1] S. Allegrini Júnior, A.C. Silva, M. Tsujita, M.B. Salles, S.A. Gehrke, F.J.C. Braga, Microsc. Res. Tech. **81** (2018) 1.
[2] S. Dasgupta, K. Maji, S.K. Nandi, Mater. Sci. Eng. C **94** (2019) 713.
[3] D.F. Williams, The Williams dictionary of biomaterials, Liverpool Un. Press, Liverpool (1999).
[4] D.F. Williams, Biomaterials **30** (2009) 5897.
[5] R.Z. LeGeros, Clin. Orthop. Relat. Res. **395** (2002) 81.
[6] W. Zhang, D. Yao, Q. Zhang, J.G. Zhou, P.I. Lelkes, Biofabrication **2** (2010) 1.
[7] J.S. Sun, W.H.S. Chang, L.T. Chen, Y.C. Huang, L.W. Juang, F.H. Lin, Biomaterials **25** (2004) 607.
[8] J.H. Lee, B.S. Chang, H.S. Ryu, C.K. Lee, Drug Chem. Toxicol. **32**, 3 (2009) 277.
[9] D.W. Kim, J.S. An, I.S. Cho, Ceram. Int. **44** (2018) 9689.
[10] I.K. Karoussis, K. Kyriakidou, J. Papaparaskevas, I.A. Vrotsos, M. Simopoulou, G.A. Kotsakis, J. Biomed. Mater. Res. Part. B Appl. Biomater. **106**, 7 (2018) 2645.
[11] M. Gutierres, M. Ascensão Lopes, N. Sooraj Hussain, A. Trigo Cabral, L. Almeida, J. Domingos Santos, Arq. Med. **19** (2005) 153.
[12] J.R. Jones, Acta Biomater. **23** (2015) S53.
[13] D. Navarro da Rocha, R.L.S.B. Marçal, R.M. Barbosa, J.R.M. Ferreira, M.H. Prado da Silva, Biomater. Med. Appl. **1**, 2 (2018) 2.
[14] M. Elbadawi, Z.J. Wally, I.M. Reaney, J. Am. Ceram. Soc. **101** (2018) 3541.
[15] C. Carlo, B. Borges, A. Pacheco, D.F. Rezende, C. Maria, C. Lopes, C. César, S. Pontes, K. Cristine, S. Duarte, Rev. Ceres. **54**, 316 (2007) 492.
[16] M.H. Prado da Silva, C.M. Ramirez, J.M. Granjeiro, A.M. Rossi, Key Eng. Mater. **361** (2008) 229.
[17] D. Navarro da Rocha, L.R.O. Cruz, J.L. Prado Neto, N.M.E. Ayad, L.A. Gobbo, M.H. Prado da Silva, Key Eng. Mater. **587** (2014) 128.
[18] F.B. Miguel, A.A. Barbosa Júnior, F.L. Paula, I.C. Barreto, G. Goissis, F.P. Rosa, J. Mater. Sci. Mater. Med. **24** (2013) 2567.
[19] A.K.M.V. Cardoso, A.A. Barbosa Jr, F.B. Miguel, E. Marcantonio, M. Farina, G.D.A. Soares, F.P. Rosa, Cells Tissues Organs **184** (2007) 128.
[20] R.S. Almeida, I.I.A. Ribeiro, M.H. Prado da Silva, D. Navarro da Rocha, F.B. Miguel, F.P. Rosa, Rev. Ciên. Méd. Biol. **13**, 3 (2014) 331.
[21] S.V. Dorozhkin, Biomaterials **31** (2010) 1465.
[22] R. Mulongo-Masamba, T. El Kassri, M. Khachani, S. Arsalane, M. Halim, A. El Hamidi, J. Therm. Anal Calorim. **124**, 1 (2016) 171.
[23] A.D. Anastasiou, S. Strafford, O. Posada-Estefan, C.L. Thomson, S.A. Hussain, T.J. Edwards, Mater. Sci. Eng. C **75** (2017) 885.
[24] J.H. Lee, B.S. Chang, U.O. Jeung, K.W. Park, M.S. Kim, C.K. Lee, Clin. Orthop. Surg. **3**, 3 (2011) 238.
[25] T. Ariizumi, H. Kawashima, H. Hatano, T. Yamagishi, N. Oike, T. Sasaki, H. Umezu, Y. Xu, N. Endo, A. Ogose, J. Biomater. Nanobiotechnol. **10**, 3 (2019) 159.
[26] D. Navarro da Rocha, M.H. Prado da Silva, J.B. Campos, R.L.S.B. Marçal, D.Q. Mijares, P.G. Coelho, L.R. Cruz, J. Mater. Res. Technol. **7**, 4 (2018) 479.
[27] G.M. Cooper, M.P. Mooney, A.K. Gosain, G. Phil, J.E. Losee, J. Huard, Plast. Reconstr. Surg. **125**, 6 (2011) 1685.
[28] A. Neamat, A. Gawish, A.M. Gamal-Eldeen, Arch. Oral Biol. **54** (2009) 1083.
[29] D. Apelt, F. Theiss, A.O. El-Warrak, K. Zlinszky, R. Bettschart-Wolfisberger, M. Bohner, S. Matter, J.A. Auer, B. von Rechenberg, Biomaterials **25** (2004) 1439.
[30] S. Jensen, N. Broggini, E. Hjorting-Hansen, R. Schenk, D. Buser, Clin. Oral Implants Res. **17**, 3 (2006) 237.
[31] M.M. Ferreira, A.F. Brito, C.F. Marques, L.F. Freitas, E. Carrilho, A.M. Abrantes, Ceram. Int. **44** (2018) 5025.
[32] D.G. Wang, C.Z. Chen, X.X. Yang, X.C. Ming, W.L. Zhang, Ceram. Int. **44** (2018) 14528.
[33] S.D. de Campos, É.A. de Campos, C.B. da Silveira, R.A. Bini, Cerâmica **51**, 319 (2005) 274.
[34] T. Zambanini, R. Borges, P.C. Faria, G.P. Delpino, I.S. Pereira, M.M. Marques, J. Marchi, Int. J. Appl. Ceram. Technol. **16**, 5 (2019) 2028.
[35] J.M. Anderson, Annu. Rev. Mater. Res. **31** (2001) 81.
[36] J.M. Anderson, A. Rodriguez, D.T Chang, Semin. Immunol. **20**, 2 (2008) 86.
[37] K.J.L. Burg, S. Porter, J.F. Kellam, Biomaterials **21** (2000) 2347.
[38] T. Albrektsson, C. Johansson, Eur. Spine J. **10** (2001) 96.

(Rec. 26/12/2018, Rev. 23/09/2019, 01/11/2019, Ac. 05/11/2019)

BY-NC

Electron paramagnetic resonance of manganese-doped strontium titanate

(Ressonância paramagnética eletrônica de titanato de estrôncio dopado com manganês)

R. S. de Biasi[1]*, M. L. N. Grillo[2]

[1]Instituto Militar de Engenharia, Seção de Engenharia de Materiais, 22290-270, Rio de Janeiro, RJ, Brazil

[2]Universidade do Estado do Rio de Janeiro, Instituto de Física, 20550-013, Rio de Janeiro, RJ, Brazil

Abstract

Electron paramagnetic resonance (EPR) spectra of manganese-doped strontium titanate were investigated for several Mn concentrations. The spectra of Mn^{2+} and Mn^{4+} ions were observed and attributed, respectively, to Mn ions occupying Sr^{2+} and Ti^{4+} sites. The relative intensity of the spectra suggested that the manganese ions occupy preferentially Ti^{4+} sites. The results showed that the EPR peak-to-peak linewidth of the Mn^{4+} spectrum increases with manganese concentration according to the theoretical equation $\Delta H_{pp}=0.45+210.f.(1-f)^{80}$ (mT). This suggested that the exchange interaction between tetravalent manganese ions in strontium titanate has an approximate range of 0.96 nm, comparable to that of Gd^{3+} in the same compound.

Keywords: ceramics, electron paramagnetic resonance, strontium titanate, manganese.

Resumo

Espectros de ressonância paramagnética eletrônica de titanato de estrôncio dopado com manganês foram investigados para várias concentrações de Mn. Os espectros dos íons de Mn^{2+} e Mn^{4+} foram observados e atribuídos, respectivamente, a íons de Mn ocupando sítios do Sr^{2+} e do Ti^{4+}. A intensidade relativa dos dois espectros sugeriu que os íons de manganês ocupam preferencialmente os sítios do Ti^{4+}. Os resultados mostraram que a largura de linha pico a pico do espectro do Mn^{4+} aumenta com a concentração de manganês de acordo com a equação teórica $\Delta H_{pp}=0,45+210.f.(1-f)^{80}$ (mT). Isto sugeriu que a interação de câmbio entre íons de manganês tetravalente tem um alcance aproximado de 0,96 nm, comparável ao do Gd^{3+} no mesmo composto.

***Palavras-chave**: cerâmicas, ressonância paramagnética eletrônica, titanato de estrôncio, manganês.*

INTRODUCTION

Strontium titanate ($SrTiO_3$) is a ceramic material with several industrial applications [1-5] whose properties can be improved by doping [6-10]. In this work, we investigate the influence of the degree of Mn doping on the electron paramagnetic resonance (EPR) linewidth of Mn^{4+} in polycrystalline $SrTiO_3$. In this way, one can use the EPR results to measure, rapidly and nondestructively, small concentrations of Mn in commercial $SrTiO_3$, as it has been done for other ions and other ceramic materials [11-16]. In addition, the extent of the interaction of tetravalent manganese ions in manganese-doped strontium titanate may be helpful for the investigation of the magnetic behavior of manganese-doped barium titanate, which could be used as a multiferroic material, since, in these materials, magnetic and electric properties coexist and manganese is a dopant with a strong influence on both electric and magnetic properties [9, 10, 17]. A previous investigation by EPR of manganese-doped strontium titanate [17] has shown that Mn ions may occupy either Sr^{2+} sites or Ti^{4+} sites. The Mn^{2+} spectrum is described by a spin Hamiltonian with parameters g=2.0032 and $A=82.8x10^{-4}$ cm^{-1}, while the Mn^{4+} spectrum is described by a spin Hamiltonian with parameters g=1.9920 and $A=71.2x10^{-4}$ cm^{-1}.

EPR of paramagnetic impurities in solids: according to previous works [18, 19], the peak-to-peak first derivative linewidth is given by:

$$\Delta H_{pp}=\Delta H_o+\Delta H_d=\Delta H_o+c.f_e \quad (A)$$

where ΔH_o is the intrinsic linewidth, ΔH_d is the dipolar broadening, c is a constant, and f_e is the concentration of substitutional ions of the paramagnetic impurity not coupled by the exchange interaction, which can be expressed as:

$$f_e=f.(1-f)^{z(r_c)} \quad (B)$$

where f is the impurity concentration, $z(r_c)$ the number of cation sites included in a sphere of radius r_c, and r_c the effective range of the exchange interaction.

EXPERIMENTAL PROCEDURE

Sample preparation: the sample preparation method

**rsbiasi@ime.eb.br*

https://orcid.org/0000-0001-8897-5969

was the same as in [20]. The starting materials were reagent grade $SrTiO_3$ (Aldrich, <5 μm, 99%) and MnO_2 (Carlo Erba, 99%). The powders of $SrTiO_3$ and 0.1 to 3.0 mol% of MnO_2 were ground together, and then the mixtures were fired for 24 h at 1200 °C in air.

Measurements: X-ray diffraction measurements were performed in a Panalytical X'Pert Pro diffractometer with CuKα radiation (0.154 nm). All magnetic resonance measurements were performed at room temperature and 9.50 GHz using an electron paramagnetic resonance (EPR) spectrometer (Varian, E-12) with 100 kHz field modulation. The microwave power was 200 mW, and the modulation amplitude was 0.1 mT. The magnetic field was calibrated with an NMR gaussmeter.

EXPERIMENTAL RESULTS

X-ray diffraction: all diffractograms (a typical one is shown in Fig. 1) were indistinguishable from the diffractogram of pure $SrTiO_3$ (JCPDS 86-0179). This was expected, since the Mn doping, up to only 3.00 mol%, was not enough to change either the lattice constant or the amplitude of the diffraction peaks as long as the Mn ions remained in solid solution, as attested by the fact that no other lines than those attributed to $SrTiO_3$ were observed. Moreover, the lines were very narrow, as expected from micron-sized particles.

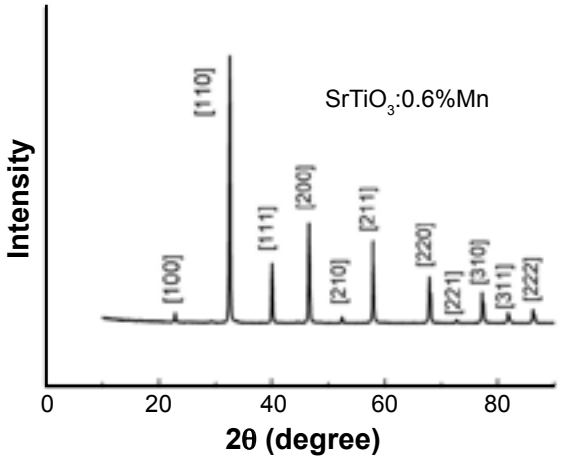

Figure 1: X-ray diffraction pattern of a $SrTiO_3$ sample doped with 0.6 mol% Mn. The indices were taken from the file JCPDS 86-0179.
[Figura 1: Difratograma de raios X de uma amostra de $SrTiO_3$ dopada com 0,6 mol% de Mn. Os índices foram obtidos do arquivo JCPDS 86-0179.]

EPR spectra: the spectrum of a typical sample is displayed in Fig. 2. Two sextets were seen, one with g=2.00 and another with g=1.99. Due to the similarity of the measured g-values and hyperfine constants to those of previously reported spectra [14], the first sextet was attributed to Mn^{2+} ions occupying Sr^{2+} sites and the second to Mn^{4+} ions occupying Ti^{4+} sites. The intensity of the second sextet was much larger than that of the first for all concentrations and increased with Mn concentration, while the intensity of the first sextet remained the same and was thus discarded from our calculations. On the other hand, the data showed that the intensity of a broad line that was seen in all spectra and was attributed to Mn-rich clusters [21, 22] increased at the same rate as the spectrum of Mn^{4+} ions. Even if a significant fraction of the doping Mn is incorporated to Mn-rich clusters, this does not invalidate our analysis, as long as the intensity of this line increases at the same rate as the intensity of the Mn^{4+} spectrum with Mn concentration, since this lack of correspondence between the nominal doping and the effective concentration of Mn in Mn^{4+} sites leads only to a small decrease in the value of c in Eq. A, but does not affect the concentration dependence of the linewidth of the Mn^{4+} ions. The linewidths of the hyperfine lines of the sextet with g=1.99 appear in Table I for several manganese concentrations. We concentrated our attention on the line pointed out by an arrow in Fig. 3 because it is the one with less superposition with the lines of the other sextet.

DISCUSSION

In the discussion that follows, the contribution of Mn^{2+} in Sr^{2+} sites is ignored, since, according to intensity data, the fraction of ions in these sites was negligibly small. The theoretical functions for ΔH_{pp}, given by Eq. A, are shown in Fig. 4 for ΔH_0=0.45 mT and 8 different values of r_c, computed from the lattice constant of $SrTiO_3$ [17], a_o=0.3901 nm. The values of $z(r_c)$, given in Table II for n= 1 to 8, are those consistent with the crystal lattice of $SrTiO_3$. The experimental results, also displayed in Fig. 2, followed closely the theoretical function for n=7, given by Eq. C, which, as can be seen in Table II, corresponded to r_c=0.96 nm.

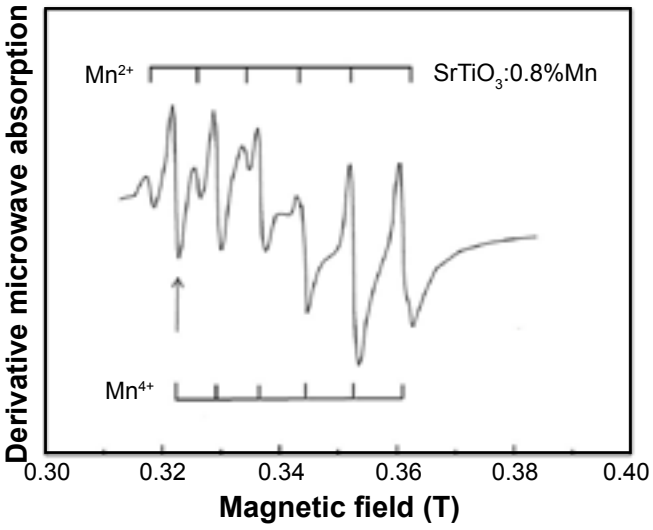

Figure 2: EPR spectrum of an $SrTiO_3$ sample doped with 0.8 mol% Mn.
[Figura 2: Espectro de RSE de uma amostra de $SrTiO_3$ dopada com 0,8 mol% Mn.]

Table I - Experimental results for the Mn^{4+} peak-to-peak linewidth in $SrTiO_3$ (T=300 K, ν=9.50 GHz).
[Tabela I - Resultados experimentais para a largura de linha pico a pico de Mn^{4+} em $SrTiO_3$ (T=300 K, ν=9,50 GHz).]

f (mol%)	0.10	0.20	0.40	0.60	0.80	1.00	1.50	2.00	2.50	3.00
ΔH_{pp} (mT)	0.63	0.84	1.10	1.20	1.30	1.40	1.35	1.24	1.24	1.06

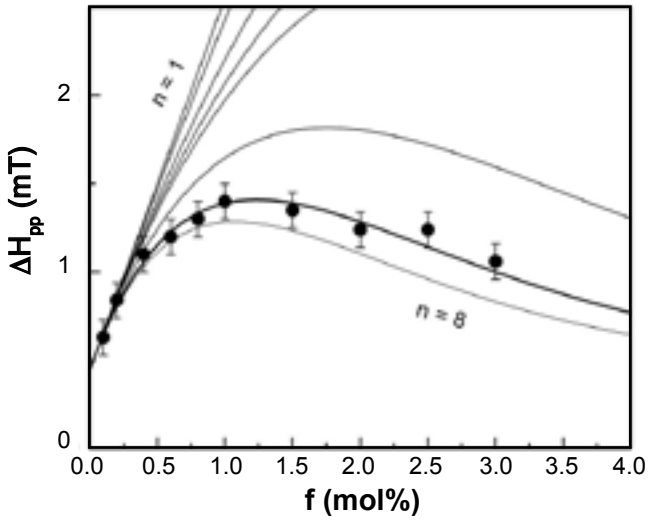

Figure 3: Concentration dependence of the peak-to-peak linewidth, ΔH_{pp}, in Mn-doped $SrTiO_3$. The circles are experimental points; the curves represent the results of theoretical calculations for 8 different ranges of the exchange interaction.
[Figura 3: Variação da largura de linha pico a pico, ΔH_{pp}, com a concentração em amostras de $SrTiO_3$ dopadas com Mn. Os círculos são pontos experimentais; as curvas mostram o resultado de cálculos teóricos para 8 alcances diferentes da interação de câmbio.]

$$\Delta H_{pp}=0.45+210.f.(1-f)^{80} \quad (C)$$

The peak-to-peak linewidth of Mn^{2+} in $SrTiO_3$ is compared in Fig. 4 with that of Gd^{3+} in the same host lattice, which can be approximated by the equation $\Delta H_{pp}=0.60+600.f.(1-f)^{80}$ (mT) [18]. Although r_c is the same for both ions, the value of c in Eq. A is much larger for Gd^{3+}, i.e., the linewidth rises much faster with the Gd^{3+} concentration than with the Mn^{4+} concentration. A probable explanation is that, according to Table III, the difference in ionic radii is much higher between Sr^{2+} and Gd^{3+} than between Ti^{4+} and Mn^{4+}, since, as discussed in [24], the coefficient c in Eq. A increases with the difference Δr between the ions of the dopant and the replaced element. Moreover, as previously discussed, the presence of a broad line showed that not all Mn ions were incorporated as independent Mn^{4+} ions in Ti^{4+} sites and this led to a decrease in the value of c, although this decrease seems to be not sufficient to explain the large difference between the c coefficients in Gd^{3+} and Mn^{4+} doped $SrTiO_3$.

Table III - Ionic radii [23] and their differences.
[Tabela III - Raios iônicos [23] e suas diferenças.]

Ion	Coordination	Radius (nm)	Difference (nm)
Sr^{2+}	12	0.144	0.044
Gd^{3+}	12	0.100	
Ti^{4+}	6	0.061	0.008
Mn^{4+}	6	0.053	

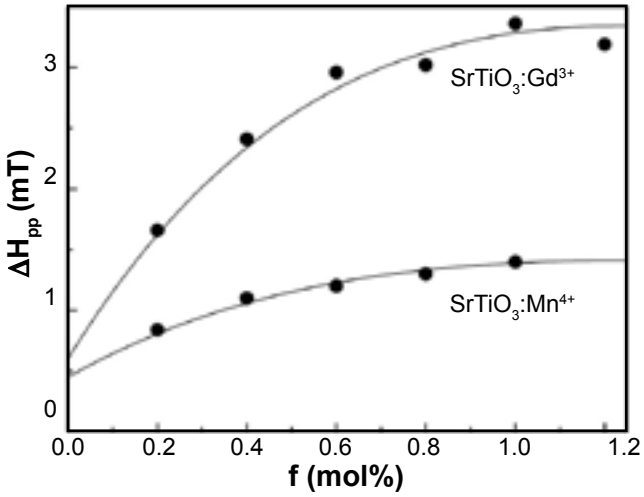

Figure 4: Concentration dependence of the peak-to-peak linewidth, ΔH_{pp}, in Gd-doped and Mn-doped $SrTiO_3$. The circles are experimental points; the curves are theoretical: $\Delta H_{pp}=0.60+600.f.(1-f)^{80}$ for Gd-doped $SrTiO_3$ [20], and $\Delta H_{pp}=0.45+210.f.(1-f)^{80}$ for Mn-doped $SrTiO_3$ (this study).
[Figura 4: Variação da largura de linha pico a pico, ΔH_{pp}, com a concentração em $SrTiO_3$ dopado com Gd e Mn. Os círculos são pontos experimentais; as curvas são teóricas: $\Delta H_{pp}=0,60+600.f.(1-f)^{80}$ para $SrTiO_3$ dopado com Gd [18] e $\Delta H_{pp}=0,45+210.f.(1-f)^{80}$ para $SrTiO_3$ dopado com Mn (este estudo).]

Table II - Values of r_c and $z(r_c)$ for $SrTiO_3$.
[Tabela II - Valores de r_c e $z(r_c)$ para $SrTiO_3$.]

n	1	2	3	4	5	6	7	8
r_c (nm)	0.00	0.39	0.55	0.68	0.78	0.87	0.96	1.11
$z(r_c)$	0	6	18	26	32	56	80	92

CONCLUSIONS

The EPR spectra of Mn^{4+} and Mn^{2+} were observed in $SrTiO_3$ powders doped with different concentrations of manganese. The measurements showed that Mn ions occupy preferentially Ti^{4+} sites. It was also found that the EPR peak-to-peak linewidth of Mn^{4+} increased predictably with Mn concentration and that the range of the exchange interaction between Mn^{4+} ions was about 0.96 nm. These results may contribute to the study of the magnetic properties of manganese-doped strontium titanate.

ACKNOWLEDGMENTS

The authors thank CNPq and CAPES for financial support.

REFERENCES

[1] W.L. Suchanek, M. Yoshimura, J. Am. Ceram. Soc. **81** (1998) 2864.
[2] G.H. Haertling, J. Am. Ceram. Soc. **82** (1999) 797.
[3] V.V. Srdic, R.R. Djenadic, J. Optoelectron. Adv. Mater. **7** (2005) 3005.
[4] F. Xiang, H. Wang, H. Yang, Z.Y. Shen, X. Yao, J. Electroceram. **24** (2010) 20.
[5] Y.T. Qian, K.D. Li, W.S. Wang, J.H. Wang, X.C. Cheng, Y.L. Zhou, J.M. Du, H.J. Chen, B. Zhang, D.J. Kang, J. Nanosci. Nanotechnol. **9** (2019) 5707.
[6] A.G. Sale, S. Kazan, J.I. Gatiiatova, V.F. Valeev, R.I. Khaibullin, F.A. Mikailzade, Mater. Res. Bull. **48** (2013) 2861.
[7] D.M Long, B.Y. Cai, J.N. Baker, P.C. Bowes, T.J.M. Bayer, J.J. Wang, R. Wang, L.Q. Chen, C.A. Randall, D.L. Irving, E.C. Dickey, J. Am. Ceram. Soc. **102** (2019) 3567.
[8] E.R. Silva, M. Curi, J.G. Furtado, H.C. Ferraz, A.R. Secchi, Ceram. Int. **45** (2019) 9761.
[9] P. Singh, P. Singh, O. Parkash, D. Kumar, J. Mater. Sci. **43** (2008) 989.
[10] C.L. Diao, H. Li, Y. Yang, H. Hao, Z.H. Yao, H.X. Liu, Ceram. Int. **45** (2019) 11784.
[11] R.S. de Biasi, A.A.R. Fernandes, J. Am. Ceram. Soc. **64** (1984) C173.
[12] R.S. de Biasi, A.A.R. Fernandes, M.L.N. Grillo, J. Am. Ceram. Soc. **76** (1993) 223.
[13] R.S. de Biasi, A.A.R. Fernandes, M.L.N. Grillo, J. Am. Ceram. Soc. **79** (1996) 2179.
[14] R.S. de Biasi, M.L.N. Grillo, J. Am. Ceram. Soc. **86** (2003) 195.
[15] R.S. de Biasi, M.L.N. Grillo, J. Am. Ceram. Soc. **91** (2008) 3469.
[16] R.S. de Biasi, M.L.N. Grillo, Ceram. Int. **39** (2013) 2171.
[17] V.V. Laguta, I.V. Kondakova, P. Bykov, M.D. Glinchuk, A. Tkach, P.M. Vilarinho, L. Jastrabik, Phys. Rev. B **76** (2007) 54104.
[18] C. Kittel, E. Abrahams, Phys. Rev. **90** (1953) 238.
[19] R.S. de Biasi, A.A.R. Fernandes, J. Phys. C Solid State Phys. **16** (1983) 5481.
[20] R.S. de Biasi, M.L.N. Grillo, Mater. Chem. Phys. **130** (2011) 409.
[21] A. Zorko, M. Pregelj, H. Luetkens, A.-K. Axelsson, M. Valant, Phys. Rev. B **89** (2014) 94418.
[22] D. Daraselia, D. Japaridze, Z. Jibuti, A. Shengelaya, K.A. Müller, J. Appl. Phys. **121** (2017) 145104.
[23] R.D. Shannon, Acta Cryst. A **32** (1976) 751.
[24] R.S. Biasi, M.L.N. Grillo, Mater. Res. **18** (2015) 288.
(Rec. 04/04/2019, Rev. 04/06/2019, 01/07/2019, 12/11/2019, Ac. 15/11/2019)

CC BY-NC

Clarification of used lubricating oils by application of chemically-modified clays

(Clarificação de óleo lubrificante usado por aplicação de argilas quimicamente modificadas)

M. S. L. Rosa[1]*, T. Knoerzer[2], F. C. Figueiredo[1], J. R. dos Santos Júnior[1]
[1]Federal University of Piauí, Center of Natural Sciences, 64049-550, Teresina, PI, Brazil
[2]US Air Force Academy, Department of Chemistry, CO80840, USA

Abstract

Clay is a material that exhibits excellent adsorbent properties which can be applied for the clarification of used motor oils. We describe a comparative analysis between natural and chemically-modified clays as an environmentally sound method of clarification. Previously, a sample of clay was chemically treated with KOH and H_2SO_4 with a concentration of 2.0 M at 150 °C. Both the natural and chemically-treated samples were characterized using the techniques of XRD, FTIR, SSA, and thermal analysis to observe the structural change after the chemical treatment. These characterizations indicated that there was an increase in surface area and microporous space creation in the acid-treated sample as a result of the clay exfoliation. The acid-treated sample exhibited the potential of clarification of waste oil and high performance relative to the natural sample and the base-treated sample.
Keywords: clay, clarifying, waste lubricant oil.

Resumo

Argila é um material que exibe excelentes propriedades adsorventes que pode ser aplicada para a clarificação de óleos de motor usado. Descreve-se uma análise comparativa entre argilas natural e quimicamente modificadas como um método de clarificação ambientalmente correto. Previamente a argila foi tratada quimicamente com KOH e H_2SO_4 com concentração 2,0 M a 150 °C. Amostras natural e quimicamente tratadas foram caracterizadas usando as técnicas de DRX, FTIR, SSA e análise térmica para observar a mudança estrutural após o tratamento químico. Estas caracterizações indicaram que houve aumento na área superficial e criação de espaço microporoso na amostra tratada com ácido, como resultado da esfoliação da argila. A amostra tratada com ácido exibiu potencial de clarificação do óleo usado e alto desempenho em relação à amostra natural e amostra tratada com base.
***Palavras-chave**: argila, clarificante, óleo lubrificante usado.*

INTRODUCTION

Motor lubricant oil is an important product needed in the operation of the internal combustion engine but is known to suffer degradation by temperature and other chemical reactions. Most notably, oxidation and the formation of reaction by-products such as organic acids, ketones, and polynuclear aromatic hydrocarbons (PAHs) result in a deep black-colored product that is highly viscous and comprised of potentially carcinogenic compounds [1-3]. Ultimately, the 'burned oil' product that is generated poses a serious environmental concern and is thus worthy of remediation. One of the primary means of remediation is the incineration of the spent oil, but this method has the clear disadvantage of releasing high concentrations of dioxins in air and landfills, thus contaminating the soils and also limiting the potential for material recovery [4-7]. Indeed, recovery is the most desirable means of remediation, both environmentally and economically [7]. However, the most commonly used industrial treatment process consumes considerable time and energy due to the various reagents employed and the extensive steps needed to achieve clarification of the used or contaminated oil [8-11].

To reduce the amount of time, energy, and resources needed, several studies have simplified the process to obtain a lubricant that complies with the laws in force to only two steps: a) extraction with polar solvents with up to four carbon atoms such as methanol, ethanol, isopropanol, or butanol; and b) clarification using adsorbent materials such as peanut shell, nutshell, eggshell, natural clay, or acid clay [1-24]. Among the adsorbent materials, clays appear to be the most attractive option because these materials are easily found in nature, have a low cost, and are non-toxic. Furthermore, the clays may contain other weathered minerals such as quartz, kaolinite, and palygorskite, which have also been widely applied in the clarification processes of vegetable, animal, and mineral oils due to the presence of a negative charge moiety within the structure of silicate minerals [13-20]. This

**mirnasales01@hotmail.com*
https://orcid.org/0000-0003-3509-9824

negative charge can be counteracted by the adsorption of positively charged cations such as dyes [21]. In addition, clays have a large surface area, which contributes to their high adsorption capacity, and consequently, for the oil clarification [21-22].

In the chemical industry, natural clays are modified with acid to enhance the clarification process. In acid-activated clay, acid attacks the edges of the mineral coverslips, leading to exfoliation and generating pores on the surfaces of the coverslips, ensuring the increase of specific surface and pore volume, which in turn ensures greater adsorption. Besides, acid activation dissolves organic and inorganic impurities and replaces diatomic and triatomic cations by H^+ ions (Fig. 1a). Perhaps this can be attributed to the clay functioning as a Bronsted-Lowry acidic active site of which can adsorb organic impurities such as anionic dyes by electrostatic attraction (Fig. 1b) or even covalent bonding, such as cationic dyes (Fig. 1c) [19, 20]. The acid-modified approach appears to produce a distinct opportunity to apply this chemical approach in conjunction with a clay matrix in order to provide an ideal combined approach for successful oil remediation. Therefore, we report the use of modified clays for the clarification of lubricating oils by application of KOH and H_2SO_4 chemical modification. Our findings are further illustrated by the observed changes in the structure and specific surface area determinations of both untreated and treated clays.

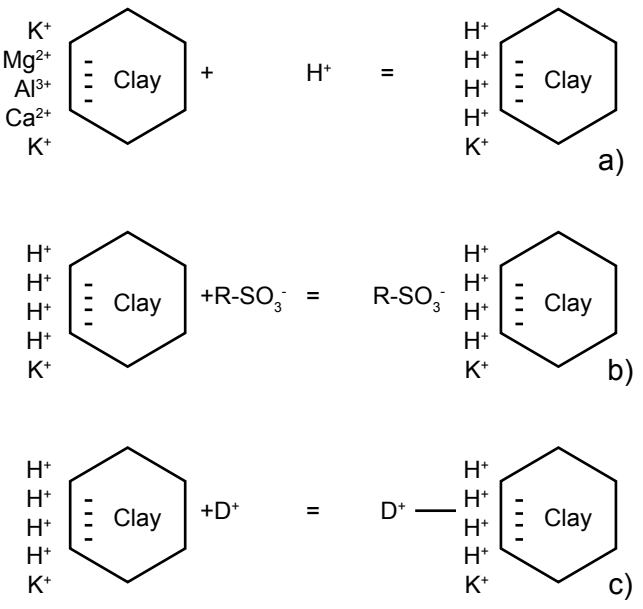

Figure 1: Illustrations of: a) cation exchange between acidic H^+ ions and clay cations; b) adsorption mechanisms by electrostatic attraction between clay and anionic dye [R-$(SO_3)^-$]; and c) adsorption mechanism by covalent bonding between clay and cationic dye (D^+).

[Figura 1: Ilustração de: a) troca catiônica entre íons H^+ do ácido e os cátions da argila; b) mecanismo de adsorção por atração eletrostática entre a argila e corante aniônico [R-$(SO_3)^-$]; e c) mecanismo de adsorção por ligação covalente entre a argila e corante catiônico (D^+).]

MATERIALS AND METHODS

Clay preparation: a clay was acquired from a mine in the city of Guadalupe, State of Piauí, Brazil. Initially, the natural sample was submitted to a manual quartering process in order to obtain a more homogeneous final sample. The clay was hammer milled and macerated with a porcelain mortar and pestle. Subsequently, the sample was sifted in a 120 mesh sieve and dried at 80±10 °C for 12 h to eliminate the excess water from the sample. *Clay chemical modification*: from the previously dried and disaggregated natural sample, two 4 g portions of clay were weighed and subjected to chemical treatment with solutions 2 M KOH (reagent grade, Dinâmica) and 2 M H_2SO_4 (reagent grade, Dinâmica), and then treated at 150 °C for 6 h in an oven with a heating rate of 10 °C/min. The resulting samples were labeled as CNAT for natural clay, and CTKOH and CTH_2SO_4 for the clays treated with potassium hydroxide and sulfuric acid, respectively.

X-ray diffraction (XRD): the clay samples before and after chemical modification were characterized by XRD using a Malvern Panalytical Empyrean diffractometer, in the 2θ range between 1.4° and 70° with CoKα radiation (wavelength of 1.79290 Å), and a scan speed of 5 °/min. *Fourier-transform infrared spectroscopy (FTIR)*: analyses were performed using KBr-containing pellet sample using Perkin Elmer 100FT-IR spectrometer (in the region from 4000 up to 400 cm^{-1}) with 16 scans and resolution of 4 cm^{-1}. *Specific surface area (BET)*: for obtaining nitrogen adsorption-desorption isotherms, the samples of CNAT, CTKOH, and CTH_2SO_4 were degassed at 100 °C for 16 h. Surface area measurements, from physical adsorption of nitrogen, were obtained at 77 K using a Quantachrome NOVA 10.01 analyzer to estimate the possible changes on the clay surface. *Thermal analysis*: thermogravimetric (TG) analysis was performed in a TA Instr. V20.9 SDT Q600, using an inert atmosphere of nitrogen with a gas flow of 100.0 mL/min and a heating rate of 20 °C/min. Samples were prepared precisely with a mass of 18.5080 mg using alumina crucibles and the temperature range for heat cycling was from 20 to 600 °C.

Extraction and yield of the isoamyl pre-treated oil: the lubricating oil was semi-synthetic with a viscosity classification of SAE 15W-40 and was purchased commercially. The used lubricating oils were supplied by Garagem do Monobloco (Teresina, Brazil), by removal from select petrol motor vehicles with a total odometer value of 15000 km. Isoamyl alcohol (PA, Dinâmica) was used in the crude oil extraction process with a 3:1 proportion of isoamyl alcohol to lubricating oil. The mixture was stirred for 30 min, and a precipitate of additives, impurities, and carbonaceous particles was formed. The precipitate was separated from the supernatant by filtration. Then, the alcohol was removed from the oil by rotary evaporation. The yield of resulting pre-treated oil was determined in comparison with the original amount of crude oil. *Application of clay samples to clarify isoamyl pre-treated oil*: the clarification process of the used lubricating oil was according to the ASTM D1500 standard

[25]. The lubricant clarification process was performed after pre-treatment with isoamyl alcohol. The resulting pre-treated oil sample was then submitted to the clarification process initially by eluting with a ratio of lubricant:hexane 1:1 (w/w). Both natural and treated clays were clarified using the same process. Fractions from filtration were collected and transferred to the vacuum distillation flask to recover the solvent and obtain the lubricant clarified at 50 °C. The resultant clarified oil was stored in an amber container for subsequent physicochemical characterization.

Physicochemical characterization of oil samples: the lubricating oils samples were characterized by the ASTM D1500-12 color [25], kinematic viscosity at 40 and 100 °C (ASTM D445-18) [26], total number of acidity (ASTM D974-04) [27] and ash content (ASTM D 482-13) [28]. *Colorimetric analysis*: the color measurement of the new lubricating oil (OLN), used lubricating oil (OLU), lubricating oil clarified with natural clay (OLCCNAT), lubricating oil clarified with clay and KOH (OLCCTKOH), and lubricating oil clarified with clay and H_2SO_4 (OLCCTH_2SO_4) was performed using a Seta-Lovibond Color Voltage 24v 15260-4 U instrument. Comparisons were made between the color of the analyzed samples and the Lovibond colors scale, which considers the measures of color to red and yellow. This technique comprises the combination of the color of the light transmitted through a specific depth of oil with the color of the light transmitted from the same source of the set of filters as the reference color [25]. *Kinematic viscosity*: was determined by the product of the time of the constant flow of Cannon-Fenske: 150 capillary viscometer at 100 °C; and 300 viscometer at 40 °C. The measurements were performed using a Quimis Q383SR26 automatic viscometer [26]. *Total number of acidity*: the acidity of the samples of lubricants was measured by the amount of potassium hydroxide required for neutralization (mg KOH/g lubricant) and resulting in the total number of acidity [27]. *Ash content*: the lubricating oil samples were transferred to a crucible and burned until they became ashes and carbon. Carbonaceous residues of the samples were reduced to ashes by heating in an oven at approximately 775 °C, cooled, and weighed [28]. *UV-vis analysis*: the capacity of natural sample and chemically-activated clays to discolor the used lubricating oil was determined using a digital Thermo Fisher Sci., Genesys 10S, UV-vis spectrophotometer operating from 100 to 1000 nm. Hexane was used to dilute the samples in the proportion of 1:10, and all the measurements were performed in triplicate [12].

RESULTS AND DISCUSSION

Initially, the results of X-ray diffraction (XRD) were evaluated to determine the matrix consistencies of the clay material employed in this study. The XRD pattern of the natural sample (Fig. 2a) showed reflections that were typically indexed to palygorskite [$Mg_5Si_8O_{20}(OH)_2(OH_2)_4.4H_2O$], kaolinite [$Al_2Si_2O_5(OH)_4$], and quartz ($SiO_2$), all of which were consistent with the files JCPDF 00-021-0958, 00-029-1488, and ICSD 01-079-1910, respectively. The reflection of higher intensity of palygorskite at 10.14° (d=10.11 Å) corresponded to the plane (110), and at 22.88° d=4.50 Å [12-17]. The presence of kaolinite was implicated by reflections at 14.35° (d=7.16 Å), 29.25° (d=3.54 Å), and 73.06° (d=1.50 Å). The presence of quartz corresponded to reflections at 24.41° (d=4.23 Å), 31.03° (d=3.34 Å), 40.46° (d=2.58 Å), 42.88° (d=2.44° Å), and 58.92° (d=1.81 Å). For the chemically-activated clay with H_2SO_4 sample (Fig. 2b), there was a gradual reduction in intensity and widening of the peaks in the palygorskite and kaolinite phases because of clay exfoliation [29]. Furthermore, the presence of quartz was maintained in the sample CTH_2SO_4, which suggested that the chemical treatment had little influence in this phase. With regard to the CTKOH sample (Fig. 2c), there was a slight reduction and widening of peaks of all crystalline phases, suggesting that chemical treatment had little influence on palygorskite, kaolinite, and quartz phases.

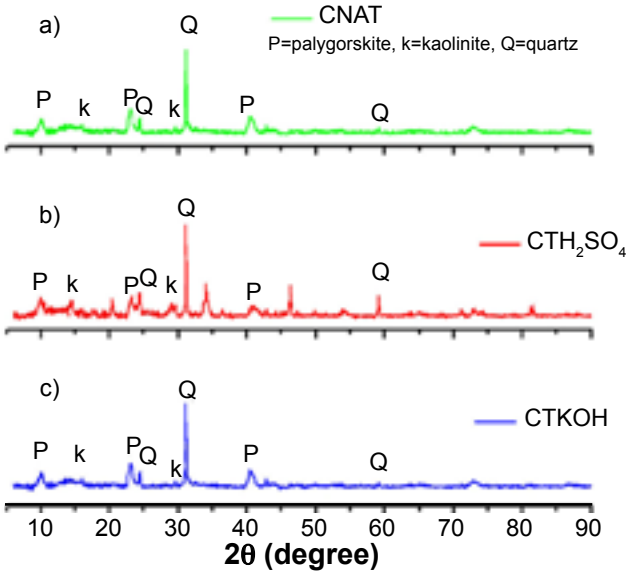

Figure 2: XRD patterns of the samples: a) CNAT; b) CTH_2SO_4; and c) CTKOH.
[Figura 2: Padrões de DRX das amostras: a) CNAT; b) CTH_2SO_4; e c) CTKOH.]

Fig. 3 shows the results of infrared spectroscopy of the samples CNAT (Fig. 3a), CTH_2SO_4 (Fig. 3b), and CTKOH (Fig. 3c). The bands at 3705 and 3618 cm^{-1} corresponded to the hydroxyl mixture of clay minerals (palygorskite and kaolinite) linked to metal (Me), where Me corresponds to the ions Al^{3+}, Mg^{2+} or Fe^{3+} [30-36]. The bands in the range from 3406 to 3516 cm^{-1} were attributed to the elongation vibrational mode of water absorbed by clay [12]. The band at 1643 cm^{-1} represented the deformation of water molecules [19] and at 913 cm^{-1} of the octahedral leaf (Al-OH) [17]. The absorption at 1029 cm^{-1} referred to the stretching of Si-O groups from the tetrahedral sheet for kaolinite and palygorskite [34-38]. The band at 796 cm^{-1} was attributed to the quartz impurity crystalline phase [34]. The bands at 682 and 537 cm^{-1} were attributed to angular deformation of

Si-O-Me [33], and around 467 cm^{-1} corresponded to Si-O-Si [37-40]. After the chemical modification, the bands from 3706 to 3406 cm^{-1} disappeared in both CTKOH and CTH_2SO_4 spectra. The disappearance of these bands confirmed the leaching of clay due to chemical treatment [17-30]. The bands presented in the region of shorter wavelength, for example at 1029, 913, 796, 682, 537 and 467 cm^{-1}, corresponded to vibrations related to the silica. Silica retention in samples of CTKOH and CTH_2SO_4 suggested that the chemical treatment had little influence on the quartz phase, corroborating the XRD results. The main observed bands presented in the IR spectral data set are briefly specified in Table I.

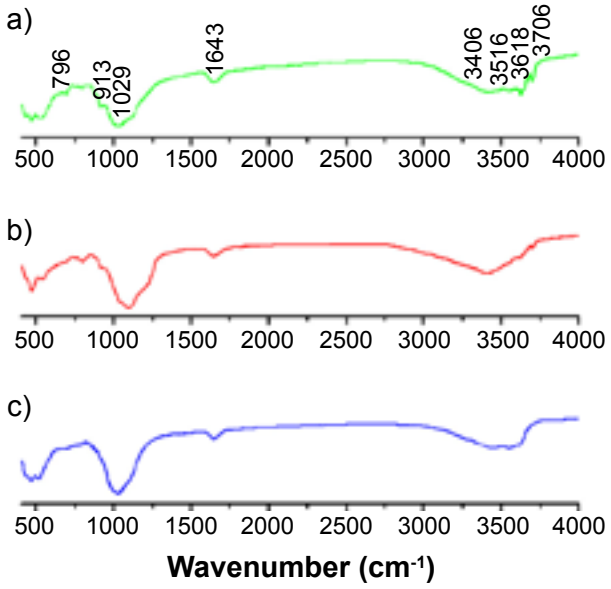

Figure 3: FTIR spectra of the samples: a) CNAT; b) CTH_2SO_4; and c) CTKOH.
[Figura 3: Espectros de FTIR das amostras: a) CNAT; b) CTH_2SO_4; e c) CTKOH.]

Table I - Allocation of the vibration bands on the infrared spectrum of clay.
[Tabela I - Atribuição das bandas de vibração no espectro infravermelho da argila.]

Wavenumber (cm^{-1})	Attribution	Ref.
3706	Stretching OH-Me	[30-36]
3618	Stretching OH-Me	[30-36]
3516	Stretching H_2O	[12]
3406	Stretching H_2O	[12]
1643	Deformation H_2O	[17]
1029	Stretching Si-O	[34-38]
913	Deformation Al-OH	[17]
796	Stretching Si-O-Si	[34]
682	Angular deformation Si-O-Me	[33]
537	Angular deformation Si-O-Me	[33]
467	Stretching Si-O-Si	[34, 37-40]

Fig. 4 shows adsorption-desorption isotherms of nitrogen for CTKOH, CTH_2SO_4, and CNAT. Each isotherm seemed to indicate type IV behavior with the presence of both meso and micropores (IUPAC classification) [41]. In Table II, the sample chemically-treated with acid showed a higher specific surface area (152.0 m^2/g) in comparison with the samples CTKOH (113.8 m^2/g) and CNAT (124.6 m^2/g). The pore volume was 0.047 $cm^3.g^{-1}$ for CTKOH, 0.051 $cm^3.g^{-1}$ for CNAT, and 0.063 $cm^3.g^{-1}$ for CTH_2SO_4. The increase in the specific surface area and pore volume in CTH_2SO_4 can be attributed to the leaching of cations Al^{3+} and Mg^{2+} of octahedral leaf, dehydroxylation of silanol and aluminol groups from tetrahedral and octahedral leaves of clay, and consequent progressive destruction of the chemical structure and generation of meso and microporous space with Bronsted-Lowry acidic sites after the acid treatment [30].

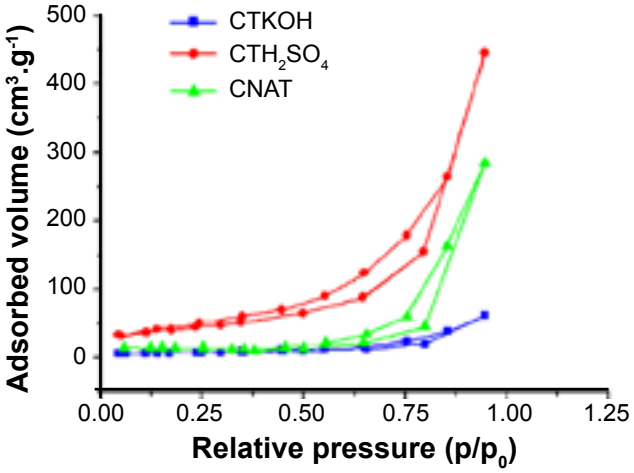

Figure 4: Nitrogen adsorption-desorption isotherms of the clay samples.
[Figura 4: Isotermas de adsorção-dessorção de nitrogênio das amostras de argila.]

TG/DTG analysis provided information about the changes following chemical treatment, further delineating the range of mass losses. Fig. 5 shows the thermal behavior of clay under a nitrogen atmosphere (TG/DTG curves for CNAT, CTKOH, and CTH_2SO_4). The samples had thermal events that were related to the mass loss of water from clay [17-30]. CNAT displayed three distinct events (Fig. 5). The first event occurred in the range between 20 and 126 °C and was associated with the release of physically adsorbed water [12], showing a loss of mass (PM1) of 7.25%. The second event occurred in the range between 126 and 287 °C, with a loss of mass of approximately 1.5% (PM2), which corresponded to the loss of mass of zeolitic water present in the channels [15-17]. Finally, the third event occurred in the range between 287 and 600 °C with a loss of mass of 7.05% (PM3) and was related to water loss and loss of the hydroxyls of the silanol (Si-OH) and aluminol groups

Table II - Results of specific surface area and pore volume of CNAT, CTH_2SO_4, and CTKOH.
[Tabela II - Resultados de área superficial específica e volume de poros de CNAT, CTH_2SO_4 e CTKOH.]

Sample	Surface area ($m^2.g^{-1}$)	Pore volume ($cm^3.g^{-1}$)
CNAT	124.6	0.051
CTKOH	113.8	0.047
CTH_2SO_4	152.0	0.063

(Al-OH) [15-19]. Above 600 °C, no further loss of mass occurred in the clay yielding a total mass loss of 15.80%. Likewise, CTKOH showed three events that were related to the mass loss of water from the clay [12-38]. The first event between 20 and 151 °C showed a loss of mass (PM1) of about 6.0% and was associated with the release of physically adsorbed water [12]. The second event occurred between 151 and 292 °C with a loss of mass (PM2) of 0.72%. The third event with a less intense band than CNAT occurred in the range between 292 and 597 °C with loss of mass (PM3) of 2.03% and was related to water loss and loss of the hydroxyls of the silanol (Si-OH) and aluminol groups (Al-OH) [19-37]. Above 600 °C, no further loss of mass occurred in the clay and therefore, a total mass loss of 9.08% was observed. The TG/DTG curves of CTH_2SO_4 revealed only two events. The first from 33 to 130 °C with loss of mass (PM1) of 7%, and the second from 130 to 490 °C with a mass loss of 11%, yielding a total mass loss of 18%. The final temperatures of the two events were smaller in CTH_2SO_4 and the loss of total mass of clay was greater in CTH_2SO_4, which was likely due to the acid treatment which expedited the leaching of clay at lower temperatures [20-40]. It is worth remembering that the morphology is still preserved with acid treatment because the silica generated during the acid treatment could behave as a protective gel preserving the morphology of the clay minerals present [19, 20]. The number of events and their respective mass loss found in thermal analysis of the samples CNAT, CTH_2SO_4, and CTPKOH are summarized in Table III.

Extraction and yield of the base oil: the yield of the pre-treated oil was calculated based on the ratio between the mass of recovered oil (free of alcohol) and water, and the mass of used oil [(MOrec/MOuse).100]. For the lubricating oil used for 15000 km, the yield obtained by extraction with isoamyl alcohol was 78% by mass.

Physicochemical characterization of new lubricating oil (OLN), used lubricating oil (OLU), lubricating oil clarified with natural clay (OLCCNAT), lubricating oil clarified with clay treated with KOH (OLCCTKOH) and lubricant oil clarified with clay treated with H_2SO_4 ($OLCCTH_2SO_4$): Table IV presents the results of physicochemical characterization of OLN, OLU, OLCCNAT, OLCCTKOH, and $OLCCTH_2SO_4$, compared to the limits of kinematic viscosity at 40 and 100 °C, ASTM color, acidity, and ash content established by the standards

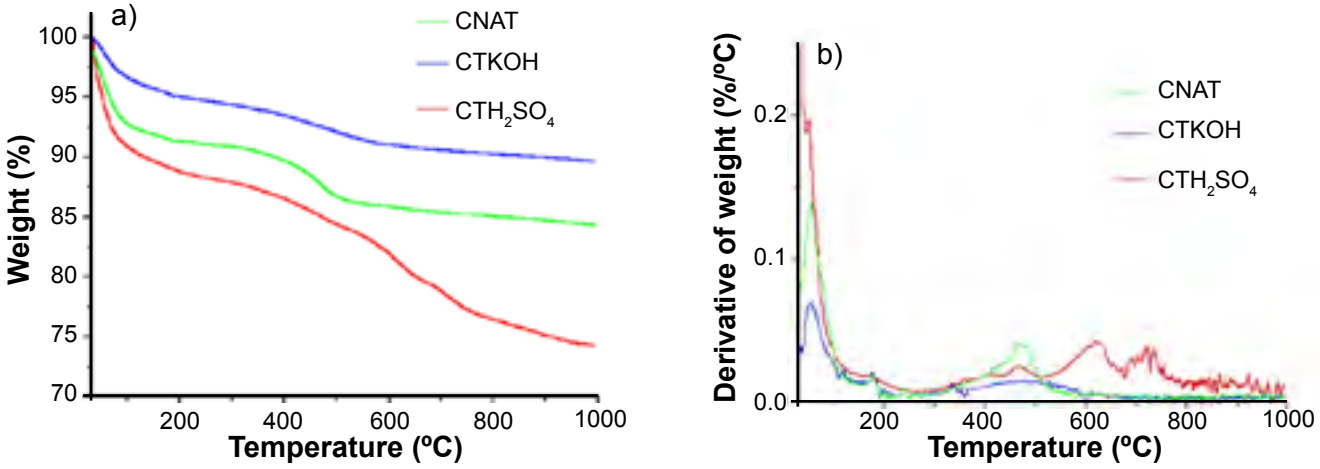

Figure 5: TG (a) and DTG (b), a derivative of TG, curves of the CNAT, CTKOH, and CTH_2SO_4 samples.
[Figura 5: Curvas TG (a) e DTG (b), derivada de TG, das amostras de CNAT, CTKOH e CTH_2SO_4.]

Table III - Results of thermal analysis of adsorbing materials.
[Tabela III - Resultados de análise térmica dos materiais adsorventes.]

Sample	ΔT1 (°C)	PM1 (%)	ΔT2 (°C)	PM2 (%)	ΔT3 (°C)	PM3 (%)	PMT (%)
CNAT	20-126	7.25	126-287	1.50	287-600	7.05	15.80
CTKOH	21-151	6.33	151-292	0.72	292-597	2.03	9.08
CTH_2SO_4	33-130	7.00	130-490	11.00	-	-	18.00

ΔTi: temperature range of thermal event; PMi: loss of mass; PMT: total mass loss.

Table IV - Results of physicochemical characterizations of OLN, OLU, OLCCNAT, OLCCTKOH, and OLCCTH_2SO_4 compared with the limits from ASTM standards.
[Tabela IV - Resultados de caracterização físico química de OLN, OLU, OLCCNAT, OLCCTKOH e OLCCTH_2SO_4 comparados com limites de normas da ASTM.]

Test		OLN	OLU	OLCCNAT	OLCCTKOH	OLCCTH_2SO_4	Limit
Kinematic viscosity (mm^2/s)	at 40 °C	100.2	114.0	34.5	30.6	27.5	26-32
	at 100 °C	16.8	18.7	14.0	9.5	7.4	-
ASTM color		1.0	8.0	6.5	6.0	5.0	≤3
Acidity (mg KOH/g)		2.09	5.97	0.048	-	0.045	≤0.05
Ash content (mass%)		0.01	1.52	1.30	0.50	0.05	≤0.02

OLN: new lubricating oil; OLU: used lubricating oil; OLCCNAT: lubricating oil clarified with natural clay; OLCCTKOH: lubricating oil clarified with clay treated with KOH; OLCCTH_2SO_4: lubricant oil clarified with clay treated with H_2SO_4.

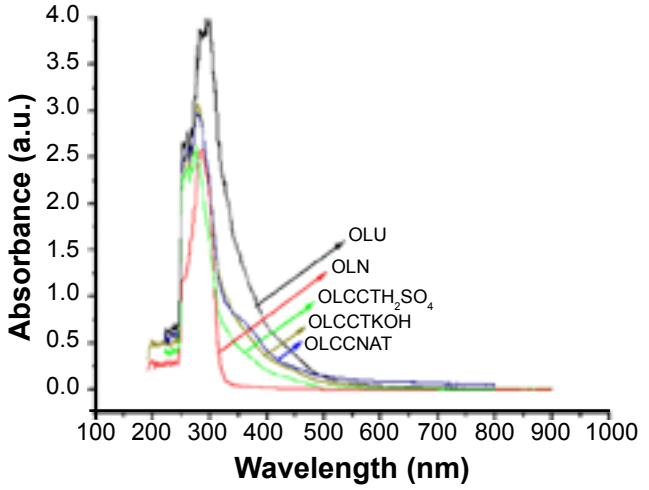

Figure 6: UV-vis absorption spectra of OLN, OLCCTKOH, OLCCNAT, OLCCTH_2SO_4, and OLU.
[Figura 6: Espectros de absorção UV-vis de OLN, OLCCTKOH, OLCCNAT, OLCCTH_2SO_4 e OLU.]

ASTM D445-18, ASTM D1500-12, ASTM D974-04, and ASTM D482-13 that regulate the commercialization of recovered lubricating oils. After the recovery process of used lubricating oil (OLU) by extraction with isoamyl alcohol and adsorption with the clays, the results of the samples OLCCNAT, OLCCTKOH, and OLCCTH_2SO_4 approached the limits established by ASTM [29-30]. OLCCTH_2SO_4 also presented the best whitening result of the used lubricating oil due to the creation of meso and microporous Bronsted-Lowry acidic sites, increasing the process of adsorption of metallic cations and dye. Moreover, the results found in this study were consistent with the results found in [32, 42]. The absorbance spectrum in the wavelength range from 200 to 700 nm (Fig. 6) showed that the OLCCTH_2SO_4 clarified oil sample was the one that most closely approached the color of new lubricating oil (OLN), likely due to the adsorption of organic, inorganic, and metal contaminants on the adsorbent surface. This observation can be explained by hydrogen bonding capacity in Bronsted-Lowry sites that may form in clay enabled with sulfuric acid [43-46].

CONCLUSIONS

The use of natural and chemically modified clays is an environmentally friendly method of clarifying the used lubricating oil. The acid-treated sample was more efficient in dye adsorption, being responsible for the dark color of the used lubricating oil and, consequently, promoted effective oil clarification confirmed by the results obtained by the colorimeter and UV-vis analyses.

REFERENCES

[1] R.R. Mohammed, I.A.R. Ibrahim, A.H.T. McKay, Chem. Eng. J. **220** (2013) 343.
[2] T. Zaky, S.M. Tawfik, Fuel Process. Technol. **92** (2011) 447.
[3] J. Rincon, P. Canizares, M.T. García, Ind. Eng. Chem. Res. **44** (2005) 4373.
[4] E.A. Eman, A.M. Shoaib, Pet. Coal **55** (2013) 179.
[5] A.H. Durrani, I.M. Panhwar, A.R. Kazi, Mehran Univ. Res. J. Eng. Technol. **30** (2011) 237.
[6] M.A. Kamal, S.M.D. Naqvi, F. Khan, Sci. World J. **1** (2014) 1.
[7] O.C.J. Santos, G.M.I. Santos, G.A. Souza, V.E. Sobrinho, J.V. Fernandes, Fuel **83** (2004) 2393.
[8] A.M. Ghouti, L. Atoum, J. Environ. Manage. **90** (2009) 187.
[9] E. Arthur, M. Tuller, T. Norgaard, P. Moldrup, L.W. De Jonge, Geoderma **350** (2019) 40.
[10] S.L. Shiung, D.A. Russell, A.H. Chase, Energy **35** (2010) 2985.
[11] H. Wagner, R. Luther, T. Mang, Appl. Catal. A Gen. **221** (2001) 429.
[12] K.M.C. Xavier, M.S.F. Santos, J.A. Osajima, A.B. Luz, M.G. Fonseca, E.C. Silva Filho, Appl. Clay Sci. **119** (2016) 338.
[13] J.S. Patricio, D. Hotza, A. De Noni Júnior, Cerâmica **60**, 354 (2014) 171.
[14] S.M.W. Ali, A. Ripin, A. Ahmad, J. Appl. Sci. **10** (2010) 2688.
[15] C. Duanmu, Y. Gu, Y. Qian, X. Gu, L. Feng, J. Jiang, Appl. Clay Sci. **55** (2012) 108.

[16] P.S. Santos, *Tecnologia de argilas* **1**, Edgard Blücher, S. Paulo (1975) 70.
[17] L. Boudrichea, R. Calvet, B. Hamdi, H. Balard, Colloid Surface A **392** (2011) 45.
[18] H. Chen, J. Zhao, A. Zhong, Y. Jin, Chem. Eng. J. **174** (2011) 143.
[19] E. Srasra, N. Frini-Srasra, Desalination **250** (2010) 26.
[20] H.C. Starkey, D. Carrol, Clays Clay Miner. **19** (1971) 321.
[21] A. Kausar, M. Iqbal, A. Javed, K. Aftab, Zill-i-Huma, N.H.N. Bhatti, S. Nouren, J. Mol. Liq. **256** (2018) 395.
[22] Y. Jiang, A. Khan, H. Huang, Y. Tian, X. Yu, Q. Xu, L. Mou, J. Lv, P. Zhang, P. Liu, L. Deng, X. Li, Sci. Total Environ. **646** (2019) 606.
[23] A.I. Hafez, N.S. Gerges, H.N. Ibrahim, W.S.A. El Magd, A.I. Hashem, Egypt. J. Pet. **26** (2017) 533.
[24] S. Salem, A. Salem, A.A. Babaei, J. Ind. Eng. Chem. **23** (2015) 154.
[25] ASTM D1500-12, "Standard test method for ASTM color of petroleum products (ASTM color scale)", ASTM Int., West Conshohocken (2012).
[26] ASTM D445-18, "Standard test method for kinematic viscosity of transparent and opaque liquids (and calculation of dynamic viscosity)", ASTM Int., West Conshohocken (2018).
[27] ASTM D974-04, "Standard test method for acid and base number by color-indicator titration", ASTM Int., West Conshohocken (2004).
[28] ASTM D482-13, "Standard test method for ash from petroleum products", ASTM Int., West Conshohocken (2013).
[29] J.P. Neto, S.L.M. Almeida, R.M. Carvalho, in "Tecnologia mineral", 64, CETEM, Brazil (1993) 1.
[30] K.A. Sampaio, J. Vila-Ayala, S.M. Silva, R. Ceriane, R. Verhe, A.J.A.J. Meireles, J. Am. Oil Chem. Soc. **90** (2013) 191.
[31] T.E. Oladimeji, J.A. Sonibare, J.A. Omoleye, A.A. Adegbola, H.I. Okagbuec, Data Brief **19** (2018) 2240.
[32] A.E.A. de Lima, H.B. Sales, L.C. de Lima, J.C.O. Santos, I.M.G. dos Santos, A.G. de Souza, R. Rosenhain, Cerâmica **63**, 368 (2017) 517.
[33] C. Stan, C, Andreescu, M. Toma, Procedia Manuf. **22** (2018) 709.
[34] D.I. Osman, S.K. Attia, R.A. Taman, Egypt. J. Pet. **27** (2018) 221.
[35] M.A. Morales-Carrera, C.D.F.A. Varajao, A.M. Goncalves, S.A. Stachissini, Quím. Nova **32** (2009) 2287.
[36] K.B. Amorim, R.S. Angélica, Cerâmica **57**, 344 (2011) 483.
[37] W. Wang, G. Tian, Z. Zhang, A. Wang, Chem. Eng. J. **265** (2015) 228.
[38] A. Wang, W. Wang, Z. Zhang, Appl. Clay Sci. **107** (2015) 230.
[39] A. Wang, Y. Zhao, H. Chen, J. Hazard. Mater. **149** (2007) 346.
[40] R. Naidu, Y. Liu, J. Churchman, B. Biswas, B. Sarkar, R. Rusmin, Appl. Clay Sci. **134** (2016) 65.
[41] D. Papoulis, S. Komarneni, A. Nikolopoulou, P. Tsolis-Katagas, D. Panagiotaras, H.G. Kacandes, P. Zhange, S. Yin, T. Sato, H. Katsuki, Appl. Clay Sci. **50** (2010) 118.
[42] S.L.M. Melo, "Avaliação da qualidade dos óleos básicos rerrefinados brasileiros e a determinação de metais por espectrometria de fluorescência de raios X", Dr. Thesis, Un. Brasília (2015).
[43] I.M. Sato, J.O.W.V. Bustillos, C.L. Duarte, M.A. Scapin, Radiat. Phys. Chem. **78** (2009) 733.
[44] T. Chen, H. Liu, J. Li, D. Chen, D. Chang, D. Kong, R.L. Frost, Chem. Eng. J. **166** (2011) 1017.
[45] H. Chen, J. Zhao, A. Zhong, Y. Jin, Chem. Eng. J. **174** (2011) 143.
[46] E.L. Foletto, C. Volzone, A.F. Morgado, L.M. Porto, Cerâmica **47**, 304 (2001) 208.
(Rec. 27/06/2019, Rev. 16/09/2019, 06/11/2019, 11/11/2019, Ac. 17/11/2019)

BY-NC

Synthesis and application of a composite NaA zeolite/gamma-alumina membrane for oil-water separation process

(Síntese e aplicação de uma membrana compósita zeólita NaA/gama-alumina para o processo de separação de óleo/água)

T. L. A. Barbosa[1], F. M. N. Silva[1], A. S. Barbosa[1], E. G. Lima[1], M. G. F. Rodrigues[1]*
[1]Universidade Federal de Campina Grande, Unidade Acadêmica de Engenharia Química, Av. Aprígio Veloso 882, 58429-970, Campina Grande, PB, Brazil

Abstract

This study proposed the development of an efficient membrane composed of zeolite-alumina to be used for water-oil separation of wastewater effluents contaminated by oil extraction processes. The efforts made to care for the environment and to decontaminate bodies of water are extremely valuable and constantly being updated. Little research has been done on this subject and this study contributed to remedying this lack. Membrane technology is a reasonable alternative to conventional procedures if economics and eco-sustainability are considered. The objective of this study was to examine the performance of a composite membrane produced through mechanical mixing. The potential of the composite membrane (NaA zeolite/gama-alumina) to separate oil-water emulsions was tested. The results obtained demonstrated that the composite membrane is an excellent alternative for the oil/water emulsion separation process; the membranes are efficient and low-cost alternatives for treating oily wastewater.
Keywords: composite membrane, zeolite NaA, gamma-alumina, oily wastewater, oil-water emulsion.

Resumo

Este estudo propôs o desenvolvimento de uma membrana eficiente composta por zeólita-alumina a ser utilizada na separação óleo/água de efluentes contaminados por processos de extração de óleo. Os esforços feitos para cuidar do meio ambiente e descontaminar reservas de água são extremamente valiosos e constantemente atualizados. Pouca pesquisa foi feita sobre este assunto e este estudo contribuiu para remediar essa falta. A tecnologia de membrana é uma alternativa razoável para procedimentos convencionais, se economia e ecossustentabilidade forem consideradas. O objetivo deste estudo foi examinar o desempenho da membrana compósita produzida através de mistura mecânica. O potencial da membrana compósita (zeólita NaA/gama-alumina) para separar as emulsões óleo/água foi testado. Os resultados obtidos demonstraram que a membrana compósita é uma excelente alternativa para o processo de separação da emulsão óleo/água; as membranas são alternativas eficientes e de baixo custo para o tratamento de efluentes oleosos.
***Palavras-chave**: membrana compósita, zeólita NaA, gama-alumina, águas residuais oleosas, emulsão de óleo/água.*

INTRODUCTION

During drilling and production activities, considerable waste is generated that must be treated. Waste treatment seeks to lower the potential hazards associated with waste by reducing its toxicity, minimizing its volume, and/or altering its state so that it is suitable for specific disposal methods. Treatment is required for many diverse types of waste prior to final disposal, and various treatment methods are available for most wastes, but not all methods can be used for all waste streams. These different treatment methods may vary considerably in both effectiveness and cost [1-3]. Traditional methods of managing wastewater do not adequately satisfy petroleum industry requirements for treatment in compliance with discharge and reuse standards [3-5]. Thus, there is a substantial need for new innovative membrane technologies. The existing literature regarding these processes and recent advancements in membrane technology applications in the petroleum industry are insufficient [4-8]. Inorganic membranes exhibit unique characteristics that make them attractive for use in the separation processes, such as mechanical and thermal stability. The membranes also contain some materials that have been applied as chemical adsorbents [9-12]. Over the past few years, inorganic membrane separation technology has seen accelerated growth and innovation [13]. Various membrane separation processes have been developed, and new processes are continually being studied in both academia and the industry.

Zeolite membranes are porous and thermally stable, acidic

**meiry.rodrigues@ufcg.edu.br*
https://orcid.org/0000-0003-2258-4230

or basic in nature, and present hydrophilic or organophilic properties [14-23]. In comparison with other procedures, the results of green membrane technology generate effluents of good quality. The operation is simple and requires only a small area to function, without the need for additional chemicals, thereby reducing the risk of incrustation [24]. Certainly, membrane technology is a reasonable alternative to conventional procedures, when taking into account economics and eco-sustainability. Polycrystalline Linde Type A (LTA) zeolites are intensely hydrophilic and have a central pore of ~4.2 Å [14]. Single LTA zeolite nanoparticles have shown high rejection of small molecules in gas separations [25]. These properties give zeolites significant potential for aqueous membrane separation applications. The NaA zeolite/α-alumina membrane was evaluated for the process of treatment of oil-contaminated water [26]. NaA zeolite microfiltration membranes were synthesized on an α-alumina tube by the hydrothermal synthesis method. The results were 99% of oil rejection for the membrane NaA zeolite/α-alumina. Our research group has published some papers on the production of zeolite membranes and composite membranes [27-39]. Zhan et al. [40] demonstrated novel thermally and chemically stable composite membranes consisting of halloysite nanotubes (HNTs) intercalated with graphene oxide (GO) coating on porous poly(arylene ether nitrile) (PEN) nanofibrous mat, which were prepared by controlled assembly of HNTs intercalated GO (skin layer) onto the surface of electrospun PEN nanofibrous mats (supporting layer) and further mussel-inspired polydopamine coating. The resulting composite membranes exhibited a high preferable rejection ratio (more than 99.0%) and remarkable antifouling performance for various oil/water emulsions. Furthermore, flexible channel control of the skin layer by intercalation of HNTs, porous PEN supporting layer, and super-wetting property endowed the composite membranes with high permeate flux (1130.56 L/m^2.h) [40]. Yang et al. [41] studied hydrophilic modification of PVDF membrane processed by a mussel-inspired method. Multi-wall carbon nanotubes (MWCNTs) were functionalized by grafting 3-aminopropyltriethoxysilane (APTES) and then directly decorated on PVDF membrane surface by dopamine copolymerization. The modified membranes could be applied to separate different kinds of oil-in-water emulsions with high permeate flux (about 900 L/m^2.h under 0.09 MPa) and ultrahigh oil rejection ratio (nearly 99%). More importantly, the as-prepared superhydrophilic PVDF membranes showed durable oil-fouling repellency, which could be easily recycled with a recovery of flux ratio up to 90%.

The literature is scarce regarding the use of zeolitic membranes for oil-water removal. In this regard, it is interesting to study the use of these membranes for the water separation process. In order to achieve an easy and effective synthesis of the composite membrane (NaA zeolite/gamma-alumina), the mechanical mixing method was used. This method is advantageous because of its relative simplicity, low operating cost, and low energy consumption requirements. The composite membrane produced through mechanical mixing can be completed in less than 4 h after the fabrication of the materials. In light of the growth potential, the composite membrane (NaA zeolite/gamma-alumina) is expected to be used in processes that separate oil from water.

MATERIALS AND METHODS

Materials: aluminum sulfate [$Al_2(SO_4)_3.18H_2O$] P.A., sodium metasilicate ($Na_2SiO_3.5H_2O$), sodium hydroxide pellets (Prolabo, 98%), sodium aluminate ($Na_2O.Al_2O_3.3H_2O$, Riedel-de Haen), deionized water, oleic acid, PABA (para-aminobenzoic acid), ethanol (C_2H_6O, Vetec, 99%), and chloroform P.A. (Synth) were used.

Preparation of gamma-alumina (powder): the thermal decomposition of aluminum sulfate was carried out in a muffle furnace at 1000 ºC for 2 h using a heating rate of 5 ºC/min to produce gamma-alumina crystal phase [32].

Preparation of ceramic membrane: the ceramic membrane (asymmetric support of gamma-alumina) was manufactured by using the uniaxial dry compaction method. A mixture of alumina with additives in a total of 200 mL of dispersion with the composition of 40% of produced gamma-alumina, 0.2% of PABA (dissolved in ethanol), 0.5% oleic acid (lubricant), and 59.3% ethyl alcohol was prepared. After 1 h milling, the mixture was transferred to a reservoir and then dried at 60 ºC for 24 h. 3 g of the material was inserted into a stainless steel mold and pressed for 2 min with 4 ton. In order to increase the mechanical strength, the ceramic membrane was sintered in air for 2 h at 700 ºC; the heating rate was 5 °C/min from room temperature to 700 °C. A ceramic flat membrane (gamma-alumina) was produced with a diameter of 26.6 mm and a thickness of 3.6 mm [31].

Synthesis of NaA zeolite: zeolite NaA was synthesized by hydrothermal synthesis based on the procedure reported in [42] with some modifications. The preparation consisted of the following steps: 1) 0.723 g of sodium hydroxide was added to deionized water, then mixed until NaOH was completely dissolved; afterward, the solution was divided into two equal volumes in polypropylene bottles; 2) in a half of (1), 8.258 g of sodium aluminate was added and then mixed in a capped bottle until the mixture became clear; 3) in the second half of (1), 15.48 g of sodium metasilicate was added and also mixed in a capped bottle until clear; 4) the silicate solution (2) was quickly poured into the aluminate solution (3) to form a thick gel. Finally, the resultant gel was stored in a sealed autoclave. After crystallization at 100 °C for 4 h, the final product was washed, then dried in air at 100 °C for 24 h. The sample was synthesized with a molar composition of $4.62Na_2O:1Al_2O_3:6SiO_2:180H_2O$.

Preparation of composite membrane of NaA zeolite/gamma-alumina: the composite membrane was manufactured by the mechanical mixing of gamma-alumina and NaA zeolite. The ratio of 50% (w/w) gamma-alumina/NaA zeolite was used. The mixture was poured in a stainless steel mold and pressed with 4 ton for 2 min. After that, the membrane was submitted to a heat treatment at 550 °C for 4 h to improve

its mechanical strength. After these steps, it was obtained a planar composite membrane (NaA/gamma-alumina) with a diameter of 26.6 mm and a thickness of 3.6 mm.

Characterization: X-ray diffraction: XRD analysis of the samples was performed using a Shimadzu XRD 6000 diffractometer with CuKα radiation, operated at 30 mA and 40 kV, with a goniometer velocity of 2 °/min and a step of 0.02° in the scanning range of 2θ from 2º to 50º. *Nitrogen adsorption-desorption*: N_2 gas adsorption/desorption isotherms were obtained at -196 °C using a Micrometrics ASAP 2020 equipment in the range of relative pressure (P/P_0) between 0.02 and 1.0. The values of the average pore diameter and surface area (S_{BET}) were obtained by the BET method and the pore sizes and total pore volumes were determined by the Barrett-Joyner-Halenda (BJH) method from desorption branches of the isotherms. *Scanning electron microscopy*: SEM images were obtained with a Philips XL 30 microscope. *Mercury porosimetry*: it was performed in a mercury porosimeter, Micromeritics Autopore IV 9500 V1.05. *Mechanical strength*: the tensile strength of the ceramic support (gamma-alumina) was determined by the diametral compression test following the ASTM C158 standard in a universal testing machine (1000 kN Emic). To ensure that the samples were tested under plane stress conditions, samples with dimensions of 26x3 mm (diameter x thickness) were used. *Bubble point*: the bubble point method gives information about the pores that control the permeation, and it is used to measure pores with size above 50 nm (ASTM F316-03). It consists of filling the porous structure of the membrane with a liquid and measuring the air pressure necessary to displace the liquid inside the pores. The minimum pressure necessary to blow the first observed air bubble corresponds to the largest pore size of the membrane; this value is known as the bubble point [43, 44]. The mathematical relationship between pressure and pore size is given by the Washburn equation:

$$\Delta P = \frac{4.\gamma.\cos\phi}{Dp} \qquad (A)$$

where ΔP is the pressure drop (bar), Dp is the pore size (μm), ϕ is the contact angle between the fluid and pore walls, and γ is the liquid surface tension (isopropyl alcohol). In order to be able to use the Washburn equation, the pores are assumed to be cylindrical. To reduce surface tension and facilitate measurement, liquids with low surface tension are used, such as alcohol. The scheme of the bubble point experimental equipment is presented in Fig. 1.

Separation experiments of oil-in-water emulsion: Fig. 2 shows the system used in the process of separation of oil/water emulsion. For the tests, oil/water emulsions were produced with a concentration of 100 $mg.L^{-1}$. Oily wastewater was prepared emulsifying lubricant mineral oil (Lubrax, Petrobras, SL SAE 20W/50 API SL) in distilled water under stirring (high-speed stirrer) for 20 min to produce a stable emulsion. The concentration of oil present in the aqueous phase was determined by the analysis of absorbance using a spectrophotometer (UV-visible, UV-1800, Shimadzu). A

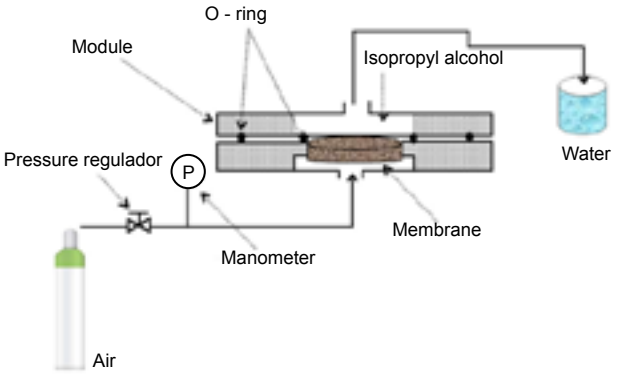

Figure 1: Scheme of the bubble point experimental equipment: 1) gas cylinder; 2) pressure regulator; 3) pressure gauge; 4) membrane; 5) module; 6) O-ring; 7) isopropyl alcohol; and 8) tank. *[Figura 1: Esquema do equipamento experimental do ponto de bolha: 1) cilindro de gás; 2) regulador de pressão; 3) manômetro; 4) membrana; 5) módulo; 6) O-ring; 7) álcool isopropílico; e 8) tanque.]*

calibration curve of absorbance versus concentration using different concentrations of oil ranging from 0 to 100 $mg.L^{-1}$ was built with a coefficient of determination (R^2) of 0.9963. Chloroform was used as a solvent for extraction because of an excellent response (significant peak) at a wavelength of 262 nm for the samples analyzed. The absorbance at this wavelength is commonly used to estimate the concentration of oil in water samples and also in produced water. Bands of aromatic CH in the medium are measured at this wavelength. Based on this, the absorbance was measured at this wavelength. This procedure was designed to normalize the determination of oil and grease contents [45]. The permeate flux was calculated by dividing the permeate volume by the product of the membrane area and the sampling time. The oil retention coefficient R was calculated as a percentage according to:

$$R = \frac{C_f - C_p}{C_f} .100 \qquad (B)$$

where C_f is the oil concentration in the feed, and C_p is the oil concentration in the permeate. Flow membrane operation was used in the filtration experiments with the apparatus shown in Fig. 2. The membrane disk was sealed with a pair of O-rings in the homemade stainless steel membrane housing. *Water flux measurements*: Fig. 2 presents the system used for measurements of pure water flux through the membranes of gamma-alumina and composite NaA zeolite/gamma-alumina as a function of time. A flat sheet membrane module made of stainless steel was used in the two experiments. The effective area of the membrane in the module was 0.22 m^2. Experiments were carried out at a pressure of 1.5 bar, at 27 °C, during 60 min, and the flux was calculated by:

$$Flux = \frac{Q}{A.t} \qquad (C)$$

where Q is the quantity of permeate (m^3), A is the effective membrane area (m^2), and t is the sampling time (h).

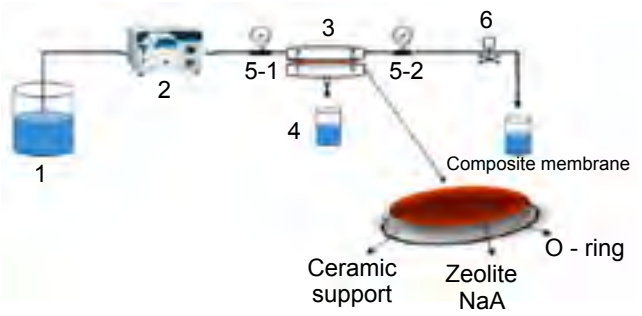

Figure 2: System used for flux measurements: 1) feed tank; 2) peristaltic pump; 3) permeation/separation module (stainless steel); 4) permeated volume; 5-1) pressure gauge before module input; 5-2) pressure gauge after module input; and 6) pressure regulator (concentrate).
[Figura 2: Sistema utilizado para medições de fluxo: 1) tanque de alimentação; 2) bomba peristáltica; 3) módulo de permeação/separação (aço inoxidável); 4) volume permeável; 5-1) manômetro antes da entrada do módulo; 5-2) manômetro após o módulo entrada; e 6) regulador de pressão (concentrado)].

RESULTS AND DISCUSSION

Powders: the N_2 adsorption-desorption isotherm of the gamma-alumina powder is presented in Fig. 3a, while the pore size distribution curve determined by the Barret-Joyner-Hatenda (BJH) model is presented in Fig. 3b. The isotherm for the sample was of type IV and exhibited a well-defined H1 hysteresis loop according to the IUPAC classification, relative to the mesoporous structure (Table I) [46]. A steep hysteresis loop can be seen in Fig. 3a, typical for mesoporous materials that exhibit capillary condensation and evaporation [47]. The existence of a large mesopore structure in this material [48] was shown by the sharp rise in the nitrogen-desorption isotherms at high relative pressures (P/P_0 near 0.97). The pore sizes of the sample were concentrated in the 5-50 nm range (Fig. 3b). The textural analysis of the gamma-alumina is presented in Table I. According to the evaluation by the BET method, the specific surface area was 150 m^2/g, and the total pore volume was 0.6492 cm^3/g. The value of mesopore volume (0.6446 cm^3/g) was higher than the value of micropore volume (0.0046 cm^3/g). It was observed that the values of the properties of gamma-alumina were according to the literature [46]. The BET analysis also showed that the NaA zeolite (Table I) presented a specific surface area of 196 m^2/g and a pore volume of 0.218 cm^3/g. These results were in accordance with those obtained in [33].

Membranes: the results of average pore diameter, porosity, and mechanical strength of the ceramic membrane are presented in Table II. The tensile strength of the ceramic membrane (gamma-alumina support sintered at 700 ºC) was 1.3 MPa, the average pore diameter was 0.02 μm, and porosity was 37.95%. The tensile strength of the composite membrane (sintered at 550 ºC) was 1.0 MPa, the average pore diameter was 0.012 μm, and porosity was 38.94%. Zeolite membranes have unique pore structures containing two types of pores: uniform subnanometer zeolitic pores

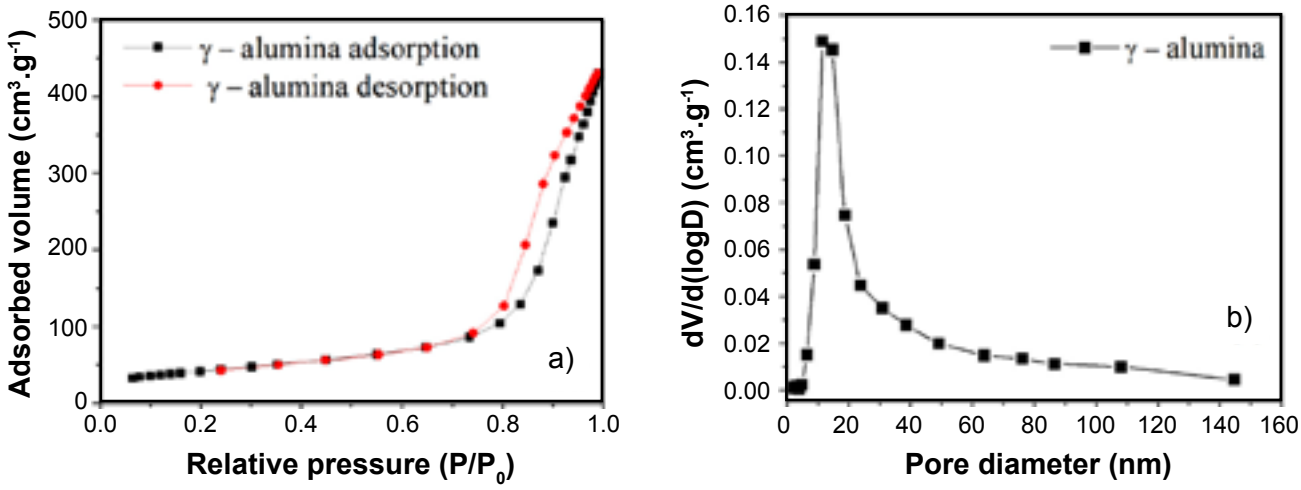

Figure 3: Nitrogen adsorption-desorption isotherm at -196 °C (a) and BJH pore size distribution curve (b) of gamma-alumina (powder).
[Figura 3: Isoterma de adsorção-dessorção de N_2 a -196 °C (a) e curva de distribuição de tamanho de poros pelo método BJH (b) da gama-alumina (pó).]

Table I - Results of textural analysis of gamma-alumina and NaA zeolite powders.
[Tabela I - Resultados da análise textural de pós de gama-alumina e zeólita NaA.]

Sample	S_{BET} (m^2/g)	V_P (cm^3/g)	V_{Micro} (cm^3/g)	V_{Meso} (cm^3/g)	D_P # (nm)
Gamma-alumina	150	0.6492	0.0046	0.6446	20.00
NaA zeolite	196	0.2180	-	-	3.23

- *pore size derived from the desorption isotherm determined by the BJH method.*

Table II - Average pore diameter, porosity, and mechanical strength of ceramic and composite membranes.
[Tabela II - Diâmetro médio dos poros, porosidade e resistência mecânica das membranas cerâmica e compósita.]

Membrane	Sintering temperature (°C)	Average pore diameter (μm)	Porosity (%)	Mechanical strength (MPa)
Ceramic	700	0.020	37.95	1.3
Composite	550	0.012	38.94	1.0

and inter-crystal micropores with certain size distribution [49, 50]. Water is expected to transport across both the inter-particle pores and the intra-particle pores [26].

Bubble point: the bubble point measurement was performed to estimate the average pore size of the membranes developed herein. This method only provides one measure of the largest active pore of a given membrane. In Table III the pore diameter values calculated from Eq. A are presented at certain pressures using isopropyl alcohol as the impregnating liquid. The composite membrane of NaA required relatively much higher pressure to expel the first bubble, confirming the presence of resistance in accordance with XRD and SEM characterizations. In the case of asymmetric membranes, the measurement of pore size distribution by intrusion mercury porosimetry or bubble point would not reflect the size of the pores controlling the flow. Another limitation in the case of asymmetric membranes is the inability of this method to distinguish between the pores that determine the flux and the largest pores in the support [51].

Table III - Results of bubble point test of ceramic and composite (NaA zeolite/gamma-alumina) membranes.
[Tabela III - Resultados de teste de ponto de bolha de membranas cerâmica e compósita (zeólita NaA/alumina-gama).]

Membrane	Ceramic	Composite
ΔP (bar)	0.500	1.000
Dp (μm)	1.664	0.832

X-ray diffraction: the results of NaA zeolite, gamma-alumina, and composite membrane are presented in Fig. 4. The diffractogram of the zeolite NaA (Fig. 4a) presented a typical profile for the NaA zeolite structure, with main peaks at 2θ of 7.17°, 10.28°, 12.78°, 16.26°, and 47.3° characterizing the crystalline phase of the NaA zeolite, with no other secondary phases identified (according to the International Center for Diffraction Data, JCPDS 43-0168), characteristics of crystalline and pure materials. This showed that the synthesis method conditions employed in this research were effective for the production of the NaA zeolite [42]. From the XRD pattern shown in Fig. 4b, it is possible to observe the characteristics and well-resolved peaks of the gamma-alumina phase. After calcination at 700 °C for 2 h, peaks at 2θ of 19°, 32-45°, and 60-67° were observed, indicating that the precursor was converted to gamma-alumina (JCPDS 10-0425). Fig. 4c shows the XRD pattern of the composite membrane (NaA zeolite/gamma-alumina). It was possible to identify two distinct phases as the constituents of the composite membrane structure: NaA zeolite and gamma-alumina. The diffraction peaks presented by the membrane revealed the existence of crystalline structures with well-defined peaks, indicating high crystallinity.

Scanning electron microscopy: SEM images of the surfaces of the NaA zeolite, ceramic membrane, and composite membrane are shown in Fig. 5. It can be seen in the micrograph of the NaA zeolite (Fig. 5a) particles with morphology consisting of cubic symmetry distributed

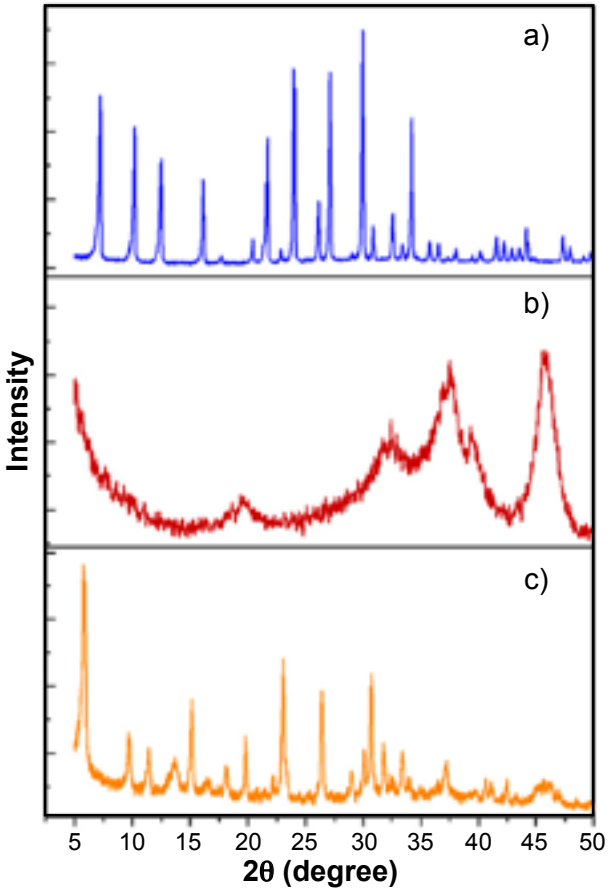

Figure 4: XRD patterns of: a) NaA zeolite (powder); b) gamma-alumina; and c) composite membrane.
[Figura 4: Padrões de DRX de: a) zeólita NaA (pó); b) gama-alumina; e c) membrana compósita.]

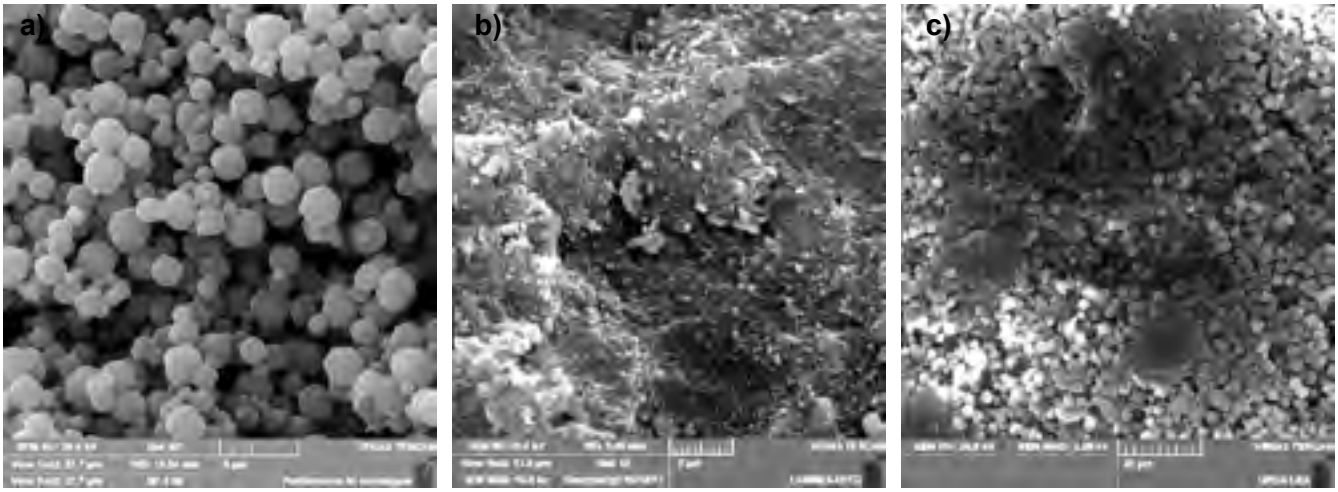

Figure 5: SEM images of: a) NaA zeolite (powder); b) ceramic membrane; and c) composite membrane.
[Figura 5: Imagens de MEV de: a) zeólita NaA (pó); b) membrana cerâmica; e c) membrana compósita.]

uniformly, besides having flat faces, with intergrowth of cubic crystals, which are characteristics of the NaA zeolite structure [51]. The micrograph in Fig. 5b (ceramic membrane sintered at 700 °C) clearly shows that there were no cracks. It was seen that the obtained gamma-alumina exhibited the plate-like morphology, many plates overlapped and interconnected with each other, and had some residual pores with different sizes [51]. The reason that led to this phenomenon suggests that pore structures were occupied by water during the sintering process. In the SEM image of Fig. 5c, it can be seen two distinct crystals as the constituents of the composite membrane structure: NaA zeolite and gamma-alumina.

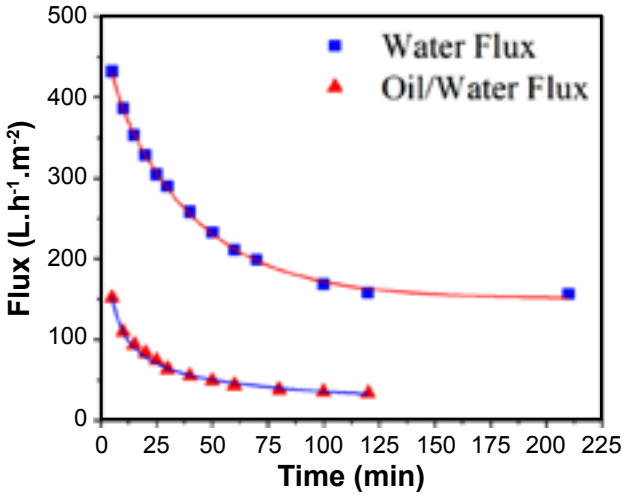

Figure 6: Pure water flux measurements and removal of oil-water emulsion as a function of time for the composite membrane. Experimental conditions were 2.0 bar, 25 °C, running time = 210 and 120 min, pH oil-water emulsion = 6.
[Figura 6: Medições de fluxo de água pura e remoção da emulsão óleo/água em função do tempo para a membrana compósita. As condições experimentais foram 2,0 bar, 25 ° C, tempo de execução = 210 e 120 min, pH da emulsão = 6.]

Pure water flux measurements and separation experiments of oil-in-water emulsion: pure water permeation experiments are one of the essential procedures for determining the structure of prepared membranes. Pure water flux is affected by the membrane structure (porosity) and afterward by preparation variables [9]. The water flux through the composite membrane was evaluated using pure water as a permeate. Fig. 6 also illustrates the flux as a function of time obtained using water-oil emulsion for the composite membrane. A typical flux-time curve of microfiltration was observed. It was seen that the flux decreased after the deposition of the top layer. This result was expected and was attributed to the addition of NaA zeolite to the gamma-alumina. This may be related to the characteristics of NaA zeolite (porosity, pore size

Table IV - Results of microfiltration of inorganic membranes used for oil-water emulsion separation.
[Tabela IV - Resultados de microfiltração de membranas inorgânicas utilizadas para separação de emulsão óleo-água.]

Membrane[#]	Operational parameters	Parameters	Flux ($L.m^{-2}.h^{-1}$)	Rejection efficiency (%)	Ref.
NaA/gamma-alumina	2.0 bar, 25 ºC	Synthetic oil wastewater, C_f=100 $mg.L^{-1}$, C_p=2.2 $mg.L^{-1}$	150	97.8	This study
ZSM-5/gamma-alumina	Atmospheric pressure, 25 ºC	Wastewater, C_f=600 $mg.L^{-1}$	264	91.3	[30]

[#] - *both membranes were prepared by the mechanical mixing method*

distribution, and hydrophilicity), which is characterized as small-pore zeolite with a cubic structure. This zeolite is highly hydrophilic and has a low Si/Al ratio [52]. Also, it was noted that the composite membrane had a flux of 450 $L.h^{-1}.m^{-2}$ at 2 bar. Physical properties such as pore size and its distribution throughout the membrane are key to separation performance [53]. Particle size distribution is a significant material characteristic in the preparation of an asymmetric membrane because it is precisely associated with porosity and pore size [54]. Zeolite NaA is widely used to separate polar from non-polar molecules by permeation because it is extremely hydrophilic due to its low Si/Al ratio. Due to its hydrophilic nature and relative ease of preparation, the NaA zeolite membrane is of special interest for the selective separation of hydrophilic/hydrophobic liquid mixtures [24].

The permeate volume was measured continuously during the process using the composite membrane. The membrane was used to separate contaminated water (100 $mg.L^{-1}$ theoretical). As shown in Fig. 6, the performed tests indicated a gradual decline of the oil concentration in the feed, similar to what has been noted in the literature [30]. This showed that the flux of the oil/water emulsion through the membrane became lower in the course of time. This decrease in flux through the membrane is observed in the literature because the particles of oil are deposited on the membrane surface or in its pores. This problem can be solved with frequent cleaning or can be reduced depending on the type of pretreatment used for the residue [30, 55]. Under these conditions, the pressure exerted upon the oil droplets is considerably higher than the repelling force of the hydrophilic surface. The oil droplets penetrate through the ceramic membrane pores by deformation, resulting in an increase in the oil concentration in the filtrate.

Based on the oil separation test, the composite membrane was efficient, removing up to 97.8% of the oil. Similar results were found in [30], using zeolite ZSM-5/gamma-alumina membranes and evaluating them for oil/water separation, under the same conditions, except for the atmospheric pressure and the ZSM-5 zeolite utilized. The oil/water removal using this composite membrane showed high oil retention (91.3%). However, it was noted that the composite NaA/gamma-alumina membrane (present study) removed more than the composite ZSM-5/gamma-alumina membrane [30]. This fact can be explained by two factors: i) different zeolite structures; and ii) different pressure. Results of the performance of other inorganic microfiltration membranes used for the oil-water emulsion separation are shown in Table IV. In comparison with the results found in the literature, the results of the composite membrane produced in this study were satisfactory [30]. Since the technique used to obtain the composite membrane was the mechanical mixing of two materials (NaA zeolite and gamma-alumina), the membrane thickness was very large. This fact may explain the low water flow (150 $L.m^{-2}.h^{-1}$).

CONCLUSIONS

The effect of the insertion of the NaA zeolite to gamma-alumina membrane was investigated, determining permeate flux and oil removal efficiency. The performance of the membrane for the separation of the oil-in-water emulsion was excellent. The permeate concentrations were less than that allowed for the disposal according to the specifications of the Brazilian legislation, CONAMA/2007, which determines the maximum oil content in the water for disposal of 29 mg/L.

ACKNOWLEDGMENT

The authors gratefully acknowledge CAPES (Coordenação de Aperfeiçoamento de Pessoal de Nível Superior).

REFERENCES

[1] A. Al-Futaisi, A. Jamrah, B. Yaghi, R. Taha, J. Hazard. Mater. **141** (2007) 557.
[2] G. Chen, G. He, Sep. Purif. Technol. **31** (2003) 83.
[3] A. Fakhru'l-Razi, A. Pendashteh, L.C. Abdullah, D.R.A. Biak, S.S. Madaeni, Z.Z. Abidin, J. Hazard. Mater. **170** (2009) 530.
[4] M. Reed, S. Johnsen (Eds.), "Produced water 2: environmental issues and mitigation technologies", Plenum Publ., New York (1996).
[5] R. Sandarea, "Comprehensive assessment of world crude oil supply through 2030", Penn En. Res. Center, Oklahoma (2012).
[6] B.R. Hansen, S.R. Davies, Chem. Eng. Res. Des. **72** (1994) 176.
[7] K.S. Ashaghi, M. Ebrahimi, P. Czermak, Open Environ. Sci. **1** (2007) 1.
[8] B.H. Diya'uddeen, W.M.A.W. Daud, A.R.A. Aziz, Process Saf. Environ. Prot. **89** (2011) 95.
[9] H.P. Hsieh, *Inorganic membranes for separation and reaction* **3**, Elsevier Sci., Amsterdam (1996).
[10] A.J. Burggraaf, L. Cot (Eds.), "Fundamentals of inorganic membrane science and technology" **4**, Elsevier Sci., Amsterdam (1996).
[11] L. Cot, A. Ayral, J. Durand, C. Guizard, N. Hovnanian, A. Julbe, A. Larbot, Solid State Sci. **2** (2000) 313.
[12] S.P. Nunes, Membr. Sci. Technol. **13** (2008) 121.
[13] A. Basile, C. Charcosset, *Integrated membrane systems and processes*, John Wiley Sons (2016).
[14] S.M. Auerbach, K.A. Carrado, P.K. Dutta (Eds.), "Handbook of zeolite science and tecnology", Marcel Dekker, New York (2003).
[15] A. Julbe, Stud. Surf. Sci. Catal. **168** (2007) 181.
[16] J. Caro, M. Noack, P. Kölsch, R. Schäfer, Micropor. Mesopor. Mater. **38** (2000) 3.
[17] J. Caro, M. Noack, Micropor. Mesopor. Mater. **115** (2008) 215.
[18] J. Caro, M. Noack, in "Advances in nanoporous

materials" **1**, S. Ernst (Ed.), Elsevier (2010) 1.
[19] J. Gascon, F. Kapteijn, B. Zornoza, V. Sebastián, C. Casado, J. Coronas, Chem. Mater. **24** (2012) 2829.
[20] Y.S. Lin, M.C. Duke, Curr. Opin. Chem. Engin. **2** (2013) 209.
[21] C. Perego, R. Bagatin, M. Tagliabue, R. Vignola, Micropor. Mesopor. Mater. **166** (2013) 37.
[22] J. Caro, in "Zeolites and zeolite-like materials", B.F. Sels, L.M. Kustov (Eds.), Elsevier, Amsterdan (2016) 283.
[23] N. Kosinov, J. Gascon, F. Kapteijn, E.J.M. Hensen, J. Membr. Sci. **499** (2016) 65.
[24] T.C. Bowen, R.D. Noble, J.L. Falconer, J. Membrane Sci. **245** (2004) 1.
[25] D.W. Breck, W.G. Eversole, R.M. Milton, T.B. Reed, T.L. Thom, J. Am. Chem. Soc. **78** (1956) 5963.
[26] J. Cui, X. Zhang, H. Liu, S. Liu, K.L. Yeung, J. Membr. Sci. **325** (2008) 420.
[27] A.P. Araújo, V.J. Silva, A.C. Crispim, R.R. Menezes, M.G.F. Rodrigues, Mater. Sci. Forum **660-661** (2010) 1058.
[28] A.P. Araújo, M.G.F. Rodrigues, Av. Cien. Ing. **3** (2012) 51.
[29] A.S. Barbosa, A.S. Barbosa, M.G.F. Rodrigues, 11th Int. Conf. Catal. Membr. React., Porto (2013).
[30] J.R. Scheibler, E.R.F. Santos, A.S. Barbosa, M.G.F. Rodrigues, Desalin. Water Treat. **26** (2015) 3561.
[31] A.S. Barbosa, A.S. Barbosa, M.G.F. Rodrigues, Mater. Sci. Forum **805** (2014) 272.
[32] A.S. Barbosa, A.S. Barbosa, M.G.F. Rodrigues, Desalin. Water Treat. **56** (2015) 3665.
[33] F.M.N. Silva, T.L.A. Barbosa, M.G.F. Rodrigues, 12th Int. Conf. Catal. Membr. React., Szczecin (2015).
[34] F.M.N. Silva, E. G. Lima, T.L.A. Barbosa, M.G.F. Rodrigues, 13th Int. Conf. Catal. Membr. React., Houston (2017).
[35] R.S. Souza Cunha, J.D. Mota, M.F. Mota, M.G.F. Rodrigues, F. Machado, Mater. Sci. Forum **912** (2018) 263.
[36] A.S. Barbosa, A.S. Barbosa, T.L.A. Barbosa, M.G.F. Rodrigues, 13th Int. Conf. Catal. Membr. React., Houston (2017).
[37] A.S. Barbosa, A.S. Barbosa, M.G.F. Rodrigues, Mater. Sci. Forum **912** (2018) 12.
[38] A.S. Barbosa, A.S. Barbosa, T.L.A. Barbosa, M.G.F. Rodrigues, Sep. Purif. Technol. **200** (2018) 141.
[39] A.S. Barbosa, A.S. Barbosa, M.G.F. Rodrigues, Mater. Sci. Forum **958** (2019) 23.
[40] Y. Zhan, S. He, X. Wan, S. Zhao, Y. Bai, J. Membr. Sci. **567** (2018) 76.
[41] X. Yang, Y. He, G. Zeng, X. Chen, H. Shi, D. Qing, F. Li, Q. Chen, Chem. Eng. J. **321** (2017) 245.
[42] R.W. Thompson, M.J. Huber, J. Cryst. Growth **56** (1982) 711.
[43] E. Jakobs, W.J. Koros, J. Membr. Sci. **124** (1997) 149.
[44] ISO 4003, "Permeable sintered metal materials: determination of bubble test pore size" (1977).
[45] S.B. Henderson, S.J.W. Grigson, P. Johnson, B.D. Roddie, Mar. Pollut. Bull. **38** (1999) 1141.
[46] G. Busca, in "Advances in catalysis" **57**, F.C. Jentoft (Ed.), Elsevier, Amsterdan (2014) 319.
[47] S.J. Gregg, K.S.W. Sing, *Adsorption, surface area and porosity*, 2nd ed., Academic Press, New York (1982).
[48] H. Zhu, D.J. Jones, J. Zajac, R. Dutartre, M. Rhomari, J. Rozière, Chem. Mater. **14** (2002) 4886.
[49] M. Kazemimoghadam, Desalination **251** (2010) 176.
[50] L. Xing-Dong, W. Yi-Pin, C. Xue-Mim, H. Yan, M. Jin, Powder Technol. **243** (2013) 184.
[51] P.A. Badkar, J.E. Bailey, J. Mater. Sci. **11** (1976) 1794.
[52] W. Zhu, L. Gora, A.W.C. Van den Berg, F. Kapteijn, J.C. Jansen, J.A. Moulijn, J. Membr. Sci. **253** (2005) 57.
[53] F. Li, Y. Yang, Y. Fan, W. Xing, Y. Wang, J. Membr. Sci. **397-398** (2012) 17.
[54] L. De Angelis, M.M.F. Cortalezzi, Sep. Purif. Technol. **118** (2013) 762.
[55] S. Rezaei, M.R. Abadi, M.R. Sebzari, M. Hemati, F. Rekabdar, T. Mohammadi, Desalination **265** (2011) 222.
(Rec. 25/06/2019, Rev. 08/10/2019, 21/11/2019, Ac. 24/11/2019)

BY-NC

Effect of temperature on the photocatalytic properties of TiO_2-CeO_2 multilayer thin films obtained by spin coating method

(Efeito da temperatura nas propriedades fotocatalíticas de filmes finos multicamadas de TiO_2-CeO_2 obtidos por spin coating)

T. B. O. Nunes[1], N. F. Andrade Neto[1*], L. M. P. Garcia[1], R. M. Nascimento[1], M. R. D. Bomio[1], F. V. Motta[1]
[1]Federal University of Rio Grande do Norte, Department of Materials Engineering, Laboratory of Chemical Synthesis of Materials, P.O. Box 1524, Natal, RN, Brazil

Abstract

TiO_2-CeO_2 multilayer thin films were deposited by the spin coating method and calcined at 500 and 700 °C. Thin films were characterized by X-ray diffraction (XRD), field emission scanning electron microscopy (FE-SEM), atomic force microscopy (AFM), and diffuse reflectance spectroscopy. Photocatalytic properties were estimated by varying the concentration of the methylene blue dye (MB) when illuminated by UV radiation. The XRD patterns showed that the temperatures of 500 and 700 °C were effective to obtain TiO_2 and CeO_2 phases. The difference in the homogeneity of TiO_2 and CeO_2 films was evident in the AFM images, where the films showed an average roughness of 2.0 and 5.3 nm, respectively. The CeO_2-TiO_2 thin film obtained at 700 °C showed the best photocatalytic activity, reducing the concentration of MB by approximately 80%, while the CeO_2 and TiO_2 films obtained at 700 °C reduced only 20% and 29%, respectively. The reuse test showed that the thin films maintained their photocatalytic activity after 4 cycles, and there was no need for thermal treatment, indicating that it is an immobilized photocatalyst with high efficiency in the degradation of organic dyes.
Keywords: spin coating, multilayer thin films, CeO_2-TiO_2, photocatalytic reuse.

Resumo

Filmes finos multicamadas de TiO_2-CeO_2 foram depositados pelo método de spin coating e calcinados a 500 e 700 °C. Os filmes finos foram caracterizados por difração de raios-X (DRX), microscopia eletrônica de varredura por emissão de campo (MEV-FEG), microscopia de força atômica (MFA) e espectroscopia de reflectância difusa. As propriedades fotocatalíticas foram estimadas variando a concentração do corante azul de metileno (AM) quando iluminado por radiação UV. Os padrões de DRX mostraram que as temperaturas de 500 e 700 °C foram efetivas para obter as fases de TiO_2 e CeO_2. A diferença na homogeneidade dos filmes de TiO_2 e CeO_2 foi evidente nas imagens de MFA, onde os filmes apresentaram rugosidade média de 2,0 e 5,3 nm, respectivamente. Filme fino de TiO_2-CeO_2 obtido a 700 °C apresentou a melhor atividade fotocatalítica, reduzindo a concentração de AM em aproximadamente 80%, enquanto os filmes de CeO_2 e TiO_2 obtidos a 700 °C reduziram apenas 20% e 29%, respectivamente. O teste de reutilização mostrou que os filmes finos mantiveram sua atividade após 4 ciclos, não havendo necessidade de tratamento térmico, indicando ser um fotocatalisador imobilizado com alta eficiência na degradação do corante orgânico.
***Palavras-chave**: spin coating, filmes finos multicamadas, CeO_2-TiO_2, reuso fotocatalítico.*

INTRODUCTION

The combination of different materials to optimize their properties has been extensively studied [1]. The interaction among different ions promotes synergy effects, generating properties not found by the isolated phases. These materials can be obtained as particulate materials (core-shell or composites) and thin films when deposited on alternating layers [2, 3]. The use of thin films stands out in comparison to particulate materials because they do not generate residues after being treated, and they are easy to be reused [4]. Thin films can be obtained by various methods, such as atomic layer positioning [5], dip-coating [6], spin coating [7], and spray-pyrolysis [8].

The spin coating method is widely used because it is easy to use, has low-cost, and produces uniform films [9]. Due to these characteristics, the spin coating is used for the deposition of thin films of various materials in photocatalytic applications. Oxide materials, such as TiO_2 and CeO_2, are widely studied for photocatalysis because they have high chemical stability and the ability to degrade organic dyes [10, 11]. Besides, CeO_2 is also well studied for oxygen storage and mobility because of the easy conversion between the Ce^{3+} in Ce^{4+} oxidation states [12]. The synthesis of TiO_2 and CeO_2 multilayer films makes possible the

**netoandrade@ufrn.edu.br*
https://orcid.org/0000-0003-1421-2904

improvement of the properties of the isolated oxides, where CeO_2 acts to increase the chemical stability and reduce the rate of recombination of the charge carriers through the heterojunctions formed [13, 14]. Yi et al. [15] synthesized CeO_2-Bi_2MoO_6 heterostructures by hydrothermal method, obtaining superior optical properties than that obtained for the isolated materials. Cano-Franco et al. [16] showed that the TiO_2-CeO_2 combination shifts the absorption band to the visible region, reducing the energy required for the excitation of the electrons in the valence band to the conduction band.

In this study, TiO_2 and CeO_2 multilayer thin films were obtained by the spin coating method and calcined at 500 and 700 °C. The thin films were characterized by X-ray diffraction, field emission scanning electron microscopy, atomic force microscopy, and diffuse reflectance spectroscopy. The activity of TiO_2 and CeO_2 multilayer thin films was analyzed in comparison to the pure oxide films by the variation in the concentration of the methylene blue dye when illuminated by UV radiation. The photocatalytic reuse of the thin films was investigated by 4 consecutive cycles, drying the films in the air after each cycle.

MATERIALS AND METHODS

Cerium nitrate (Sigma Aldrich, 99%), titanium isopropoxide (Sigma Aldrich, 97%), citric acid (Synth, 99.5%), ethylene glycol (Synth, 99.5%), and deionized water were used to obtain the polymer resins by polymeric precursor method (PPM). For the PPM method, cerium nitrate was dissolved in water, and isopropoxide was dissolved in isopropyl alcohol; the solutions were kept under stirring at 60 °C. After full dissolution, citric acid was used to form the metal citrate. Finally, ethylene glycol was added, and the resin was stirred until the viscosity reached 25 cps. The resins were deposited on (100) silicon substrates. The cleaning of the substrates was divided into two steps. First, the substrates were washed with water and neutral soap; then, they were kept in an ultrasonic bath for 15 min in isopropyl alcohol and 15 min in deionized water. In the second step, the substrates were immersed in a solution of deionized water, ammonium hydroxide, and hydrogen peroxide maintained at 70 °C for 15 min. Drying occurred at room temperature. The resins were deposited by the spin coating method, with a rotation speed of 7000 rpm for 20 s. Then, the resin was calcined at two temperatures, 500 and 700 °C, to obtain the thin film layer. The process was repeated to obtain a thin film composed of 4 layers. The multilayer films were obtained with the CeO_2 and TiO_2 in intercalated layers, varying the oxide that remained on the first layer. Fig. 1 illustrates the multilayer thin film-forming model.

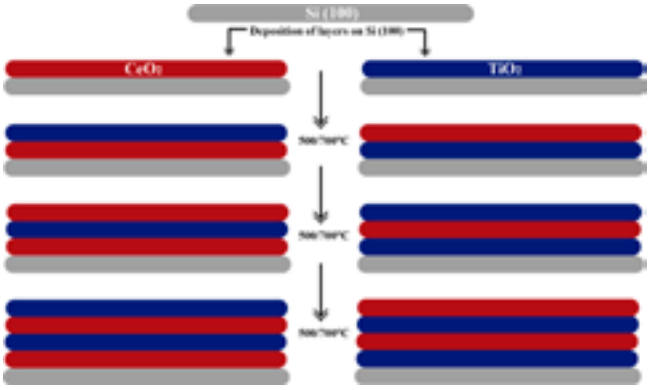

Figure 1: Scheme for the formation of TiO_2-CeO_2 multilayer thin films.
[Figura 1: Esquema para a formação dos filmes finos multicamadas de TiO_2-CeO_2.]

Thin films were characterized by X-ray diffraction (XRD) at low angles with a diffractometer (Shimadzu, XRD-6000) using CuKα radiation (1.5418 Å). Field emission scanning electron microscopy (FE-SEM) was used to observe the surface and cross-section of the thin films. The film thickness was determined using ImageJ software [17]. Atomic force microscopy (AFM) was performed with a microscope (Shimadzu, SPM-9700) to obtain information about the surface roughness of thin films. UV-visible spectroscopy was performed with a spectrophotometer (Shimadzu, UV-2550) in the diffuse reflectance mode, with wavelength ranging from 200 to 900 nm. Kubelka-Munk [18] function was used to convert reflectance data in absorption, and Wood and Tauc equation [19] was applied based on the direct permissible transition (k=1/2). The linear portion of the curve was extrapolated to y-axis=0 to estimate the band gap (E_{gap}). The photocatalytic activity of the thin films was estimated by the variation of the concentration of the methylene blue dye (MB) by the test time when the samples were submitted to UV radiation. Thin films with 6x6 mm were placed in contact with 10 mL of 10^{-5} mol.L^{-1} methylene blue dye ($C_{16}H_{18}ClN_3S$, Mallinckrodt, 99.5% purity). At 30 min intervals, an aliquot was withdrawn to analyze the variation of the dye absorption band. After the first test, the film was washed and dried in the air; after drying, it was again placed in contact with the MB to carry out the subsequent cycle. This reuse process was repeated 3 times, resulting in 4 test cycles.

RESULTS AND DISCUSSION

Fig. 2 shows the XRD patterns obtained for the multilayer thin films. The CeO_2 characteristic peaks were characterized by the ICSD 88759 file of the cerianite phase (cubic system and spatial group Fm-3m). The characteristic peaks of TiO_2 were characterized by the ICSD 24276 file of the anatase phase (tetragonal system and spatial group l41/amd). In Fig. 2, it can be seen that the temperatures of 500 and 700 °C were effective in obtaining CeO_2 and TiO_2 thin films without the formation of secondary phases. The Scherrer equation [20], which relates the width of an XRD peak (full width at half maximum - FWHM) to the crystallite size, was used to investigate the effect of temperature on the peak width. For this, the most intense peak of each phase was used, which was (101) and (111) for TiO_2 and CeO_2, respectively. Table I presents the crystallite size values obtained by the Scherrer equation. The energy provided by the increase in the

calcination temperature favored the growth of crystallites, as observed by the increase in the sharpness and intensity of the diffraction peaks [18]. Higher energy in the system, due to the calcination temperature, caused the particles to increase in size to reduce the total energy related to the particle's surface area [21]. A similar result was shown in another study [22], in which a higher annealing temperature generated thin films with larger crystallite size and crystallinity. According to Table I, the reduction in the microstrain of the unit cells was observed as the calcination temperature increased, due to the relaxation promoted by the higher energy supplied to the system.

Fig. 3 shows the micrographs obtained by FE-SEM for multilayer thin films calcined at 500 and 700 °C. It was noticed that when the upper layer was formed by TiO_2, the films presented a regular morphology and low porosity. The films had a higher porosity when CeO_2 was used as the top layer. It was also verified that as TiO_2 had a smaller particle size than CeO_2, it generated denser films. The thickness values in Table I were consistent with the results of the XRD patterns, where the increase in temperature generated larger grains, which consequently generated thicker films. Singh et al. [23] obtained thin films of TiO_2 by sputtering and calcination at 600 °C and observed that the thicker films provided higher densification due to their smaller average grain size, a fact opposite to that observed in this study, in which the thicker films had larger grains. EDX analysis (energy-dispersive spectroscopy coupled to SEM) was performed in the TiO_2-CeO_2 and CeO_2-TiO_2 thin films calcined at 700 °C and the results are shown in Fig. 4. According to the chemical dot mapping, the TiO_2-CeO_2 film presented more CeO_2 at the surface. The opposite holds for the CeO_2-TiO_2 film, which presented more TiO_2 near the surface.

AFM was performed to obtain more information about the surface of the thin films. Fig. 5 shows the 3D micrographs obtained by AFM for TiO_2-CeO_2 (Figs. 5a and 5b) and CeO_2-TiO_2 (Figs. 5c and 5d) multilayer thin films obtained at 500 and 700 °C. As can be seen, an increase in the temperature provided the growth of grains on the film surface. The growth of grains changed the roughness of the films. According to the roughness values presented in Table I, it was observed that the CeO_2 thin films exhibited greater roughness than that of TiO_2, as well as when CeO_2 was in the upper layer. It is expected that the films formed by smaller grains have lower surface roughness [24].

The band gap (E_{gap}) of the materials is associated with the energy barrier found by the electrons when migrating from the valence band to the conduction band [25]. This value depends on several factors, such as intermediate energy levels between the bands and defects [26]. Wood and Tauc methodology [19] was used to estimate E_{gap} for the thin films obtained. Fig. 6 shows the absorbance curves by

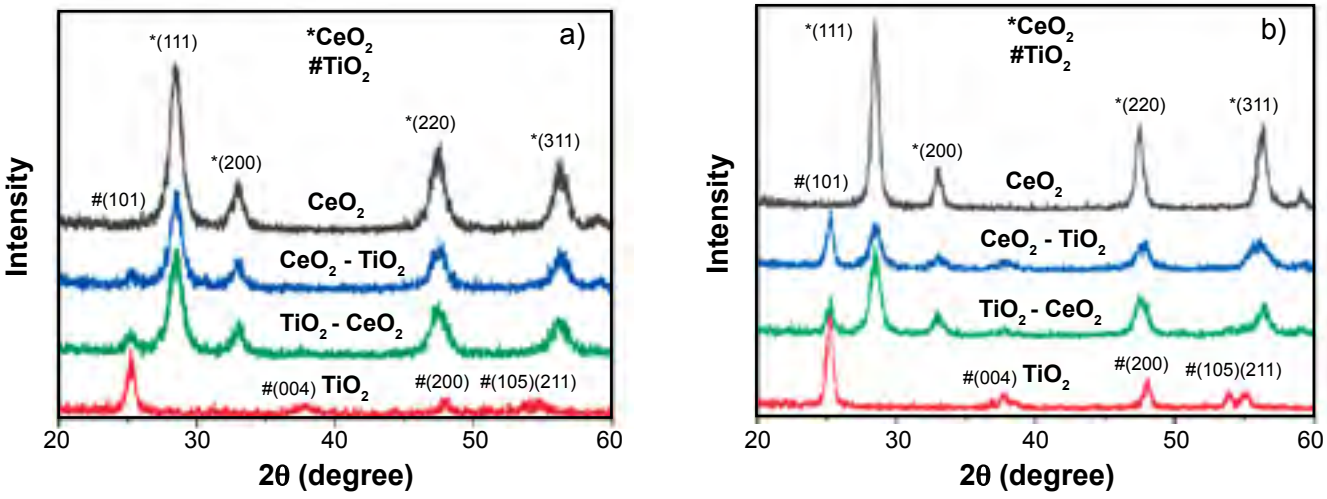

Figure 2: XRD patterns of the thin films obtained at 500 °C (a) and 700 °C (b).
[Figura 2: Difratogramas de raios X dos filmes finos obtidos a 500 °C (a) e 700 °C (b).]

Table I - Crystallite size, thickness, and apparent roughness of the thin films obtained at 500 and 700 °C.
[Tabela I - Tamanho de cristalito, espessura e rugosidade aparente dos filmes finos obtidos em 500 e 700 °C.]

Sample	Crystallite size (nm)		Microstrain (εx10^{-3})		Thickness (nm)		Roughness (nm)	
	500 °C	700 °C	500 °C	700 °C	500 °C	700 °C	500 °C	700 °C
CeO_2	7.7	13.5	1.11	0.63	232.1	239.7	5.26	7.96
CeO_2-TiO_2	8.0	14.8	1.07	0.53	177.8	241.6	3.17	4.89
TiO_2-CeO_2	8.8	14.5	1.01	0.57	193.7	241.0	3.83	6.47
TiO_2	10.9	15.2	0.86	0.41	194.2	240.3	2.01	4.75

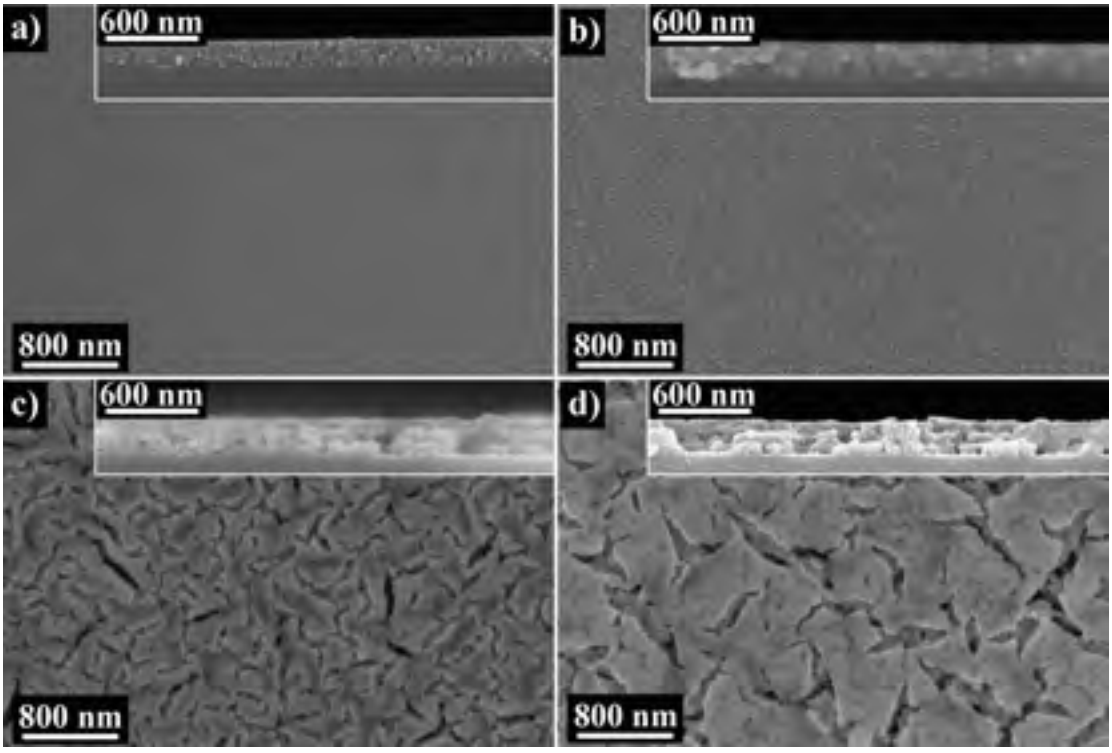

Figure 3: FE-SEM images of the surface and cross-section of the multilayer thin films of CeO_2-TiO_2 (a,b) and TiO_2-CeO_2 (c,d) obtained at 500 °C (a,c) and 700 °C (b,d).
[Figura 3: Imagens de MEV-FEG da superfície e da seção transversal dos filmes finos multicamadas de CeO_2-TiO_2 (a,b) e TiO_2-CeO_2 (c,d) obtidos em 500 °C (a,c) e 700 °C (b,d).]

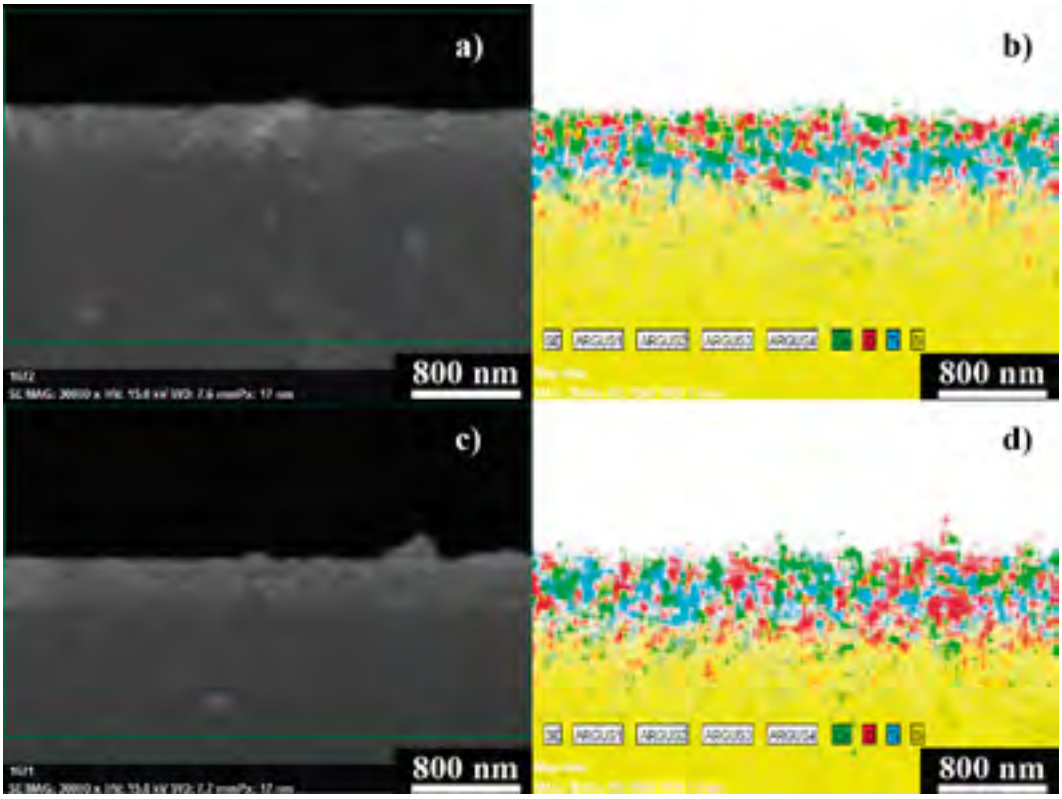

Figure 4: FE-SEM images of the cross-section (a,c) and respective EDX dot maps (b,d) for TiO_2-CeO_2 (a,b) and CeO_2-TiO_2 (c,d) thin films obtained at 700 °C.
[Figura 4: Imagens de MEV-FEG da seção transversal (a,c) e respectivo mapeamento elementar por EDX (b,d) para os filmes finos de TiO_2-CeO_2 (a,b) e CeO_2-TiO_2 (c,d) obtidos em 700 °C.]

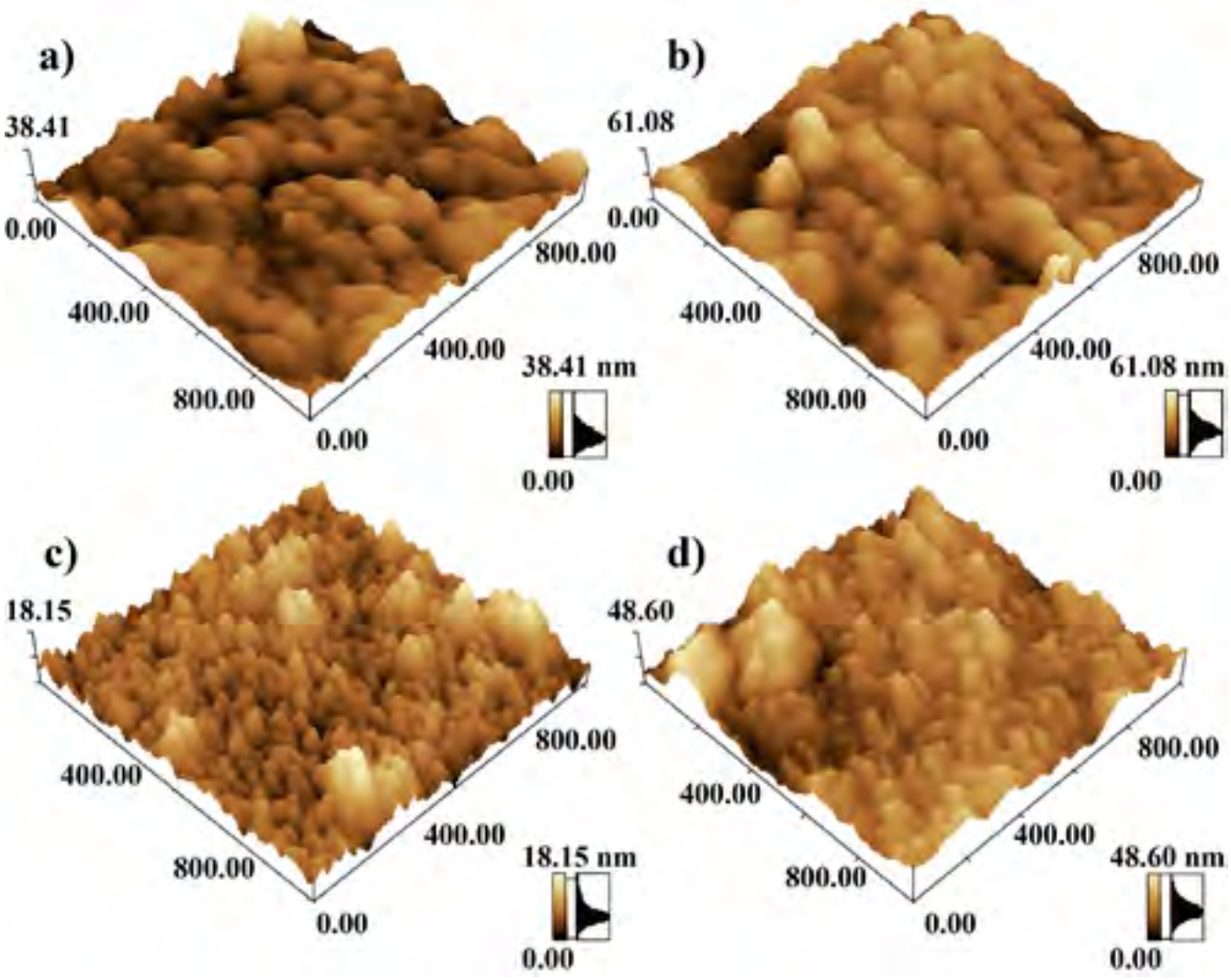

Figure 5: 3D micrographs obtained by atomic force microscopy for TiO_2-CeO_2 (a,b) and CeO_2-TiO_2 (c,d) thin films obtained at 500 **°C** (a,c) and 700 °C (b,d).

[Figura 5: Micrografias 3D obtidas por microscopia de força atômica para os filmes finos de TiO_2-CeO_2 (a,b) e CeO_2-TiO_2 (c,d) obtidos em 500 °C (a,c) e 700 °C (b,d).]

photon energy for the multilayer films. Thin films reduced their E_{gap} with increasing crystallization temperature. TiO_2 reduced E_{gap} from 3.00 to 2.77 eV, while CeO_2 reduced from 3.13 to 2.99 eV. The E_{gap} is generally associated with the size of particles, where smaller particles have a larger E_{gap} [27]. According to Fig. 6, the multilayer films did not show significant variation with the order of the layers. The E_{gap} of the multilayer films ranged between 2.90 and 2.98 eV and did not change with the temperature increase. The E_{gap} values obtained for the thin films were in agreement with the literature [28-31].

The photocatalytic activity of the thin films was estimated by the variation of the methylene blue dye (MB) concentration when submitted to UV-vis radiation. Fig. 7 shows the variation of MB concentration by the test time. Before the photocatalytic test, the thin films remained in contact with the dye for 60 min to eliminate possible adsorption effects. Fig. 7a shows the curves for the TiO_2 and CeO_2 thin films obtained at 500 and 700 °C and Fig. 7b shows the curves for multilayer thin films. It was seen that the increase in the crystallization temperature of the thin films from 500 to 700 °C increased the photocatalytic activity (Fig. 7a). For the thin film of TiO_2 calcined at 500 °C, MB concentration after 150 min reduced approximately 4%, while for the film obtained at 700 °C the reduction was approximately 29%. For CeO_2 thin film obtained at 500 °C, the reduction was about 17% of the MB concentration after 150 min, while for the CeO_2 thin film obtained at 700 °C the reduction was approximately 20%. Analyzing the increase in the photocatalytic activity of the films with the increase in calcination temperature, there was a more significant increase for the TiO_2 thin films. The photocatalytic process may be described by a first-order kinetic model with relation to the absorbance of the methylene blue [32], and the results obtained are shown in Figs. 7c and 7d. The graphs showed a linear relationship of $\ln(C/C_0)$ by the irradiation time and Eq.

A was used to determine the kinetic constant (k):

$$\frac{-\ln C_t}{C_o} = k.t \qquad (A)$$

where C_t is the absorbance of methylene blue at time t, C_o the initial absorbance, and t the irradiation time. According to Fig. 7, the kinetic constant (k) increased with increasing calcination temperature, where this increase was more evident for the multilayer films compared to the pure films. The increase in the photocatalytic activity of thin films is directly related to the increase in their surface area [5]. As shown in Table I, the increase in crystallization temperature increased the average surface roughness of the thin films, thus contributing to the increase of their contact area with the MB molecules. The higher photocatalytic activity of the TiO_2 film obtained at 700 °C was in accordance with studies found in the literature, where TiO_2 thin films exhibit better photocatalytic activity than CeO_2 thin films [33-35]. Moreover, as previously seen, the increase of the calcination temperature promoted the relaxation in the TiO_2 and CeO_2 unit cells, promoting a greater generation of oxygen vacancies [36]. Oxygen vacancies, in contact with the MB solution, generate reactive oxygen species (ROS), which have a high oxidative capacity, accelerating decolorization. The increase of the crystallization temperature also favored the photocatalytic activity of the multilayer thin films, as shown in Fig. 7b. CeO_2-TiO_2 and TiO_2-CeO_2 thin films obtained at 700 °C showed high photocatalytic activity after 150 min, where the CeO_2-TiO_2 thin films reduced approximately 80% of the MB concentration and the TiO_2-CeO_2 thin films reduced 65%. CeO_2-TiO_2 multilayers have higher photocatalytic activity and chemical stability for the degradation of organic dyes because the heterojunction formed between the CeO_2 and TiO_2 layers has a higher light absorption range than the single-phase compounds, causing the light to suffer multiple reflections and expand its propagation path, increasing the use of incident light [10, 14]. Obtaining CeO_2 and TiO_2 heterostructures provides the optimization of the properties of the isolated oxides, with higher photocurrent and photoelectric conversion [37]. The

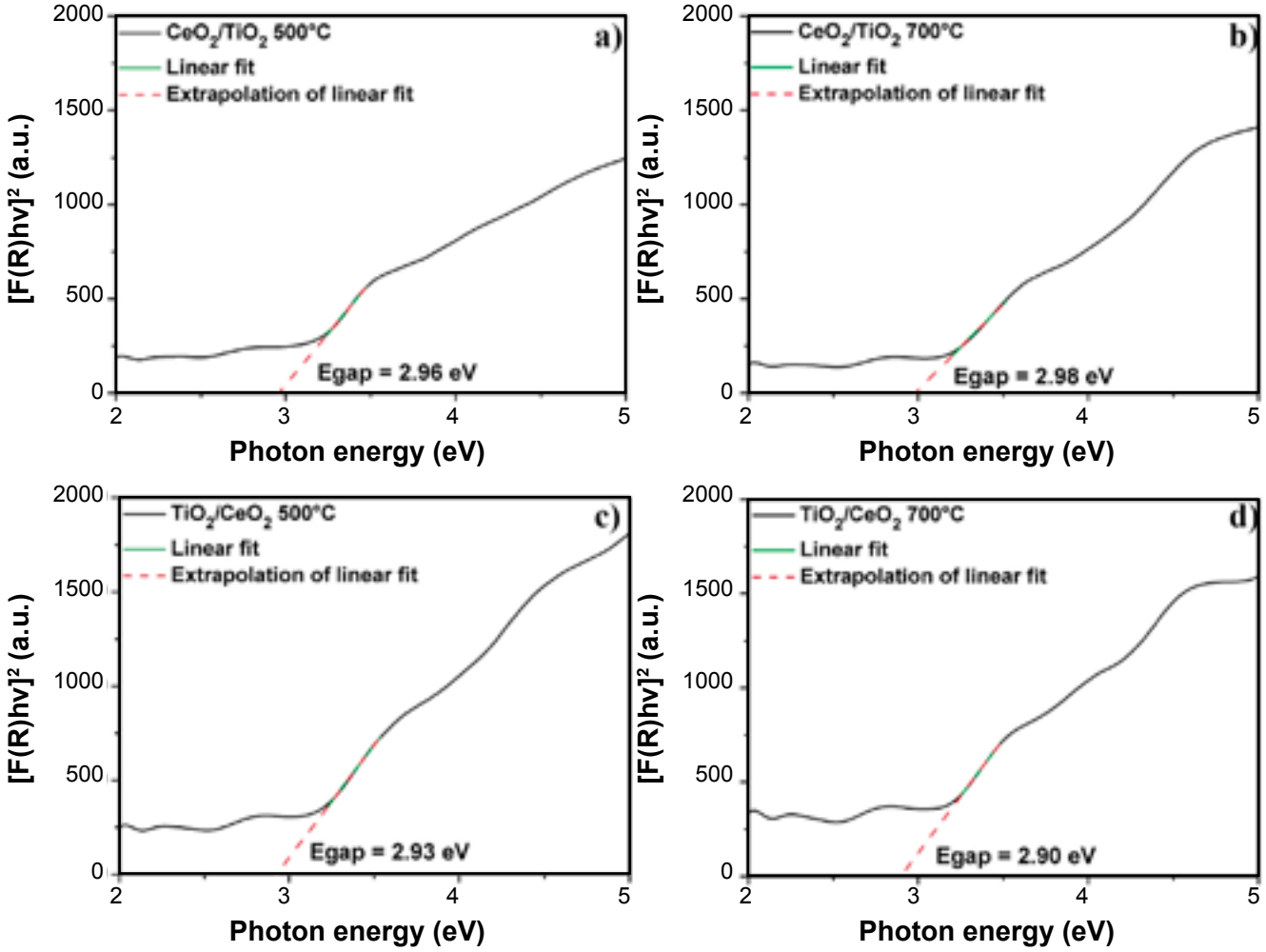

Figure 6: Wood and Tauc plots of CeO_2-TiO_2 (a,b) and TiO_2-CeO_2 (c,d) thin films obtained at 500 **°C** (a,c) and 700 °C (b,d), showing the extrapolation of the linear portion of the curve to estimate E_{gap}.

[Figura 6: Gráficos de Wood e Tauc dos filmes finos multicamadas de CeO_2-TiO_2 (a,b) e TiO_2-CeO_2 (c,d) obtidos em 500 °C (a,c) e 700 °C (b,d), mostrando extrapolação da porção linear da curva para determinação de E_{gap}.]

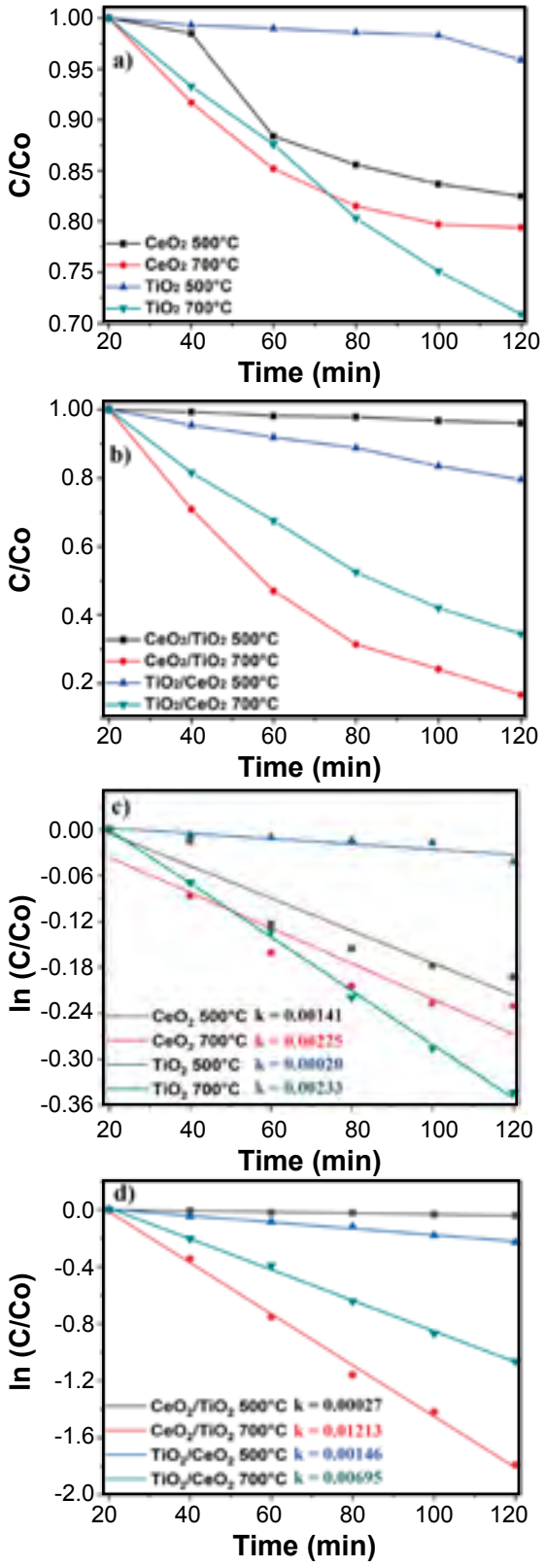

Figure 7: Variation of methylene blue concentration C/C_0 (a,b) and respective linearized plot lnC/C_0 (c,d) with test time for pure (a,c) and multilayer (b,d) thin films obtained by spin coating.

[Figura 7: Variação da concentração de azul de metileno C/C_0 (a,b) e respectivo gráfico linearizado lnC/C_0 (c,d) com o tempo de ensaio para os filmes finos puro (a,c) e multicamadas (b,d) obtidos por spin coating.]

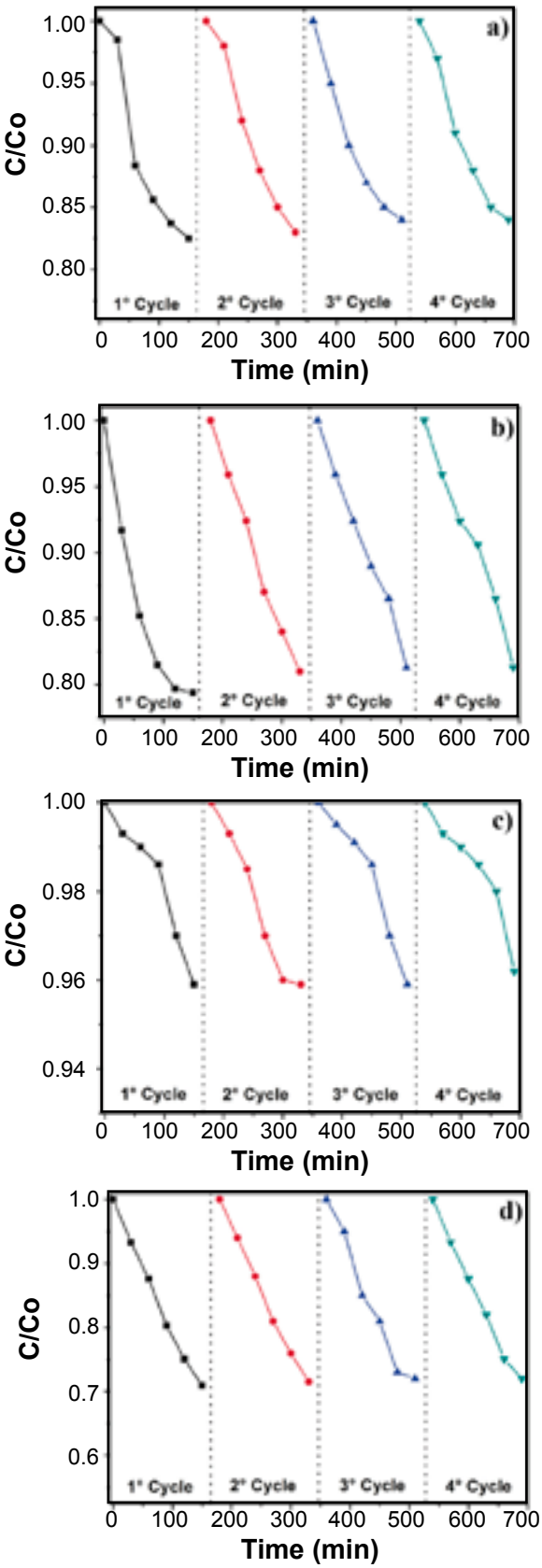

Figure 8: Results of photocatalytic reuse test (4 cycles) for thin films of CeO_2 (a,b) and TiO_2 (c,d) obtained at 500 °C (a,c) and 700 °C (b,d).

[Figura 8: Resultados do ensaio de reuso fotocatalítico (4 ciclos) para filmes finos de CeO_2 (a,b) e TiO_2 (c,d) obtidos em 500 °C (a,c) e 700 °C (b,d).]

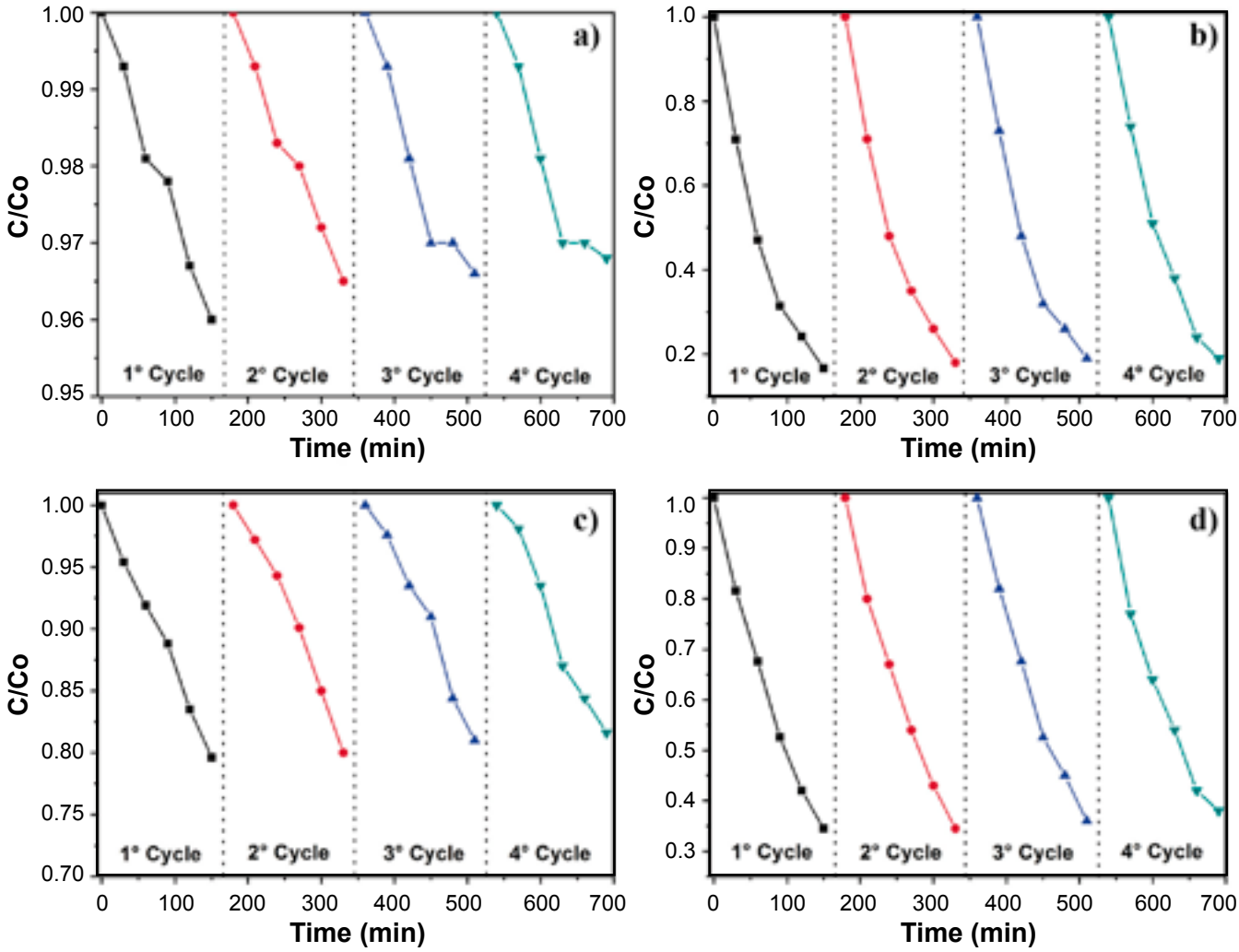

Figure 9: Results of photocatalytic reuse test (4 cycles) for thin films of CeO_2-TiO_2 (a,b) and TiO_2-CeO_2 (c,d) obtained at 500 °C (a,c) and 700 °C (b,d).
[Figura 9: Resultados do ensaio de reuso fotocatalítico (4 ciclos) para filmes finos de CeO_2-TiO_2 (a,b) e TiO_2-CeO_2 (c,d) obtidos em 500 °C (a,c) e 700 °C (b,d).]

photocatalytic results of multilayer films were consistent with those obtained with pure films, where the presence of TiO_2 on the surface promoted better catalytic performance.

The use of thin films as photocatalysts is widely studied due to the non-generation of secondary residues, which would require further treatment, as in the case of materials in powder form [38]. In addition to the high photocatalytic property, the film's ability to be reused is of great importance. The reusability of thin films takes into account their chemical stability and the maintenance of the photocatalytic property with the sequence of cycles to which they are submitted [7]. The reuse capacity of produced thin films in the photocatalytic activity was investigated through the use in 4 cycles, without accomplishing the heat treatment. Figs. 8 and 9 show the reuse curves for single and multilayer thin films. According to the curves shown in Fig. 8, it is observed that the photocatalytic activity of single-phase thin films was maintained, even after the 4 cycles tested. This fact was also observed for multilayer thin films, as shown in Fig. 9. The maintenance of the photocatalytic property after the 4 cycles indicated that the thin films were chemically stable under UV radiation [39].

CONCLUSIONS

The spin coating method proved to be efficient for the deposition of uniform thin films, where TiO_2 film had higher densification than CeO_2 film due to the smaller particle size. Calcination temperatures of 500 and 700 °C were sufficient to obtain pure (TiO_2 or CeO_2) and multilayer (CeO_2-TiO_2 and TiO_2-CeO_2) films without forming secondary phases. Increasing the crystallization temperature caused the growth of crystallite size and film thickness; moreover, it increased the average apparent roughness of the films. The increase in the roughness and porosity of the thin films provided a higher surface area for contact with the dye, providing greater photocatalytic activity. The synergistic effect caused the multilayer films to have superior photocatalytic properties

than the single-phase films, where the multilayer film with the upper layer of TiO_2 reduced approximately 80% of the methylene blue concentration after 150 min of UV radiation; this film is a good candidate to be used in the treatment of textile effluents.

ACKNOWLEDGMENTS

This study was financed in part by the Coordenação de Aperfeiçoamento de Pessoal de Nível Superior - Brasil (CAPES) - Finance Code 001 and the authors give thanks for the financial support of the Brazilian research funding institutions: CNPq No. 307546/2014-4 and CAPES/ PROCAD 2013/2998/2014.

REFERENCES

[1] X. Hou, X. Wang, W. Mi, J. Alloys Compd. **765** (2018) 1127.
[2] H. Miyazaki, T. Matsuura, T. Ota, Compos. Commun. **10** (2018) 136.
[3] L.-Y. Lin, H.-Y. Lin, W.-L. Hong, L.-Y. Lin, Thin Solid Films **7** (2018) 69.
[4] O.K. Echendu, S.Z. Werta, F.B. Dejene, V. Craciun, J. Alloys Compd. **769** (2018) 201.
[5] A. Di Mauro, M.E. Fragalà, V. Privitera, G. Impellizzeri, Mater. Sci. Semicond. Process. **69** (2017) 44.
[6] S.H. Chaki, K.S. Mahato, T.J. Malek, M.P. Deshpande, J. Sci. Adv. Mater. Devices **2** (2017) 215.
[7] L.M.P. Garcia, M.T.S. Tavares, N.F. Andrade Neto, R.M. Nascimento, C.A. Paskocimas, E. Longo, M.R.D. Bomio, F.V. Motta, J. Mater. Sci. Mater. Electron. **29** (2018) 6530.
[8] C. Nefzi, M. Souli, Y. Cuminal, N. Kamoun-Turki, Superlattices Microstruct. **124** (2018) 17.
[9] C. Wang, T. Liu, X. Wang, J. Li, H. Jin, J. Yu, M. Yi, Y. Mo, Sens. Actuators B Chem. **270** (2018) 518.
[10] J. Tian, Y. Sang, Z. Zhao, W. Zhou, D. Wang, X. Kang, H. Liu, J. Wang, S. Chen, H. Cai, H. Huang, Small **9** (2013) 3864.
[11] H. Abdullah, M.R. Khan, M. Pudukudy, Z. Yaakob, N.A. Ismail, J. Rare Earths **33** (2015) 1155.
[12] B. Li, B. Zhang, Q. Guan, S. Chen, P. Ning, Int. J. Hydrog. Energy **43** (2018) 19010.
[13] L. Jing, J. Zhou, J.R. Durrant, J. Tang, D. Liu, H. Fu, Energy Environ. Sci. **5** (2012) 6552.
[14] C. Han, L. Yan, W. Zhao, Z. Liu, Int. J. Hydrog. Energy **42** (2017) 12276.
[15] J. Yi, H. Mo, B. Zhang, J. Song, D. Liu, G. Zhuo, Sep. Purif. Technol. **211** (2019) 474.
[16] J.C. Cano-Franco, M. Álvarez-Láinez, Mater. Sci. Semicond. Process. **90** (2019) 190.
[17] C.A. Schneider, W.S. Rasband, K.W. Eliceiri, Nat. Methods **9** (2012) 671.
[18] N.F. Andrade Neto, Y.G. Oliveira, C.A. Paskocimas, M.R.D. Bomio, F.V. Motta, J. Mater. Sci. Mater. Electron. **29** (2018) 19052.
[19] D.L. Wood, J. Tauc, Phys. Rev. B **5** (1972) 3144.
[20] V.Y. Zenou, S. Bakardjieva, Mater. Charact. **144** (2018) 287.
[21] D. Portnikov, H. Kalman, Powder Technol. **336** (2018) 393.
[22] M. Emami, R. Goodarzi, Optik **171** (2018) 397.
[23] J. Singh, S.A. Khan, J. Shah, R.K. Kotnala, S. Mohapatra, Appl. Surf. Sci. **422** (2017) 953.
[24] P. Kumar, B. Ahmad, F. Chand, K. Asokan, Appl. Surf. Sci. **452** (2018) 217.
[25] F.V. Motta, A.P.A. Marques, J.W.M. Espinosa, P.S. Pizani, E. Longo, J.A. Varela, Curr. Appl. Phys. **10** (2010) 16.
[26] E. Nurfani, M.A.K. Purbayanto, T. Aono, K. Takase, Y. Darma, Opt. Mater. **84** (2018) 453.
[27] S. Rehman, A. Mumtaz, S.K. Hasanain, J. Nanoparticle Res. **13** (2011) 2497.
[28] E. Şilik, S. Pat, S. Özen, R. Mohammadigharehbagh, H.H. Yudar, C. Musaoğlu, Ş. Korkmaz, Thin Solid Films **640** (2017) 27.
[29] M. Kang, S.W. Kim, H.Y. Park, J. Phys. Chem. Solids **123** (2018) 266.
[30] Y. Li, W. Song, J. Liu, Z. Zhao, M. Gao, Y. Wei, Q. Wang, J. Deng, Chem. Eng. J. **330** (2017) 926.
[31] C. Liu, H. Tai, P. Zhang, Z. Yuan, X. Du, G. Xie, Y. Jiang, Sens. Actuators B Chem. **261** (2018) 587.
[32] M.M. Momeni, M. Hakimian, A. Kazempour, Ceram. Int. **41** (2015) 13692.
[33] V. Madhavi, P. Kondaiah, G. Mohan Rao, Appl. Surf. Sci. **436** (2018) 708.
[34] F. Bensouici, M. Bououdina, A.A. Dakhel, R. Tala-Ighil, M. Tounane, A. Iratni, T. Souier, S. Liu, W. Cai, Appl. Surf. Sci. **395** (2017) 110.
[35] P. Singh, K.M.K. Srivatsa, A. Barvat, P. Pal, Curr. Appl. Phys. **16** (2016) 1388.
[36] G.H. Tariq, D.W. Lane, M. Anis-ur-Rehman, Appl. Phys. A **120** (2015) 1407.
[37] Y. Tan, S. Zhang, R. Shi, W. Wang, K. Liang, Int. J. Hydrog. Energy **41** (2016) 5437.
[38] S.-M. Oh, S.-S. Kim, J.E. Lee, T. Ishigaki, D.-W. Park, Thin Solid Films **435** (2003) 252.
[39] K. Dai, Z. Chen, L. Lu, G. Zhu, Z. Liu, Q. Liu, Thin Solid Films **539** (2013) 23.

(Rec. 11/04/2019, Rev. 17/07/2019, 26/11/2019, Ac. 30/11/2019)

BY-NC

Influence of microstructural and morphological properties of raw natural clays on the reactivity of clay brick wastes in a cementitious blend matrix

(Influência das propriedades microestruturais e morfológicas de argilas in natura na reatividade de resíduos de tijolos em uma matriz cimentícia)

A. Schackow[1]*, S. L. Correia[2], C. Effting[1]

[1]State University of Santa Catarina, Center of Technological Sciences, Department of Civil Engineering, Civil Engineering Graduate Program, 89219-710, Joinville, SC, Brazil

[2]State University of Santa Catarina, Center of Technological Sciences, Materials Science and Engineering Graduate Program, 89219-710, Joinville, SC, Brazil

Abstract

The physical, chemical, and mineralogical characteristics of raw clays used in the industries interfere greatly in the production process and final ceramic product. Raw clays from 4 industries in the South of Brazil were characterized by the XRD, XRF, FTIR, DSC, and SEM techniques. In addition, the pozzolanic potential was also verified based on the kaolinite content of the raw samples. The raw clay that presented the highest pozzolanic potential had a quantity of kaolinite of 69.7%. The use of 40% of the brick waste produced with this raw clay (particle size of 75 μm) replacing Portland cement in a mortar resulted in a gain of 51% in compressive strength at 28 days. The analysis of the hydration products resulting from the $Ca(OH)_2$ reaction from the cement hydration with the ceramic waste showed the presence of $Al_2O_3.2SiO_2$ forming the C-S-H gel.

Keywords: raw clay characterization, clay brick waste, clay microstructure, pozzolanic clay, cement hydration product.

Resumo

Características físicas, químicas e mineralógicas das argilas in natura utilizadas nas indústrias interferem no processo produtivo e produto cerâmico final. Foram caracterizadas argilas in natura de 4 indústrias do Sul do Brasil pelas técnicas de DRX, FRX, FTIR, DSC e MEV. Além disso, o potencial pozolânico também foi verificado com base no teor de caulinita das amostras in natura. A argila que apresentou o maior potencial pozolânico teve quantidade de caulinita de 69,7%. O uso de 40% de resíduo de tijolo produzido com esta argila (tamanho de partícula de 75 μm) substituindo cimento Portland em uma argamassa resultou em aumento de 51% na resistência à compressão em 28 dias. A análise dos produtos de hidratação resultantes da reação de $Ca(OH)_2$ da hidratação do cimento com o resíduo cerâmico mostrou a presença de $Al_2O_3.2SiO_2$ formando o gel de C-S-H.

***Palavras-chave**: caracterização de argila, resíduo de tijolo cerâmico, microestrutura de argila, material pozolânico, produto de hidratação do cimento.*

INTRODUCTION

Knowledge of the main characteristics of ceramic raw materials is important during the development and production stages of any ceramic product. Physical and mechanical properties of structural ceramic products depend on the physical, chemical, and mineralogical characteristics of the different kinds of raw materials, which also control the overall processing of the unfired and fired bodies [1, 2]. Some byproducts such as fly ash and ground granulated blast-furnace slag can be used as activators in the unfired clay brick technology and influence the properties of structural ceramic products [3]. During the processing of traditional ceramic products (brick, porcelain, tiles), the raw clays contribute to the plasticity and green strength required at the forming stage. Clay minerals are formed by the decomposition of feldspathic rocks by geological processes. Kaolinite, the most common clay mineral, is a 1:1 sheet silicate composed of alternating layers of $[Si_2O_5]^{2-}$ and $[Al_2(OH)_4]^{2+}$. Kaolinitic clays usually contain kaolinite together with other minerals such as smectite, illite, micas, and 2:1 sheet silicates of variable composition [4-8]. The physical, chemical and mineralogical characteristics of raw clays depend on their geological history and location [9], and there is an increasing need for new studies related to the characterization of raw clays from different locals for traditional ceramic products. Wastes with pozzolanic characteristics such as fly ash, silica fume, sludge, and ceramics [10, 11] have been used as partial replacement

**adilson.schackow@udesc.br*

https://orcid.org/0000-0003-2561-5231

of Portland cement. The use of red ceramic brick waste as cementitious materials has been studied by several authors [12, 13]. The main advantage of this residue is that it has already gone through a firing process (usually between 600 and 900 ºC), which results in metakaolinite in this waste.

This study describes the chemical and mineralogical characterization of 4 clays raw materials mined from different regions of the North of the Santa Catarina State, Brazil, seeking to find new applicability in the ceramic industry and other sectors. There are practically no studies on the clays from this local, and little information has been published about the characteristics of these materials. Furthermore, after determining which raw clay has the greatest pozzolanic potential, an application of this clay (after firing and in the form of ground brick) in a building mortar was tested. It was possible to verify the influence of the properties of the raw clay on the reactivity with $Ca(OH)_2$ from the cement hydration in a mortar.

MATERIALS AND METHODS

Materials: the raw clays used in this study were obtained from different sources after mining, which are used for the production of structural brick at 4 industries located in different cities in the North of Santa Catarina (Brazil): Joinville (industries A and B), Garuva (industry C), and São Bento do Sul (industry D). Table I shows some data related to the production of these companies. Samples of the clayey masses used in these industries were dried in an oven at 100 ºC for 24 h and then milled in a pestle; the material passed through a 75 μm sieve was used for the analyses. The clay brick waste (bricks discarded due to problems with dimensions, incorrect firing, or broken) was milled and sieved with a 75 μm sieve, and then used in mortar and cement paste to verify the pozzolanic activity.

Characterization of raw clays: samples of the raw clays were prepared and characterized by X-ray fluorescence (XRF) spectroscopy, X-ray diffraction (XRD), Fourier-transform infrared (FTIR) spectroscopy, thermal analysis (differential scanning calorimetry - DSC, and thermogravimetry - TG), and scanning electron microscopy (SEM). The qualitative phase composition was determined using an X-ray diffractometer (Shimadzu, XRD 6000) using CuKα radiation, the chemical composition was determined using an XRF spectrometer (Philips, PW 2400), and a Perkin-Elmer (Spectrum One) equipment was used to evaluate the FTIR spectra in the range of 4000-560 cm^{-1}. The microstructures of the raw clays were obtained using a scanning electron microscope (Hitachi, SU-70). The DSC/TG tests were performed using a Netzsch (STA 449 C Jupiter) equipment from 10 to 1300 ºC with a heating rate of 10 ºC.min^{-1} and argon atmosphere.

Mortar preparation and testing: to evaluate the effect of the fired clay (brick waste - BW) in a common application in constructions, mortars without and with 40% of fired brick waste from industry B (BW-B, grain size <75 μm, firing temperature about 800-900 ºC) were tested. The BW-B was chosen because, in the raw form, it presented the highest pozzolanic potential. A previous study [14] showed satisfactory results for 40% substitution, so this content was chosen in this study. The BW-B showed an average particle diameter of 6.04 μm, a BET surface area of 35.16 m^2/g, and the XRD analysis detected only the quartz phase. The proportion of materials used for mortars was, by volume, 1:1.5:6 (cement:lime:sand) commonly used in construction. This proportion was transformed from volume to mass. The cement used was type CPII-Z-32. The preparation of the mortars was carried out according to the NBR 13276 standard [15]. The amount of clay brick waste replacing the cement added to the mixture was calculated relative to the mass of the cement (Table II). The compressive strength test was performed according to the NBR 13279 standard

Table I - Information about the industries that supplied the clayey masses.
[Tabela I - Informações sobre as indústrias que forneceram as massas argilosas.]

Industry	A	B	C	D
Clayey ceramic mass composition	83% clay+17% other raw materials	85% clay+15% other raw materials	30% clay+70% other raw materials	50% clay+50% other raw materials
Annual production of bricks	7 million	1.4 million	2.16 million	3 million
Amount of discarded bricks	1-5% (6000 to 30000 pieces/month)	1% (1200 pieces/month)	5% (9000 pieces/month)	2% (6000 pieces/month)

Table II - Mass of components used to prepare 1.75 L of mortars.
[Tabela II - Massas dos componentes usados para preparação de 1,75 L de argamassas.]

Mortar	Cement (g)	BW 75 μm (g)	Lime (g)	Sand (g)	Water (g)
Reference	157.6	-	163.6	1322.0	394.4
M40BW	86.7	57.8	190.7	1519.3	361.1

[16]. For the analysis of SEM and EDS (energy dispersive spectroscopy), a cementitious matrix without sand (with 40% BW) was prepared to identify the possible hydration products present. The pastes used had the water to cement (w/c) ratio of 0.5.

RESULTS AND DISCUSSION

Chemical and mineralogical characterizations

Fig. 1 shows the XRD patterns of the raw clays A, B, C, and D as obtained after dry milling. The results of the analysis showed, for all samples, the major peaks corresponding to the phases kaolinite [$Al_2Si_2O_5(OH)_4$], halloysite [$Al_2Si_2O_5(OH)_4.2H_2O$], α-quartz (SiO_2), gibbsite [$Al(OH)_3$], and hematite (Fe_2O_3) [17, 18]. A previous study [19] related to the mineralogical characterization of the clays of the Santa Catarina State, Brazil, reported the absence of montmorillonite and the majority presence of kaolinite and halloysite in the samples.

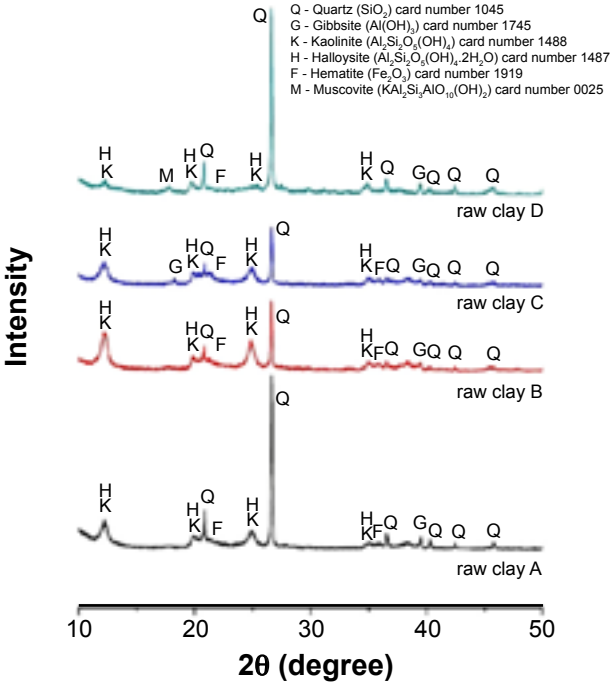

Figure 1: XRD patterns of *in natura* clayey ceramic masses A, B, C, and D.
[Figura 1: Padrões de DRX das massas cerâmicas de argila in natura A, B, C e D.]

Table III shows the chemical composition of samples A, B, C, and D. The results showed the predominance of Al_2O_3 and SiO_2 in all samples. The Al_2O_3 may be primarily associated with the kaolinite and halloysite clay minerals, as well as gibbsite, as observed in XRD patterns. The silica is present in the kaolinite and halloysite, and also associated with the quartz phase and probably feldspar, which was not observed in the XRD pattern. Likewise, the small amount of K_2O in the chemical analysis may indicate the presence of small amounts of illite clay mineral and K-feldspar in all samples, although not seen in XRD patterns. Other studies have reported similar results [20]. The molar ratio of SiO_2/Al_2O_3 was 4.40 for the clay A, which was higher than the theoretical molar ratio (2.00) of kaolinite (or halloysite). Molar ratios higher than the theoretical suggest the presence of quartz and other silicates in the samples [19]. Since the presence of feldspathic minerals was not observed, the results suggested that the clay A contained a large amount of free silica (quartz) as an impurity. As for the clay A, it was observed Al_2O_3 and SiO_2, and also the other components, in clays B, C, and D. The molar ratio of SiO_2/Al_2O_3 was 3.07 for the clay B, similar to the result of 3.03 for the clay C. In the clay D, a higher amount of K_2O (3.59%) was observed compared to the clays A, B, and C, indicating the presence of a small amount of a phase containing this element (illite or K-feldspar, for example), although not seen in XRD pattern. The molar ratio of SiO_2/Al_2O_3 was 4.97 for the clay D, probably due to the high quartz content. Besides qualitative analysis by XRD to identify the mineralogical phases present in the samples, it is important to estimate the

Table III - Chemical composition (% by mass) of raw clays A, B, C, and D.
[Tabela III - Composição química (% em massa) das argilas in natura A, B, C e D.]

Oxide	A	B	C	D
SiO_2	58.53	49.76	47.14	59.67
Al_2O_3	22.54	27.52	26.42	20.34
Fe_2O_3	6.56	7.58	10.33	7.11
TiO_2	1.39	1.69	1.30	0.94
K_2O	0.77	0.88	0.56	3.59
CaO	0.20	0.18	0.17	0.09
MgO	0.54	0.34	0.40	1.03
Na_2O	0.21	0.10	0.11	0.13
P_2O_5	0.10	0.16	0.11	0.13
MnO	0.05	0.05	0.08	0.06
LOI*	9.10	11.74	13.39	6.56

* - *loss on ignition*.

Table IV - Quantification of the phases (% by mass) present in raw clayey ceramic masses.
[Tabela IV - Quantificação de fases (% em massa) presentes nas massas cerâmicas de argila in natura.]

Clay	Kaolinite/ halloysite	Quartz (impurity)	Hematite	Others*
A	57.1	32.0	6.5	4.4
B	69.7	17.3	7.6	5.4
C	66.9	16.1	10.3	6.7
D	51.5	35.7	7.1	5.7

* - *including gibbsite*.

amounts of the phases present. The content was estimated by the stoichiometry of the phases using the results of chemical and mineralogical analysis [21, 22]. The results are shown in Table IV.

In samples that do not contain illite in its composition, the total amount of Al_2O_3 present can be attributed to kaolinite. The ideal composition of kaolinite is 46.5% SiO_2+39.5% Al_2O_3+13.96% H_2O [21]. Assuming that the samples had no illite and that the total amount of Al_2O_3 present in the sample was from kaolinite, it was possible to quantify the total amount of kaolinite in the samples. Likewise, it was possible to quantify the SiO_2 content present in kaolinite of the sample. The amount of quartz as an impurity can be calculated by subtracting the total quantity of silica of the sample from the amount of silica in kaolinite. The excess SiO_2 was attributed to the presence of quartz, as shown by XRD patterns. The contents of kaolinite and quartz as an impurity of all samples, calculated according to the method used in [23], are shown in Table IV. The samples A and D had the highest levels of quartz; sample B had the greatest amount of kaolinite (69.7%) and 17.3% quartz as an impurity, results that were consistent with a SiO_2/Al_2O_3 molar ratio of 3.07. Similar to sample B, sample C showed 66.9% kaolinite and the smallest amount of quartz as an impurity (16.1%). The quantitative estimate of the phases of sample D was 51.5% kaolinite and halloysite, and 35.7% quartz. Materials that exhibit high silica content (generally above 50%) and low amount of alumina (generally less than 25%) are considered 'weak kaolin' [24]; a kaolinite rock is considered when the amount of kaolinite is higher than 50% [25]. Thus, all samples may be considered kaolinite, considering they showed amounts of kaolinite and halloysite higher than 50%. The importance of estimating the kaolinite content in the material is justified by the fact that it affects the pozzolanic activity. The contents of kaolinite+halloysite of the raw clays in Table IV show that clay B had the highest potential to have pozzolanic activity with cement after firing, followed by clays C, A, and D. The presence of hematite in all samples is commonly found in masses of red ceramic. In this way, the amount of about 6.5% of hematite may come from the addition of red mud or is isomorphic substitutions of Fe in the clay structures, such as illite [23], which was not detected by the XRD. The presence of TiO_2 also helps to provide color to the clay.

Fig. 2 shows the FTIR spectra of the 4 raw clays studied. The corresponding vibrations to hydroxyls present in the kaolinite and halloysite were shown in two bands at ~3700 and 3620 cm^{-1}. A difference between kaolinite and halloysite is that kaolinite has two slightly smaller bands between 3669 and 3652 cm^{-1} (Fig. 2b) [26]. Another difference is the shoulder of vibration from the surface hydroxyls of Al_2OH groups at 939 cm^{-1} more prominent in kaolinite than in halloysite [27]. The bands at 3695 and 3622 cm^{-1} corresponded to the OH vibrations related to Al octahedral sheet. In addition, the vibrations of Al-OH bonds were observed at 911 cm^{-1} [28]. The bands at 1002 and 1109 cm^{-1} were associated with the stretching of the Si-O bond. Bands associated with Si-O and Si-O-Si were observed at 1109 and 1027 cm^{-1} [28]. Also, the Si-O-Si asymmetric vibration mode was connected to the band at 1106 cm^{-1} [29]. Bands of Si-O bonds at 791, 743, 693, 539, and 464 cm^{-1} also indicated the presence of quartz [28]. Other features related to kaolinite bands mentioned in the literature [30] are: OH: 3700, 3670, 3650, 3620 cm^{-1}; Al-OH: 913 cm^{-1}; Si-O: 1115, 1032, 1008, 469 cm^{-1}; Si-O-Al_{IV}: 789, 754 cm^{-1}; and Si-O-Al_{VI}: 538 cm^{-1}.

The Fig. 3 shows the most important physical and chemical phenomena according to the results of the thermal analysis (DSC/TG) for raw clays A, B, C, and D. The thermal events were similar for all the samples, with small temperature variations, which are justified by the characteristics of each material (particle size, composition, etc.). The first peak (apparent in Fig. 3 when expanded) up to about 150 ºC corresponded to the loss of adsorbed water [27], with mass loss of 1.27% for clay A, 0.55% for clay B, 1.40% for clay C, and 1.84% for clay D. The second peak

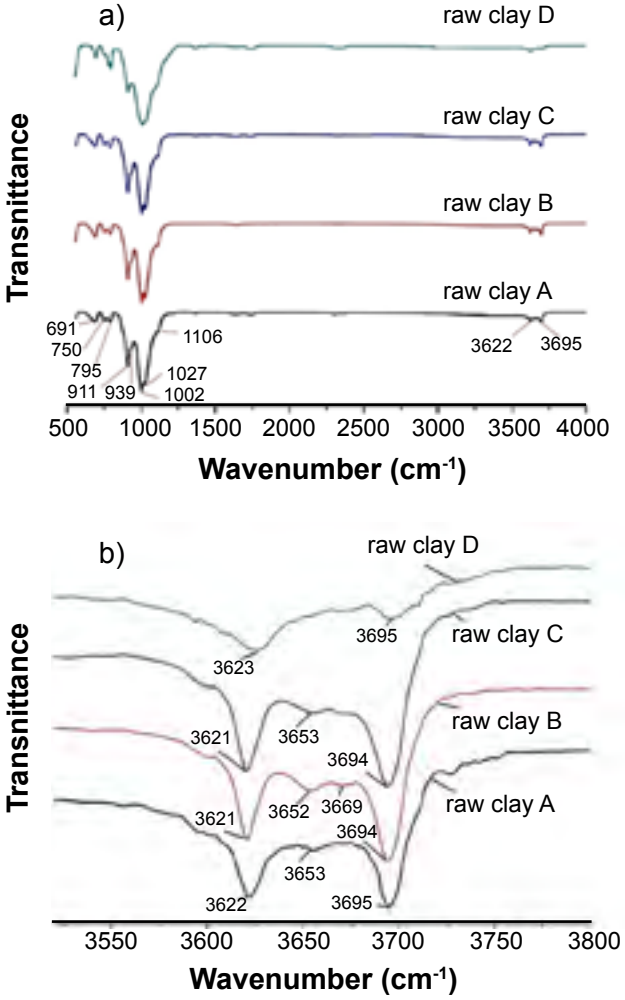

Figure 2: FTIR spectra of *in natura* clayey ceramic masses A, B, C, and D in the range of 500 to 4000 cm^{-1} (a), and enlarged in the range of 3520 to 3800 cm^{-1} (b).

[Figura 2: Espectros de FTIR das massas cerâmicas de argila in natura A, B, C e D na faixa de 500 a 4000 cm^{-1} (a) e ampliados na faixa de 3520 a 3800 cm^{-1} (b).]

from 200 to 350 ºC showed the gibbsite decomposition, shown in Fig. 3c for the clay C. The third peak corresponded to the dehydroxylation of the kaolinite and halloysite clay minerals with mass loss [27, 31, 32], associated with an endothermic peak in DSC curves at 474 ºC for clay A, 483 ºC for clay B, 479 ºC for clay C, and 473 ºC for clay D. The endothermic dehydroxylation of kaolinite occurs between 450 and 600 ºC producing disordered metakaolinite, but the loss of hydroxyls can continue up to 900 ºC [33-35]. The theoretical mass loss of the dehydroxylation process for kaolinite is 13.96%, considering the composition proposed (46.5% SiO_2+39.5% Al_2O_3+13.96% H_2O) [21]. For the clay A (Fig. 3a), the mass loss considering the temperature of 650 ºC (600 ºC is sufficient to occur the dehydroxylation [36]) was 8.21%, already considering the amount of water lost until 150 ºC. The amount of kaolinite estimated for the clay A was 57.1%, which would cause ~8% of mass loss. The difference between the values of the theoretical material and clay A was not significant and could be likely due to the other materials present in all the samples, such as quartz and hematite. For the clay B (Fig. 3b), with 69.7% of kaolinite (~10% of expected theoretical loss), the observed mass loss at 650 ºC was 11.51%. This result confirmed that the clay B had a higher content of kaolinite and halloysite compared to the clay A. For the clay C (Fig. 3c), which contained 66.9% of kaolinite (~9% of expected theoretical loss), the corresponding mass loss of the dehydroxylation was 11.87%, similar to clay B, but the process seemed to be less intense than the clays A and B, indicating a difference in the formation of metakaolinite. Finally, for the clay D (Fig. 3d), with 51.5% of kaolinite (~7% of expected theoretical loss), the mass loss was 5.34%. Only in this case, the observed mass loss was less than the theoretically calculated value and was much lower than the other samples. In the fourth event, at 573 ºC, α-quartz transformed to β-quartz by a reversible change in the crystal structure with a linear expansion of 0.45%. This reversal can lead to cracks in the ceramic if cooling occurs very rapidly [37]. In the fifth event with heating at 925-950 ºC, the metakaolinite was converted to an aluminum-silicon spinel-type crystal structure. The exothermic peak at 970 ºC can correspond to recrystallization, beginning of the formation of the spinel phase, which allows the formation of mullite at 1050-1100 ºC [38]. Finally, after calcination above 1050 °C, the nucleated spinel phase transformed to mullite with platelet shape and highly crystalline cristobalite [28]. It is well-known the amorphous form of metakaolinite. However, metakaolinite is not a simple mixture of amorphous silica and alumina, but rather a complex amorphous structure that retains some orders due to their hexagonal stacking layers [33]. The phenomena of the quartz phase change and formation of the spinel-type phase [37] were observed in all samples.

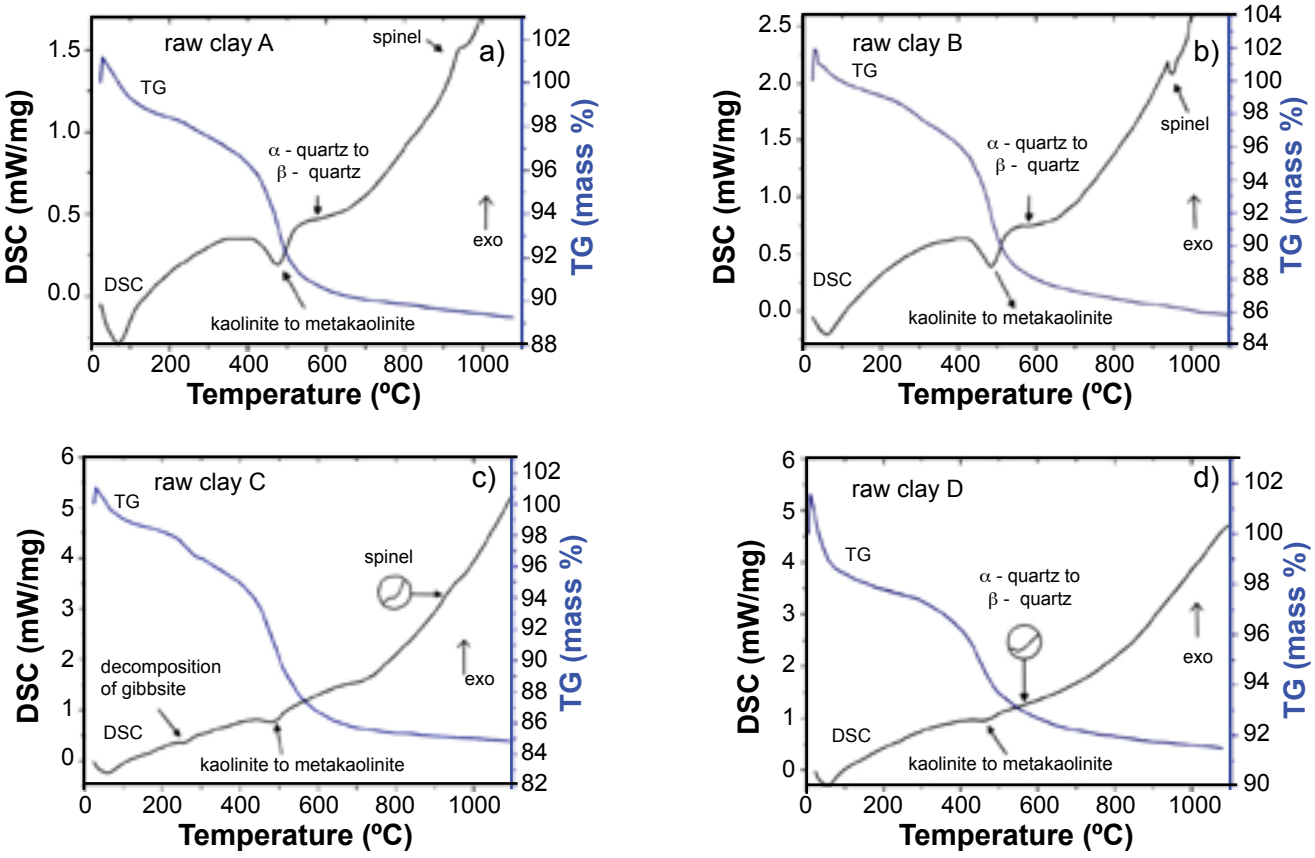

Figure 3: Differential scanning calorimetry (DSC) and thermogravimetric analysis (TG) curves of *in natura* clayey ceramic masses: a) A; b) B; c) C; and d) D).

[Figura 3: Curvas de calorimetria exploratória diferencial (DSC) e análise termogravimétrica (TG) das massas cerâmicas de argila in natura: a) A; b) B; c) C; e d) D.]

Morphological characterizations

The kaolinitic clay minerals are usually present as plates in empty spaces, fractures, and breakups, possibly due to the discharge of hydrothermal fluids. It may also occur as hexagonal or pseudo-hexagonal crystals, exhibiting stacking layers [20]. Information on clay can be supplied by the knowledge of the geochemical environment during formation and diagenesis [39]. The amount of impurity (quartz, hematite, etc.) in the clay sample affects particle morphology [23]. The shape of the halloysite is of elongated tubes, while the shape of kaolinite is of stacked pseudo-hexagonal plates [40]. Raw clay samples A, B, C, and D, which showed 17-35% quartz as impurity were analyzed by scanning electron microscopy (SEM), by secondary electrons, in order to evaluate possible differences in the morphology of phases (Fig. 4). The micrographs showed that kaolinite and halloysite were disorderly arranged and stacked, with crystals of different sizes and shapes, more or less agglomerated with some differences according to the clay. The morphologies observed by SEM was correlated with the XRD and FTIR results. The clay A showed layers of pseudo-hexagonal plates of kaolinite well-defined with sizes of about 100 to 500 nm. The presence of a few tubular halloysite crystals was also observed, which may be an indication that clay A had a small amount of halloysite. No other morphologies were observed (well-defined crystals) of materials different from the clay minerals. Clay B had similar morphological characteristics to clay A, but with more irregular sheets, losing the hexagonal structure, and showing the presence of tubular halloysite structures. The microstructure of the clay C had similar characteristics to clay B; however, there was a greater presence of other minerals, affecting the ordering of layers. It was observed a higher concentration of tubular crystals in clay C, indicating a higher concentration of halloysite in this clay. It was also observed the presence of materials with morphology different from the clay minerals, probably not crystalline materials. For clay D, the same characteristics of the layers observed in the clay B were found. In this case, however, it was observed an agglomeration of materials whose morphologies were not related to the clay minerals. These materials were probably not crystalline materials from organic or inorganic impurities.

Fig. 5 shows an SEM image of the clay brick waste B, which was used to replace cement in a construction mortar. The halloysite microcrystals are smaller than those of kaolinite and have a longer profile. This was kept for metakaolinite and metahalloysite in calcined clays. A flake morphology corresponds to a part of the amorphous material. In clays containing low amounts of kaolinite and high amounts of impurities such as quartz, calcite, and muscovite, heat treatment has much less influence on morphology (as in the waste of fired clay brick) [41].

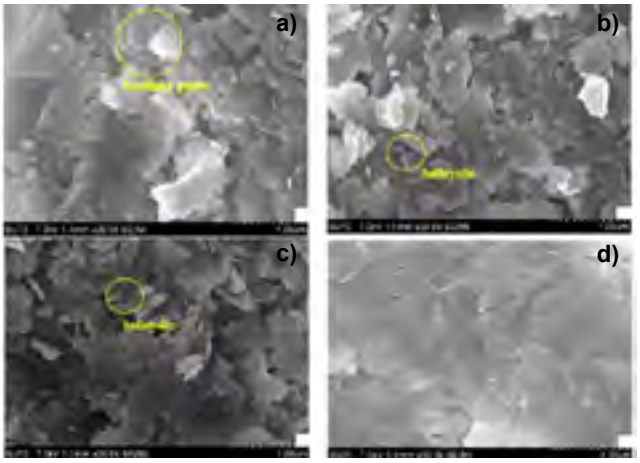

Figure 4: Micrographs obtained by SEM (secondary electrons) of *in natura* clayey ceramic masses: a) A; b) B; c) C; and d) D.
[Figura 4: Micrografias obtida por MEV (elétrons secundários) das massas cerâmicas de argila in natura: a) A; b) B; c) C; e d) D.]

Figure 5: Micrograph obtained by SEM (secondary electrons) of clay brick waste B (after firing).
[Figura 5: Micrografia obtida por MEV (elétrons secundários) do resíduo de tijolo B (após queima).]

Table V - Properties of mortars.
[Tabela V - Propriedades das argamassas.]

Mortar	BW (%)	w/c ratio	Consistency index (mm)	Compressive strength, 28 days (MPa)	Compressive strength, 90 days (MPa)
Reference	0	2.50	267	2.5 ± 0.7	5.7 ± 0.4
M40%BW	40	2.50	190	6.4 ± 0.2	6.5 ± 0.8

BW: brick waste; w/c: water/cement.

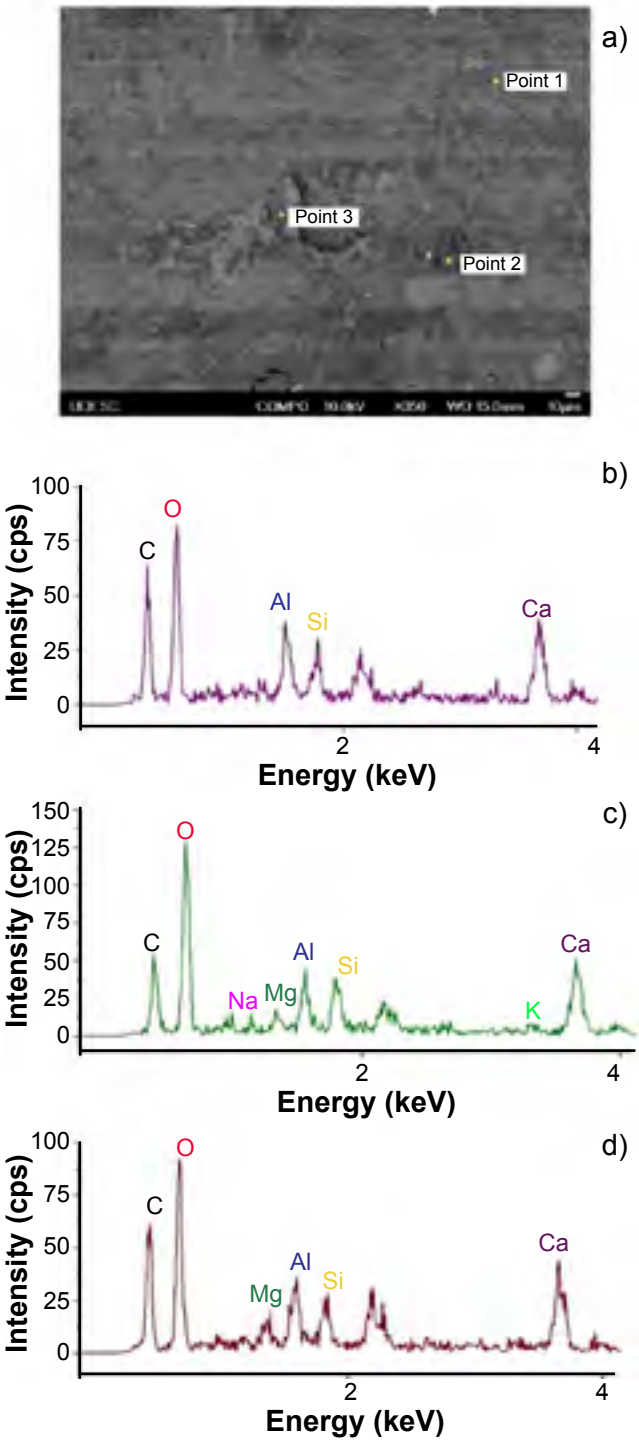

Figure 6: SEM micrograph (backscattered electron - BSE) of polished sample of M40%BW paste at 28 days curing (a), and EDS spectra of the points 1 (b), 2 (c), and 3 (d).
[Figura 6: Micrografia de MEV (elétrons retroespalhados - BSE) de amostra polida da pasta M40%BW com 28 dias de cura (a) e espectros de EDS dos pontos 1 (a), 2 (b) e 3 (d).]

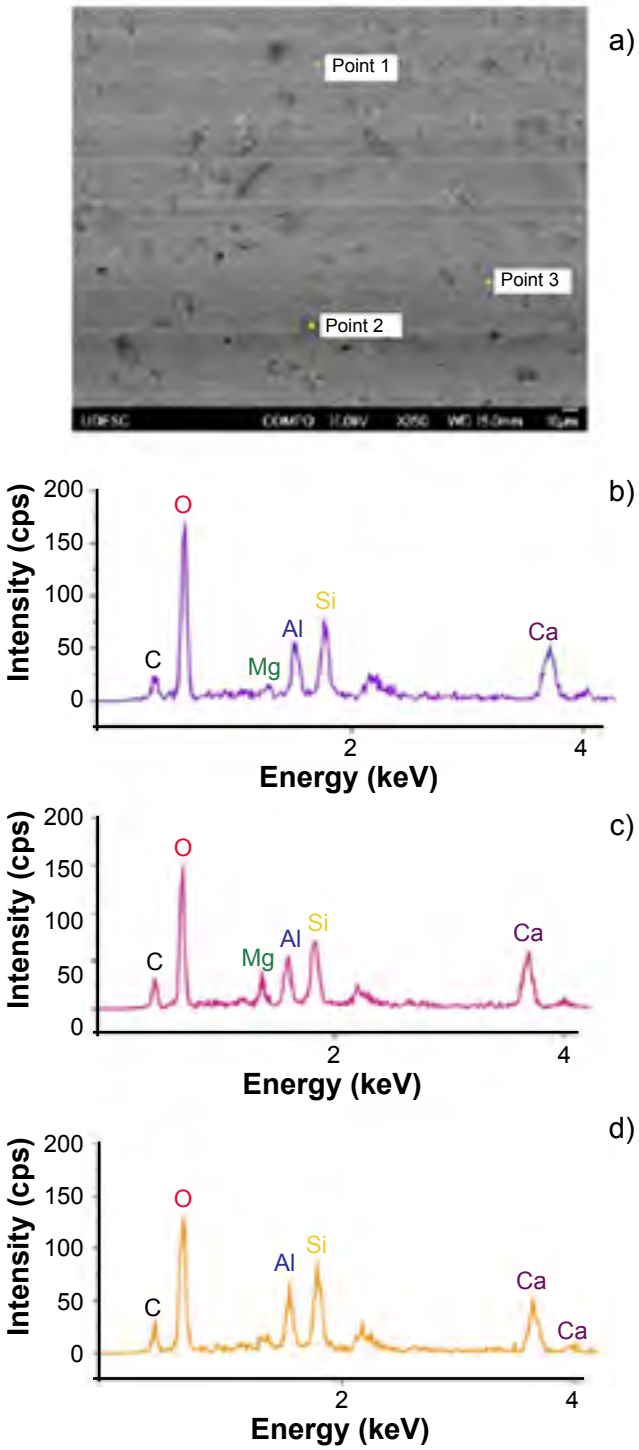

Figure 7: SEM-BSE image of another polished sample of M40%BW paste at 28 days curing (a), and EDS spectra of the points 1 (b), 2 (c), and 3 (d).
[Figura 7: Imagem de MEV-BSE de outra amostra polida da pasta M40%BW com 28 dias de cura (a) e espectros de EDS dos pontos 1 (a), 2 (b) e 3 (d).]

Application of fired and ground clay (brick waste) in a construction mortar

Table V shows the properties of the construction mortars tested. The use of 40% of clay brick waste (75 μm) replacing Portland cement in a mortar resulted in a gain of 51% in compressive strength at 28 days. The use of CPII-Z-32 cement (with pozzolan) favored the increase of compressive strength at later ages in the reference mortar. The strength gain in the M40%BW mortar between 28 and 90 days was

Table VI - Results of semi-quantitative chemical analysis by EDS of points 1, 2 and 3 indicated in Figs. 6 and 7.
[Tabela VI - Resultados da análise química semiquantitativa por EDS dos pontos 1, 2 e 3 indicados nas Figs. 6 e 7.]

Figure	Point	C	Na	MgO	Al_2O_3	SiO_2	K_2O	CaO
6	1	17.40	-	-	16.18	15.56	-	50.86
	2	12.58	1.13	3.15	12.24	17.45	3.58	49.87
	3	18.46	-	5.16	14.06	13.63	-	48.68
7	1	5.09	-	2.50	15.32	28.51	-	48.58
	2	6.09	-	4.63	14.83	28.68	-	45.78
	3	5.77	-	-	14.57	34.18	-	45.48

not so significant because the reference mortar had more pozzolanic cement. The clay brick waste had not only pure pozzolan but also impurities. This residue contributed to the mortar strength by the pozzolanic effect and also by the void filling effect. The reduction in the consistency due to water absorption by the waste clay brick also favored the strength in the M40%BW mortar at 28 days.

Fig. 6a shows an SEM image of a polished surface of 28-day cured M40%BW paste indicating the sites where the EDS analysis was conducted. In addition, Figs. 6b to 6d show the EDS spectra of points 1, 2, and 3 (Fig. 6a), and Table VI shows the results of the semi-quantitative chemical analysis of these points. The results of EDS analyses of points 1 and 3 were similar and revealed silicon, oxygen, calcium, and aluminum as major elements. The Si/Al molar ratio was 0.88 at these two points. The Si/Al molar ratio of metakaolinite ($Al_2O_3.2SiO_2$) is 1.00. Due to high amounts of Ca in these sites, it could be a particle of metakaolinite reacted with portlandite phase [$Ca(OH)_2$] forming other Portland cement hydration products. The Ca/Si molar ratios of points 1 and 3 were not similar to those found for Portland cement hydration products, probably because the reactions were still in progress. The results of the qualitative and semi-quantitative analyses of point 2 revealed silicon, oxygen, calcium, and aluminum as major elements, while potassium, magnesium, and sodium were found in small amounts. The Si/Al molar ratio of point 2 was 1.30, close to the Si/Al molar ratio (1.00) of the metakaolinite. The difference of 0.30 can be attributed to the quartz contained in the clay brick waste. The small amounts of Na and K present may be from a ceramic phase, while Ca was related to a hydration product of the clay brick waste particle. Thus, point 2 may represent a metakaolinite particle that reacted to form C-S-H gel, although no other hydrated phases were detected, probably due to the progress of incomplete reactions. Three possible reactions can be proposed to represent the phenomenon [42]:

$$AS_2+6CH+9H\rightarrow C_4AH_{13}+2CSH_I \quad (A)$$

$$AS_2+5CH+3H\rightarrow C_3AH_6+2CSH_I \quad (B)$$

$$AS_2+3CH+7H\rightarrow C_2ASH_8+2CSH_I \quad (C)$$

where A = Al_2O_3, S = SiO_2, C = CaO, and H = H_2O.

Fig. 7 shows another SEM image of a polished surface of the paste with clay brick waste and EDS spectra (Figs. 7b to 7d) of the 3 points indicated on the micrograph (Fig. 7a). According to the EDS results of point 1 (similar to point 2), it could probably be a grain of a crystalline phase containing mainly (Ca,Mg)CO_3, calcium carbonate with Mg substituting Ca atoms in the crystal structure. The presence of Si may indicate that this phase reacted with metakaolinite ($Al_2O_3.2SiO_2$) forming the C-S-H gel. The amounts of aluminum and magnesium determined by EDS of points 1 and 2 may indicate that these elements were incorporated in the C-S-H gel phase [43, 44]. The presence of magnesium may also be related to the hydrotalcite phase $[Mg_{0.75}Al_{0.25}(OH)_2](CO_3)_{0.125}(H_2O)_{0.5}$ [45]. The EDS of point 3 (Fig. 7d) indicated the main presence of Ca, Si, and Al. The Ca/Si molar ratio was 2.87, close to the Ca/Si molar ratio of 2.90 of the hydrated tetracyclic aluminate ($4CaO.Al_2O_3.19H_2O$) cement phase.

CONCLUSIONS

Four types of *in natura* clayey ceramic masses from different ceramic industries of red bricks were characterized. The sample (raw material) with the highest potential for pozzolanic activity was identified and applied in replacement of Portland cement, in the form of clay brick waste powder (after firing). The determined characteristics can contribute to improving the production process and the final ceramic product in the industries. Knowing the exact temperature of dehydroxylation and mass loss can help improve the ceramic firing process and prevent cracking and failure. The temperature that occurred dehydroxylation of the kaolinite and halloysite clay minerals was 483 ºC for the clay with the best characteristics to produce pozzolanic material ('clay B'). The analysis of the morphology of the raw clays showed the presence of pseudo-hexagonal plates of kaolinite and tubular crystals of halloysite, mainly in the raw clay B. The mass loss associated with dehydroxylation was 11.51% for clay B, similar to a theoretical value considering stoichiometric kaolinite. The *in natura* clayey ceramic masses showed characteristics such as the content of kaolinite, halloysite, quartz, and hematite, and morphological properties favorable to produce a pozzolanic material. Clay B had the greatest amount of kaolinite (69.7%). Qualitative analysis

by XRD and FTIR contributed to the identification of the mineralogical phases present in the samples. The properties of the *in natura* (raw) clays influence the reactivity of the clayey ceramic masses after firing (clay brick waste). The higher amount of kaolinite and a lower amount of impurities, besides the morphology with a larger surface area (halloysite) in raw clay, can result in a ceramic material with higher pozzolanic potential after firing. The compressive strength at 28 days of mortar with 40% of fired brick waste (ground to 75 μm) produced from clay B, replacing Portland cement, improved 51% compared with the reference mortar. The analysis of the hydration products suggested the presence of $Al_2O_3.2SiO_2$ forming the C-S-H gel, hydrotalcite phase $[Mg_{0.75}Al_{0.25}(OH)_2](CO_3)_{0.125}(H_2O)_{0.5}$, and hydrated tetracyclic aluminate cement phase ($4CaO.Al_2O_3.19H_2O$). There are two advantages to the environment when using ceramic brick wastes: reduction of the use of Portland cement (CO_2 emission reduction) and minimization of residue disposals.

ACKNOWLEDGMENTS

The authors appreciate the financial support received from the Santa Catarina State Research Agency FAPESC (Project 510-17), and are also grateful for the support of CAPES - Coordination of Improvement of Higher Education Personnel of the Brazilian Ministry of Education through the Doctoral Exchange Program at the University of Aveiro/ Portugal (Project 99999.013937/2013-08 - A. Schackow). We also thank the University of Aveiro for providing equipment and structure used for all the tests.

REFERENCES

[1] V. Beltran, E. Sanchez, J. Garcia, F. Fernando, Tile Brick Int. **12** (1996) 320.
[2] P. Sánchez-Soto, J. Diaz-Hernandez, M. Raigón-Pichardo, A. Ruiz-Conde, G. Garcia-Ramos, Br. Ceram. Trans. **93** (1994) 196.
[3] J. Oti, J. Kinuthia, J. Bai, Eng. Geol. **107** (2009) 130.
[4] G.W. Brindley, G. Brown (Eds.), "Crystal structures of clay minerals and their X-ray identification" **5**, Miner. Soc. Great Brit. Ireland (1980).
[5] J. Konta, Appl. Clay Sci. **10** (1995) 275.
[6] D.M. Moore, R.C. Reynolds, *X-ray diffraction and the identification and analysis of clay minerals,* Oxford Un. Press, Oxford (1989).
[7] H.M. Fentaw, T. Mengistu, Appl. Clay Sci. **13** (1998) 149.
[8] W.M. Carty, U. Senapati, J. Am. Ceram. Soc. **81** (1998) 3.
[9] G. Ballas, S. Garziglia, N. Sultan, E. Pelleter, S. Toucanne, T. Marsset, V. Riboulot, S. Ker, Eng. Geol. **240** (2018) 175.
[10] F. Deschner, F. Winnefeld, B. Lothenbach, S. Seufert, P. Schwesig, S. Dittrich, F. Goetz-Neunhoeffer, J. Neubauer, Cem. Concr. Res. **42** (2012) 1389.
[11] R. Silva, J. de Brito, R. Dhir, Constr. Build. Mater. **105** (2016) 400.
[12] K.L. Lin, B.Y. Chen, C.S. Chiou, A. Cheng, Waste Manag. Res. **28** (2010) 647.
[13] S. Subasi, H. Öztürk, M. Emiroglu, Constr. Build. Mater. **149** (2017) 567.
[14] A. Schackow, D. Stringari, L. Senff, S.L. Correia, A.M. Segadães, Cem. Concr. Compos. **62** (2015) 82.
[15] ABNT NBR 13276, "Mortars applied on walls and ceilings: determination of consistency index", Braz. Ass. Techn. Stand., Rio Janeiro (2005).
[16] ABNT NBR13279, "Mortars applied on walls and ceilings: determination of flexural and compressive strength in the hardened stage", Braz. Ass. Techn. Stand., Rio Janeiro (2005).
[17] B. Szczepanik, P. Slomkiewicz, M. Garnuszek, K. Czech, D. Bana, A. Kubala-Kuku, I. Stabrawa, J. Mol. Struct. **1084** (2015) 16.
[18] H. Tchakoute, C. Rüscher, J. Djobo, B. Kenne, D. Njopwouo, Appl. Clay Sci. **107** (2015) 188.
[19] S.L. Correia, K. Curto, D. Hotza, A.M. Segadães, Mater. Sci. Forum **498** (2005) 447.
[20] S. Kadir, H. Erman, H. Erkoyun, Clay Miner. **59** (2011) 250.
[21] A.C.D. Newman (Ed.), in "Chemistry of clays and clays minerals", Miner. Soc. Monogr. **6**, Longman, London (1987) 2.
[22] C. Coelho, N. Roqueiro, D. Hotza, Mater. Lett. **52** (2002) 394.
[23] M. Felhi, A. Tlili, M. Gaied, M. Montacer, Appl. Clay Sci. **39** (2008) 208.
[24] M. Dondi, G. Guarini, P. Ligas, M. Palomba, M. Raimondo, Appl. Clay Sci. **18** (2001) 145.
[25] T. Dombrowski, in "Science of whitewares II", W.M. Carty, C.W. Sinton (Eds.), Am. Ceram. Soc., Westerville (2000) 3.
[26] G. Nirmala, G. Viruthagiri, Spectrochim. Acta A **135** (2015) 76.
[27] L. Zatta, "Kaolinite and halloysite in-nature and activated with acids minerals as heterogeneous catalysts for ethylic esterification of fatty acid", Master Thesis, Fed. Un. Parana (2010).
[28] M.B. Ogundiran, S. Kumar, Appl. Clay Sci. **108** (2015) 173.
[29] L. Deng, Z. Shi, J. Alloys Compd. **637** (2015) 188.
[30] J.D. Russel, in "Laboratory methods in infrared spectroscopy", H. Willis (Ed.), Wiley, New York (1987).
[31] C. Bich, J. Ambroise, J. Péra, Appl. Clay Sci. **44** (2009) 194.
[32] T. Zhang, X. Yue, Y. Deng, D. Zhang, S. Liu, Constr. Build. Mater. **73** (2014) 51.
[33] M. Bellotto, A. Gualtieri, G. Artioli, S. Clark, Phys. Chem. Miner. **22** (1995) 207.
[34] A.M. Neville, J.J. Brooks, *Concrete technology*, Bookman (2013).
[35] M.F. Nuruddin, S.U. Khan, N. Shafiq, Appl. Mech. Mater. **567** (2014) 375.

[36] A. Chakchouk, B. Samet, T. Mnif, Appl. Clay Sci. **33** (2006) 79.
[37] A. Dodd, D. Murfin, *Dictionary of ceramics*, 3rd ed., Inst. Miner., London (1994).
[38] V. Mymrin, W. Klitzke, K. Alekseev, R.E. Catai, A. Nagalli, R.L.S. Izzo, C.A. Romano, Appl. Clay Sci. **107** (2015) 28.
[39] Y.Z. Chen, W.H. Zhou, F. Liu, S. Yi, X. Geng, Eng. Geol. **256** (2019) 84.
[40] H.H. Murray, *Applied clay mineralogy: occurrences, processing and applications of kaolins, bentonites, palygorskite-sepiolite, and common clays*, Elsevier (2007).
[41] S. Selmani, N. Essaidi, F. Gouny, S. Bouaziz, E. Joussein, A. Driss, A. Sdiri, S. Rossignol, J. Afr. Earth Sci. **103** (2015) 113.
[42] R. Siddique, J. Klaus, Appl. Clay Sci. **43** (2009) 392.
[43] P.D. Tennis, H.M. Jennings, Cem. Concr. Res. **30** (2000) 855.
[44] C. Famy, K. Scrivener, A. Crumbie, Cem. Concr. Res. **32** (2002) 1465.
[45] G.C. Isaia, M.A. Cincotto, *Concrete: science and technology*, Ibracon, Brazil (2011).
(Rec. 11/09/2019, Rev. 05/11/2019, 17/12/2019, Ac. 20/12/2019)

CC BY-NC

Artificial stone production using iron ore tailing (IOT)

(Produção de rocha artificial utilizando rejeito de minério de ferro)

C. B. da Silva[1]*, P. R. P. de Paiva[1]
[1]Centro Federal de Educação Tecnológica de Minas Gerais, Departamento de Engenharia de Materiais, Belo Horizonte, MG, Brazil

Abstract

Artificial stone materials (ASM) were produced with an iron ore tailing (IOT) from the disruption of Fundão's tailing dam, located in Mariana, Minas Gerais State, Brazil. The IOT was separated in 3 powders with different particle sizes: D_{AG} (<600 μm), D_{AR} (600 to 75 μm), and D_{SA} (<75 μm); then, each powder was characterized and mixed with a polymer resin (polyester or epoxy). ASM samples were prepared using the transfer molding technique; vacuum vibration technology was also applied to half of the samples. After curing, the ASM samples were characterized for mechanical properties and physical parameters. The microstructure of polished ASM samples was also analyzed by scanning electron microscopy. All results indicated that ASM samples produced with epoxy resin were superior to the samples made with polyester resin. The features found for the different compositions and shaping conditions for the produced ASM samples can allow various applications for these alternative materials in the construction industry, such as floor and wall tiles, providing a means of reducing the amount of IOT deposited in the tailing dams and adding economic value to this waste.
Keywords: iron ore tailing, artificial stone material, polyester resin, epoxy resin, vacuum vibration technology.

Resumo

Materiais rochosos artificiais (ASM) foram produzidos com rejeito de minério de ferro (IOT) proveniente do rompimento da barragem de rejeitos do Fundão, localizada em Mariana-MG, Brasil. O IOT foi separado em três pós com diferentes tamanhos de partículas: D_{AG} (<600 μm), D_{AR} (600 a 75 μm) e D_{SA} (<75 μm); em seguida cada pó foi caracterizado e misturado com uma resina polimérica (poliéster ou epóxi). Amostras de ASM foram preparadas usando a técnica de moldagem por transferência; a tecnologia de vibração a vácuo também foi aplicada à metade das amostras. Após a cura, as amostras de ASM foram caracterizadas quanto às propriedades mecânicas e parâmetros físicos. A microestrutura de amostras de ASM polidas também foi analisada por microscopia eletrônica de varredura. Todos os resultados indicaram que as amostras de ASM produzidas com resina epóxi foram superiores às amostras feitas com resina poliéster. As características encontradas para as diferentes composições e condições de preparação para as amostras de ASM produzidas podem permitir várias aplicações para esses materiais alternativos na indústria da construção, como na forma de revestimentos verticais e horizontais, proporcionando um meio de reduzir a quantidade de IOT depositada em barragens de rejeito e agregando valor econômico para este rejeito.
Palavras-chave: *rejeito de minério de ferro, material rochoso artificial, resina poliéster, resina epóxi, tecnologia de vibração a vácuo.*

INTRODUCTION

Worldwide production of iron ore in 2018 is estimated at around 2.5 billion tons, 19.6% of which in Brazil, the second-largest producer [1]. The mineral industry stands out for contributing decisively to generate surpluses to the Brazilian trade balance. The iron ore is of great importance for the Brazilian economy, which was the main mineral commodity exported in 2018, with a 64.2% of participation. The consumption of iron ore is concentrated in the steel industry (pig iron) and pelletizing plants (pellets) [2, 3]. However, the iron ore beneficiation stages generate large amounts of industrial by-products or tailings [4]. Boscov [5] reported that for each ton of iron ore produced, on average, 0.5 ton of tailings are eliminated, a mass ratio between the final product and the tailings produced of 2:1. Based on the annual Brazilian mining reports, the volume of tailings generated as a result of mineral processing for 2018 is estimated at 231.5 million tons [6]. Regarding the rejects generated by the mining activity, it is estimated that 99.99% have an internal destination (within the mining zone), with the main form of disposition (94.58%) in dams [7]. The iron ore tailings (IOT) can be in the form of pulp (solid and water), granular (medium and fine sand granulometry) or sludge (silt and clay granulometry) [8]. Although tailing dams are a way to reduce environmental degradation by storing rejects in a single place, they need a large space for building the reservoir and remain at risk of disruption [9]. Thus, tailing dams impact the local biome directly, causing insecurity in the population that resides in the vicinity of the dam. Furthermore, the expenses with handling and inspecting tailing dams are onerous [10].

Due to the increasing generation and deposition of iron ore tailings in dams, studies are required for the improvement of ore processing and the reuse of tailings.

**cecilia_balduino@hotmail.com*
https://orcid.org/0000-0003-0341-1473

Recycling is the most appropriate reuse option [11, 12]. Fontes et al. [13] evaluated the technical feasibility of using IOT waste as a building material, such as mortars and tiles. Bastos et al. [9] evaluated the feasibility of using IOT from tailing dams as an alternative material for road infrastructure. Das et al. [14] explored the possibility of using the IOT in the production of geopolymeric bricks. Shettima et al. [15] evaluated the IOT replacing river sand in concrete manufacturing and compared it with conventional concrete. Luo et al. [16] investigated the possibility of utilizing IOT to completely replace the clay as an aluminum silicate raw material for the Portland cement clinker production. Fontes et al. [17] disclosed the development of a sustainable cement tile produced with IOT from tailing dams. Silva et al. [18] studied the technological feasibility of using the IOT as an additive in cement pavers (concrete blocks) for the mechanical properties' optimization and color modulation. Zuccheratte et al. [19] obtained synthetic gravel from sandy IOT and recycled polyethylene terephthalate for the use in concrete.

The artificial stone material has increased commercial interest and is a strong competitor to other building materials, such as ornamental stones because it reproduces very well the aesthetic pattern of natural stones with diversified designs [20]. The production of artificial stone enables countries that produce ornamental stones, such as Brazil, to reduce the volume of daily produced tailings, also allowing the insertion of new products in the civil construction industry catalogs [21-23]. According to the literature, research has been developed to produce artificial stone from different mineral fillers and polymeric bases. Carvalho et al. [24] evaluated the possibility of fabricating artificial stone as an epoxy composite incorporated with a dust residue collected from the electrostatic precipitator of the sintering stage of a steelmaking plant to be used as plates for housing and road construction. Ribeiro et al. [25] studied the possibility of producing ornamental stone using marble residue embedded in a polyester resin. Peng and Qin [26] elaborated a high-quality artificial stone slab using a SiO_2 crucible waste mixed with quartz sand and unsaturated polymer resin as a binder. Gomes et al. [27] obtained an artificial stone from a brick residue and quarry dust in an epoxy matrix. The addition of mineral fillers as a nucleating agent in polymeric matrices favors heterogeneous nucleation by reducing the critical energy required for stable nucleation [28]. Usually, mineral fillers are produced by controlling geometry and particle size. The smaller the particle size, the larger is the surface area and, consequently, the number of filler/polymer interfaces also increases. Mechanical properties are expected to improve with increasing adhesion points. However, the larger the surface area, the greater is the difficulty in dispersing the filler in the matrix or in controlling the processing viscosity [29]. The aim of this study was to produce artificial stone materials (ASM) with iron ore tailings of different granulometry using polyester and epoxy resins by transfer molding and vacuum vibration techniques, and also to evaluate the effect of the microstructure on the physical and mechanical behavior of ASM samples. To the best of the authors' knowledge, no other study has been reported in the literature for similar objectives.

MATERIALS AND METHODS

Raw materials: the iron ore tailing (IOT) was collected at Carmo's riverbanks, near the formation of Doce river's basin, located in Barra Longa (20°16'33" south, 43°2'30" west); the material came from the rupture of Fundão's tailing dam, located in Mariana, State of Minas Gerais, Brazil. IOT was dried at 110 °C for 24 h to remove moisture, which could reduce the curing process efficiency and adhesion between tailing and resin [30]. It was then disaggregated, homogenized, and sieved, according to the ABNT NBR 7181:84 standard [31]. Then, it was separated in 3 samples (powders) with different particle sizes (Fig. 1): <600 μm (D_{AG}); 600 to 75 μm (D_{AR}); and <75 μm (D_{SA}). Particles of IOT bigger than 600 μm (6.9 wt%) were discarded since their diameter was not ideal for ASM production. The particle size distributions of the powders D_{AG}, D_{AR}, and D_{SA} were determined using a Cilas 1090 laser granulometer; the results are showing in Fig. 2 and Table I. An orthophthalic unsaturated polyester resin

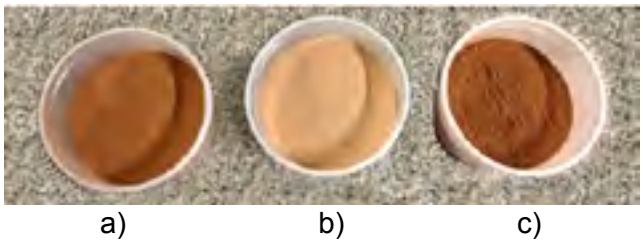

Figure 1: Image of IOT powders with different particle sizes: a) D_{AG} (<600 μm); b) D_{AR} (600-75 μm); and c) D_{SA} (<75 μm).
[Figura 1: Imagem de pós de IOT com diferentes tamanhos de partículas: a) D_{AG} (<600 μm); b) D_{AR} (600-75 μm); e c) D_{SA} (<75 μm).]

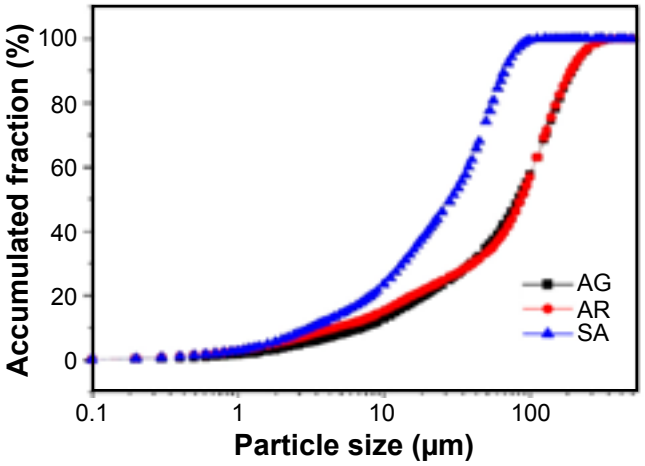

Figure 2: Particle size distribution curves of IOT powders D_{AG}, D_{AR}, and D_{SA}.
[Figura 2: Curvas de distribuição granulométrica dos pós de IOT D_{AG}, D_{AR} e D_{SA}.]

Table I - Results of laser granulometric test of IOT powders. *[Tabela I - Resultados do ensaio de granulometria a laser dos pós de IOT.]*

Powder	D10 (μm)	D50 (μm)	D90 (μm)	$D_{average}$ (μm)
D_{AG}	7.2	83.4	193.6	93.2
D_{AR}	4.6	87.1	191.0	93.0
D_{SA}	3.2	28.7	67.3	32.5

Centerpol 626 (PO) with a medium viscosity, 1.05 g.cm^{-3} of density at 25 °C, and a gel time of 15 min at 25 °C was one of the resins used to formulate the artificial stone. As a catalyst, a methyl ethyl ketone peroxide (MEKP) 1% w/w (relative to PO mass) was used. An epoxy resin Araldite LY 1564 BR (EP) with low viscosity, 1.15 g.cm^{-3} of density at 25 °C, and gel time of 35 min at 25 °C was the other resin used. As the initiator, Araldur 2963 BR 48% w/w (relative to EP mass) was used.

Shaping and curing: the samples of artificial stone material (ASM) were prepared by mixing the raw materials according to the compositions described in Table II, using a disperser (Contenco, I-1018-D) at 10000 rpm for 5 min. After complete homogenization, the mixture was poured in a silicone mold (27.5x15.0x76.0 mm), previously lubricated with carnauba wax to assist in demolding. Half of the samples were cured at 25 °C for 7 days and then removed. The other samples were first submitted to a vibration and vacuum (VV) system for 15 min applying a mechanical vibration of 3 Hz and vacuum suction (1.3x10^{-1} Pa), then cured at 25 °C for 7 days before demolding. ASM samples without and with VV were named with the addition of numbers 1 and 2 to the sample name, respectively.

Methods of characterization: quantitative mineralogical composition of IOT samples was obtained by X-ray diffraction (XRD) analysis, which was performed using a Shimadzu XRD-7000 diffractometer using CuKα radiation (35 kV, 40 mA), speed of goniometer of 0.02° in 2θ per step, counting time of 5 s/step, and 2θ range from 5° to 80°. XRD pattern interpretations were performed by comparison with reference XRD patterns of the ICDD PDF-2 database. The semi-quantitative chemical composition of the IOT powders was obtained by X-ray fluorescence (XRF) spectroscopy, performed with a Shimadzu EDX-720 equipment in vacuum. A leaching test was performed to analyze the level of contaminants in the IOT, according to standards ABNT NBR 10005:2004 [32] and ABNT NBR 10006:2004 [33]. The water absorption, density, and apparent porosity tests of ASM samples were determined according to the ASTM C373-88 standard [34]. For these tests, the samples were dried at 50 ºC for 24 h, weighed, and placed inside a desiccator. Distilled water was added to a beaker up to twice the height occupied by previously added ASM samples and then heated to 100 ºC for 4 h; water was added when necessary so that the samples were always immersed in water. Finally, the set was cooled at room temperature for 24 h, and then both immersed and water-saturated samples were weighed. For the mechanical strength, the three-point bending test of ASM samples was carried out in a universal testing machine Shimadzu AG-X; the load was applied at the center of the sample at a crosshead speed of 1.0 mm/min until failure. Bending strength was calculated according to the ASTM C1161-18 standard [34]. Five samples of each composition were evaluated for each test. The morphological analysis of IOT and ASM samples was performed using a Shimadzu SSX-550 scanning electron microscope (SEM) operating at 15 kV with samples covered with a thin gold layer; the magnifications of 600x and 50x were used to observe IOT and ASM samples, respectively. IOT particle morphology was analyzed, and the existence of cracks and voids was evaluated on polished surfaces of ASM specimens (Fig. 3).

Table II - Raw material compositions of ASM samples in mass fraction (volumetric fraction in parentheses). *[Tabela II - Composições de matérias-primas das amostras ASM em fração mássica (fração volumétrica entre parênteses).]*

Sample	IOT	Matrix
PR	0%	PO 100%
ER	0%	EP 100%
PAG	D_{AG} 70% (67.8%)	PO 30% (32.2%)
PAR	D_{AR} 70% (72.3%)	PO 30% (27.7%)
PSA	D_{SA} 70% (62.0%)	PO 30% (38.0%)
EAG	D_{AG} 70% (70.7%)	EP 30% (29.3%)
EAR	D_{AR} 70% (75.0%)	EP 30% (25.0%)
ESA	D_{SA} 70% (65.3%)	EP 30% (34.7%)

IOT: iron ore tailing; D_{AG}: <600 μm; D_{AR}: 600-75 μm; D_{SA}: <75 μm; PO: polyester resin; EP: epoxy resin.

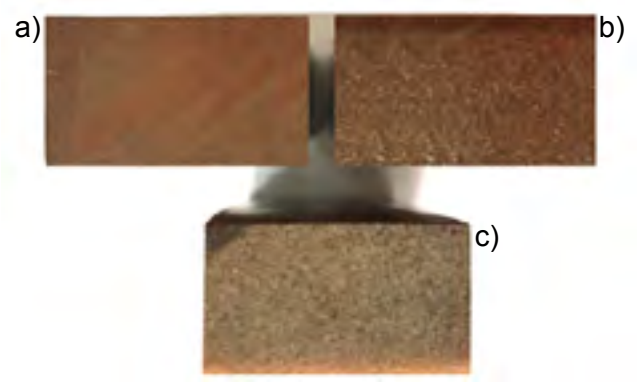

Figure 3: Images of polished ASM samples made with epoxy resin: a) ESA2; b) EAG2; and c) EAR2.
[Figura 3: Imagens de amostras de ASM polidas feitas com resina epóxi: a) ESA2; b) EAG2; e c) EAR2.]

RESULTS AND DISCUSSION

Characterization of IOT powders: Table III shows the chemical compositions of the IOT powders with different

granulometry. The powder D_{AR} (600-75 μm) presented high content of silicon oxide and low content of iron oxide, whereas the powder D_{SA} (<75 μm) presented the content of iron oxide higher than silicon oxide. This result was expected; as the grain size of IOT decreased, the concentration of iron oxide increased due to the greater presence of the iron oxide in silts and clays [36]. Fig. 4 shows the phases present in the IOT powders: quartz, hematite, goethite, and kaolinite. The combined XRF and XRD analyses showed a correlation between substances that appeared in significant concentrations in the IOT, ratifying results from the literature [9]. The iron content (Fe_2O_3) is responsible for the reddish-brown color of the final material [17], a characteristic that can be observed in Fig. 1. So, D_{SA} powder of the IOT can be used as a pigment due to the high iron oxide content in its composition, improving aesthetic aspects. The high content

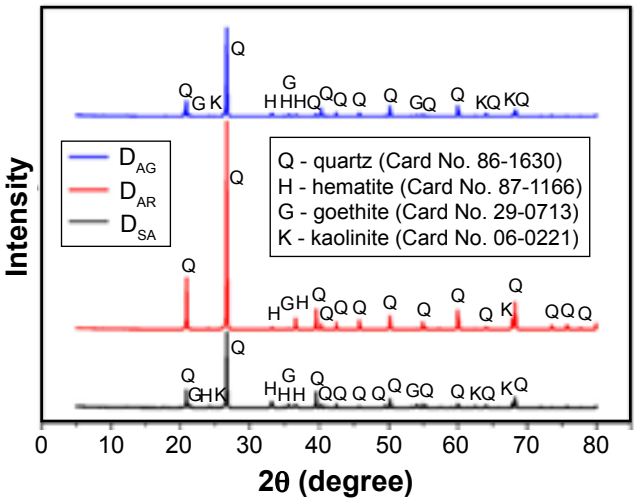

Figure 4: XRD patterns of IOT powders.
[Figura 4: Difratogramas de raios X dos pós de IOT.]

of quartz in D_{AR} powder (Table III) was already expected once the main impurity contained in iron ores from the Iron Quadrangle (State of Minas Gerais, Brazil) is quartz [37]. The presence of aluminum oxide in IOT powders is explained by the geology of the region where the iron ore was extracted (Alegria district). This locality has deposits of amphibolitic itabirites, which may contain aluminum in the form of kaolinite [38]. The existence of traces of goethite (Table III, Fig. 4) can be explained by the fact that in regions with limited drainages, such as in tailing dams, hematite hydration probably occurs, transforming it into goethite [39]. According to the ABNT NBR 10004:2004 standard [40], IOT was classified as Class II B, non-dangerous and inert residue. Fig. 5 shows the scanning electron microscopy (SEM) images for the D_{AG}, D_{AR}, and D_{SA} powders. It was found that the IOT morphology presented large, slightly rounded, irregular, and angular particles probably of quartz, as well as tabular particles probably of hematite, characteristics that corroborate a study in the literature [41]. As reported in [37], the micrographs shown in Figs. 5a and 5c presented a significant number of small particles (of tabular morphology) adhered to the surface of larger particles of irregular granular character. This behavior is characteristic of clay materials [41, 42].

Mechanical strength of ASM samples: the results of the ultimate strength (modulus of rupture) of bending tests for the ASM samples are shown in Fig. 6a. In general, it was possible to identify that ASM samples produced with polyester resin presented lower mechanical resistance than those produced with epoxy resin because the mechanical properties of epoxy resin are higher than those of polyester resin since the chemical bonds of the epoxy are stronger [43]. In addition, comparing samples made with the same resin and IOT particle size, those submitted to vacuum vibration (VV) technology usually showed lower bending strength

Table III - Chemical compositions (wt%) of IOT powders D_{AG}, D_{AR}, and D_{SA}.
[Tabela III - Composições químicas (% em massa) dos pós de IOT D_{AG}, D_{AR} e D_{SA}.]

Powder	SiO_2	Fe_2O_3	Al_2O_3	SO_3	CaO	K_2O	MnO
D_{AG}	46.0±2.0	45.3±1.8	5.3±0.5	2.4±0.2	<1.0	<1.0	<1.0
D_{AR}	76.9±4.5	19.6±0.9	3.2±0.3	-	<1.0	<1.0	-
D_{SA}	42.7±1.6	50.1±3.0	5.7±1.0	1.2±0.1	-	<1.0	<1.0

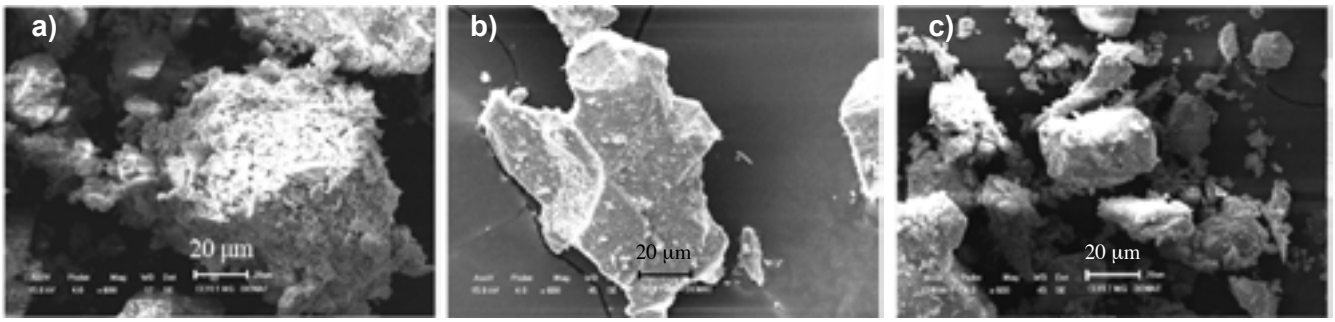

Figure 5: SEM micrographs of the IOT powders: a) D_{AG}; b) D_{AR}; and c) D_{SA}.
[Figura 5: Micrografias de MEV dos pós de IOT: a) D_{AG}; b) D_{AR}; e c) D_{SA}.]

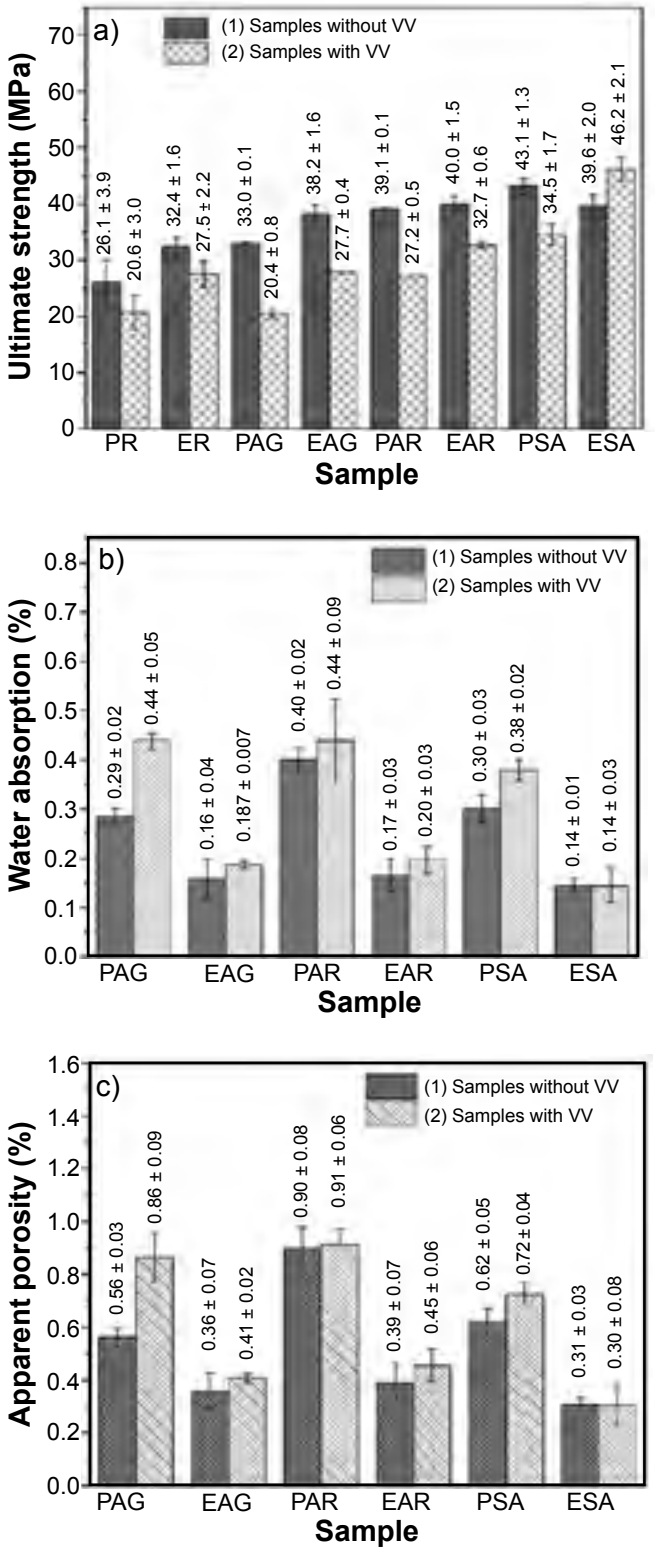

Figure 6: Results of ultimate bending strength (a), water adsorption (b), and apparent porosity (c) for ASM samples prepared without and with the application of vacuum vibration (VV).
[Figura 6: Resultados de resistência à flexão (a), adsorção de água (b) e porosidade aparente (c) das amostras de ASM preparadas sem e com aplicação de vibração a vácuo (VV).]

than samples without VV. The explanation is attributed to the fact that both resins had fast curing time, causing the gases released by the curing process to be trapped inside the ASM samples' structure, not being efficiently eliminated, reflecting in the formation of micropores in the inner part of the material [21], as shown in Figs. 7 to 9. As an exception, when comparing the samples ESA1 and ESA2, it was observed that the ultimate bending strength increased as the composition ESA was subjected to VV. This can be explained by the efficient adhesion and interaction between the D_{SA} particles and the epoxy resin (Fig. 9d). Comparing artificial marble to the ASM samples produced, it was noticed that the materials commonly produced from marble waste have mostly lower mechanical strength (26.6 MPa). This was associated with a low amount of SiO_2 in their composition [21]. However, when ASM samples were compared with an 80% incorporated epoxy-matrix artificial stone with sintering residue from the steelmaking industry (57.57 MPa), ASM samples exhibited lower bending strength because they had a lower amount of Fe_2O_3 in their compositions [24]. Lee et al. [22] reported values from 27.9 to 52.7 MPa for bending strength of an artificial granite with glass powder and 8 wt% of unsaturated polyester employing vacuum vibratory compaction under different conditions. In a specific condition of 9.8 MPa of compression pressure, vibration frequency of 50.0 Hz, and vacuum of 50 mmHg, the artificial stone presented a bending strength of 46.3 MPa [22], which can be compared to the highest value (46.2 MPa) obtained by the sample ESA2 prepared with the particles of IOT <75 μm. According to the limit values for modulus of rupture in bending test [44, 45], all the samples produced in this study had higher values than the minimum values established and can be used as cladding materials, therefore, corresponding to high-strength materials appropriate for civil construction.

Water absorption, apparent porosity, and density: Figs. 6b and 6c show the results of water absorption and apparent porosity, respectively, and Table IV shows the apparent density for the ASM samples produced from the IOT powders D_{AG}, D_{AR}, and D_{SA}. As there are no regulatory standards with limit values for the physical-mechanical properties of artificial ornamental stones used as cladding, the results of these tests were compared with the limit values suggested by the ABNT NBR 15844:2010 [44] and ASTM C615-99 [45] standards, which specify the physical and mechanical characteristics required for granites intended for vertical and horizontal facing of interior and exteriors of buildings. Comparing the results observed in Figs. 6b and 6c and Table IV to these standards, it was observed that all samples (except PAG2 and PAR2) were within limits established for water absorption. Regarding the results obtained for the apparent porosity, all ASM samples presented values lower than 1% within limits. All the results obtained for the apparent density were lower than the values established by both standards. However, this fact does not prevent the ASM produced in this study to be employed as an ornamental stone for cladding, since a slightly smaller density does not cause negative impacts on its use for this purpose [21]. The reason for obtaining lower values for apparent density for ASM samples when compared to those established by the standards [44, 45] is explained by the compositions with 30% w/w of resins (polymeric fillers),

which have lower densities than those derived from mineral fillers. Lee et al. [21] reported values from 2.030 to 2.448 g.cm^{-3} for density and values from 0.011% to 0.221% for water absorption, close to the results found for ASM samples produced with epoxy resin. Carvalho et al. [24] presented values of 0.45% and 0.65% for apparent porosity of artificial stones produced with the incorporation of 80% and 85% of sintering residue, respectively.

Microstructural analysis of ASM samples: Figs. 7, 8, and 9 show the SEM micrographs of polished surfaces of ASM samples made with D_{AG}, D_{AR}, and D_{SA}, respectively, at the same magnification. The microstructure was as expected, with irregularly shaped particles of IOT powders (Fig. 5),

Table IV - Apparent density of ASM samples.
[Tabela IV - Densidade aparente das amostras de ASM.]

Sample	IOT	Matrix	VV	Density (g.cm^{-3})
PAG1	D_{AG}	PO	No	2.159±0.062
PAG2			Yes	1.969±0.001
PAR1	D_{AR}	PO	No	2.289±0.065
PAR2			Yes	2.053±0.015
PSA1	D_{SA}	PO	No	2.064±0.052
PSA2			Yes	1.913±0.005
EAG1	D_{AG}	EP	No	2.291±0.164
EAG2			Yes	2.182±0.014
EAR1	D_{AR}	EP	No	2.214±0.008
EAR2			Yes	2.184±0.021
ESA1	D_{SA}	EP	No	2.118±0.003
ESA2			Yes	2.122±0.023

IOT: iron ore tailing; D_{AG}: <600 μm; D_{AR}: 600-75 μm; D_{SA}: <75 μm; PO: polyester resin; EP: epoxy resin; VV: vacuum vibration.

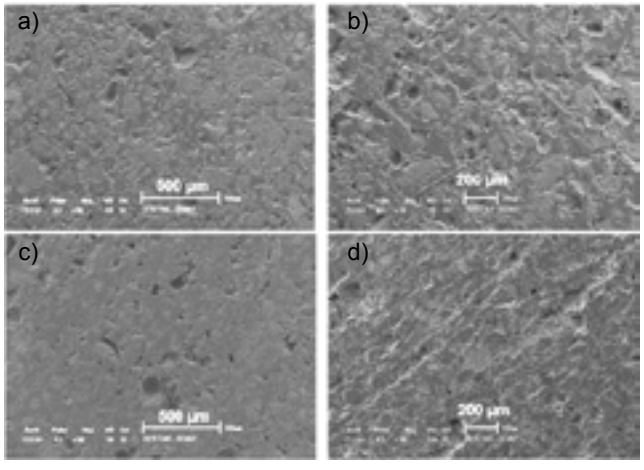

Figure 7: SEM micrographs of polished ASM samples made with the powder D_{AG} (<600 μm): a) PAG1; b) PAG2; c) EAG1; and d) EAG2.
[Figura 7: Micrografias de MEV de amostras de ASM polidas feitas com o pó D_{AG} (<600 μm): a) PAG1; b) PAG2; c) EAG1; e d) EAG2.]

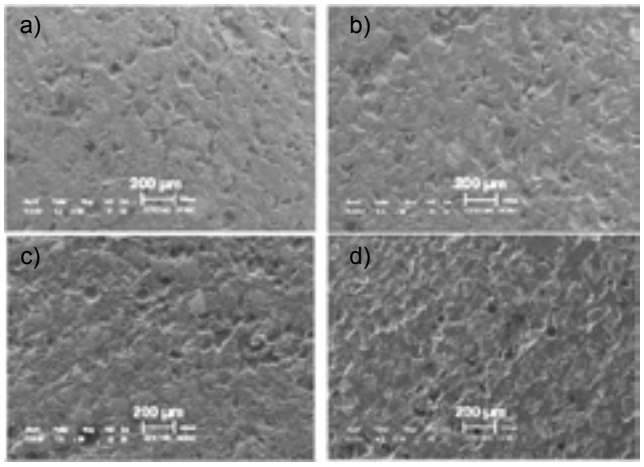

Figure 8: SEM micrographs of polished ASM samples made with the powder D_{AR} (600-75 μm): a) PAR1; b) PAR2; c) EAR1; and d) EAR2.
[Figura 8: Micrografias de MEV de amostras de ASM polidas feitas com o pó D_{AR} (600-75 μm) a) PAR1; b) PAR2; c) EAR1; e d) EAR2.]

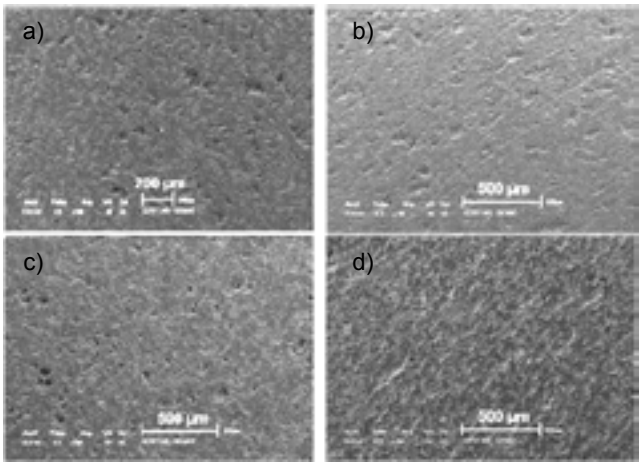

Figure 9: SEM micrographs of polished ASM samples made with the powder D_{SA} (<75 μm): a) PSA1; b) PSA2; c) ESA1; and d) ESA2.
[Figura 9: Micrografias de MEV de amostras de ASM polidas feitas com o pó D_{SA} (<75 μm): a) PSA1; b) PSA2; c) ESA1; e d) ESA2.]

which were well dispersed in the resin [15]. SEM analysis showed that all the ASM samples had voids. The pores were generated, as previously mentioned, by the entrapment of volatiles eliminated by the resin curing process because of the need to insert a catalyzer to obtain a suitable resin flow in this methodology, resulting in an exothermic reaction [21]. The microstructural differences of micrographs of Figs. 7a and 7c, which show relatively dense and smooth structures, compared, respectively, with the micrographs of Figs. 7b and 7d with rough structures can be clearly seen. These results showed that applying vacuum vibration (VV) technology to prepare the samples of PAG and EAG compositions caused a less consistent adhesion between D_{AG} particles and polyester and epoxy resins. This behavior

was coincident with the bending strength variation of these samples (Fig. 6a). Ribeiro et al. [21] reinforce the relevance of microstructure to understand the mechanical properties of the ASM samples. It was observed that the polyester and epoxy resins were well-adhered to the particles of D_{AR} (Figs. 8a and 8c, respectively), which contributed to an effective interfacial bonding and resulted in a more homogeneous distribution of stress between the phases of the samples PAR1 and EAR1. In contrast, samples PAR2 and EAR2 showed interfaces with weaker adhesion causing detachment of IOT particles from the polymer matrix (Figs. 8b and 8d, respectively). This is strong evidence that interfacial bonding was less efficient due to the use of VV technology. Fig. 9 shows that the 4 polished samples exhibited dense morphology with homogeneous particle/resin dispersion, which can be explained by the higher presence of kaolinite in the D_{SA} powder. This constituent reproduced a nucleation effect, similar to aluminum seeding [46], clearly illustrating the cohesion of the formed matrix. However, significant microstructural differences can be detected between Figs. 9a and 9b, such as between the Figs. 9c and 9d. Observing Fig. 9d, it can be seen that the ESA2 sample presented the best morphological structure obtained among the ASM samples produced, in agreement with the mechanical property showed in Fig. 6a for this sample, which was also the best.

CONCLUSIONS

The results of mineralogical and chemical analyses of the iron ore tailing (IOT) powders with different granulometry showed that IOT is a crystalline, inorganic, and stable material, therefore a suitable raw material for the production of an artificial stone material (ASM). In general, the results presented by ASM samples prepared with and without application of vacuum vibration (VV) of similar composition showed the relevance of knowledge of the microstructure to understand the physical and mechanical properties obtained, which were also related to the efficacy of interfacial bonding and compaction of particles. All physical and mechanical properties of the samples produced with epoxy resin were better than those made with polyester resin. Except for the ESA2 sample (IOT <75 μm+epoxy resin), the other samples of similar composition presented better results when the VV technology was not applied. The ESA2 sample presented the best results in all the tests performed and a more homogeneous microstructure with no pores. The bending strengths of ASM samples were superior to those obtained from other conventional artificial stones incorporated with residues from marble industries and similar to the commercial artificial stone made with granite. The properties and microstructure of the ASM samples with IOT suggested several applications in the construction industry, such as cladding and tiles.

ACKNOWLEDGMENT

The authors acknowledge the CEFET-MG for financial support.

REFERENCES

[1] U.S. Geol. Survey, “Mineral commodity summaries 2019”, Reston (2019) 200.
[2] Depto. Nac. Prod. Min., “Mineral summary 2017”, DNPM, Brasilia (2019) 36.
[3] Ag. Nac. Min., “Mineral report Jan-Jun 2018”, ANM, Brasilia (2018) 16.
[4] L. Rocha, A.E.C. Peres, Rev. Esc. Minas **62**, 3 (2009) 544.
[5] M.E.G. Boscov, *Environmental geotechnics*, Ofic. Textos, S. Paulo (2008) 248.
[6] A.P.M. da Silva, J.P. Viana, A.L.B. Cavalcante, “Diagnosis of solid waste from mining activity of non-energy substances”, Ipea, Brasilia (2012) 46.
[7] Fund. Est. Meio Amb., “Mining waste inventory, base year 2017”, FEAM, B. Horizonte (2018) 47.
[8] A.A. Campos, M.L. de A. Medeiros, R.R.C.C. Gerken, J.A. Nogueira, Rev. Pensar Eng. **5**, 1 (2017) 1.
[9] L.A. de C. Bastos, G.C. Silva, J.C. Mendes, R.A.F. Peixoto, J. Mater. Civ. Eng. **28**, 10 (2016).
[10] F.A. Kuranchie, S.K. Shukla, D. Habibi, Int. J. Min. Reclam. Environ. **30**, 2 (2016) 460.
[11] R. Kumar, P. Das, M. Beulah, H.R. Arjun, G. Ignatius, J. Adv. Manuf. Syst. **16**, 3 (2017) 410.
[12] S.A. Latif, M.S.A. Rahman, O. Sikiru, Rom. J. Mater. **47**, 3 (2017) 556.
[13] W.C. Fontes, J.C. Mendes, S.N. da Silva, R.A.F. Peixoto, Constr. Build. Mater. **112** (2016) 1158.
[14] P. Das, B. Matcha, N. Hossiney, M.K. Mohan, A. Roy, A. Kumar, in “Geopolymer science and applications”, IntechOpen (2018) 1.
[15] A.U. Shettima, M.W. Hussin, Y. Ahmad, J. Mirza, Constr. Build. Mater. **120** (2016) 642.
[16] L. Luo, Y. Zhang, S. Bao, T. Chen, Adv. Mater. Sci. Eng. **2016** (2016) 596047.
[17] W.C. Fontes, G.G. Fontes, E.C.P. Costa, J.C. Mendes, G.J.B. Silva, R.A.F. Peixoto, Amb. Constr. **18**, 4 (2018) 459.
[18] F.L. da Silva, F.G.S. Araújo, C.G. Castro, J.J. Mendes, F.L. von Krüger, Mater. Sci. Forum **775-776** (2014) 760.
[19] A.C.V. Zuccheratte, C.B. Freire, F.S. Lameiras, Constr. Build. Mater. **151** (2017) 859.
[20] Ass. Bras. Ind. Rochas Ornam., “Balance of Brazilian exports and imports of ornamental stones in 2018”, Rep. 01/2019, ABIROCHAS, Brasilia (2019).
[21] C.E.G. Ribeiro, R.J.S. Rodriguez, E.A. de Carvalho, Constr. Build. Mater. **149** (2017) 940.
[22] M.Y. Lee, C.H. Ko, F.C. Chang, S.L. Lo, J.D. Lin, M.Y. Shan, J.C. Lee, Cem. Concr. Comp. **30**, 7 (2008) 1026.
[23] T.H. Panzera, A.L.R. Sabariz, K. Strecker, P.H.R. Borges, D.C.L. Vasconcelos, W.L. Wasconcelos, Cerâmica **56**, 337 (2010) 77.
[24] E.A.S. Carvalho, V.R. Marques, R.J.S. Rodrigues, C.E.G. Ribeiro, S.N. Monteiro, C.M.F. Vieira, Mater. Res. **18**, suppl. 2 (2015) 301.
[25] C.E.G. Ribeiro, R.J.S. Rodriguez, C.M.F. Vieira, E.A. Carvalho, V.S. Candido, S.N. Monteiro, Mater. Sci. Forum

775-776 (2014) 760.
[26] L. Peng, S. Qin, Constr. Build. Mater. **171** (2018) 1016.
[27] M.L.P.M. Gomes, E.A.S. Carvalho, L.N. Sobrinho, S.N. Monteiro, R.J.S. Rodriguez, C.M.F. Vieira, J. Mater. Res. Technol. **7**, 4 (2018) 616.
[28] M.S. Rabello, *Polymer additivation*, Artliber, S. Paulo (2000).
[29] B. Pukanszky, in "Polypropylene: structure, blends and composites" **3**, J. Karger-Kocsis (Ed.), Germany (1994) 392.
[30] C. Ignacio, V. Ferraz, R.L. Oréfice, J. Appl. Polym. Sci. **108**, 5 (2008) 772.
[31] ABNT NBR 7181, "Soil: grain size analysis", Ass. Bras. Norm. Técn., Rio Janeiro (2004).
[32] ABNT NBR 10005, "Procedure for obtention leaching extract of solid wastes", Ass. Bras. Norm. Técn., Rio Janeiro (2004).
[33] ABNT NBR 10006, "Procedure for obtention of solubilized extraction of solid wastes", Ass. Bras. Norm. Técn., Rio Janeiro (2004).
[34] ASTM C373-88, "Test method for water absorption, bulk density, apparent porosity and apparent specific gravity of fired whiteware products", Am. Soc. Test. Mater. (2006).
[35] ASTM C1161-18, "Standard test method for flexural strength of advanced ceramics at ambient temperature", Am. Soc. Test. Mater. (2018).
[36] A.P. Wolff, G.M. da Costa, F.C. Dutra, in Proc. 3rd Int. Meet. Ironmaking, 2nd Int. Symp. Iron Ore, Maranhao (2008) 472.
[37] A.P. Wolff, G.M. da Costa, F.C. Dutra, Min. Proces. Extract. Metall. Rev. **32** (2011) 288.
[38] C.H. Maxwell, "Geology and ore deposits of the Alegria district, Minas Gerais, Brazil", US Dept. Interior, USA (1972).
[39] I.O. Barbosa, M.P.C. Lacerda, M.R. Bilich, Rev. Bras. Cien. Solo **33**, 5 (2009) 1917.
[40] ABNT NBR 10004, "Solid waste: classification", Ass. Bras. de Norm. Técn., Rio Janeiro (2004).
[41] W.C. Fontes, J.M.F. de Carvalho, L.C.R. Andrade, A.M. Segadães, R.A.R. Peixoto, Constr. Build. Mater. **206** (2019) 716.
[42] S.K. Jena, H. Sahoo, S.S. Rath, D.S. Rao, S.K. Das, B. Das, Min. Proces. Extrac. Metall. Rev. **36** (2015) 409.
[43] T.W.G. Solomons, C.B. Fryhle, *Organic chemistry*, 10th ed., Wiley (2009).
[44] ABNT NBR 15844, "Rocks for cladding: requirements for granite", Ass. Bras. Norm. Técn., Rio Janeiro (2010).
[45] ASTM C615-99, "Standard specification for granite dimension stone", Am. Soc. Test. Mater. (1999).
[46] H.M. Khater, Cerâmica **65**, 373 (2019) 153.
(Rec. 03/09/2019, Rev. 11/11/2019, Ac. 06/01/2020)

BY-NC

Produção de geopolímeros utilizando cinza da casca de arroz como fonte complementar de sílica

(Production of geopolymers using rice husk ash as supplementary source of silica)

P. H. Apolonio[1], J. S. Lima[1*], E. P. Marinho[2], A. C. V. Nobrega[2], J. C. O. Freitas[3], A. E. Martinelli[4]

[1]Universidade Federal de Pernambuco, Programa de Pós-graduação em Engenharia Civil, Centro de Tecnologia e Geociências, Recife, PE, Brasil

[2]Universidade Federal de Pernambuco, Programa de Pós-graduação em Engenharia Civil e Ambiental, Caruaru, PE, Brasil

[3]Universidade Federal do Rio Grande do Norte, Departamento de Química, Natal, RN, Brasil

[4]Universidade Federal do Rio Grande do Norte, Programa de Pós-graduação em Ciência e Engenharia de Materiais, Natal, RN, Brasil

Resumo

O silicato de sódio é a fonte complementar utilizada na reação de geopolimerização. Entretanto, esse reagente é produzido em alta temperatura ou em autoclave a alta pressão, o que gera muito impacto ambiental. Visando a produção de geopolímeros mais ecológicos, produziu-se um silicato de sódio alternativo (ASW) a partir da dissolução da sílica presente na cinza de casca de arroz (CCA). Foram preparados geopolímeros nas razões molares SiO_2/Al_2O_3 de 3,0, 3,5 e 4,0 e com concentrações de NaOH de 8 e 10 M. Os corpos de prova foram submetidos a ensaios de resistência à compressão (7 e 28 dias), FTIR e DRX. O desempenho mecânico dos geopolímeros produzidos com ASW foi semelhante aos produzidos com silicato de sódio comercial. A análise do comportamento mecânico e dos espectros de infravermelho sugeriu que ocorreu maior dissolução da CCA com o aumento da relação molar SiO_2/Al_2O_3 e da concentração do álcali.

Palavras-chave: geopolímero, cinza da casca de arroz, silicato de sódio, fonte alcalina.

Abstract

Sodium silicate is a complementary source used in the geopolymerization reaction. However, this reagent is produced at high temperature or in an autoclave at high pressure, which generates a significant environmental impact. Aiming the production of greener geopolymers, an alternative sodium silicate (ASW) from the dissolution of silica present in rice husk ash (RHA) was produced. Geopolymers were prepared at SiO_2/Al_2O_3 molar ratios of 3.0, 3.5, and 4.0, and concentrations of 8 and 10 M NaOH. The specimens were subjected to compressive strength (7 and 28 days), FTIR and XRD tests. The mechanical performance of ASW-produced geopolymers was similar to those made with commercial sodium silicate. Analysis of the mechanical behavior and infrared spectra suggested that there was a greater dissolution of RHA with increasing SiO_2/Al_2O_3 molar ratio and alkali concentration.

***Keywords**: geopolymer, rice husk ash, sodium silicate, alkaline source.*

INTRODUÇÃO

Os geopolímeros são polímeros inorgânicos reticulados de longa cadeia formados por unidades tetraédricas de AlO_4 e SiO_4, obtidos em meio fortemente alcalino [1, 2]. Possuem uma estrutura tridimensional no estado amorfo [1], resultante da polimerização de monômeros de aluminossilicato em uma solução alcalina [3]. Os geopolímeros apresentam alta resistência à compressão e durabilidade [1, 4-6], baixa retração, baixa condutividade térmica, resistência ao fogo, resistência ao ácido [4, 5, 7], resistência à corrosão e resistência à umidade [8]. Entre as diversas aplicações dos materiais geopoliméricos, destaca-se seu uso como aglomerante. Entre os componentes que são utilizados para a produção do concreto geopolimérico, o mais impactante do ponto de vista energético e da emissão de CO_2 é o silicato de sódio que demanda 63,4% da energia e é responsável por 67,2% da emissão de CO_2 [9]. Os silicatos de sódio e potássio comerciais são utilizados como fonte complementar de sílica (solúvel na solução ativadora) na produção do geopolímero, e leva à formação de uma estrutura compacta e densa, com alta resistência mecânica. Entretanto, este componente é o mais caro para produção do geopolímero e sua produção provoca grande impacto ambiental, devido ao seu processo de fabricação [10, 11].

**jofresl@gmail.com*
https://orcid.org/0000-0001-6097-6230

Sabe-se que a emissão de CO_2 pelo concreto geopolimérico é até 3,6 vezes menor do que a emissão pelo concreto tradicional. A síntese de geopolímeros pode ser ainda mais ecológica se forem utilizadas matérias-primas mais limpas para produção de silicato de sódio. Ativadores alcalinos baseados em silicato de potássio comercial fornecem uma emissão maior de CO_2, aproximadamente 1,1 ton/m^3 de geopolímero produzido, enquanto ativadores baseados em fontes alternativas geram em torno de 572,3 kg/m^3 para a cinza da casca de arroz e 660,2 kg/m^3 para a sílica ativa, sendo assim, considerados materiais mais ecologicamente corretos [12]. Em todo o mundo e no Brasil a produção de arroz é grande, atingindo em 2014 cerca de 741,3 milhões [13] e 12,1 milhões [13] de toneladas, respectivamente. A casca de arroz quando queimada nas caldeiras gera cerca de 25% de cinza, o que corresponde a aproximadamente 40,8 milhões de toneladas/ano de cinza da casca de arroz no mundo, sendo 665,5 mil toneladas no Brasil [14]. A cinza da casca de arroz (CCA) torna-se uma opção interessante para produção do silicato de sódio por possuir alto teor de SiO_2 amorfo (80-95% em massa) [15], podendo ser dissolvida em solução alcalina [2, 6, 16-20]. Além disso, a casca do arroz é o principal resíduo vegetal na produção de cinza através do processo de incineração [21].

Diversos estudos [2, 6, 16-20] apontam o silicato de sódio obtido através de CCA como um ativador alcalino eficiente para produção de geopolímeros, apresentando valores de resistência mecânica semelhante aos valores obtidos com silicatos de sódio comerciais. No entanto, faltam estudos mais aprofundados referentes à substituição total do silicato de sódio comercial pelo silicato de sódio produzido através da dissolução de CCA em hidróxido de sódio para produção de geopolímeros. O objetivo desta pesquisa foi sintetizar silicato de sódio a partir da dissolução em meio alcalino da sílica existente na CCA e uso deste silicato como fonte complementar para produção de geopolímeros. Para tal, foi estudada a influência da concentração do hidróxido de sódio e da relação SiO_2/Al_2O_3 na resistência à compressão e na estrutura, por espectroscopia no infravermelho com transformada de Fourier (FTIR) e difração de raios X (DRX), das pastas geopoliméricas produzidas.

MATERIAIS E MÉTODOS

Materiais: o precursor geopolimérico empregado para produção dos geopolímeros foi o Metacaulim HP (MK) da Metacaulim do Brasil. Foi utilizado hidróxido de sódio (pureza mínima de 97%) da Química Moderna e o silicato de sódio neutro R3342 da Diatom Mineração como fonte complementar de sílica. A cinza de casca de arroz (CCA) utilizada foi Silroz 325 da Marina Tecnologia (Rio Grande Sul/Brasil). As características físico-químicas das matérias-primas são apresentada na Tabela I. O pó de CCA se apresentou como uma estrutura composta principalmente de partículas irregulares e porosas [22].

Síntese do silicato de sódio: foram produzidas soluções ativadoras usando CCA como fonte de sílica. Os silicatos de sódio foram preparados em solução aquosa de NaOH (8 e 10 M). As soluções foram aquecidas em sistema de refluxo a 90 °C por 2 h. Para garantir a temperatura e uniformidade do sistema, foi utilizado evaporador rotativo, mantendo rotação controlada em 2 rpm em banho de óleo.

Tabela I - Características físico-químicas do metacaulim (MK), silicato de sódio comercial (SW) e cinza de casca de arroz (CCA).
[Table I - Physico-chemical characteristics of metakaolin (MK), commercial sodium silicate (SW), and rice husk ash (RHA).]

Característica	MK	SW[#]	CCA
SiO_2 (%)	53,06	30,0	80,00
Al_2O_3 (%)	36,50	-	-
Na_2O (%)	-	9,0	-
K_2O (%)	1,36	-	3,44
CaO (%)	0,86	-	1,14
MgO (%)	0,27	-	-
Fe_2O_3 (%)	4,42	-	0,82
MnO (%)	-	-	2,85
SO_3 (%)	-	-	1,34
Outros (%)	1,37	-	0,82
Perda ao fogo (%)	2,15	39,0	9,59
Umidade (%)	1,18	61,0	2,41
Massa específica (g/cm^3)	2,53	1,41	2,16
Área específica* (m^2/kg)	1242	-	1672

[#] *- dados do fornecedor; * - medida pelo método Blaine.*

Síntese do geopolímero: os geopolímeros foram preparados adicionando a solução ativadora gradativamente ao metacaulim e misturado durante 5 min. Um resumo das misturas está relatado na Tabela II. Após mistura, as amostras de geopolímero fresco foram colocadas rapidamente em recipientes cilíndricos com dimensões 25x50 mm confeccionados em PVC [23]. A cura das amostras de geopolímero foi realizada ao ar e temperatura ambiente (25 ºC).

Caracterização das matérias-primas, silicatos de sódio e geopolímeros: as composições químicas do metacaulim (MK) e da cinza de casca de arroz (CCA) foram determinadas por fluorescência de raios X (XRF), em espectrômetro Ray Ny EDX-720, Shimadzu. As análises de DRX foram feitas no difratômetro XRD-6000, Shimadzu, com as seguintes condições de operação: radiação CuKα (40 kV/30 mA), velocidade do goniômetro de 0,02° 2θ por passo com tempo de contagem de 1,0 s por passo e no intervalo 2θ de 10º a 80º. As curvas termogravimétricas foram obtidas em termobalança SDT Q500, TA Instruments, com taxa de aquecimento de 10 °C/min até 900 °C em atmosfera de ar com vazão de 60 mL/min. Os espectros de infravermelho (FTIR) foram obtidos no espectrofotômetro IRPrestige-21, Shimadzu, sendo as amostras analisadas na forma de pastilhas de KBr no intervalo espectral entre 4000 e 400 cm^{-1}

Tabela II - Resumo das pastas geopoliméricas produzidas.
[Table II - Summary of geopolymers produced.]

Amostra	Razão molar SiO_2/Al_2O_3	Molaridade	Silicato utilizado
3.0NaOH8SW	3,0	8 M	SW
3.0NaOH10SW	3,0	10 M	SW
3.5NaOH8SW	3,5	8 M	SW
3.5NaOH10SW	3,5	10 M	SW
4.0NaOH8SW	4,0	8 M	SW
4.0NaOH10SW	4,0	10 M	SW
3.0NaOH8ASW	3,0	8 M	ASW
3.0NaOH10ASW	3,0	10 M	ASW
3.5NaOH8ASW	3,5	8 M	ASW
3.5NaOH10ASW	3,5	10 M	ASW
4.0NaOH8ASW	4,0	8 M	ASW
4.0NaOH10ASW	4,0	10 M	ASW

SW: silicato de sódio comercial; ASW: silicato de sódio de CCA.

e resolução de 2 cm^{-1}. A resistência à compressão uniaxial dos geopolímeros foi medida aos 7 e 28 dias à temperatura ambiente usando uma prensa hidráulica de acionamento elétrico e módulo eletrônico de leitura (PC200C, Imec) com capacidade de 2000 kN e velocidade de carregamento correspondente de 0,20 MPa/s. Foram ensaiadas três amostras para cada medida e determinados os valores médios.

RESULTADOS E DISCUSSÃO

Caracterização das matérias-primas e do silicato de sódio

Na Tabela I são apresentados os resultados de composição química. Observou-se que o metacaulim (MK) apresentou SiO_2 e Al_2O_3 em elevadas proporções, 53,06% e 36,50%, respectivamente. O teor de SiO_2 da cinza de casca de arroz (CCA) foi de aproximadamente 80% e os demais óxidos estavam presentes como impurezas [2]. A CCA apresentou óxido férrico, que não foi encontrado no silicato comercial. Embora a presença de ferro em geopolímeros seja um assunto ainda pouco estudado, é provável que a presença deste elemento químico altere a reação de geopolimerização [24]. Gomes et al. [25] sugerem que a relação atômica silício/alumínio seria semelhante à relação atômica silício/(alumínio+ferro) para precursores ricos em ferro. No difratograma de raios X do MK (Fig. 1a), observou-se a predominância de halo amorfo na faixa entre 15° e 32°, indicando que houve sílica e alumina amorfa [15]; observaram-se também picos característicos de impurezas de quartzo (2θ 26,6°) e muscovita em menor quantidade [26, 27]. A presença dessas fases cristalinas afeta a reatividade do MK durante a geopolimerização. Pela análise do difratograma foi possível concluir que o MK não possuiu a estrutura da caulinita, caracterizando um material reativo adequado à reação de geopolimerização [13]. No difratograma de raios X da CCA (Fig. 1b), foram observados picos cristalinos característicos de cristobalita desordenada e o halo amorfo próximo de 15-30°. A fase cristobalita foi confirmada pelos picos em 21,94°, 28,44°, 30,51° e 36,06° [28].

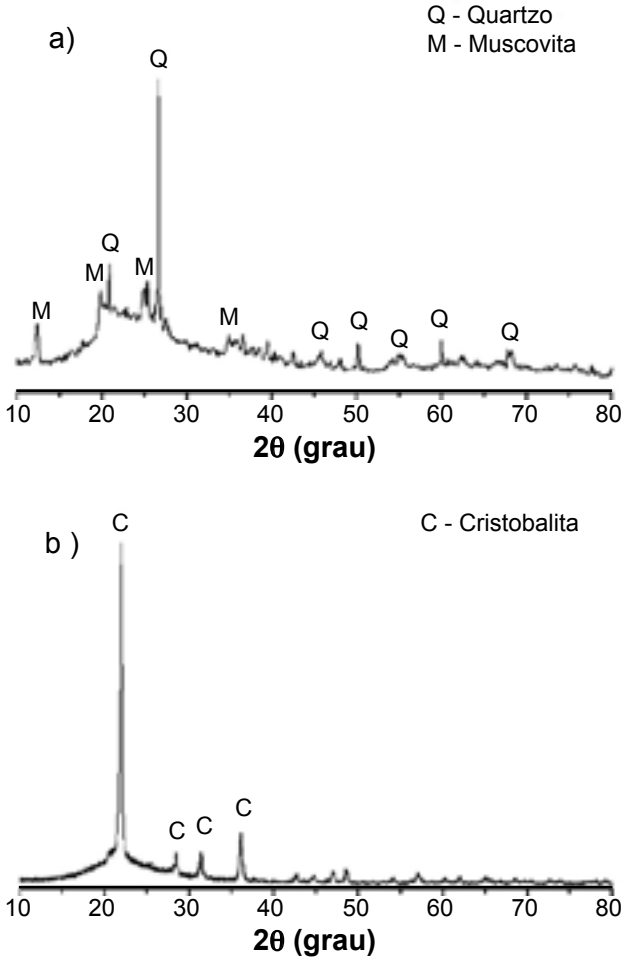

Figura 1: Difratogramas de raios X de: a) metacaulim (MK); e b) cinza da casca de arroz (CCA).
[Figure 1: XRD patterns of: a) metakaolin (MK); and b) rice husk ash (RHA).]

A curva de termogravimetria (TG) do MK (Fig. 2a) apresentou perda de massa inicial menor que 1% relacionada à umidade. No intervalo entre 400 e 800 °C, a perda de massa foi da ordem de 8% atribuída à liberação das hidroxilas estruturais, sugerindo que o processo industrial foi eficiente e que a amostra foi predominantemente MK [29], conforme já sugerido pelos dados de DRX (Fig. 1a). Em relação à CCA (Fig. 2b), a análise da decomposição térmica indicou perda de aproximadamente 3% de massa até 100 °C. Essa região foi relacionada à perda de água fisicamente adsorvida. Entre 102 e 600 °C, observou-se a decomposição da celulose e da lignina [22]. Na curva termogravimétrica da CCA, houve um conjunto de eventos sucessivos entre 350 e 900 °C totalizando aproximadamente 8% de perda de massa.

Não foi possível distinguir os processos individuais nas condições que foi conduzido o experimento, mas as etapas previstas até 600 °C devem ter se somado a outros eventos de pirólise da matéria orgânica remanescente. De qualquer forma, menos de 10% da amostra foi material orgânico, o que mostrou que esta cinza teve um adequado tratamento térmico [30].

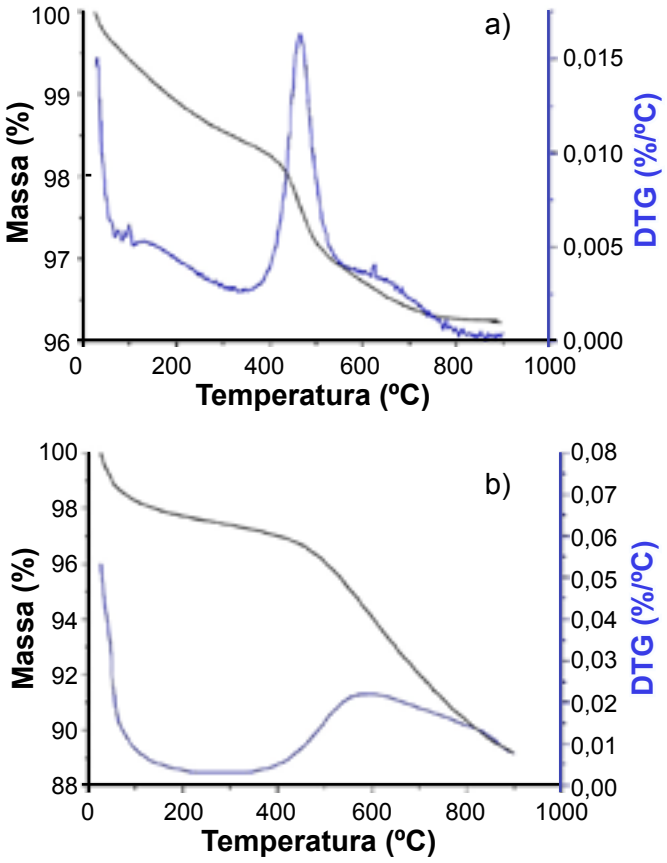

Figura 2: Curvas de TG e DTG (derivada da TG) de: a) MK; e b) CCA.
[Figure 2: TG and DTG (derivative of TG) curves of: a) MK; and b) RHA.]

O estiramento assimétrico da ligação Si-O-Si do MK (Fig. 3a) aconteceu no intervalo entre 1074 e 811 cm^{-1} devido à presença de sílica amorfa [26]. No espectro FTIR mostrado na Fig. 3a, observa-se um ombro em 1069 cm^{-1} atribuído a este estiramento. As bandas características da caulinita entre 1400 a 400 cm^{-1} não foram observadas no espectro do MK. As bandas em 777, 1345 e 469 cm^{-1} são características do MK. De acordo com esses dados, o material passou por um eficiente processo de desidroxilação, com potencial de ser um bom precursor geopolimérico. No espectro FTIR da CCA (Fig. 3b), as vibrações em 3450 cm^{-1} foram características do estiramento -OH, HOH [31-34]. O pico em 1090 cm^{-1} foi relacionado à vibração de alongamento assimétrico Si-O-Si e dá uma indicação do comprimento e ângulo das ligações em uma rede de silicato [2]. O pico observado em 798 cm^{-1} correspondeu à vibração de alongamento simétrico Si-O-Si e o pico em 465 cm^{-1} foram de vibrações de deformação angular Si-O-Si ou O-Si-O. Identificou-se também um pico em 465 cm^{-1} associado ao grau de 'amorfização' do material [28].

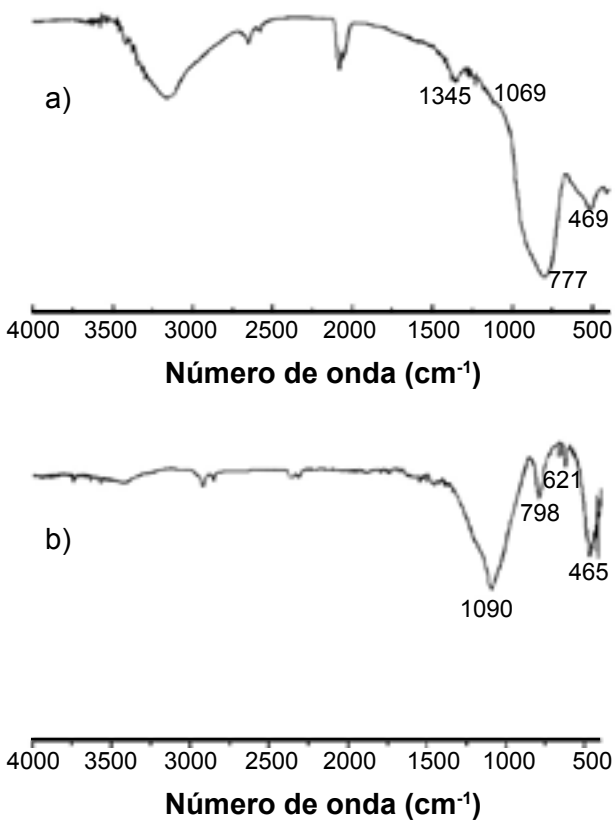

Figura 3: Espectros de FTIR de: a) MK; e b) CCA.
[Figure 3: FTIR spectra of: a) MK; and b) RHA.]

Caracterização dos geopolímeros

Resistência à compressão: na Fig. 4a são apresentados os dados de resistência à compressão dos geopolímeros produzidos a partir do silicato de sódio comercial, onde se pode verificar que a relação SiO_2/Al_2O_3 igual a 4,0 resultou no melhor desempenho, com incremento aos 28 dias. Para geopolímeros, o aumento da resistência à compressão está associado à maior dissolução dos aluminossilicatos, que são determinantes no processo de formação da rede tridimensional [35]. Os dados de resistência à compressão dos geopolímeros produzidos com silicato de sódio de cinza de casca de arroz (ASW) estão apresentados na Fig. 4b. Observou-se que a maior resistência à compressão também foi da amostra com razão SiO_2/Al_2O_3 de 4,0 e concentração de hidróxido de sódio igual a 10 M, podendo estar associada com a formação de oligômeros [36]. Observam-se resultados semelhantes na literatura [2, 6, 35], confirmando que o silicato de sódio produzido com a cinza da casa de arroz contribuiu para formação de estrutura mais densa e compacta, aumentando a resistência do geopolímero. A resistência à compressão mais baixa foi relacionada com a menor quantidade de átomos de Si e razoável ausência de sílica solúvel do silicato de sódio

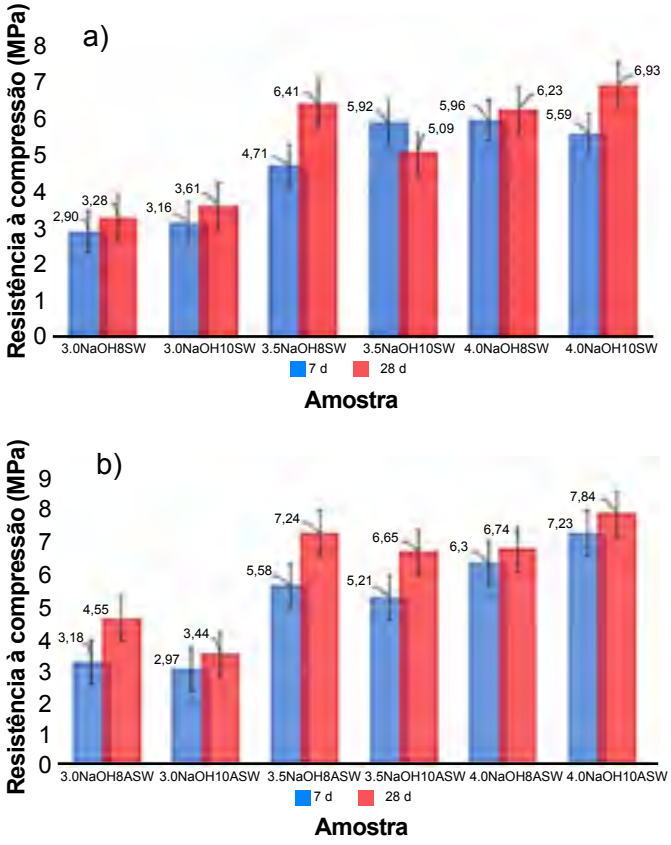

Figura 4: Resistência à compressão dos geopolímeros fabricados com SW (a) e ASW (b).
[Figure 4: Compressive strength of geopolymers prepared with SW (a) and ASW (b).]

a partir da cinza da casca de arroz [2]. O excesso de álcali propicia a formação de carbonato de sódio, logo, os álcalis devem ser suficientes apenas para garantir o equilíbrio das redes de geopolimerização.

Espectroscopia no infravermelho: nos espectros FTIR dos geopolímeros (Fig. 5) foi identificado que ocorreu o processo de geopolimerização através da formação de um gel, comprovado pelas bandas entre 1001 e 1024 cm^{-1}. Pode-se considerar o grau de geopolimerização através destas bandas características, que são atribuídas ao estiramento assimétrico das ligações Si-O-Si e Si-O-Al [2]. Observou-se que os picos em 1069 e 798 cm^{-1} nos espectros de infravermelho do MK e da CCA, respectivamente, sofreram deslocamento no processo de geopolimerização para o número de onda a 1001 cm^{-1} proveniente da dissolução dos materiais, gerando a reorganização das redes de aluminossilicatos [37]. A presença de bandas próximas a 1567 cm^{-1} atribuídas a carbonatos pode ser explicada pela existência de hidróxido de sódio ou silicato de sódio que não participaram da reação de geopolimerização, deixando íons Na^+ disponíveis para reagir com CO_2 atmosférico [37]. Em geopolímeros, a frequência das bandas de absorção está relacionada com a razão Si/Al; quanto maior a quantidade de átomos de alumínio, maior é a tendência de deslocamento dos picos de absorção de cerca de 80-90 cm^{-1} na direção dos números de onda mais baixos [2, 37].

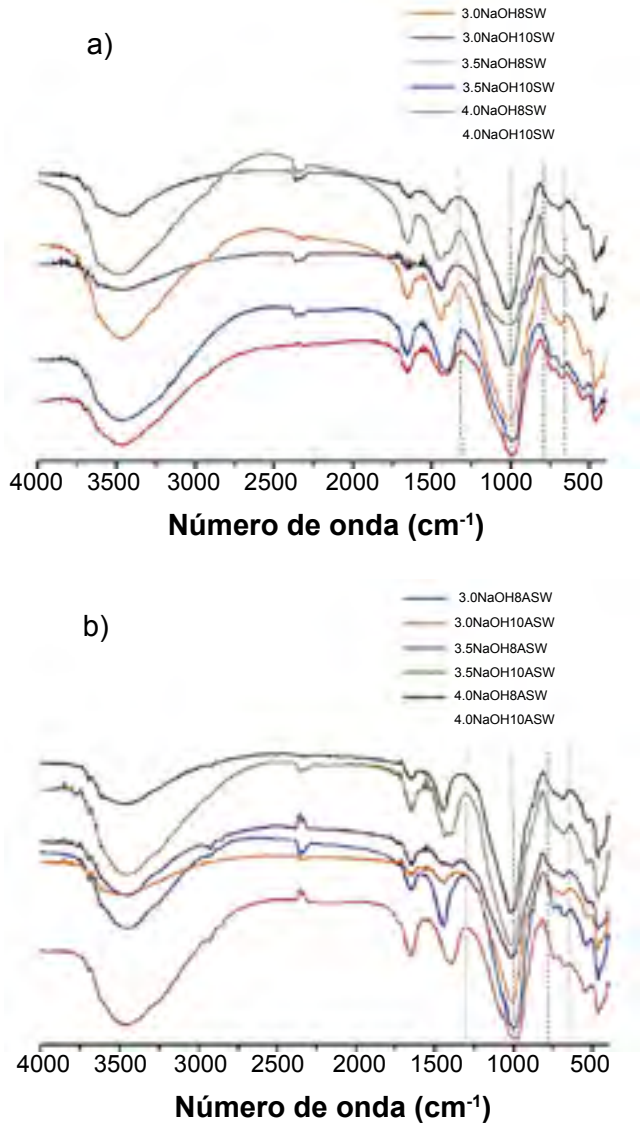

Figura 5: Espectro de FTIR de geopolímeros fabricados com SW (a) e ASW (b).
[Figure 5: FTIR spectra of geopolymers prepared with SW (a) and ASW (b).]

Os espectros FTIR das amostras de geopolímeros produzidas com o silicato de sódio de cinza de casca de arroz (ASW) mostraram a dissolução da cinza da casca de arroz através da ausência do pico característico em 850 cm^{-1} e formação de bandas entre 706 e 714 cm^{-1} referentes aos tetraedros dos geopolímeros [17]. Nos espectros foi observado pico em 710 cm^{-1}, sugerindo a formação de Al tetraédrico relacionada ao processo de geopolimerização [37]. O pico em 501 cm^{-1} se refere à formação de material cristalino através da ligação Si-O-Si, sugerindo que as fases encontradas nos precursores geopoliméricos não participaram da reação, comprovando a atribuição de sílica cristalina [2, 37]. As bandas próximas à região de 460 cm^{-1} são relacionadas aos planos de curvatura de Al-O e Si-O que são encontrados na faixa de 463 a 672 cm^{-1} [37]. As bandas entre 950 e 1150 cm^{-1} resultaram da reação de geopolimerização do

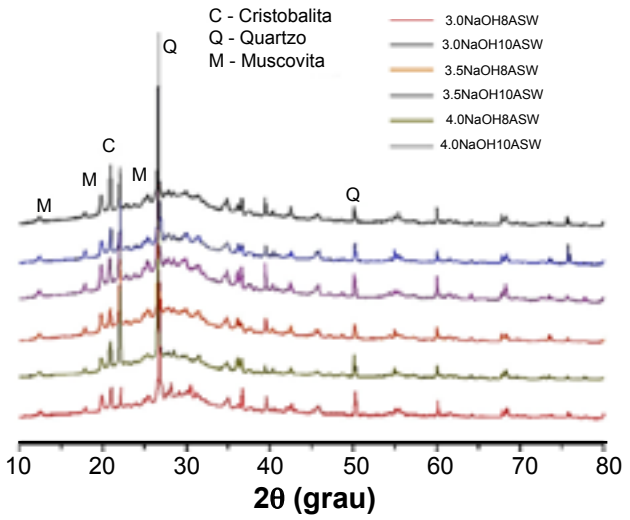

Figura 6: Difratogramas de raios X dos geopolímeros produzidos com silicato de sódio de CCA (ASW).
[Figure 6: X-ray diffraction patterns of geopolymers prepared with ASW.]

metacaulim com a solução ativadora [10]. Todas as amostras de geopolímeros produzidas com silicato de sódio comercial (SW) e silicato de sódio de cinza de casca de arroz (ASW) apresentaram bandas entre 998 e 1038 cm^{-1} com estiramento assimétrico de Si-O-Si e Si-O-Al, sugerindo que em todas as amostras ocorreu a formação de geopolímero.

Difratogramas de raios X de geopolímeros com silicato de sódio de CCA (ASW): na Fig. 6 são mostrados os difratogramas de raios X dos geopolímeros produzidos com silicato de sódio de cinza de casca de arroz. Foi possível identificar uma predominância de um halo amorfo característico em todas as amostras no intervalo 2θ de 20° a 35° [12], indicando a formação de um gel amorfo durante o processo de geopolimerização. O quartzo e a muscovita foram as principais fases cristalinas encontradas nos geopolímeros produzidos e foram oriundas do metacaulim utilizado na reação. Isso sugeriu que estas formas de sílica não reagem. Entretanto, observou-se que a cristobalita, forma de sílica mais reativa, parece participar da reação, uma vez que a intensidade dos picos desta fase foi reduzida nos geopolímeros.

CONCLUSÕES

De acordo com os dados obtidos, foi possível usar cinza de casca de arroz (CCA) para produzir geopolímeros. Os resultados sugeriram que tanto a concentração de NaOH quanto a relação SiO_2/Al_2O_3 afetam muito a resistência à compressão das amostras de geopolímeros resultantes. Acredita-se que as impurezas presentes na CCA não afetaram o sistema, uma vez que os melhores resultados foram alcançados nas amostras com maior razão molar SiO_2/Al_2O_3, portanto, com maior quantidade de CCA. As amostras de geopolímero preparadas com solução de NaOH 10 M e silicato de sódio com cinza de casca de arroz apresentaram resistência à compressão que foram comparáveis ou mesmo superiores às amostras produzidas com silicato de sódio comercial. Os dados de FTIR confirmaram que a geopolimerização ocorreu de maneira similar nas amostras independente do silicato de sódio utilizado.

AGRADECIMENTOS

Os autores agradecem ao CNPq pelo apoio financeiro - Projeto Casadinho/PROCAD, e às empresas Metacaulim do Brasil e Diatom Mineração pelas amostras doadas.

REFERÊNCIAS

[1] M. Xu, Y. He, C. Wang, X. He, X. He, J. Liu, X. Cui, Appl. Clay Sci. **115** (2015) 254.
[2] H.K. Tchakouté, C.H. Rüscher, S. Kong, E. Kamseu, C. Leonelli, Constr. Build. Mater. **114** (2016) 276.
[3] E. Najafi Kani, A. Allahverdi, J.L. Provis, Cem. Concr. Compos. **34** (2012) 25.
[4] R. Pouhet, M. Cyr, Constr. Build. Mater. **120** (2016) 150.
[5] P. Duxson, S.W. Mallicoat, G.C. Lukey, W.M. Kriven, J.S.J. van Deventer, Colloid Surface A **292** (2007) 8.
[6] H.K. Tchakoute, C.H. Rüscher, J.N.Y. Djobo, B.B.D. Kenne, D. Njopwouo, Appl. Clay Sci. **107** (2015) 188.
[7] S. Zeng, J. Wang, Constr. Build. Mater. **121** (2016) 386.
[8] T. Wang, Y. Xue, M. Zhou, Y. Lv, Y. Chen, S. Wu, H. Hou, Constr. Build. Mater. **131** (2017) 361.
[9] B.C. McLellan, R.P. Williams, J. Lay, A. van Riessen, G.D. Corder, J. Clean. Prod. **19** (2011) 1080.
[10] M. Criado, A. Palomo, A. Fernandez-Jimenez, Fuel **84** (2005) 2048.
[11] K.-H. Yang, J.-K. Song, A.F. Ashour, E.-T. Lee, Constr. Build. Mater. **22** (2008) 1981.
[12] M.A. Villaquirán-Caicedo, R.M. de Gutiérrez, Mater. Lett. **230** (2018) 300.
[13] R. Pode, Renew. Sust. Energ. Rev. **53** (2016) 1468.
[14] K.K. Rao, P. Pranav, D. Anusha, Int. J. Eng. Sci. Technol. **3** (2011) 8076.
[15] J. He, "Synthesis and characterization of geopolymers for infrastructural applications", Doct. Diss., LSU, Louisiana (2012).
[16] U. Kalapathy, Bioresour. Technol. **73** (2000) 257.
[17] E.L. Foletto, E. Gratieri, L.H. de Oliveira, S.L. Jahn, Mater. Res. **9** (2006) 335.
[18] V. Živica, Cem. Concr. Compos. **28** (2006) 21.
[19] S.A. Bernal, E.D. Rodríguez, R. Mejia De Gutiérrez, J.L. Provis, S. Delvasto, Waste Biomass Valori. **3** (2012) 99.
[20] E. Kamseu, L.M. Beleuk à Moungam, M. Cannio, N. Billong, D. Chaysuwan, U.C. Melo, C. Leonelli, J. Clean. Prod. **142** (2017) 3050.
[21] FAO, "The state of food and agriculture: innovation in family farming", Food Agric. Org. UN, Rome (2017).
[22] D. Geetha, A. Ananthiand, P.S. Ramesh, Res. Rev. J. Pure Appl. Phys. **4** (2016) 20.
[23] F. Slaty, H. Khoury, H. Rahier, J. Wastiels, Appl. Clay Sci. **104** (2015) 229.

[24] J.S. Lima, "Efeito da relação molar SiO_2/Al_2O_3 e das condições de cura nas propriedades de geopolímeros obtidos com silicato de cinza da casca de arroz", Diss. Mestr., Un. Fed. Pernambuco, Caruaru (2018).
[25] K.C. Gomes, S.M. Torres, Z.E. da Silva, N. Perazzo Barbosa, M.R.F. Lima Filho, Key Eng. Mater. **600** (2014) 329.
[26] M. Sarkar, K. Dana, S. Das, J. Mol. Struct. **1098** (2015) 110.
[27] I. Ozer, S. Soyer-Uzun, Ceram. Int. **41** (2015) 10192.
[28] C.L. Hwang, T.P. Huynh, Constr. Build. Mater. **101** (2015) 1.
[29] A. Gharzouni, E. Joussein, B. Samet, S. Baklouti, S. Rossignol, J. Non Cryst. Solids **410** (2015) 127.
[30] G.C. Cordeiro, R.D. Toledo Filho, E.M.R. Fairbairn, Amb. Constr. **9** (2009) 99.
[31] P. Yu, R.J. Kirkpatrick, B. Poe, P.F. McMillan, X. Cong, J. Am. Ceram. Soc. **82** (2004) 742.
[32] R. García, R. Vigil de la Villa, I. Vegas, M. Frías, M.I. Sánchez de Rojas, Constr. Build. Mater. **22** (2008) 1484.
[33] I. García Lodeiro, A. Fernández-Jimenez, A. Palomo, D. Macphee, Cem. Concr. Res. **40** (2010) 27.
[34] J. Madejova, P. Komadel, Clays Clay Miner. **49** (2001) 410.
[35] Y.M. Liew, C.Y. Heah, A.B. Mohd Mustafa, H. Kamarudin, Prog. Mater. Sci. **83** (2016) 595.
[36] H. Xu, J.S.J. van Deventer, Miner. Eng. **15** (2002) 1131.
[37] M. Romagnoli, C. Leonelli, E. Kamse, M. Lassinantti Gualtieri, Constr. Build. Mater. **36** (2012) 251.
(Rec. 05/07/2019, Rev. 29/12/2019, 04/01/2020, Ac. 07/01/2020)

BY-NC

Utilization of diverse cheap materials as pore generating agent to manufacture low-cost porous ceramic

(Utilização de diversos materiais baratos como agente gerador de poros na fabricação de cerâmica porosa de baixo custo)

M. M. Salman[1], N. S. Radhi[1], O. H. Sabr[1], H. T. Nhabih[1]*
[1]Babylon University, Faculty of Materials Engineering, Babylon, Iraq

Abstract

Paper waste, corn starch, and sawdust were utilized as pore generating agents to produce a porous ceramic. Kaolin clay, sodium feldspar, and 20% of pore generating agent were mixed, and the samples were formed by mold method, dried at room temperature for about 72 h and in a furnace at 115 ºC for 5 h, and then fired at 1200 ºC with a soaking time of 3 h. The samples were tested for measurement of physical and mechanical properties and the microstructure was evaluated by scanning electron microscopy and mercury intrusion porosimetry. The results showed that the sample prepared with corn starch had the highest porosity, lowest mechanical properties and permeability, and smallest pore size, while the characteristics of the sample prepared with sawdust were contrary; finally, the sample of paper waste had the highest permeability and intermediate values of other properties.
Keywords: porous ceramics, paper waste, corn starch, sawdust.

Resumo

Resíduo de papel, amido de milho e serragem foram utilizados como agentes geradores de poros para produzir uma cerâmica porosa. Argila caulinítica, feldspato sódico e 20% de agente gerador de poros foram misturados e as amostras foram conformadas pelo método do molde, secas à temperatura ambiente por cerca de 72 h e em forno a 115 ºC por 5 h, e depois queimadas a 1200 ºC com um tempo de patamar de 3 h. As amostras foram ensaiadas para medição das propriedades físicas e mecânicas e a microestrutura foi avaliada por microscopia eletrônica de varredura e porosimetria por intrusão de mercúrio. Os resultados mostraram que a amostra preparada com amido de milho apresentou a maior porosidade, menores propriedades mecânicas e permeabilidade, e menor tamanho de poro, enquanto as características da amostra preparada com serragem foram contrárias; finalmente, a amostra de resíduo de papel apresentou a maior permeabilidade e valores intermediários de outras propriedades.
***Palavras-chave**: cerâmica porosa, resíduo de papel, amido de milho, serragem.*

INTRODUCTION

The recycling of some waste materials in the ceramic manufacturing has been widely studied in recent years, in order to economically justify the great costs related to its manufacture as well as to avoid the landfill of these wastes [1-5]. Porous ceramic has many fields of application, ranging from catalyst supports to filters for molten metals, high-temperature thermal insulation, separators in electrochemical reactors, bioreactors and bone tissue engineering, light-weight sandwich structures, microporous membranes for water purification, and wastewater treatment. Also, porous ceramic preforms are utilized for the preparation of ceramic-polymer and ceramic-metal composites [6]. Ceramics can outperform their polymer and metal competitors for many applications due to their relatively low density, which means lightweight, corrosion resistance, including hot corrosive liquids and gases, thermal stability, chemical inertness, and high-temperature structural stability [7]. Ceramics have excellent mechanical and thermal properties that have been widely used for tribological applications [8].

Depending on the intended application, the requirements of the ceramic microstructures are different. For example, the fluid transport with fluids ranging from gases to suspensions requires open pores and permeability, and separation efficiency depends on the degree of pore opening, connectivity, size, cross-section shape, and uniformity. Thermal insulation requires closed pores, and the thermal conductivity for porous ceramic may be lower than that of air, as the pore size is small enough, nanosized, i.e., lower than the mean free path for the gas particles enclosed. On the other hand, porous bioceramics for bone ingrowth require open pores with a high degree of connectivity and a small pore size in the range of 100 to 200 μm, and catalyst supports are often in the form of functionally graded material systems with a layered structure of variable porosity and/or pore size and a top layer with a high surface area. Rather special applications exist for porous ceramic with tailored electrical properties. For example, porous piezoelectric ceramic is

**eng.hussein.t@uobabylon.edu.iq*
https://orcid.org/0000-0003-3071-4998

advantageous for medical imaging and hydrophones, due to its improved pairing with liquid or biological tissue because of the matching of the acoustic impedance [9]. The production of porous ceramic often comprises a material that decomposes through the thermal treatment of sintering by melting, evaporation, decomposition, or burning [10]. For example, the decomposition of urea described in [11], the melting and vaporization of poly(methyl methacrylate) studied in [12], or the burning of flour researched in [13]. The variety of substances utilized to generate porosity in ceramics is large [10]. The use of a temperature-sensitive substance to generate porosity in support is employed in the fabrication of membranes of advanced ceramics such as zirconia, titania, and alumina, and traditional compositions with sawdust [14], and local raw materials such as clay [15] and perlite [16]. Various substances have been utilized as pore formers beginning with natural products such as poppy seeds [17], rice bran [18], and palm fibers [19], going through chemically pure materials such as urea [11] and ending in treated materials such as corn starch [20] or wastes such as fly ash [21] and sawdust [14].

In the present study, a paper waste, corn starch, and sawdust were used as a pore-forming agent with kaolin clay and sodium feldspar to produce a low-cost porous ceramic. The clay consisted of kaolinite, which gave plasticity to the green paste and was the precursor of mullite crystals [22]. The materials used as a pore-forming agent in this study were cheap, easy to burn, non-toxic, and environmentally non-hazardous [10]. Starch is largely used as a substance to generate porosity in the ceramic body since it produces pores through burning out at about 500 ºC [20, 23, 24]. Also, the paper waste is one of the environmental problems of solid wastes, where it is one of the common problems from which the countries suffer, due to its harmful effects on the environmental and general health [25]. The paper waste and sawdust are solid wastes, and they are employed to form pores in ceramics during the firing stage. This study aims to prepare, compare, and determine the material which can be more suitable between diverse cheap kinds of materials used as a pore generating agent to manufacture low-cost porous ceramic. The use of three different types of materials as a pore generating agent in the same clayey mass gives the chance to study the sample properties without varying the ratio of the raw materials or the processing variables through the experiments, and it gives the chance to compare between these properties to determine the material which provides an excellent combination to the mechanical and physical properties in the ceramic.

MATERIALS AND METHODS

In this study, paper waste, corn starch, and sawdust were used as a pore-forming agent with kaolin clay used as matrix material and sodium feldspar used as flux material to produce low-cost porous ceramics. Na-feldspar was used to obtain acceptable mechanical properties for the porous ceramic body because it contributes to the densification of the fired ceramic materials. Although the use of Na-feldspar reduces the porosity of the samples, it is beneficial to obtain an acceptable combination of mechanical properties and porous structure for the samples.

Data of raw materials and residues: an Iraqi kaolin clay was used as matrix material; its chemical composition is shown in Table I, while the physical properties are shown in Table II. As pore-forming agents, the paper waste used was residues of the paper used for writing; the sawdust used was taken from residuals of the wood obtained from big trees and its dry density was 1.63 g/cm^3, and moisture content was 16.7 wt%; and the corn starch made in Iraq had dry density and moisture content of 1.51±0.02 g/cm^3 and 14.6 wt%, respectively [26], while its particle size distribution varied from 35 to 75 μm.

Preparation of sawdust included drying in a furnace at 115 ºC for 3 h to eliminate the moisture, then grinding and sieving to obtain a powder with particle size less than 98 μm. Preparation of paper waste included passing the used paper through an apparatus of scrap paper-reduction several times to reduce its size, and then it was impregnated in water for 24 h. After that, it was mixed using an electric mixer and left for one week to dissolve the paper in closed containers to prevent water vaporization; then, the paper pulp was hand pressed using a piston to remove excess water. Samples containing paper waste were formed by mixing the paper pulp with other powders and by mold method without the addition of water, where paper pulp worked as a binder material during the molding process. Kaolin clay powder was sieved to obtain a powder with particle size less than 74 μm; its density was 1.8 to 2.6 g/cm^3 [27]. After that, weighing and mixing of powders were done. A sensitive balance with a precision of 0.0001 g (Mettler, AE200) was used to carry out the weighing process. The weight percentages of powders used in this study are shown in Table III, where the fraction of the material used as a pore generating agent was 20% because this percentage gives an acceptable combination of the mechanical properties and porous structure for the samples, according to the literature [20, 23]. The fraction of Na-feldspar was 25% for a reason mentioned above. An

Table I - Chemical composition (wt%) of Iraqi kaolin clay.
[Tabela I - Composição química (% em massa) da argila caulinítica iraquiana.]

SiO_2	Al_2O_3	MgO	TiO_2	Fe_2O_3	CaO	Na_2O	K_2O	LOI
47.4	38.5	0.3	0.1	0.5	0.3	0.3	0.6	12.0

LOI: loss on ignition.

Table II - Physical properties of Iraqi kaolin clay.
[Tabela II - Propriedades físicas da argila caulinítica iraquiana.]

Color	Melting point (°C)	Density (g/cm^3)	Water solubility
Gray	1770	1.8-2.6	Insoluble

Table III - Raw material composition (wt%) of the samples.
[Tabela III - Composição de matérias-primas (% em massa) das amostras.]

Sample	A	B	C	D
Kaolin clay	75	55	55	55
Sodium feldspar	25	25	25	25
Paper waste	0	20	0	0
Corn starch	0	0	20	0
Sawdust	0	0	0	20

electric mixer was used to carry out the mixing process. The samples were formed by mold method with the addition of 20% water (on the sample weight) as a binder material. The diameter of the formed samples was 30 mm, and their thickness was 8 mm. Specimens were dried initially in the air at room temperature for about 72 h and subsequently in a furnace at 115 ºC for 5 h, then fired at 1200 ºC with a soaking time of 3 h, and followed by furnace cooling.

Mechanical properties tests: the compressive strength was determined using a mechanical testing machine according to the ASTM C 773-88 standard, and the results were an average of 3 specimens tested for each prepared sample. Eq. A was employed to calculate the compressive strength (σ_c, MPa) [28]:

$$\sigma_c = P/A_c \quad (A)$$

where P is the applied load up to fracture (N), and A_c is the cross-section area of the specimen (mm^2). Vickers hardness was determined using a hardness tester with an indentation load of 89 N applied at about 8 s on polished surfaces of the specimens, considering an average of 3 indents for each of 3 specimens of each type of the prepared material. Vickers hardness (HV, MPa) values were calculated by [28]:

$$HV = 1.854.F/d^2 \quad (B)$$

where F is the applied load (N), and d is the diagonal of the indentation on the specimen's surface (mm).

Physical properties tests: the linear shrinkage was measured according to the ASTM C1407 standard, and the test results were an average of 3 specimens tested. Eq. C was used to calculate the specimens' linear shrinkage (LS, %):

$$LS = \frac{D_b - D_f}{D_b}.100 \quad (C)$$

where D_b and D_f are the diameters of the specimen before and after the sintering, respectively. The Archimedes method was employed to determine the specimens' density. The specimens were boiled with distilled water for about 5 h to fill the voids. The specimens were cooled in the air at room temperature. The mass of the specimen immersed in water (M_P, g) and water-saturated mass (M_S, g) were measured. Then, the dry mass (M_D, g) was measured after drying the specimen in a furnace at 115 °C for about 2 h. The density of the specimens was calculated according to the ASTM C373-88 standard using Eq. D and the results were an average of 3 specimens tested for each type of sample [29]:

$$D = \frac{M_D - D_{water}}{M_s - M_P} \quad (D)$$

where D is the bulk density of the specimen (g/cm^3), and D_{water} is the density of water (g/cm^3). Apparent porosity of the specimens was determined according to the ASTM C373-88 standard using Eq. E and the test results were an average of 3 specimens tested for each type of sample [29]:

$$P_o = \frac{M_s - M_D}{M_s - M_P}.100 \quad (E)$$

where P_o (%) is the open porosity of the specimen. Permeability test of the specimens was made, and the permeability values of water through the specimens were determined by Darcy's law (Eq. F), at 25 °C, 1 atm, considering the viscosity of water of 0.890 cP, and the test results were an average of 3 specimens tested for each sample [30-32]:

$$Q = -\frac{K.A}{L.\mu}.\Delta P \quad (F)$$

where Q is the volumetric flow of the fluid (cm^3/s), K the permeability of the sample [darcy, D=cm^2.cP/(s.atm)], A the cross-sectional area of the sample (cm^2), L the length of the sample (cm), μ the viscosity of the fluid (cP), and P is the pressure (atm).

Mercury intrusion porosimetry (MIP): the samples were tested by MIP to measure the distribution of pore sizes. MIP can give a pore size information over a wide range from 0.003 to 360 μm according to a cylindrical capillary model. Mercury can enter the pores by applied external pressure. The measurements can be obtained from mercury intrusion-extrusion curves, and then the pore information, including porosity, median pore size (d_{50}), average pore size (d_a), and cumulative mercury injection volume, can be obtained. First, the specimens were dried in a furnace for 8 h at 110 °C, then cooled to room temperature in a desiccator. Then, the MIP test was worked using a PoreMaster GT60 and the Washburn equation, supposing the pores with a cylindrical shape, was used according to [33]:

$$P = -\frac{2.\gamma.\cos\theta}{R} \quad (G)$$

where P is the applied pressure (MPa), R the pore radius (μm), γ the mercury surface tension, set as 0.48 N/m, and θ the wetting contact angle, set as 140° [34].

Microstructural analysis: the surface morphology of the porous ceramic specimens was analyzed by scanning electron microscopy (SEM).

RESULTS AND DISCUSSION

The tests made on the sintered samples were carried out to identify the appropriate material as a pore generating agent to manufacture a porous ceramic body with an excellent combination of mechanical and physical properties. Fig. 1 represents the effect of the type of the used material as a pore generating agent on the linear shrinkage, apparent porosity, and density of the sintered samples. The linear shrinkage of sample D, mixed with sawdust, was higher than the other samples: reference sample A, which did not contain a pore generating agent, sample B mixed with paper waste, and sample C prepared with corn starch; the linear shrinkage of sample B was higher than those of the samples A and C, and the linear shrinkage of the sample A was the lowest value. The shrinkage of the samples during the sintering process mainly occurs due to the loss of the moisture and the presence of a flux (sodium feldspar) in the sample composition which lead to forming a liquid phase during the firing process, and this liquid phase fill some of the voids between the particles and lead to reduce the volume of sample, causing the shrinkage [35, 36]. Since the shrinkage of the samples B, C and D was due to the prior reasons, with the burn out of the used material as a pore generating agent during the sintering process, more voids were formed which were filled by the liquid phase, thus increasing the linear shrinkage of the samples [37]. The different values of the shrinkage of the samples B, C, and D can be happened due to the difference in the burning process of the materials used and its results such as the ash content, which contains impurities related to its production process, and gases produced [26].

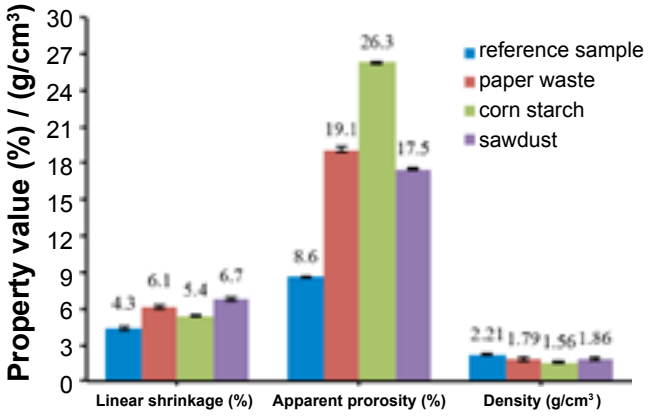

Figure 1: Linear shrinkage, apparent porosity, and density of sintered samples with different pore generating agent.
[Figura 1: Retração linear, porosidade aparente e densidade das amostras sinterizadas com diferente agente gerador de poros.]

The apparent porosity values obtained by the Archimedes method of the specimens A, B, C, and D were 8.6%, 19.1%, 26.3%, and 17.5%, respectively (Fig. 1). So, sample C had the highest value of porosity, and sample A had the lowest value. A reason of the difference among the apparent porosity values of the sintered samples B, C and D can be ascribed to the different manners that the used materials as a pore generating agent burned out during the sintering process and left the pores in the fired samples, subsequently providing an increase in the total apparent porosity [38]. But in sample A, the pores were formed from the contact among the particles of the sample, which were not removed during the sintering operation. The results were in agreement with other studies [20, 23]. Also, it can be observed from Fig. 1 that the ranking of sample's density from the highest to the lowest was the sample A, D, B and C. The difference in density values of the samples was caused by the formation of pores after the burning process of pore generating agent, which led to the decrease in the samples' mass and consequently a decrease of the density. In addition, all the used materials as a pore generating agent in this study had a density lower than that of kaolin clay (matrix material), which led to a decrease in the bulk density of the green samples and a distinctive difference between the sintered density of the sample A and the other samples B, C and D, due to the larger volume occupied by the pore generating agent than that of kaolin clay with the same weight [26]. In addition, the liquid phase formed during the firing process filled the voids between particles, which reduced the volume of the sample; consequently, it increased the sample's density [35, 36]. A similar result was found by other authors [20, 23, 39], using diverse starch contents and different preparation processes of the porous ceramic body.

Fig. 2 shows the effect of the type of pore generating agent on the permeability of the sintered samples. The permeability of the samples B, C and D was a higher than that of the sample A because of the increase in the number and volume of pore in the sintered samples B, C and D by adding a pore generating agent, which is an active method to increase the ceramic body permeation [37, 40]. The permeability of sample B was higher than that of the samples C and D, although sample C had the highest porosity since most pores in this sample were not interconnected and the connectivity among them was less than that among the pores of the samples B and D because of the agglomerated shape of the starch particles [41, 42], as shown by the SEM image of sample C (Fig. 3c). In addition, the used materials as a pore generating agent in this study had different and wide range of the characteristics such as water and impurity contents, dry density, particle size distribution, and particle shape, which influenced the properties of the porous ceramic body in both the green and sintered states such as mechanical strength, density, porosity, and pore shape, size and distribution [26]. Finally, a reason of the difference in the permeability values between the samples B and D was related with the number and type of the formed pores, where the number of the closed pores formed in sample D was higher than that in sample B because of the characteristics of the sawdust used as a pore generating agent.

Figs. 4a and 4b represent the effect of the type of pore generating agent on the hardness and compressive strength of sintered specimens, respectively. Sample A had the highest values of compressive strength and hardness. The strength of a ceramic body depends on the existence of imperfections in it, such as pores, which are regions of stress concentration [43]. The volume of closed and open pores, as shown in Fig. 3, caused the reduction of the compressive strength of the sintered specimens B, C and D, which was proportional to the apparent porosity [20, 37].

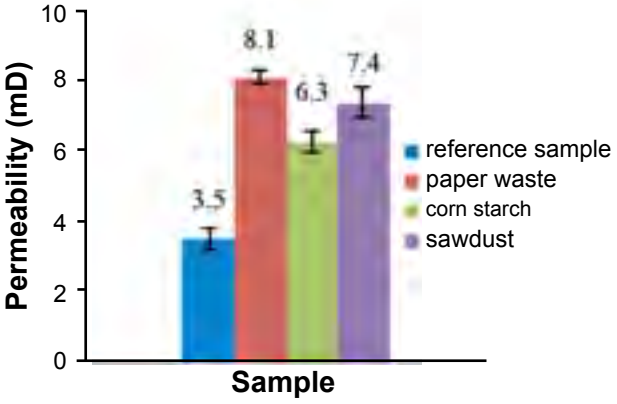

Figure 2: Permeability of sintered samples.
[Figura 2: Permeabilidade das amostras sinterizadas.]

Fig. 5 represents the cumulative porosity and relative pore volume (pore size distribution) of the sintered samples measured by the mercury intrusion porosimetry (MIP). Table IV shows the results of MIP measurements [44], specifically the total porosity and median pore diameter of the samples. The sample B mixed with paper waste had the highest MIP porosity, whereas the sample C mixed with corn starch had the highest value of the porosity obtained by Archimedes method since the most pores in this sample had less connectivity than the pores in the sample B. In addition, the sample C had the smallest size of pores due to the shape and size of the corn starch particles.

Figs. 3a, 3b, 3c, and 3d show the micrographs of sintered specimens A, B, C, and D, respectively, obtained

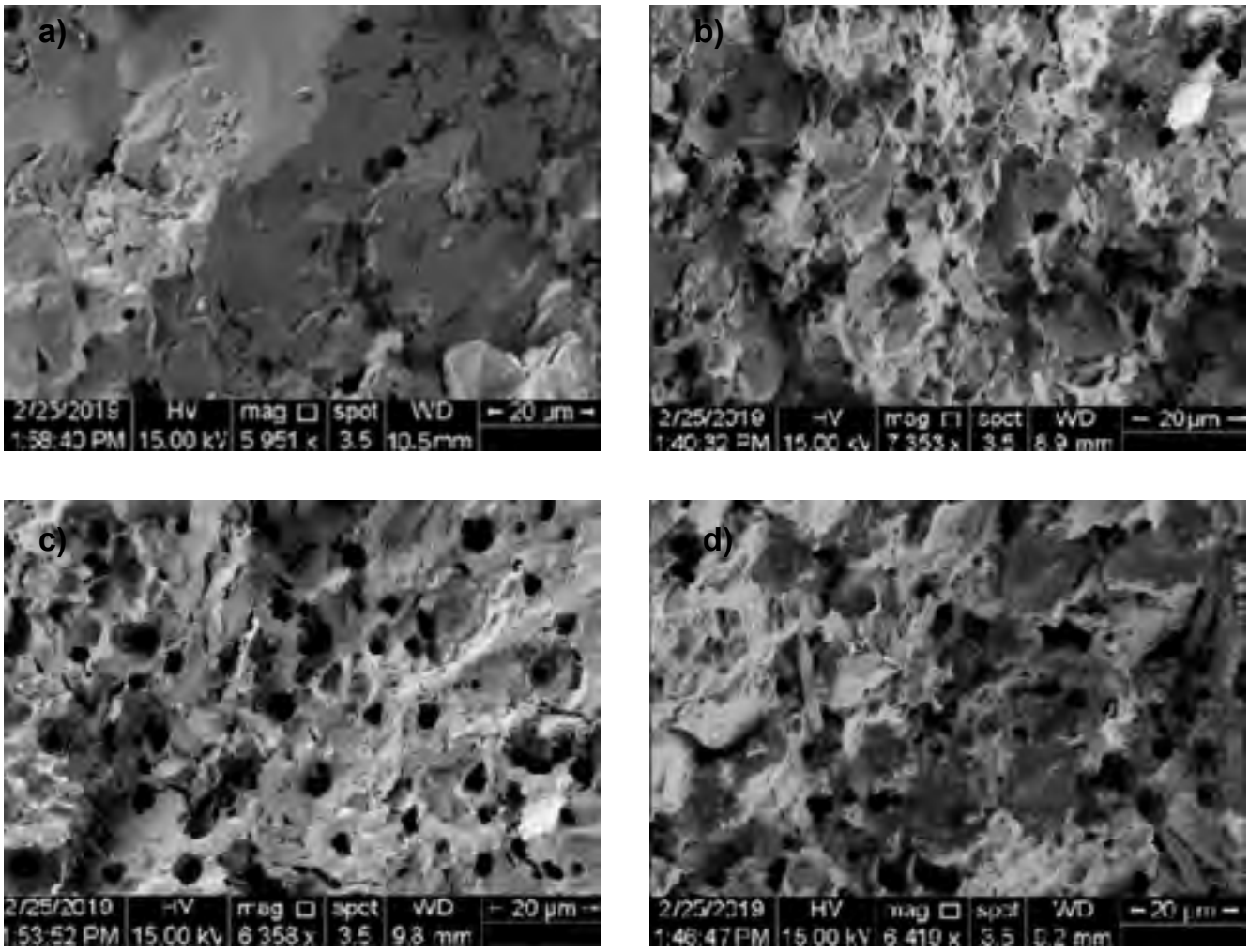

Figure 3: SEM images of the samples: a) A, not containing a pore generating agent; b) B, prepared with paper waste; c) C, prepared with corn starch; and d) D, prepared with sawdust, as pore generating agent.
[Figura 3: Imagens de MEV das amostras: a) A, não contendo agente gerador de poros; b) B, preparada com resíduo de papel; c) C, preparada com amido de milho; e d) D, preparada com serragem, como agente gerador de poros.]

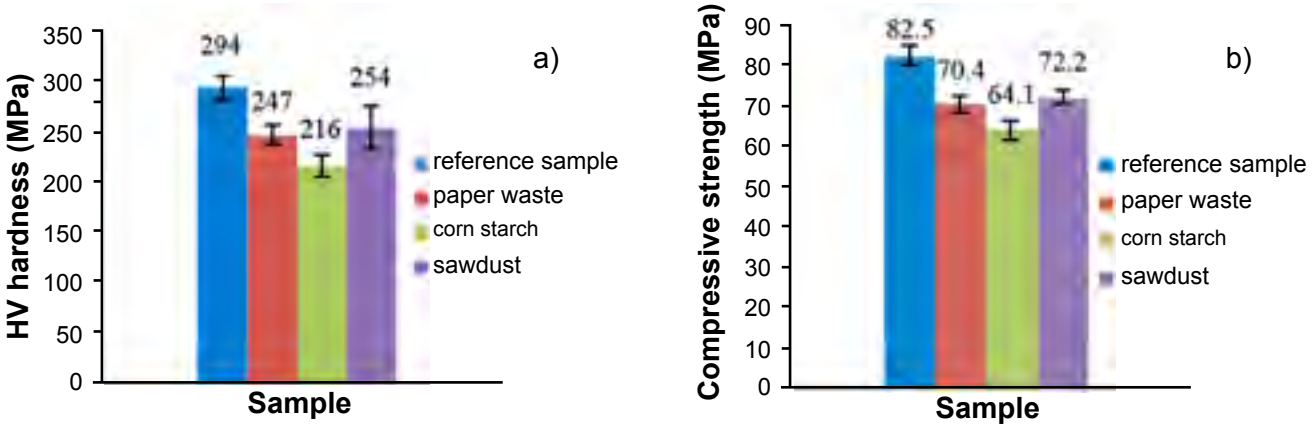

Figure 4: Effects of the type of pore generating agent on hardness (a) and compressive strength (b) of the sintered samples.
[Figura 4: Efeitos do tipo de agente gerador de poros na dureza (a) e resistência à compressão (b) das amostras sinterizadas.]

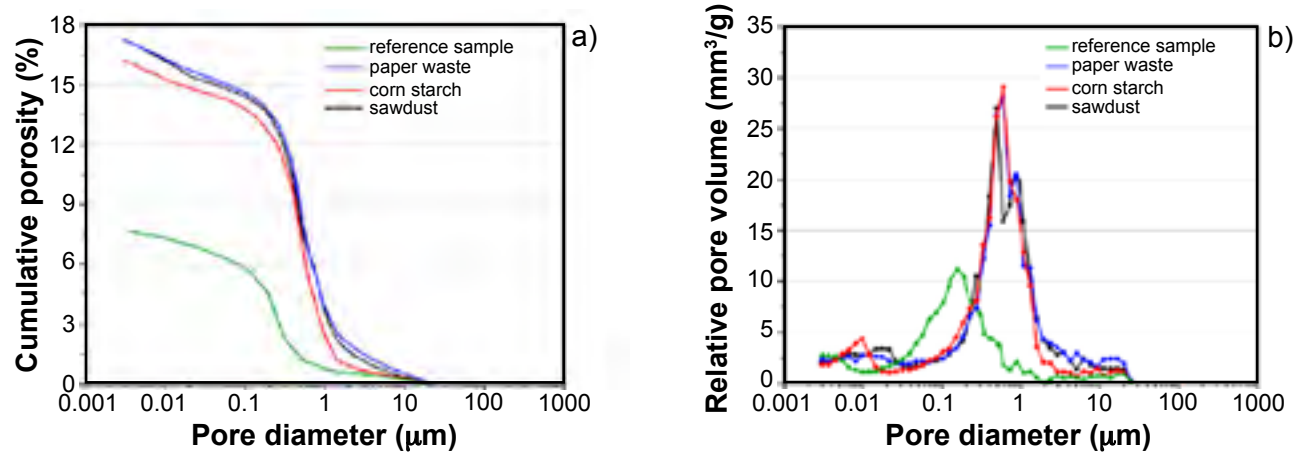

Figure 5: Cumulative porosity (a) and relative pore volume (b) as a function of pore diameter of the sintered samples.
[Figura 5: Porosidade acumulada (a) e volume de poro relativo (b) em função do diâmetro de poro das amostras sinterizadas.]

by scanning electron microscopy (SEM). Comparing the SEM images, more pores were noticed in the microstructure of the sintered sample C (Fig. 3c), showing that the added corn starch provided a more porous structure with lower connectivity among the pores and a good distribution of the pores compared to other samples. With respect to the porous structure of the other two samples, the paper waste in sample B provided a good porous structure with high connectivity among the pores in comparison with the sample D. The SEM images confirmed the interpretation of the results of the other tests of the sintered samples. From the results of the tests, it could be stated that the sample prepared with the corn starch had the highest porosity, and the lowest mechanical properties and permeability, while the sample prepared with the sawdust had contrary results. Finally, the sample prepared with the paper waste had intermediate values of porosity and mechanical properties, and the highest permeability among the studied samples.

Table IV - Results of mercury intrusion porosimetry (MIP).
[Tabela IV - Resultados de porosimetria por intrusão de mercúrio.]

Sample	Total porosity (vol%)	Median pore diameter (μm)
A	7.5	0.15
B	17.1	0.71
C	16.0	0.53
D	17.0	0.67

A: reference sample; B: sample mixed with paper waste; C: sample mixed with corn starch; D: sample mixed with sawdust.

CONCLUSIONS

Comparing the low-cost porous ceramic samples manufactured using paper waste, corn starch, and sawdust as a pore generating agent, and a reference sample manufactured without a pore generating agent, it can be stated that the utilization of different materials as a pore generating agent increased the porosity and permeability depending on the characteristics of these materials, where the sample which contained the corn starch had the highest porosity, the lowest permeability, and minimum mechanical properties. On the contrary, the sample which contained the sawdust had the lowest porosity, the highest mechanical

properties, and the intermediate value of permeability, while the sample which contained the paper waste had the intermediate values of porosity and mechanical properties and the highest permeability. In addition, the sample mixed with corn starch had the smallest pore size according to the results of mercury intrusion porosimetry. Consequently, the paper waste was the more suitable among the diverse cheap kinds of materials used as a pore generating agent in this study to manufacture a low-cost porous ceramic because it provided a preparation of a sample with a good combination of the mechanical properties, porosity, and permeability, which are considered the most important properties of the porous ceramic in application. In addition, the use of paper waste is beneficial to reduce its disposal, which is considered one of the environmental problems of solid wastes.

REFERENCES

[1] M.L.P. Antunes, A. Botignon de Sá, P.S. Oliveira, E.C. Range, Cerâmica **65**, Suppl.1 (2019) 1.
[2] P.R. Monich, D. Desideri, E. Bernardo, Adv. Appl. Ceram. **118**, 6 (2019) 366.
[3] A. Karamanov, Adv. Appl. Ceram. **108**, 1 (2009) 14.
[4] H.R. Fernandes, D.U. Tulyaganov, J.M.F. Ferreira, Adv. Appl. Ceram. **108**, 1 (2009) 9.
[5] I. Ponsot, R. Detsch, A.R. Boccaccini, E. Bernardo, Adv. Appl. Ceram. **114**, Sup.1 (2015) S17.
[6] E. Gregorová, Z. Živcová, W. Pabst, Fruit Veg. Cereal Sci. Biotech. **3**, Spec. Is. 1 (2009) 115.
[7] M. Scheffler, P. Colombo (Eds.), "Cellular ceramics: structure, manufacturing, properties and applications", Wiley-VCH, Weinheim (2005) 645.
[8] S. Ahn, K. Nam, J. Ceram. Process. Res. **18**, 11 (2017) 767.
[9] L. Palmquist, K. Lindquist, C. Shaw, Key Eng. Mater. **333** (2007) 215.
[10] E. Chevalier, D. Chulia, C. Pouget, M. Viana, J. Pharm. Sci. **97** (2008) 1135.
[11] S. Vijayan, R. Narasimman, K. Prabhakaran, J. Eur. Ceram. Soc. **33** (2013) 1929.
[12] T. Zeng, X.L. Dong, S.T. Chen, H. Yang, Ceram. Int. **33** (2007) 395.
[13] A. Slosarczyk, E. Stobierska, Z. Paszkiewic, J. Mater. Sci. Lett. **19** (1999) 1163.
[14] S. Bose, C. Das, Mater. Lett. **110** (2013) 152.
[15] N. Seffaj, Y.S. Alami, M. Persin, M. Cretin, A. Albizane, A. Larbot, Ceram. Int. **31** (2005) 205.
[16] A. Majouli, S. Tahiri, Y.S. Alami, H. Loukili, A. Albizane, Ceram. Int. **38** (2012) 4295.
[17] E. Gregorova, W. Pabst, Ceram. Int. **33** (2007) 1385.
[18] H.M. Mahmudul, M. Shafiquzzaman, A.M. Shafiul, J. Nakajima, Desalination **276** (2011) 272.
[19] F.A.M. Rahim, M.Z. Noh, M.W.A. Rashid, J.J. Mohamed, M.A.A.M. Nor, AIP Conf. Proc. **2068** (2019) 20056.
[20] G.C.C. Yang, C. Tsai, Desalination **233** (2008) 129.
[21] J. Cao, X. Dong, L. Li, Y. Dong, J. Eur. Ceram. Soc. **34** (2014) 3181.
[22] S. Kitouni, A. Harabi, Cerâmica **57**, 344 (2011) 453.
[23] S. Li, C. Wang, J. Zhou, Ceram. Int. **39** (2013) 8833.
[24] G. Topates, U. Petasch, J. Adler, F. Karaa, H. Mandal, J. Asian Ceram. Soc. **1** (2013) 257.
[25] E.M. Hadi, H.J. Abd Al-Hussien, Eng. Technol. J. **35**, 1 (2017) 227.
[26] M.M. Lorente-Ayza, M.J. Orts, V. Pérez-Herranz, S. Mestre, J. Eur. Ceram. Soc. **35** (2015) 2333.
[27] J. Robert, L. Harold, Clays Clay Miner. **41**, 4 (1993) 514.
[28] ASTM C773, "Standard test method for compressive (crushing) strength of fired whiteware materials", ASTM Int., West Conshohocken (1988).
[29] ASTM C373, "Standard test method for water absorption, bulk density, apparent porosity, and apparent specific gravity of fired whiteware products", ASTM Int., West Conshohocken (1988).
[30] A. Valconie, H. Natter, R. Hempelmann, Adv. Eng. Mater. **13** (2016) 218.
[31] G. Reyes-Villanueva, W. Cantwell, Compos. Sci. Technol. **64** (2015) 35.
[32] BS 1752, "Laboratory sintered or fritted filters", Br. Stand. Inst., London (1963).
[33] E.W. Washburn, Proc. Natl. Acad. Sci. USA **7** (1921) 115.
[34] A.H. Ellison, R.B. Klemm, A.M. Schwartz, L.S. Grub, D.A. Petrash, J. Chem. Eng. Data **12** (1967) 607.
[35] K. Kim, J. Hwang, Ceram. Int. **41** (2015) 7097.
[36] E. Bernardo, P.A. Bingham, Adv. Appl. Ceram. **110** (2011) 41.
[37] B. Achiou, H. Elomari, M. Ouammou, A. Albizane, J. Bennazha, A. Aaddane, S. Alami Younssi, I. El Amrani El Hassani, J. Mater. Environ. Sci. **9**, 3 (2018) 1013.
[38] R.M. Mesquita, A.H.A. Bressiani, Mater. Sci. Forum **727-728** (2012) 821.
[39] H.M. Alves, G. Tari, A.T. Fonseca, J.M.F. Ferreira, Mater. Res. Bull. **33** (1998) 1439.
[40] B. Achiou, H. Elomari, A. Bouazizi, A. Karim, M. Ouammou, A. Albizane, J. Bennazha, S. Alami Younssi, I.E. El Amrani, Desalination **419** (2017) 181.
[41] L. Palacio, Y. Bouzerdi, M. Ouammou, A. Albizane, J. Bennazha, A. Hernández, J.I. Calvo, Desalination **245** (2009) 501.
[42] S.A. Ajeel, N.E. Abdul Latiff, A.A. Al-Attar, Eng. Technol. J. **35**, 9 (2017) 887.
[43] J. Chandradass, H.K. Kim, D. sik Bae, K. Prasad, G. Balachandar, S. Athisaya Divya, M. Balasubramanian, J. Eur. Ceram. Soc. **29** (2009) 2219.
[44] J. Raouf, W. Steffen, K. Dietmar, Fachbeiträge **156** (2017) 46.
(Rec. 24/10/2019, Rev. 25/11/2019, 20/12/2019, 12/01/2020, Ac. 14/01/2020)

(cc) BY-NC

Investigation of mechanical, thermal and electrical parameters of gel combustion-derived cubic zirconia/epoxy resin composites for high-voltage insulation

(Investigação de parâmetros mecânicos, térmicos e elétricos de compósitos zircônia cúbica derivada de gel-combustão/resina epóxi para isolamento de alta tensão)

J. S. Sagar[1], S. J. Kashyap[1], G. M. Madhu[1]*, Pradipkumar Dixit[2]
[1]Ramaiah Institute of Technology, Department of Chemical Engineering, M S Ramaiah Nagar, MSRIT Post, Bengaluru, 560054, Karnataka, India
[2]Ramaiah Institute of Technology, Department of Electrical & Electronics Engineering, Karnataka, India

Abstract

The present study deals with the fabrication of epoxy composites reinforced with synthesized nano-zirconia, and to study their properties for high-voltage applications. The epoxy composites were extensively characterized to understand the morphology, mechanical, thermal, and electrical insulating behavior. The surface morphology and molecular structure of the nanoparticle and its interaction with the base matrix ware investigated by scanning electron microscopy, Fourier-transform infrared spectroscopy, and X-ray diffraction (XRD). XRD profiles confirmed that particles were crystalline and nanosized. Moreover, the tensile characteristics were analyzed using various theoretical models that predict the stiffness of these composites. The glass transition temperature of the epoxy/ZrO_2 composite increased with the increase in nanofiller content. The AC breakdown voltage reached a maximum of 14.8 kV for 2 wt% ZrO_2 composite. The prepared composites have the potential to act as high-performance insulation materials.
Keywords: nanofiller composite, ZrO_2, mechanical properties, thermal properties, gel combustion process.

Resumo

Este estudo trata da fabricação de compósitos de epóxi reforçado com nano-zircônia sintetizada, e o estudo de suas propriedades para aplicações de alta tensão. Os compósitos de epóxi foram extensivamente caracterizados para entender a morfologia e o comportamento mecânico, térmico e elétrico de isolamento. A morfologia da superfície e a estrutura molecular da nanopartícula e sua interação com a matriz foram investigadas por microscopia eletrônica de varredura, espectroscopia no infravermelho por transformada de Fourier e difração de raios X (DRX). Os padrões de DRX confirmaram que as partículas foram cristalinas com dimensões nanométricas. Além disso, as características de tração foram analisadas usando vários modelos teóricos que preveem a rigidez desses compósitos. A temperatura de transição vítrea do compósito epóxi/ZrO_2 aumentou com o aumento do teor de nanofíler. A tensão de ruptura dielétrica em corrente alternada atingiu máximo de 14,8 kV para o compósito com 2% em massa de ZrO_2. Os compósitos preparados têm potencial de atuar como materiais de isolamento de alto desempenho.
***Palavras-chave**: compósito nanofíler, ZrO_2, propriedades mecânicas, propriedades térmicas, processo gel-combustão.*

INTRODUCTION

The ever-increasing applications of polymeric materials with enhanced mechanical and thermal properties have always been a major objective from both academic and industrial points of view. Due to this rising popularity, the thermoset epoxy resins are widely preferred for industrial applications such as adhesives, construction materials, electrical insulation, laminates, aviation and so on [1-4]. Nonetheless, the brittleness of the cured pristine epoxy restricts its application in the real world. To counteract these problems, several techniques for toughening these epoxy systems have been introduced in the past few decades by industrialists as well as researchers. One such technique was to incorporate different modifiers derived from rubbers and thermoplastics, but these mixtures failed to outperform due to the high viscosity of the epoxy monomer mixture, which compromised its thermal properties [5, 6]. Enhancing the properties of epoxy resins was proposed by incorporating dispersed inorganic nanoparticles into the epoxy matrix. Nanofillers are considered to improve various parameters of the base matrix which include mechanical, electrical, and thermal behavior due to their smaller size effects [7-9]. There has been plenty of research associated with

**gmmadhu@gmail.com*
https://orcid.org/0000-0003-3937-7924

improving the overall performance of the polymer matrices by dispersion of inorganic nanofillers which has brought significant changes to their physical properties [10-13].

Many researchers reported the enhancement of structural and mechanical parameters of epoxy resins by the addition of a small amount of nano-reinforcements such as carbon nanotubes [13], Al_2O_3 [14], SiO_2 [15], TiO_2 [16], clay [17], fly ash [18], etc. It can be implied that these nanofillers, even at low concentrations, show good thermal and mechanical properties when incorporated into thermoset polymers. This might probably be due to the uniform distribution of the nanofillers in the dense epoxy cross-linked networks resulting in appreciable enhancement of thermo-mechanical properties of the composites. Among several nanofillers, zirconium dioxide (ZrO_2) can be employed as a promising reinforcement particle due to its characteristics like excellent stiffness and good chemical resistance along with elevated modulus, high fracture toughness, excellent wear resistance, and thermal stability [19-22]. Medina et al. [23] reported a 37% increase in the tensile modulus and a 100% increase in the fracture toughness with epoxy composite containing 10% by volume of nano-ZrO_2 compared to the neat epoxy. Furthermore, they also reported an eight-fold increase in the glass transition temperature (T_g) with 8 vol% ZrO_2 in the epoxy matrix. Halder et al. [24, 25] studied the influence of different mixing procedures on the morphological and tensile characteristics of the epoxy/ZrO_2 composites. They reported that the dispersion of nanoparticles was fairly good with ultrasonic dual mode mixing compared to mechanical mixing. They also reported that the tensile strength increased by 57% for 10 wt% of ZrO_2 relative to neat epoxy, but further increase in the filler content diminished the tensile properties as well as the fracture properties due to increased particle clusters. They further investigated the effect of silane-modified ZrO_2 (SZN) on epoxy/glass fiber composites [26]. It was concluded that the incorporation of SZNs into the glass fiber epoxy matrix resulted in a ~27% to 110% increase in the tensile strength, stiffness and toughness with respect to the control sample. Meanwhile, Chung et al. [27] and Tao et al. [28] studied epoxy incorporated with surface-modified ZrO_2 composites as LED encapsulants and concluded that refractive index and light output power increased with increase in loading percentage. Li et al. [29] studied the cryogenic mechanical parameters of epoxy/ZrO_2 composites via surface modification of nano-ZrO_2 with (3-aminopropyl)triethoxysilane (APTS). They observed a 26.4% increase in tensile strength and a 21.1% increase in failure strain compared to the control sample at cryogenic temperatures. Recently, Ma et al. [30] synthesized encapsulated nanozirconia using a silane coupling reagent and reported that the optimal mechanical properties were achieved at 3 wt% of ZrO_2 in the epoxy matrix. In summary, there are published reports mostly on the evaluation of the tensile parameters of epoxy/ZrO_2 and composites. As mentioned before, electrical insulation is one of the major applications of epoxy systems as they are widely used in electrical instruments. During operation, a high amount of electrical stress coupled with thermal stress is exerted due to the high shear exerted because of the conduction of high current and vibrational stress occurring due to the mechanical agitation of electrical equipment. Therefore, it is necessary for the composite to withstand high mechanical and electrical stress during its usage.

The present study aimed at the synthesis of nanoparticles and preparation of epoxy composites to investigate the breakdown voltage and the thermal stability of the fabricated epoxy resins loaded with varying filler (ZrO_2) concentration. In addition, the surface morphology of the synthesized nanopowders and the composites were characterized by scanning electron microscopy (SEM). Fourier-transform infrared spectroscopy (FTIR) was performed to understand the possible structural manipulations between the bulk epoxy and nanoparticles. These composites were also subjected to X-ray diffraction (XRD) in order to understand the molecular structure and crystallinity. The tensile and compressive parameters of the composites were evaluated in detail to assess the effect of filler concentration on the epoxy matrix. Various theoretical models were applied to analyze the experimental results of mechanical parameters.

EXPERIMENTAL

Reagents and materials: all chemicals were of analytical grade and used without further purification: zirconium nitrate trihydrate [$Zr(NO_3)_4.3H_2O$, ≥99%, Loba Chemie]; glycine (CH_2NH_2COOH, Fine Chemicals); Lapox-L12 (diglycidyl ether of bisphenol-A, Atul Polymers Div., India) used as the epoxy resin; TETA K-6 (triethylenetetramine, Atul) used as a hardener; and double-distilled water employed throughout the experiments.

Synthesis of ZrO_2 nanoparticles: ZrO_2 nanoparticles were synthesized via the gel combustion chemical route. The overall process involved mainly 4 steps: formation of a homogeneous solution at 50-55 °C; formation of a dried gel at 110 °C; combustion of the dried gel at 400 °C; and calcination of the product at 600 °C. In a typical synthesis, zirconium (IV) nitrate trihydrate (10.794 g) was mixed with glycine (1.168 g), which was used as a fuel to promote combustion. The fuel to nitrate (F/N) ratio was kept constant at 2:1. This mixture was taken in a 250 mL beaker, and 100 mL of double-distilled water was added. The beaker containing the mixture was kept in a muffle furnace for 10 min maintained at 400 °C. The beaker was then taken out and cooled to room temperature for 30 min. After this, the particles were taken in a crucible and ground into a fine powder. The chemical reaction involved in the synthesis of ZrO_2 by the combustion route is represented in Eq. A. The synthesized powder was calcined at 600 °C for 40 min. Finally, after cooling to room temperature, ZrO_2 nanoparticles were obtained.

$$9Zr(NO_3)_4.3H_2O+20CH_2NH_2COOH \rightarrow 9ZrO_2+40CO_2+56N_2+77H_2O \quad (A)$$

Preparation of epoxy/ZrO_2 composites: different fractions (2, 4, 6, 8, and 10 wt%) of zirconium oxide nanoparticles were added to the epoxy prepolymer and subjected to mechanical stirring for 20 min. This suspension was then sonicated for 40 min to obtain a uniform distribution of nanoparticles in the epoxy matrix. Then, the mixture was cured at room temperature, and 10% by volume of hardener was added. The as-prepared solution was poured into a suitable mold coated with Teflon sheets and was allowed to cure for 24 h. The composite laminates of dimensions 150x200x3 mm were made.

Investigation techniques: FTIR spectra of the epoxy/ZrO_2 composites were measured in the range of 4000-400 cm^{-1} using a spectrometer (Impact-410, Bruker, USA) in transmittance mode with a resolution of 4 cm^{-1}. X-ray diffraction patterns of the nanoparticle and composites were obtained using a diffractometer (X'Pert^3, PANalytical) with Ni-filtered CuKα radiation (40 kV, 20 mA) in the range of 0-80° at a scanning rate of 2 s/step and a step size of 0.02°. The composite morphologies were investigated by scanning electron microscopy (SEM) using a microscope (ESEM Quanta 200, FEI, USA) operating at a voltage of 20 kV. Elemental analysis of the as-synthesized nanopowder was performed using an energy dispersive X-ray (EDX) analyzer attached to the SEM instrument. Tensile testing of the composites was carried out according to the ASTM D638 standard at a crosshead speed of 10 mm/min (PC-2000, Kudale UTM). The gauge length between the grips was kept constant at 20 mm. Compression testing of the composites was carried out as per the ASTM D695 standard with a crosshead speed of 2 mm/min. The tests were conducted with 3 specimens for each sample, and the average values were reported. The glass transition temperature (T_g) of the composites was evaluated through a differential scanning calorimetry (DSC) according to the ASTM E1356 (Q200, TA Instr.). AC breakdown strength was estimated using an AC breakdown experimental setup as per ASTM D3756-97.

RESULTS AND DISCUSSION

Infrared spectroscopy: FTIR spectra of the composites loaded with 0-10 wt% of nanoparticles are shown in Fig. 1. The observable absorption bands in the range of 1019-1094 cm^{-1} can be assigned to the aromatic C=O stretching vibration of the epoxy polymer [31]. A peak at 1227-1382 cm^{-1} corresponded to the C=C and C-N stretching of the aromatic group [32]. Further, the band vibration in the range of 1602-1672 cm^{-1} showed the C=C stretching of the bulk matrix. The bands in the ranges of 2849-2853 and 2915-2933 cm^{-1} can be attributed to the -CH_2 stretching [33]. Absorbance bands observed at 3422 cm^{-1} indicated the OH stretching of pure epoxy [34]. Furthermore, the Zr-OH stretching band was assigned at the range of 3357-3398 cm^{-1} [31], and a band at the range of 622-755 cm^{-1} corresponded to the Zr-O stretching vibration band [32]. The additional bands observed in the range of 815-822 cm^{-1} can be attributed to the presence of inert amine in the matrix. These bands were not observed for pristine epoxy, which might be possible due to the formation of an amino-rich interface region around the nanoparticles in the bulk epoxy in the composites [25]. These results confirmed the adhesion of ZrO_2 nanoparticles with the epoxy matrix.

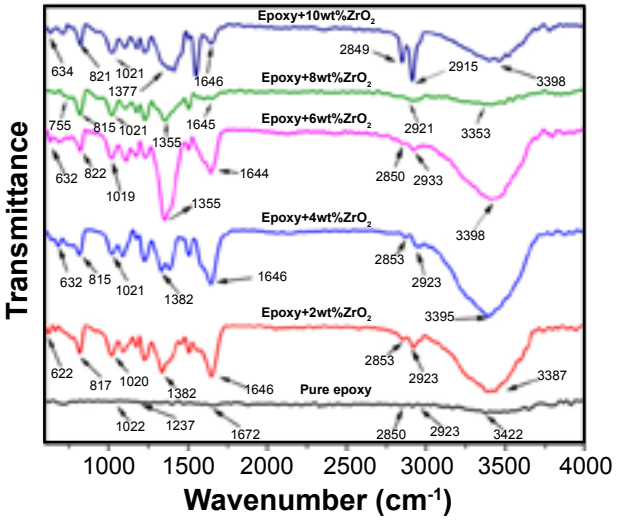

Figure 1: FTIR spectra of epoxy and ZrO_2-epoxy composites.
[Figura 1: Espectros de FTIR do epóxi e compósitos ZrO_2-epóxi.]

X-ray diffraction: XRD pattern of the synthesized ZrO_2 nanoparticles calcined at 600 °C is shown in Fig. 2. The diffraction peaks observed at 2θ= 30.21°, 34.95°, 50.38°, and 59.78° largely corresponded to the (111), (200), (220), and (311) planes, respectively, of the cubic phase of ZrO_2 which were in good agreement with the JCPDS data, powder diffraction file No. 27-0997, and also with previous research findings [33]. The average crystallite size of particles was estimated using Scherrer equation:

$$D=\frac{k.\lambda}{\beta.\cos\theta} \quad (B)$$

where D is crystallite size, k is the Scherrer constant (0.89), λ is the wavelength of X-ray (1.540598 Å), β is the full-width at half maxima (FWHM) of the diffraction peak, and θ is the Bragg angle. The average crystallite size of the nanoparticles was calculated to be 11.8 nm.

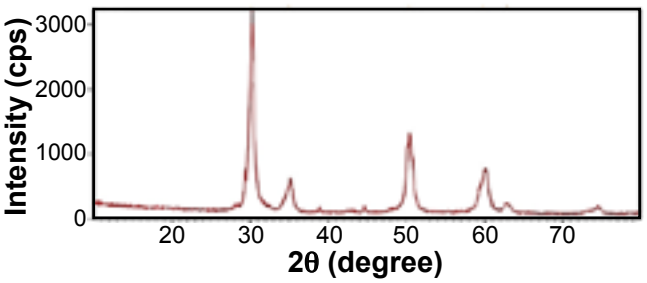

Figure 2: XRD pattern of as-synthesized ZrO_2 nanoparticles.
[Figura 2: Padrão de DRX das nanopartículas sintetizadas de ZrO_2.]

XRD patterns of pure epoxy and epoxy/ZrO_2 composites having 2, 4, 6, 8, and 10 wt% of ZrO_2 are shown in Fig. 3. Generally, alteration of crystallinity and surface morphology of the polymer matrix was observed after the incorporation of inorganic nanoparticles. From the XRD profiles, the peaks at 2θ ~30.2° showed that the nanoparticles were successfully incorporated into the epoxy base matrix. From these data, one can notice that the sharp peaks were not very intense for the epoxy matrix incorporated with 2 wt% ZrO_2 nanoparticles due to the large weight percentage of the amorphous epoxy matrix. Further increase in the fraction of the nanoparticles in the base matrix decreased the broad, amorphous band of the base matrix and increased the intensity of peaks of the inorganic nanofiller. The other peaks of ZrO_2 at 2θ 50.38° and 59.78°, which were not clearly visible at low concentration (2 wt%), increased with the increase in the filler concentration implying a higher degree of crystallinity. The approximate crystallinity of the doped composites was calculated by finding out the area of the crystalline peaks and dividing it by the total area of all the peaks in the profile. The highest percentage of crystallinity was observed for epoxy/10 wt% ZrO_2 with a calculated value of 26.1% and the lowest crystallinity was observed for epoxy/2 wt% ZrO_2 with a value of 12.2%. Epoxy filled with 4, 6, and 8 wt% of ZrO_2 had crystallinity of 14.3%, 19.1%, and 18.9%, respectively. It was observed that as the filler content in the epoxy matrix increased, the amorphous nature of the composites was gradually decreased and the crystallinity of the composites was slightly elevated. The incorporation of ZrO_2 nanoparticles also resulted in no observable phase transformation or structural manipulation.

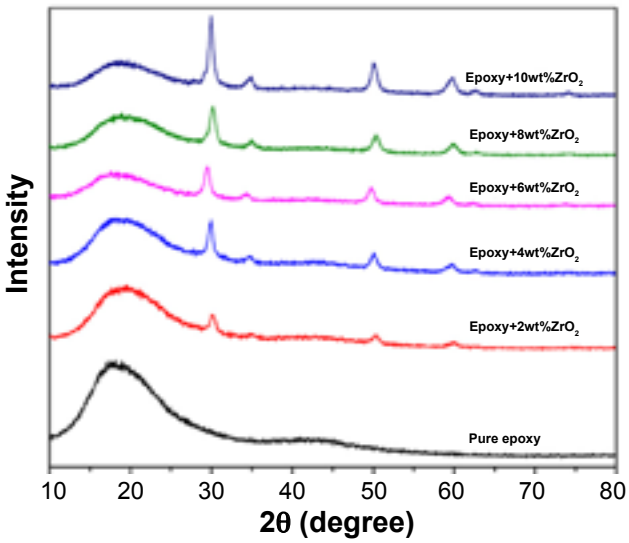

Figure 3: XRD patterns of the composites.
[Figura 3: Padrões de DRX dos compósitos.]

Scanning electron microscopy: Fig. 4 shows SEM images of the ZrO_2 nanoparticles synthesized by the gel combustion method. The nanoparticles appeared to be agglomerated to a certain extent, with the presence of small voids and roughness. These characteristics were due to the huge quantity of gases released during the combustion reaction. A substantial amount of gases escaping out assisted the formation of tiny particles while the heat released was a major factor for the crystal growth. Agglomeration of these nanoparticles is generally accounted to be a common route to reduce their surface free energy [35]. Fig. 5 shows the EDX spectrum of combustion-derived ZrO_2 nanopowder. The Zr and O peaks were clearly found, which suggested that pure ZrO_2 nanoparticles were obtained from the combustion synthesis route. Peak indexing of elements zirconium at ~1.9 keV and oxygen at ~0.6 keV can be observed in Fig. 5. The compositions obtained in the weight percentage of the elements were zirconium 61.4% and oxygen 38.6%.

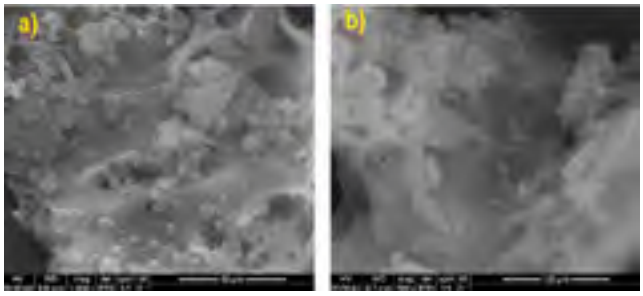

Figure 4: SEM images of ZrO_2 nanoparticles.
[Figura 4: Imagens de MEV de nanopartículas de ZrO_2.]

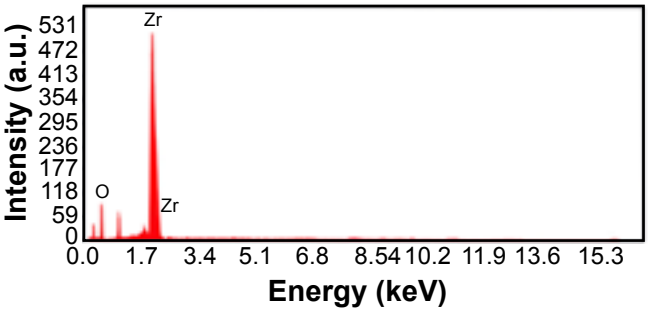

Figure 5: EDX spectrum of as-synthesized ZrO_2 nanopowder.
[Figura 5: Espectro de EDX do nanopó sintetizado de ZrO_2.]

Fig. 6 shows SEM micrographs of composites showing the presence of dispersed nanoparticles in the epoxy matrix. From Figs. 6a and 6b, it can be deduced that the nanoparticles were homogeneously distributed on the surface of the epoxy matrix at low concentrations (2 and 4 wt% of ZrO_2), with no observable agglomeration or cluster formation. The composites exhibited smooth surfaces with microsized voids developed at relatively low doping content. However, the agglomeration of nanoparticles was seen at higher concentrations in the epoxy matrix. In Figs. 6c to 6e, aggregations or chunks of nanoparticles are observed, implying non-uniform distribution of nanoparticles (6 to 10 wt% of ZrO_2) in the epoxy matrix. The tendency to form clusters of nanoparticles in epoxy is mainly due to the van der Waals force between the nanopowders and viscosity of the resin [10]. These nanoparticles were observed to be distributed closely to each other in the epoxy matrix, with an increase in ZrO_2 content. As the agglomeration increased, the

interparticle distance decreased, leading to weak distribution and interlinkage between the filler and the epoxy matrix. From the cross-sectional SEM micrographs (Fig. 7), the nanoparticles appeared to be dispersed uniformly throughout the epoxy matrix. Agglomerations of ZrO_2 nanoparticles were not quite observed in the cross-sectional views of SEM images even at relatively higher concentrations implying good adhesion and uniform distribution inside the bulk epoxy. The observed compatibility between the epoxy polymer matrix and the dopant in these images might have a positive effect on the mechanical parameters of the composites [36]. Although Fig. 7e depicting the cross-sectional view of epoxy loaded with 10 wt% of ZrO_2 shows some agglomeration, it can be accounted for the increased filler concentration resulting in the decreased interparticle distance inside the epoxy matrix. A common observation from the SEM images was the tendency of the nanoparticles to disperse closely to each other in the epoxy matrix with the increase in nanofiller concentration.

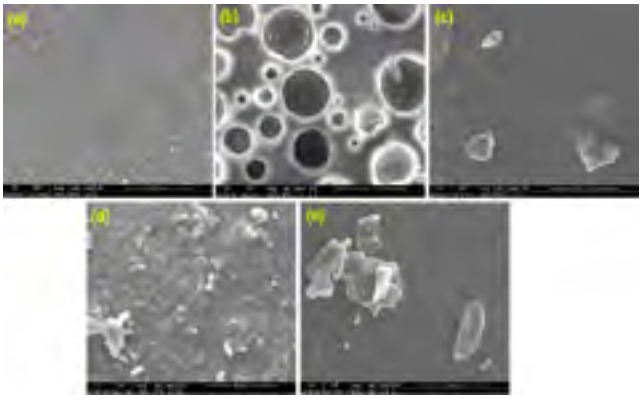

Figure 6: SEM micrographs of epoxy resin loaded with ZrO_2 nanoparticles at: a) 2 wt%; b) 4 wt%; c) 6 wt%; d) 8 wt%; and e) 10 wt%.

[Figura 6: Micrografias de MEV de resina epóxi com nanopartículas de ZrO_2 em fração mássica de: a) 2%; b) 4%; c) 6%; d) 8%; e e) 10%.]

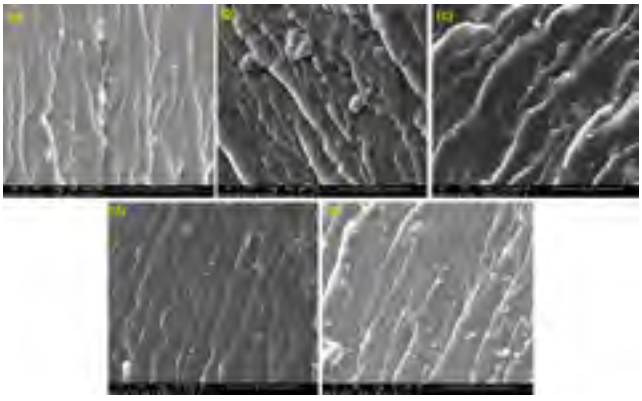

Figure 7: SEM images of the cross-section of epoxy resin with ZrO_2 nanoparticles at: a) 2 wt%; b) 4 wt%; c) 6 wt%; d) 8 wt%; and e) 10 wt%.

[Figura 7: Imagens de MEV da seção transversal de resina epóxi com nanopartículas de ZrO_2 em fração mássica de: a) 2%; b) 4%; c) 6%; d) 8%; e e) 10%.]

Tensile properties: the mechanical properties of polymer composites are an important factor in determining its suitability and applications in the real world. Fig. 8 shows the tensile stress-strain curve of the fabricated composites. It was observed that the tensile stress increased linearly with the tensile strain until the breakpoint, showing typical stress-strain characteristics of polymer composites. The various mechanical properties of epoxy/ZrO_2 composites like tensile strength, tensile modulus, elongation at break, and toughness are shown in Fig. 9. Fig. 9a shows the tensile strength of the composites loaded with nano-ZrO_2 at various concentrations. It was observed that the tensile strength of the composites increased linearly with respect to the filler content. The composites doped with ZrO_2 showed remarkably elevated tensile strengths compared to that of the control sample. It can be hypothesized from these findings that the tensile strength of the composites increases with an increase in filler content in the matrix. Epoxy loaded with 10 wt% ZrO_2 demonstrated the highest tensile strength with a whopping 125% enhancement compared to pure epoxy. However, epoxy/2 wt% ZrO_2 showed only a 40% increase in the tensile strength, which can be justified based on the amount of filler content in the matrix. Epoxy loaded with 6 and 8 wt% ZrO_2 showed 98% and 121% increase in tensile strength, respectively, with respect to the filler-free epoxy. A steady increase in the tensile strength was observed. The tensile strength enhanced even at high ZrO_2 fractions in the matrix proving that the agglomerations of nanoparticles observed in the SEM images did not seem to cause early fracture of the composites. It appears that the interparticle linkage did not play a significant role in the enhancement of tensile strength compared to particle-polymer interaction. However, the tensile strengths of epoxy loaded with 8 and 10 wt% of ZrO_2 were anomalously close (~4%) compared to the overall linearity observed, raising concerns on the dispersion of nanofillers at high concentrations.

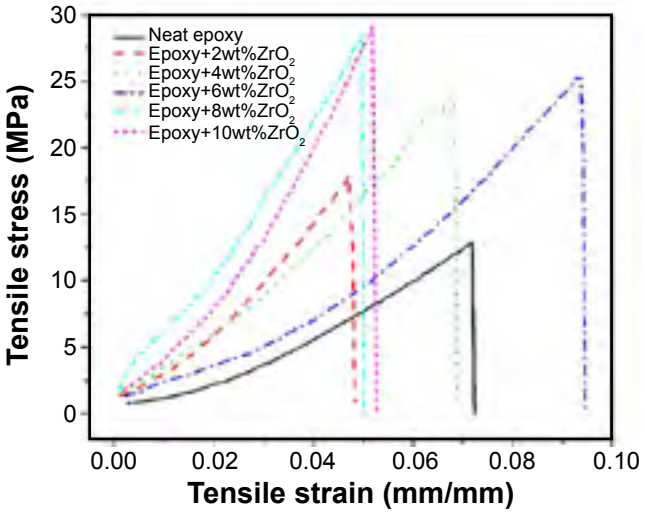

Figure 8: Tensile stress-strain curves of neat epoxy and composites with ZrO_2 at various contents.

[Figura 8: Curvas tensão-deformação em tração de epóxi puro e compósitos com diferentes teores de ZrO_2.]

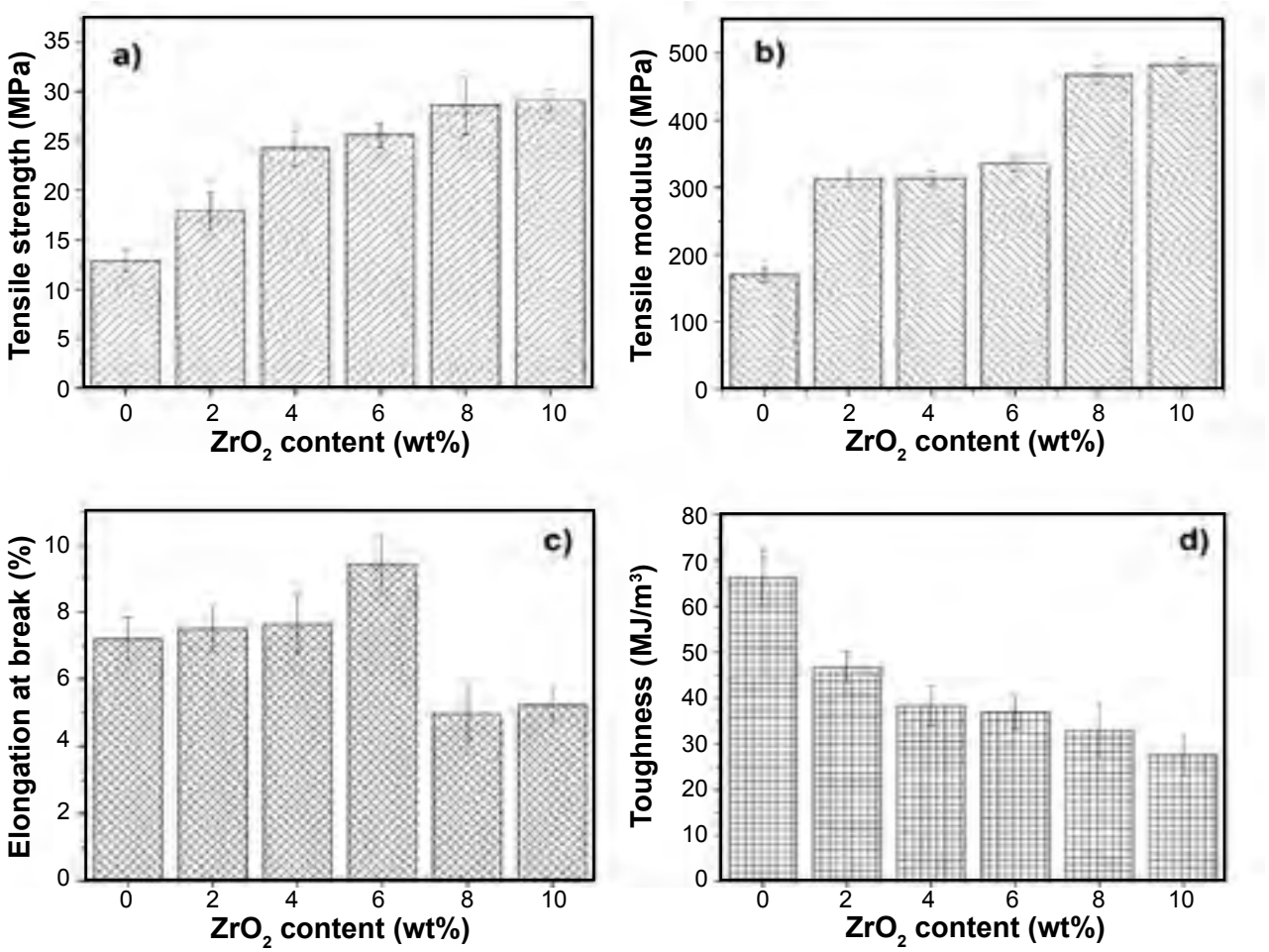

Figure 9: Results of tensile strength (a), tensile modulus (b), elongation at break (c), and toughness (d) of composites with different ZrO_2 content.

[Figura 9: Resultados da resistência à tração (a), módulo de elasticidade em tração (b), alongamento na ruptura (c) e tenacidade (d) de compósitos com diferentes teores de ZrO_2.]

The tensile moduli of the composites with varying concentrations of ZrO_2 are shown in Fig. 9b. Pristine epoxy had relatively the lowest tensile modulus of 170 MPa, and epoxy-containing 10 wt% of ZrO_2 showed the maximum tensile modulus. There was no observable trend in the tensile modulus values with respect to the filler concentration. However, the maximum tensile modulus shown by the doped composite, i.e., with 10 wt% of ZrO_2 content was ~184% higher than the pristine sample, but there was no linearity observed in the values of tensile modulus. The epoxy-containing 2 and 4 wt% ZrO_2 had more or less the same values of tensile modulus (~84% more than filler-free sample). There was a 98% increase in the tensile modulus of epoxy/6 wt% ZrO_2 compared to the control sample, after which the tensile modulus abruptly increased for the epoxy-containing 8 and 10 wt% ZrO_2. The peculiarity observed in these values may be due to the bonding of immobilized epoxy chains with aggregated nanoparticles in the matrix [37]. The elongation at break appeared to have an optimal value of 9.4% at 6 wt% filler concentration in the base matrix as shown in Fig. 9c. The elongation at catastrophic break decreased beyond that point, reaching 5%, which was ~47% and 30% lower than that of epoxy/6 wt% ZrO_2 and pure epoxy, respectively. This may be validated because of the possible cluster formation of nanoparticles in the bulk matrix which was observed in the SEM images. From Fig. 9d, one can note that the highest tensile toughness was achieved by pristine epoxy. Even a small amount of incorporation of nanoparticles tended to decrease the toughness due to the increase in brittleness of the composite. The manipulation of the morphological architecture after the introduction of nanoparticles might have caused poor adhesion between the filler and the matrix resulting in diminished toughness of the composites [38]. The restriction of polymer chain movement after incorporation of nanoparticles might have compromised the ductility and the ability of the polymer to transfer the load uniformly within the matrix. It can be concluded that there should be an optimal amount of filler in the base matrix which proves to be effective in increasing the overall tensile characteristics without compromising the structural integrity.

The tensile strength and modulus of epoxy/ZrO_2 composites were also predicted by utilizing several theoretical models. With the help of these empirical relations,

the effect of interfacial adhesion of the polymer composites can be analyzed. Three models were employed to evaluate the tensile strength. The first model was the Nicolais-Narkis model [39] for the relative tensile strength (RTS) given by:

$$RTS=(1-K.Ø'^{(\frac{2}{3})}) \quad (C)$$

where Ø' is the corrected volume fraction, which accounts for the non-linearity arising due to the aspect ratio, size, and large surface area of the nanoparticles. Taking into consideration the above factors, Ø' can be represented by:

$$Ø'=Ø.\lambda \quad (D)$$

where λ represents the additive factor, according to:

$$\lambda = a.A_f^{\ b} \quad (E)$$

where A_f is the aspect ratio considered to be 2 [25], and a and b are the empirical constants accounting non-linear behavior of the nanofillers. Volume fraction (Ø) of ZrO_2 in the epoxy matrix is determined using the relation:

$$Ø_i=\frac{w_i/\rho_i}{\sum (w_i/\rho_i)} \quad (F)$$

where w_i and ρ_i represent the weight fraction and density of the ith component, respectively. The density values of epoxy and ZrO_2 were 1.25 and 5.68 g/cm^3, respectively. The K value used in the Eq. C is a measure of the matrix-filler interfacial adhesion. A K value of 1.21 denotes poor adhesion while lower values depict improved adhesion [39]. The Nielsen model, which is based on the porosity theory, includes a stress concentration factor τ as follows:

$$RTS = \exp(-\tau.\phi') \quad (G)$$

Increased values of τ indicate poor adhesion which is generally attributed to stress concentration effect [38-43]. The Turcsanyi model [44, 45] includes a parameter B' that increases with improved interfacial adhesion as per the equation given by:

$$RTS = \frac{1-\phi'}{1+2.5.\phi'.\exp(B'.\phi')} \quad (H)$$

The results from these empirical models are plotted in Fig. 10 and their respective parameter values are tabulated in Table I. The results from the Nicolais-Narkis model showed a good match with the experimental values. It was observed that the parameter K from the Nicolais-Narkis model showed a value less than 1.21, which suggested better adhesion implying the enhanced interfacial interactions. The Nielsen model also showed a similar trend when compared to the experimental values implying improved adhesion at the interface. However, the Turcsanyi model showed an excellent match with the experimental results, as can be observed in Fig. 10. B' value of 2.5 indicated an appreciable filler adhesion in the epoxy matrix.

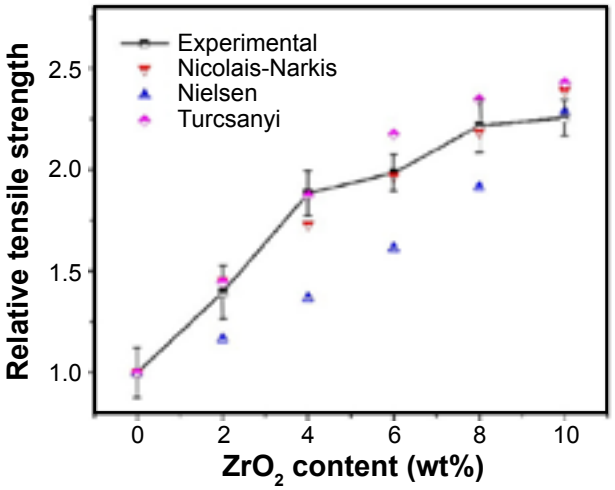

Figure 10: Plot of relative tensile strength (RTS) as a function of ZrO_2 content of the composites.
[Figura 10: Gráfico da resistência à tração relativa (RTS) em função do teor de ZrO_2 dos compósitos.]

Table I - Values of a, b, and characteristic parameter for the three models of relative tensile strength (RTS).
[Tabela I - Valores de a, b e parâmetro característico para os três modelos RTS.]

Model	a	b	Parameter	Value
Nicolais-Narkis	1.1	2.2	K	-5.7
Nielsen	-5.3	0.9	τ	3.5
Turcsanyi	-3.4	3.0	B'	2.5

Furthermore, three theoretical models have been proposed to analyze the tensile modulus: Halpin-Tsai, Kerner's, and Sato-Furukawa. The modified Kerner's model [46-48], which considers the effect of interfacial adhesion, includes matrix volume fraction and Poisson's ratio for the relative tensile modulus (RTM) according to:

$$RTM = 1+\frac{\phi'.15.(1-\nu)}{1-Ø'.(8-10.\nu)} \quad (I)$$

where ν is the Poisson's ratio of the epoxy taken as 0.33 [16]. Next, the Halpin-Tsai model [49, 50] is given by:

$$RTM = \left(\frac{3}{8}\frac{1+2.\phi'.\eta_e}{1-\eta_e\phi'}+\frac{5}{8}\cdot\frac{1+2.\eta_T.\phi'}{1-\eta_T.\phi'}\right) \quad (J)$$

$$\eta_e = \frac{\delta-1}{\delta-2.A_f} \quad (K)$$

$$\eta_T = \frac{\delta-1}{\delta+2} \quad (L)$$

where δ is the ratio of the nanofiller modulus to the matrix modulus without ZrO_2. The filler modulus has been given a value of 100 GPa [51]. Further, the Sato-Furukawa model also considers an adhesion factor ξ which varies from 0 to 1. The lowest value means the existence of perfect adhesion, whereas the highest value denotes no adhesion at all. The

equation for this model is given by:

$$RTM = \left[1 + \frac{(\phi')^{2/3}}{2-2.(\phi')^{1/3}}(1-\psi.\xi) - \frac{(\phi')^{2/3}.\psi.\xi}{[1-(\phi')^{1/3}]}\right] \quad (M)$$

$$\psi = \frac{\phi'}{3}\,\frac{1+(\phi')^{1/3}-(\phi')^{2/3}}{1-(\phi')^{1/3}+(\phi')^{2/3}} \quad (N)$$

Fig. 11 shows the plot of experimental RTM compared with numerically computed values. The modulus value was observed to increase with the increase in nanoparticle content. The values of a, b, and the characteristic parameter are tabulated in Table II. The results from all three models showed a similar trend, and a good fit of these models was seen at epoxy loaded with 6 and 10 wt% of ZrO_2. Deviations in the theoretical values can be accounted for the imperfect adhesion between the matrix and the filler. Due to the non-linear trend in the values of experimental relative tensile modulus, the theoretically computed values seem to be slightly off-track from the expected trend, thus having a negative impact on the modulus. However, with ξ value of 0.1 for the Sato-Furukawa model, it can be said that there was a good adhesion of the nanofillers with the bulk epoxy. A similar ξ value was reported for the blending of SiO_2 and multiwalled carbon nanotubes with high-density polyethylene composites [52].

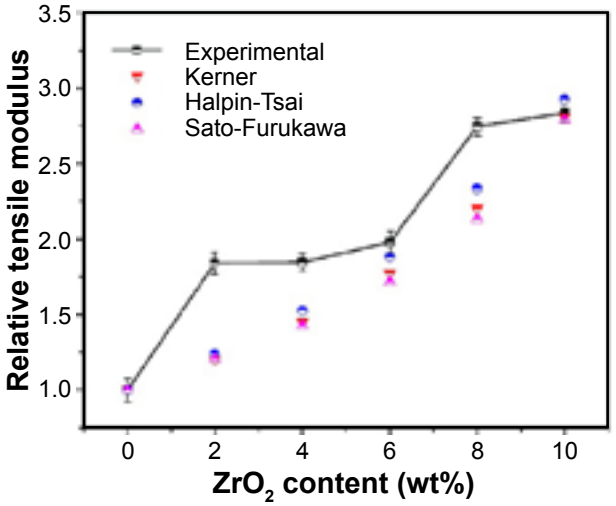

Figure 11: Plot of relative tensile modulus (RTM) as a function of ZrO_2 content of the composites.
[Figura 11: Gráfico do módulo de elasticidade à tração relativo (RTM) em função do teor de ZrO_2 dos compósitos.]

Table II - Values of a, b, and characteristic parameter for the three models of relative tensile modulus (RTM).
[Tabela II - Valores de a, b e parâmetro característico para os três modelos de RTM.]

Model	a	b	Parameter	Value
Halpin-Tsai	7.7	1.1	-	-
Kerner	9.6	1.0	-	-
Sato-Furukawa	11.0	1.1	ξ	0.1

Compressive properties: the compressive stress-strain curves of the as-prepared composites with varying ZrO_2 amounts is shown in Fig. 12. The composites somewhat deviate from linearity in terms of the compressive modulus observed. Apart from the longitudinal strength of compression, the reinforcements present in the matrix also affect the stiffness of the overall composite [53]. Fig. 13 shows the experimentally determined compressive strength and compressive modulus in terms of filler fraction present in epoxy. The compressive strength reached the highest value of 181.5 MPa for the epoxy/6 wt% ZrO_2, which was 33% higher than that of pure epoxy having a compressive strength of only 135.8 MPa (Fig. 13a). It appears from Fig. 13a that the compressive strength of the composites increased linearly with the increase in filler content up to 6 wt%. Beyond this point, the increase in ZrO_2 content failed to enhance the compressive strength of the composites. There was 8% and 17% drops in the compressive strengths of epoxy loaded with 8 and 10 wt% ZrO_2, respectively, compared to epoxy/6 wt% ZrO_2. The decrease in these values can be validated due to the agglomeration of nanoparticles and the poor interaction between the filler and the polymer. The clusters created might have caused an early fracture to the composites when subjected to shear compressive load. Observing Fig. 13b, we can say that the compressive modulus increased in the following rank: pure epoxy (2822 MPa) < epoxy/4 wt% ZrO_2 (2834 MPa) < epoxy/2 wt% ZrO_2 (3298 MPa) < epoxy/8 wt% ZrO_2 (3302 MPa) < epoxy/10 wt% ZrO_2 (3889 MPa) < epoxy/6 wt% ZrO_2 (4193 MPa). The highest value of compressive modulus of epoxy/6 wt% ZrO_2 was 48.6% higher than pure epoxy. This anomalous behavior might be explained due to the poor dispersion and slight aggregation of the nanoparticles inside the epoxy phase. The optimal values were observed for the epoxy/6 wt% ZrO_2 implying a high load-bearing capability and uniform distribution of nanoparticles inside the epoxy matrix. Beyond this limit,

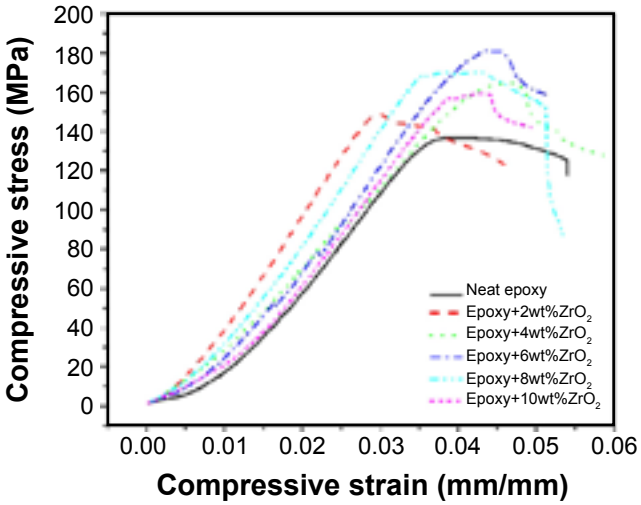

Figure 12: Compressive stress-strain curves of different types of epoxy/ZrO_2 composites.
[Figura 12: Curvas tensão-deformação em compressão de diferentes tipos de compósitos epóxi/ZrO_2.]

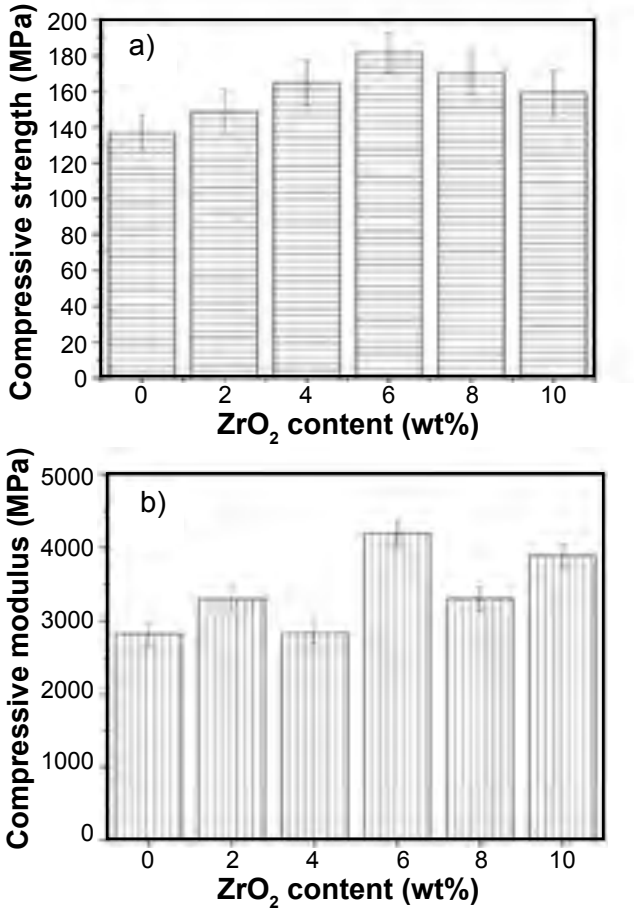

Figure 13: Results of compressive strength (a) and compressive modulus (b) of composites with different ZrO_2 content.
*[Figura 13: Resultados da resistência à compressão **(a)** e módulo de elasticidade em compressão (b) de compósitos com diferentes teores de ZrO_2.]*

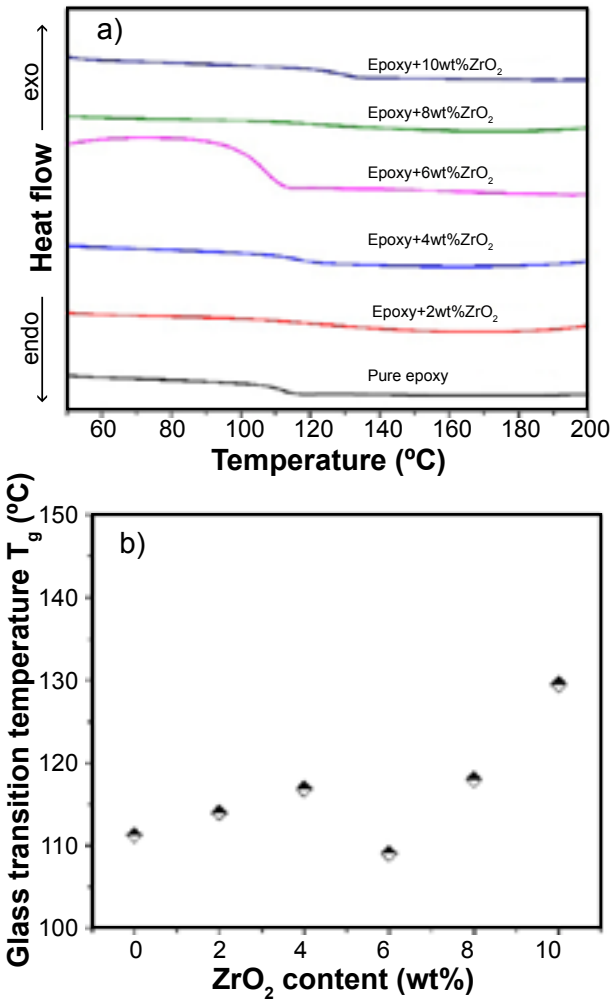

Figure 14: DSC curves of epoxy composites with varying ZrO_2 content (a) and glass transition temperature (T_g) of the composites as a function of nanoparticle content (b).
[Figura 14: Curvas de DSC de compósitos de epóxi com diferentes teores de ZrO_2 (a) e temperatura de transição vítrea (T_g) dos compósitos em função do teor de nanopartículas (b).]

the agglomeration of nanoparticles dominated, producing undesirable results.

Glass transition temperature: thermosetting polymers which exhibit enhanced insulating characteristics at temperatures below T_g might display the semiconducting characteristics at temperatures above T_g [54]. Thus, T_g can be considered as an important parameter of epoxy resins. Fig. 14a shows the DSC thermograms of the epoxy/ZrO_2 composites with respective T_g values in Fig. 14b. The T_g values appeared to increase steadily from 0 to 4 wt% of ZrO_2, after which there was a marginal drop in the T_g value for the nanofiller composite containing 6 wt% ZrO_2. The T_g further increased and reached a maximum value (129.4 ºC) for epoxy-containing 10 wt% ZrO_2 which was ~16% higher than the nanoparticle-free epoxy. Various factors including filler-matrix interface contact, cross-linking density, and polymer chain segment mobility come into picture while examining T_g values of thermoset polymers. The observed enhancement in the T_g values of the composites can be explained by the restriction of mobile chain segments of the bulk epoxy due to the filler-matrix adhesion. It can also be reasoned out due to the uniformly distributed nano-ZrO_2 in the matrix. As the loading is uniform, the particle-matrix interface would have good adhesion hindering the polymer chain mobility which results in elevate T_g [37]. However, a marginal drop in the T_g value was observed for the epoxy/6 wt% ZrO_2 composite. This might be possible due to the reduction in cross-linking density at the vicinity of the particle-matrix interface and non-uniform dispersion of nanoparticles in epoxy. This would cause a downward shift in the T_g value at a fairly high content of nanoparticles.

AC breakdown strength: the breakdown voltage of the composites was observed to reach its maximum value for epoxy/2 wt% ZrO_2, and the minimum value was observed for epoxy/10 wt% ZrO_2 which was a little more than pure epoxy (Fig. 15). The optimum amount of filler concentration, in this case, was found to be 2 wt% of ZrO_2 in the matrix, which showed a threshold voltage of ~15 kV. This value was ~12% higher than that of the pure epoxy. The high surface area of nano-ZrO_2 resulted in the altered behavior of

the polymer matrix, which in turn improved the interfacial area. Further increase in the filler concentration tended to decrease the breakdown voltage drastically as observed in Fig. 15. The optimal value shown by epoxy/2 wt% ZrO_2 might be due to the high amount of epoxy present near the vicinity of the nanoparticles, also referred to as the high interaction zone. It may be assumed that because of this, the accumulated charge at any point in the threshold field is reduced which alters the distribution of space charge [14]. In addition, the fillers incorporated into the epoxy matrix tend to act as scattering sites where the electrons fail to gain the momentum necessary to the disruption of the applied high voltage. Due to the applied electric field, electrons tend to accelerate and collide directly with the incorporated nanoparticles failing to attain momentum. This mechanism ceases the electrons to cause any catastrophic failure in the equipment and insulation [55, 56]. Hence, epoxy/ZrO_2 composites have enhanced electrical breakdown strength in contrast to the control sample, under high AC voltage.

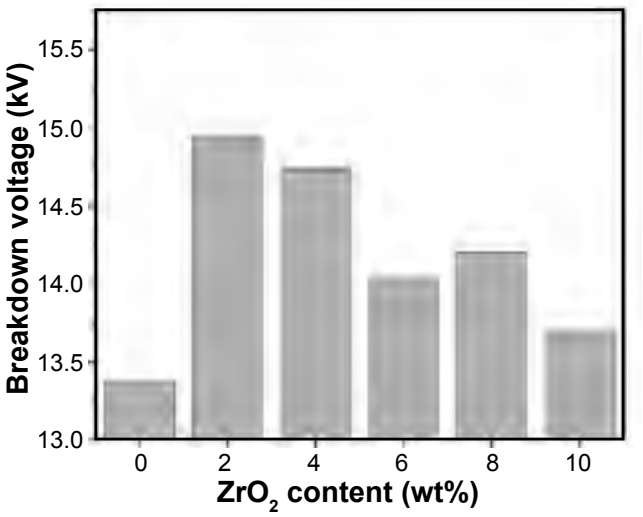

Figure 15: Breakdown voltage of epoxy/ZrO_2 composites as a function of ZrO_2 content.
[Figura 15: Tensão de ruptura dielétrica de compósitos epóxi/ZrO_2 em função do teor de ZrO_2.]

CONCLUSIONS

Epoxy composites were loaded with gel combustion-derived nano-ZrO_2 having a cubic phase with varying weight fractions (2-10 wt%). The ultrasonication method was employed to obtain a uniform distribution of the nanoparticles in the epoxy matrix. Results revealed that the tensile characteristics of the composites increased linearly with nanoparticle concentration in the matrix. The highest tensile strength was obtained for epoxy/10 wt% ZrO_2, which was 125% more than the pristine epoxy. The maximum Young's modulus was also achieved at the same content which was 184% higher than the control sample. However, the tensile toughness and the elongation at break appeared to diminish at a high concentration of nanoparticles. This was attributed to the agglomerations of nanoparticles formed at increased loading fractions which were observed in the SEM micrographs. The optimal compressive properties were noted for the epoxy loaded with 6 wt% ZrO_2. A maximum elevation of 16% in T_g for epoxy/10 wt% ZrO_2 was observed with respect to the pristine sample. The experimental tensile properties were compared with the mathematical model values. All the tested models showed similar trends in comparison with experimental values. Among the tested models, Nicolais-Narkis and Turcsanyi models were in good agreement with the experimental values for tensile strength and Sato-Furukawa model for tensile modulus. The AC breakdown voltage of the nanofiller composite was also observed to be high compared to ZrO_2-free epoxy. Hence, these composites can be employed as main slot insulating materials in electric machines and also as insulation in transformers between high-voltage winding and transformer tanks. They can also be employed in power equipment that needs high-breakdown voltage coupled with appreciable thermal, tensile, and compressive parameters.

REFERENCES

[1] T. Tanaka, G.C. Montanari, R. Mulhaupt, IEEE Trans. Dielectr. Electr. Insul. **11**, 5 (2004) 763.
[2] D. Liu, W. Zhao, S. Liu, Q. Cen, Q. Xue, Surf. Coat. Technol. **286** (2016) 354.
[3] T.C. Triantafillou, N. Plevris, Mater. Struct. **25**, 4 (1992) 201.
[4] K.-Y. Park, S.-E. Lee, C.-G. Kim, J.-H. Han, Compos. Struct. **81**, 3 (2007) 401.
[5] B. Abramoff, J. Covino, J. Appl. Polym. Sci. **46**, 10 (1992) 1785.
[6] Y. Huang, Y. Tian, Y. Li, X. Tan, Q. Li, J. Cheng, J. Zhang, RSC Adv. **7**, 77 (2017) 49074.
[7] M. Khan, A.A. Khurram, T. Li, T. Zhao, T. Subhani, I.H. Gul, Z. Ali, V. Patel, J. Mater. Sci. Technol. **34**, 12 (2018) 2424.
[8] H.N. Chrakala, B. Ramaraj, Shivakumaraiah, G.M. Madhu, Siddaramaiah, J. Mater. Sci. **47**, 23 (2012) 8076.
[9] J.K. Rao, A. Raizada, D. Ganguly, M.M. Mankad, S.V. Satyanarayana, G.M. Madhu, Polym. Bull. **72**, 8 (2015) 2033.
[10] J.K. Rao, A. Raizada, D. Ganguly, M.M. Mankad, S.V. Satyanarayana, G.M. Madhu, J. Mater. Sci. **50**, 21 (2015) 7064.
[11] H.N. Chrakala, B. Ramaraj, Shivakumaraiah, G.M. Madhu, Siddaramaiah, J. Alloys Compd. **551** (2013) 531.
[12] H.N. Chrakala, B. Ramaraj, Shivakumaraiah, G.M. Madhu, Siddaramaiah, J. Phys. Chem. C **117**, 9 (2013) 4771.
[13] M.W. Khan, S.U. Asif, K.M. Ur Rehman, W. Uddin, Mubasher, S. Ahmed, E.U. Khan, A. Tagliaferro, P. Jagdale, M. Fakhar-e-Alam, Physica B Condens. Matter **556** (2019) 17.
[14] A. Mohanty, V.K. Srivastava, Mater. Des. **47** (2013) 711.
[15] S. Kumar Singh, A. Kumar, A. Jain, Mater. Today Proc.

5, 2 (2018) 6339.
[16] H.A. Al-Turaif, Prog. Org. Coat. **69**, 3 (2010) 241.
[17] A.A. Azeez, K.Y. Rhee, S.J. Park, D. Hui, Compos. B Eng. **45**, 1 (2013) 308.
[18] G.K. Raju, G.M. Madhu, M.A. Khan, P. Reddy, Mater. Today Proc. **5** (2018) 27998.
[19] G. Gusmano, G. Montesperelli, M. Rapone, G. Padeletti, A. Cusmà, S. Kaciulis, A. Mezzi, R. Di Maggio, Surf. Coat. Technol. **201**, 12 (2007) 5822.
[20] J.F. Quinson, C. Chino, A.M. De Becdelievre, C. Guizard, M. Brunel, J. Mater. Sci. **31**, 19 (1996) 5179.
[21] R.V. Kurahatti, A.O. Surendranathan, S. Srivastava, N. Singh, A.V. Ramesh Kumar, B. Suresha, Mater. Des. **32**, 5 (2011) 2644.
[22] A. Balamurugan, S. Kannan, S. Rajeswari, Mater. Lett. **57**, 26-27 (2003) 4202.
[23] R. Medina, F. Haupert, A.K. Schlarb, J. Mater. Sci. **43**, 9 (2008) 3245.
[24] S. Halder, P.K. Ghosh, M.S. Goyat, High Perform. Polym. **24**, 4 (2012) 331.
[25] S. Halder, M. Goyat, P. Ghosh, High Perform. Polym. **28**, 6 (2016) 697.
[26] S. Halder, S. Ahemad, S. Das, J. Wang, ACS Appl. Mater. Interfaces **8**, 3 (2016) 1695.
[27] P.T. Chung, C.T. Yang, S.H. Wang, C.W. Chen, A.S.T. Chiang, C.-Y. Liu, Mater. Chem. Phys. **136**, 2-3 (2012) 868.
[28] P. Tao, Y. Li, R.W. Siegel, L.S. Schadler, J. Appl. Polym. Sci. **130**, 5 (2013) 3785.
[29] J. Li, C. Peng, Z. Li, Z. Wu, S. Li, RSC Adv. **6**, 66 (2016) 61393.
[30] X. Ma, C. Peng, D. Zhou, Z. Wu, S. Li, J. Wang, N. Sun, J. Sol-Gel Sci. Technol. **88**, 2 (2018) 442.
[31] J.M. Matos, F.A. Júnior, L.S. Cavalcante, V. Santos, S.H. Leal, L.S. Júnior, M.R. Santos, E. Longo, Mater. Chem. Phys. **117** (2009) 455.
[32] P. Rosso, L. Ye, Macromol. Rapid Commun. **28** (2007) 121.
[33] S.N. Basahel, T.T. Ali, M. Mokhtar, K. Narasimharao, Nanoscale Res. Lett. **10**, 73 (2015).
[34] J.C. Valmalette, M. Isa, Chem. Mater. **14** (2002) 5098.
[35] R. Nagaraja, N. Kottam, C.R. Girija, B.M. Nagabhushana, Powder Technol. **215** (2012) 91.
[36] S. Chhetri, N.C. Adak, P. Samanta, N.C. Murmu, T. Kuila, Polym. Test. **63** (2017) 1.
[37] M.S. Goyat, S. Rana, S. Halder, P.K. Ghosh, Ultrason. Sonochem. **40** (2018) 861.
[38] A.J. Kinloch, R.D. Mohammed, A.C. Taylor, C. Eger, S. Sprenger, D. Egan, J. Mater. Sci. **40**, 18 (2005) 5083.
[39] L. Nicolais, M. Narkis, Polym. Eng. Sci. **11**, 3 (1971) 194.
[40] E.D. Bliznakov, C.C. White, M.T. Shaw, J. Appl. Polym. Sci. **77**, 14 (2000) 3220.
[41] D. Metin, F. Tihminlioğlu, D. Balköse, S. Ülkü, Compos. A Appl. Sci. Manuf. **35**, 1 (2004) 23.
[42] T. Kunori, P.H. Geil, J. Macromol. Sci. B **18**, 1 (1980) 135.
[43] L.E. Nielsen, J. Compos. Mater. **1**, 1 (1967) 100.
[44] B. Turcsanyi, B. Pukanszky, F. Tudos, J. Mater. Sci. Lett. **7** (1988) 160.
[45] S.Y. Fu, X.Q. Feng, B. Lauke, Y.W. Mai, Compos. B Eng. **39** (2008) 933.
[46] J.G.L. Beijer, J.L. Spoormker, Polymer **41** (1988) 5443.
[47] R. Abraham, S.P. Thomas, S. Kuryan, J. Isac, K.T. Varughese, S. Thomas, Express Polym. Lett. **3** (2009) 177.
[48] E.H. Kerner, Proc. Phys. Soc. B **69** (1954) 808.
[49] A.P. Mathew, K. Oksman, M. Sain, J. Appl. Polym. Sci. **97** (2004) 2014.
[50] J.C. Halpin, J.L. Kardos, Polym. Eng. Sci. **16** (1976) 344.
[51] AZO Materials, "Zirconia-ZrO_2 zirconium dioxide", https://www.azom.com, ac. 11/08/2019.
[52] T.A. Praveen, J. Sundara Rajan, R.R.N. Sailaja, Mater. Res. Bull. **83** (2016) 294.
[53] S.N.A. Safri, M.T.H. Sultan, N. Saba, M. Jawaid, Polym. Test. **71** (2018) 362.
[54] T.S. Radoman, J.V. Džunuzović, K.B. Jeremić, B.N. Grgur, D.S. Miličević, I.G. Popović, E.S. Džunuzović, Mater. Des. **62** (2014) 158.
[55] R. Sarathi, R.K. Sahu, P. Rajeshkumar, Mater. Sci. Eng. A **445-446** (2007) 567.
[56] Z. Li, K. Okamoto, Y. Ohki, T. Tanaka, IEEE Trans. Dielectr. Electr. Insul. **17**, 3 (2010) 653.
(Rec. 12/11/2019, Rev. 23/01/2020, Ac. 24/01/2020)

BY-NC

Remoção do alaranjado de metila em meio aquoso por microcristais de h-MoO_3 obtidos pelo método micro-ondas hidrotérmico

(*Removal of methyl orange in aqueous medium by h-MoO_3 microcrystals obtained by hydrothermal microwave method*)

M. L. de Sá[1], F. X. Nobre[2], J. M. E. de Matos[1], M. R. M. C. Santos[1]*

[1]Universidade Federal do Piauí, Laboratório Interdisciplinar de Materiais Avançados, 64049-550, Teresina, PI, Brasil

[2]Instituto Federal de Educação, Ciência e Pesquisa da Amazônia, Campus Coari, 69360-000, AM, Brasil

Resumo

Nos últimos anos aumentou o interesse em lidar com o crescente problema ambiental proveniente da poluição de águas residuais oriundas das fábricas industriais. Visando minimizar esse impacto ambiental, a técnica de adsorção em meio aquoso tem sido uma alternativa bastante explorada na atualidade. Portanto, este trabalho teve como objetivo investigar a capacidade adsortiva de microcristais de trióxido de molibdênio (h-MoO_3) usando o corante alaranjando de metila (AMe) como molécula em meio aquoso. Os microcristais foram obtidos por micro-ondas hidrotermal e estruturalmente caracterizados por diversas técnicas. O estudo cinético na adsorção do AMe resultou no melhor ajuste quando adotado o modelo de pseudossegunda ordem (R^2=0,9997). O estudo da variação de temperatura indicou que a adsorção foi um processo favorável e espontâneo. Os valores obtidos tiveram boa concordância com o modelo de isoterma de Temkin, com capacidade máxima de adsorção de 656,9 mg.g^{-1} a 318 K.
Palavras-chave: h-MoO_3, adsorção, alaranjando de metila, águas residuais.

Abstract

In recent years, interest in dealing with the growing environmental problem arising from the pollution of wastewater from industrial factories has increased. In order to minimize this environmental impact, the aqueous adsorption technique has been an alternative widely explored today. Therefore, this study aimed to investigate the adsorptive capacity of molybdenum trioxide (h-MoO_3) microcrystals using the methyl orange dye (MO) as a molecule in an aqueous medium. The microcrystals were obtained by hydrothermal microwave and structurally characterized by several techniques. The kinetic study on the adsorption of MO resulted in the best fit when adopting the pseudo-second order model (R^2=0.9997). The study of temperature variation indicated that adsorption was a favorable and spontaneous process. The values obtained were in good agreement with the Temkin isotherm model, with a maximum adsorption capacity of 656.9 mg.g^{-1} at 318 K.
***Keywords**: h-MoO_3, adsorption, methyl orange, residual waters.*

INTRODUÇÃO

A água é um recurso essencial e valioso para a existência das espécies, necessitando portanto sua preservação [1]. Contudo, o adensamento populacional, industrialização, atividades agrícolas e a urbanização têm contribuído de maneira negativa para manutenção dos recursos hídricos naturais [2,3]. A poluição dos recursos hídricos por compostos orgânicos industriais, especificamente os corantes sintéticos, tem sido comumente reportada e pode provocar dentre outras complicações, alergias, irritações na pele e mucosas, câncer e mutações genéticas, além de graves problemas ambientais [4-6]. Particularmente, o alaranjado de metila (AMe) é um típico corante sintético de natureza aniônica que possui ligações do tipo azo (-N=N-) junto à estrutura aromática, que de maneira geral apresenta alta estabilidade a processos fotoquímicos e degradação por fatores naturais, implicando em uma considerável dificuldade no processo de remoção deste em águas residuais [7, 8]. A Fig. 1 apresenta a estrutura do alaranjado de metila.

Atualmente, diversas técnicas têm sido amplamente utilizadas para aplicação em remoção de corantes sintéticos de águas residuais, tais como floculação [9], oxidação química [10], degradação fotocatalítica [11] e adsorção [12]. Dentre todas as técnicas mencionadas, os processos de adsorção

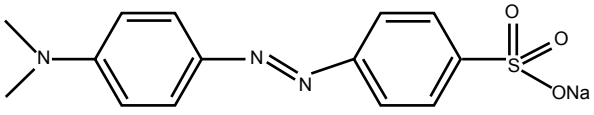

Figura 1: Representação estrutural da molécula de alaranjando de metila - AMe.
[Figure 1: Structural representation for methyl orange - MO molecule.]

**mrita@ufpi.edu.br*
https://orcid.org/0000-0001-6097-6230

utilizando sólidos demonstram ser muito adequados para a remoção de poluentes orgânicos provenientes de águas residuais, em virtude de terem baixo custo operacional, facilidade de operação e alta eficiência [13]. Neste contexto, diversos materiais têm sido explorados com a finalidade de aplicações em processos adsortivos, mais precisamente no tratamento de água residual. Dentre outros, destacam-se os óxidos metálicos h-MoS_2 [4], NiO_2 [14], ZnO [15], δ-MnO_2 [16] e MoO_3 [17], que têm sido reportados como eficientes adsorventes na remoção do corante AMe devido à sua elevada área superficial e baixo custo de regeneração [18].

No campo das aplicações tecnológicas o trióxido de molibdênio (MoO_3) tem sido destaque devido às várias propriedades exibidas e fácil obtenção por diversos métodos convencionais de síntese. Usualmente, o MoO_3 possui três formas cristalográficas: fase alfa (α-MoO_3) [19], de estrutura cristalina ortorrômbica estável termodinamicamente, e duas outras fases metaestáveis, a fase beta (β-MoO_3) [20] e hexagonal (h-MoO_3) [21] de estrutura monoclínica e hexagonal, respectivamente. Huang et al. [22] reportaram a síntese de MoO_{3-x} (0<x<1) pelo método solvotermal e usaram este adsorvente para adsorção dos corantes Rodamina B (RhB), azul de metileno (AM) e alaranjado de metila (AMe). Os resultados mostraram que o MoO_{3-x} exibe uma taxa de remoção de aproximadamente 60% e capacidade de adsorção de 154,2 $mg.g^{-1}$ para o alaranjando de metila. No entanto, estudos sobre adsorção de corantes pelo MoO_3 obtidos pelo método micro-ondas hidrotermal são pouco reportados na literatura. Desta forma, neste estudo foram sintetizados microcristais de h-MoO_3 por este método; além disso, investigou-se a capacidade adsortiva destes microcristais usando o corante alaranjado de metila (AMe) como adsorvato, avaliando o efeito das variáveis concentração inicial, massa do adsorvente, pH da solução e temperatura.

EXPERIMENTAL

Materiais: o heptamolibdato de amônio tetra-hidratado [$(NH_4)_6Mo_7O_{24}.4H_2O$, pureza >83%), ácido nítrico (HNO_3, pureza >70%), acetona (C_3H_6O, pureza >99,5%) e alaranjado de metila ($C_{14}H_{14}N_3NaO_3S$, pureza analítica) foram obtidos da Sigma Aldrich Brasil.

Síntese dos microcristais de h-MoO_3: os microcristais de trióxido de molibdênio foram sintetizados utilizando o micro-ondas hidrotérmico. Inicialmente, foram solubilizados 2 mmol de heptamolibdato de amônio tetra-hidratado (AHM) em 50 mL de água destilada em um béquer de 100 mL sob agitação magnética constante. Posteriormente, 5 mL de ácido nítrico concentrado foram adicionados ao meio reacional obtendo rapidamente uma suspensão de cor branca. Essa suspensão foi adicionada a um copo Teflon de 80 mL, fechada e submetida à síntese por micro-ondas a 140 °C por 1 h, usando potência e frequência de 700 W e 2,45 MHz, respectivamente. O precipitado coletado após a síntese foi lavado diversas vezes com água destilada usando centrifugação de 8000 rpm, durante 5 min em cada ciclo de lavagem, seguida de secagem em estufa a 80 °C por 12 h.

Caracterização: o padrão de difração de raios X dos microcristais de h-MoO_3 foi coletado usando o método do pó com um difratômetro (D2Phaser, Bruker), usando um ânodo de cobre como fonte de radiação (CuKα 1,5406 Å), obtendo informações no intervalo 2θ entre 5° e 80° com passe de 0.02°. Além disso, o refinamento estrutural usando o método de Rietveld foi usado no estudo das informações estruturais, mais precisamente os parâmetros de rede (a, b, c), coordenadas atômicas (x, y, z), linha base, volume de célula unitária (V) e parâmetros de Cagliote (U, V, W). A espectroscopia Raman foi empregada com a finalidade de identificar os modos vibracionais característicos da fase hexagonal para o trióxido de molibdênio. O espectro Raman dos microcristais foi coletado usando um equipamento da Bruker, Senterra, usando laser com comprimento de onda de 532 nm (verde) como fonte de energia de excitação das amostras. Os dados vibracionais foram coletados no intervalo entre 85 e 1100 cm^{-1}, configurando a potência, resolução e tempo de integração de 0,5 mW, 4 cm^{-1} e 10 adições, respetivamente. Os espectros vibracionais na região do infravermelho (IV) foi registrado com um espectrômetro PerkinElmer, L160000F. Inicialmente, pastilha de brometo de potássio (KBr) foi preparada por mistura de 1 mg de microcristais de h-MoO_3 com 100 mg de KBr e prensagem a 5 kPa por 1 min. Os dados foram coletados na faixa de 400 a 4000 cm^{-1} no modo de transmissão com 32 varreduras aplicadas com resolução de 2 cm^{-1}. A morfologia dos elementos presentes na composição dos microcristais foi investigada usando microscopia eletrônica de varredura com emissão de campo (FE-MEV). Para tanto, 5 mg de microcristais foram dispersos em 1 mL de acetona (pureza analítica), e sonicados à temperatura ambiente por 5 min; uma alíquota desta suspensão foi retirada e gotejada sobre um substrato de alumínio e analisada em seguida. A área de superfície específica (ASS) e a isoterma de adsorção-dessorção de nitrogênio da amostra foram determinadas em um analisador de área superficial e tamanho de poros (NOVA 2200e, Quantachrome Instr.) via adsorção de N_2 a -196 °C; a área de superfície e o tamanho de poros foram calculados usando os métodos de Brunauer-Emmett-Teller (BET) e Barrett-Joyner-Halenda (BJH), respectivamente. Antes das medições, as amostras foram desgaseificadas a 200 °C por 8 h. A massa de amostra usada no ensaio foi de 0,4321 mg.

Potencial de carga zero - pH_{pzc}: o estudo da presença de cargas na superfície dos microcristais em meio aquoso foi realizado usando a metodologia do ponto de carga zero. Foi preparada uma solução 0,1 M de KNO_3 (Vetec Quím. Fina, 99%) e inseridas alíquotas de 20 mL da solução em frascos Erlenmeyer juntamente com 20 mg dos microcristais de h-MoO_3. O pH foi ajustado na faixa de 1 a 12 usando soluções de 0,1 M de HCl (Dinâmica Quím. Contemp., 37%) e 0,1 M de NaOH (Vetec Quím. Fina, 99%). As suspensões foram mantidas sob agitação mecânica por 24 h a 180 rpm

e 298 K. O pH antes e posterior ao ensaio foi mensurado e apresentado graficamente em relação ao pH inicial e ΔpH ($pH_{inicial}$–pH_{final}). O valor de pH_{pzc} neste processo foi obtido pela interseção da curva obtida com a origem.

Ensaios de adsorção. *Efeito da dosagem*: os testes de adsorção foram realizados para investigar os fatores que influenciam o processo de adsorção (dosagem, pH, tempo, concentração e temperatura), sendo os experimentos realizados em triplicata utilizando uma incubadora (TE-420, Tecnal) com agitação mecânica a 180 rpm. O efeito da dosagem do adsorvente na remoção do corante alaranjado de metila (AMe) em solução aquosa foi avaliado utilizando as matrizes obtidas em diferentes tempos de síntese de h-MoO_3, com variação da massa de 10,0 a 50,0 mg e 20,0 mL de AMe (100,0 $mg.L^{-1}$, pH 5,5, 298 K e 24 h). Após a agitação foram realizadas centrifugações (NOVA Instr., 5000 rpm por 10 min) e, em seguida, a concentração do sobrenadante de AMe foi determinada usando um espectrofotômetro UV-vis (Cary 60, Agilent). A quantidade de AMe adsorvida (q, $mg.g^{-1}$) e a taxa de remoção (T_R, %) do corante foram calculadas por:

$$q = \frac{(C_i - C_f).V}{m} \quad (A)$$

$$T_R = \frac{C_i - C_f}{C_i}.100 \quad (B)$$

sendo C_i e C_f as concentrações inicial e final do corante ($mg.L^{-1}$), respectivamente, V o volume da solução do corante (L) e m a massa do adsorvente (g). *Efeito do pH*: para avaliar o efeito do pH, utilizou-se uma solução de 100,0 $mg.L^{-1}$ de AMe com pH de 2,0 a 12,0 e massa do adsorvente determinada no teste anterior com tempo de contato de 24 h, sendo o pH ajustado com soluções de 0,1 $mol.L^{-1}$ de HCl e/ou 0,1 $mol.L^{-1}$ de NaOH. Após este tempo, a concentração do sobrenadante de AMe foi determinada como descrito anteriormente e a quantidade de corante retida (q), em cada pH, no adsorvente foi obtida usando a Eq. A. *Efeito do tempo de contato*: para avaliar o efeito do tempo foi levado em consideração a melhor massa e pH encontrados nos testes anteriores. Foram colocados 20,0 mL de uma solução 100 $mg.L^{-1}$ de corante AMe em contato com 20,0 mg do adsorvente. Este sistema foi mantido em agitação (180 rpm) a 298 K em diferentes tempos, variando de 0 a 1440 min. Após cada tempo, a concentração do sobrenadante de AMe foi determinada e a quantidade de corante retido (q) em cada tempo no adsorvente foi obtido usando a Eq. A. Para verificar a cinética do processo de adsorção, os resultados experimentais foram ajustados com as equações lineares dos modelos de pseudoprimeira ordem, pseudossegunda ordem e Elovich. As equações usadas são mostradas na Tabela I. *Efeito da temperatura e concentração do corante*: o efeito da concentração do corante AMe no processo de adsorção foi avaliado utilizando 20,0 mg do adsorvente e 20,0 mL de solução em diferentes concentrações (10 a 700 $mg.L^{-1}$) no melhor pH e tempo da adsorção. Este sistema foi mantido em agitação (180 rpm) em diferentes temperaturas (298, 308 e 318 K). Após o tempo de equilíbrio de adsorção, a concentração do sobrenadante de AMe foi determinada e a quantidade de corante retida (q) em cada concentração no adsorvente foi obtida usando a Eq. A. Foram utilizados modelos de isotermas para avaliar o processo de adsorção em estudo. A Tabela II apresenta as equações lineares utilizadas para os modelos de Freundlich e Temkin. Os parâmetros termodinâmicos de adsorção, incluindo entalpia (ΔH), entropia (ΔS) e energia livre de Gibbs (ΔG), foram calculados através das Eqs. C e D, sendo ΔH e ΔS obtidos utilizando a equação de Van't Hoff [28, 29]:

$$\ln K_e = \frac{\Delta s}{R} - \frac{\Delta H}{R.T} \quad (C)$$

$$\Delta G = \Delta H - T.\Delta S \quad (D)$$

onde R é a constante dos gases (8,314 $J.mol^{-1}.K^{-1}$), T é a temperatura (K) e K_e é a constante de equilíbrio à temperatura T, calculada através de:

$$K_e = \frac{q_e}{C_e} \quad (E)$$

sendo q_e é a quantidade adsorvida no equilíbrio ($mg.g^{-1}$) e C_e é a concentração do corante no equilíbrio ($mg.L^{-1}$). *Ensaio de reuso*: para avaliar a reutilização dos microcristais de h-MoO_3 foi realizado o ensaio de reuso, levando em consideração os melhores resultados dos testes anteriores. Utilizaram-se 20,0 mg do adsorvente e 20,0 mL de solução do AMe a 700 $mg.L^{-1}$ em pH 4,0 no tempo de contato de 960 min. Esse sistema foi mantido em agitação (180 rpm) a 318 K. A taxa de remoção (T_R) do corante foi calculado usando a Eq. B. Após cada teste de adsorção, os adsorventes foram recuperados utilizando água em pH 12 (processo de dessorção) e em seguida secos a 45±5 °C por 24 h. Foram

Tabela I - Modelos cinéticos de adsorção e suas formas lineares.
[Table I - Kinetic models of adsorption and their linear forms.]

Modelo	Forma linear	Gráfico	Ref.
Pseudoprimeira-ordem	$\ln(q_{e,exp}-qt) = \ln q_{e,cal} - k_1.t$	$\ln(q_{e,exp}-q_t)$ vs t	[23]
Pseudossegunda-ordem	$\frac{t}{q_t} = \frac{1}{k_2.q_{e,cal}^2} + \frac{1}{q_{e,cal}}.t$; $h = k_2 q_{e,cal}^2$	t/q_t vs t	[24]
Elovich	$q_t = \frac{1}{\beta}.\ln(\alpha.\beta) + \frac{1}{\beta}.\ln t$	q_t vs lnt	[25]

Tabela II - Modelos isotérmicos de adsorção e suas formas lineares.
[Table II - Isotherm models of adsorption and their linear forms.]

Modelo	Forma linear	Gráfico	Ref.
Freundlich	$\ln q_e = \ln K_f + \frac{1}{n_f} \ln C_e$	$\ln q_e$ vs $\ln C_e$	[26]
Temkin	$q_e = \frac{R.T}{b_T} \ln A_T + \frac{R.T}{b_T} \ln C_e$	q_e vs $\ln C_e$	[27]

realizados quatro ciclos de adsorção-dessorção para o ensaio de reuso.

RESULTADOS E DISCUSSÃO

Caracterização estrutural por difração de raios X (DRX) e refinamento Rietveld: na Fig. 2 está apresentado o padrão de difração dos microcristais de trióxido de molibdênio sintetizados a 140 °C por 1 h, usando o método micro-ondas hidrotérmico (MH). A indexação dos planos de difração resultou na ótima concordância dos valores experimentais com as informações reportadas no arquivo JCPDS 21-0569, como sendo referente à fase hexagonal para o trióxido de molibdênio - h-MoO_3 (P63/m), também confirmado pelas literaturas consultadas [30, 31]. O perfil gráfico obtido para a intensidade dos picos de difração sugeriu que estes microcristais apresentaram elevado grau de cristalinidade e alta pureza, tendo em vista que não foram identificados picos associados com a presença de precursor de síntese, fase secundária ou qualquer contaminante [32-34]. Publicações recentes reportam a fórmula $MoO_{3m}NH_3.nH_2O$, onde $0{,}09 \leq m \leq 0{,}20$ e $0{,}18 \leq n \leq 0{,}60$, para o trióxido de molibdênio obtido em meio aquoso usando o heptamolibdato de amônio como reagente em meio ácido. O processo de formação desta estrutura é iniciada pela acidificação do meio reacional contendo o heptamolibdato de amônio que promove a forte interação dos clusters $[MoO_6]$-$[MoO_6]$, coordenados pelos oxigênios dispostos nos cantos dos octaedros, preferencialmente pela atração eletrostática dos grupos $OH...M^+$, onde M é o molibdênio [31, 33]. Portanto, justifica as bandas de estiramento das ligações N-H no espetro de infravermelho para os microcristais de h-MoO_3.

Na Fig. 3 está apresentado graficamente o resultado para o refinamento estrutural usando o método de Rietveld para os microcristais de h-MoO_3. A computação das informações experimentais provenientes do padrão de difração experimental dos microcristais de h-MoO_3 (Y_{obs}) correlacionadas com as informações contidas no arquivo Inorganic Crystal Structure Data - ICSD n° 87962 (Y_{cal}) foi realizada utilizando o software FullProf (versão agosto 2019). A qualidade dos dados computados foi monitorada usando os indicadores de qualidade R (R_{wp} e χ^2), obtendo resultados de convergência ideal quando o valor de χ^2 se aproximou de 1. Além disso, o perfil gráfico obtido para a linha residual (Y_{obs}–Y_{cal}), dada pela diferença de intensidades dos picos experimentais (Y_{obs}) e picos de difração teóricos

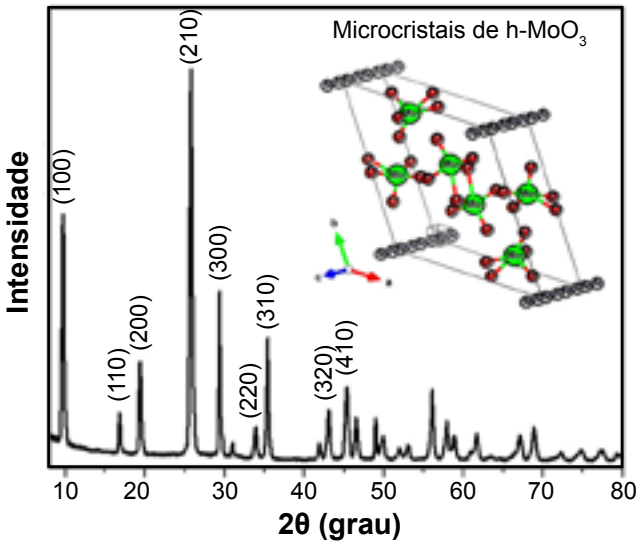

Figura 2: Padrão de DRX dos microcristais de h-MoO_3 obtidos pelo método micro-ondas hidrotérmico (MH).
[Figure 2: XRD pattern of h-MoO_3 microcrystals obtained from hydrothermal microwave (MH) method.]

(Y_{cal}), expressa graficamente a qualidade da convergência na computação dos dados. Baseado no ajuste computado (Fig. 3), foi possível notar que houve uma boa concordância para todos os picos de difração contidos no intervalo 2θ de 8° a 80°. No intervalo 2θ entre 8° a 30°, deslocamentos de pequena escala foram observados, causados principalmente

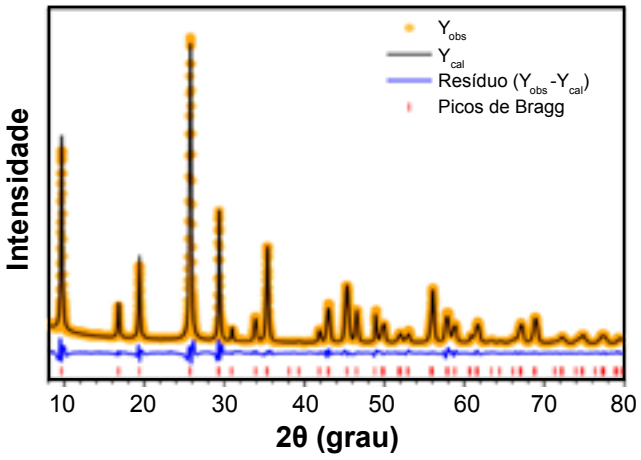

Figura 3: Gráfico do refinamento Rietveld dos microcristais de h-MoO_3.
[Figure 3: Rietveld refinement plot for h-MoO_3 microcrystals.]

pela orientação preferencial dos planos de difração (100), (110), (210) e (300), indexados aos valores 2θ de 9,6°, 16,6°, 19,2°, 25,8° e 29,3°, respectivamente.

Os valores de parâmetros de rede, tamanho de cristalito e χ^2 obtidos através do refinamento estrutural usando o método de Rietveld estão apresentados na Tabela III. Partindo destes resultados, confirmou-se a obtenção da estrutura hexagonal para os microcristais de h-MoO_3 com elevada cristalinidade e grau de pureza, destacando-se os valores de parâmetros de rede a=b=10,5577(1) Å e c=3,7133(1) Å, associados a um volume de célula unitária e tamanho de cristalito de 358,41(2) Å^3 e 20,27 nm, respectivamente. As informações complementares obtidas mediante o refinamento estrutural usando o método de Rietveld estão dispostas na Tabela IV, onde é possível consultar os valores de posições atômicas (x, y, z) para os átomos de molibdênio (Mo), oxigênio (O)

Tabela III - Valores de parâmetros de rede (a, b, c), volume de célula unitária (V) e χ^2 para os microcristais de h-MoO_3 e valores do arquivo ICSD 87962.

[Table III - Rietveld refinement results for lattice parameters (a, b, c), unit cell volume (V), and χ^2 for h-MoO_3 microcrystals and values of the file ICSD 87962.]

Identificação	Parâmetro de rede (Å)		V (Å^3)	χ^2
	a = b	c		
h-MoO_3	10,5577(1)	3,7133(1)	358,41(2)	3,6
ICSD 87962	10,576(1)	3,728(1)	361,12(12)	-

Tabela IV - Valores de posições atômicas (x, y, z), operação de simetria (Op. sim.) e símbolo obtido para o refinamento estrutural usando o método de Rietveld para os microcristais de h-MoO_3 sintetizados neste estudo e valores do arquivo ICSD 61163.

[Table IV - Atomic position values (x, y, z), symmetry operation (Op. sim.), and symbol obtained for structural refinement using the Rietveld method for the h-MoO_3 microcrystals synthesized in this study and values of the file ICSD 61163.]

Elemento	Símbolo	x	y	z	Op. sim.
h-MoO_3 (sintetizado neste estudo)					
Mo1	Mo	0,64563(21)	0,54080(18)	0,25	x,y,z
O1	O.3	0,8002(14)	0,5110(14)	0,25	x,y,z
O2	O.2	0,7426(10)	0,7321(10)	0,25	x,y,z
O3	O.3	0,4061(10)	0,5031(10)	0,25	x,y,z
Mo1	Mo	0,35437(21)	0,45920(18)	0,25	1-x,1-y,-1/2+z
Mo1	Mo	0,35437(21)	0,45920(18)	-0,25	1-x,1-y,1/2+z
Mo1	Mo	0,89517(28)	0,35437(21)	0,75	1-x+y,1-x,z
O1	O.2	0,4890(14)	0,2892(20)	0,25	1-y,x-y,z
O3	O.2	0,5939(10)	0,4969(10)	-0,25	1-x,1-y,-1/2+z
O3	O.2	0,5939(10)	0,4969(10)	0,75	1-x,1-y,1/2+z
N1	N.3	0,0	0,0	0,0	x,y,z
h-MoO_3 (ICSD 62163)					
Mo1	Mo	0,6445(4)	0,5418(4)	0,25	x,y,1/2-z
O1	O.3	0,771(3)	0,489(3)	0,25	x,y,1/2-z
O2	O.2	0,713(3)	0,720(3)	0,25	x,y,1/2-z
O3	O.3	0,415(3)	0,492(3)	0,25	x,y,1/2-z
Mo1	Mo	0,8973(6)	0,3555(4)	0,25	1-x+y,1-x,1/2-z
Mo1	Mo	0,3555(4)	0,4582(4)	-0,25	1-x,1-y,-z
Mo1	Mo	0,3555(4)	0,4582(4)	0,75	1-x,1-y,1-z
O1	O.2	0,511(3)	0,282(4)	0,25	1-y,x-y,1/2-z
O3	O.2	0,585(3)	0,508(3)	-0,25	1-x,1-y,-z
O3	O.2	0,585(3)	0,508(3)	0,75	1-x,1-y,1-z
N1	N.3	0	0	0	x-y,x,-z

e nitrogênio (N) para a microestrutura obtida, comparados com os valores apresentados no arquivo ICSD 87962. Portanto, foi possível verificar que não houve diferenças significativas para as posições atômicas em comparação ao padrão disponível, atribuindo aos pequenos valores de deslocamento observados para os átomos de oxigênio o efeito do processo hidrotérmico na obtenção desta microestrutura que sofreu o efeito da pressão e temperatura no mecanismo de aglomeração, crescimento e maturação dos microcristais.

Espectroscopia Raman: o espectro Raman experimental coletado para os microcristais de h-MoO_3 sintetizados por micro-ondas hidrotermal está apresentado na Fig. 4. Todos os modos ativos identificados nos espectros no intervalo de 85 a 1100 cm^{-1} foram em acordo com os que foram consultados na literatura [31, 35, 36], confirmando a obtenção da fase hexagonal do trióxido de molibdênio com elevado grau de pureza e cristalinidade e corroborando as informações obtidas na difração de raios X. Os modos vibracionais Raman experimentais identificados para os microcristais sintetizados no intervalo de 890 a 974 cm^{-1} foram associados com as vibrações do tipo Mo=O [37], enquanto os modos vibracionais no intervalo de 314 a 689 cm^{-1} foram definidos como característicos das ligações O-Mo-O, presentes na rede cristalina que compõem o *bulk* [38]. Por fim, os modos em 109 a 248 cm^{-1} são as assinaturas das vibrações moleculares Mo-Mo associadas às ligações dos tetraedros MoO_4 [36].

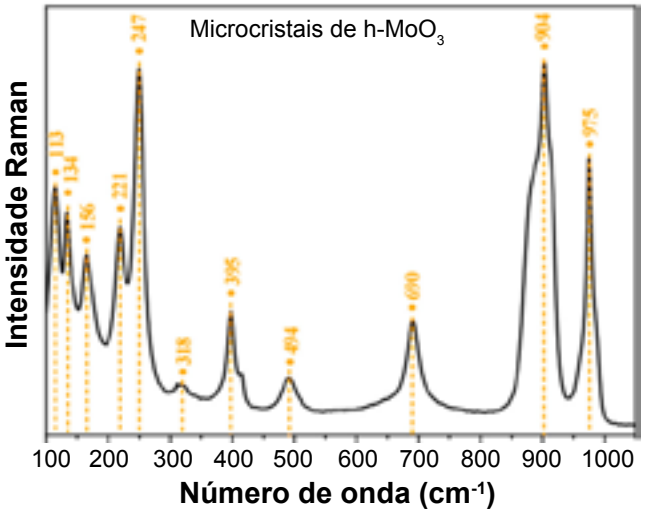

Figura 4: Espectro Raman dos microcristais de h-MoO_3.
[Figure 4: Raman spectrum of h-MoO_3 microcrystals.]

Espectroscopia vibracional no infravermelho: o espectro vibracional na região do infravermelho por transformada de Fourier (IVFT) coletado para os microcristais de h-MoO_3 sintetizados por micro-ondas hidrotermal (MH) está apresentado na Fig. 5. De acordo com as literaturas consultadas [37-39], quando a fase hexagonal para o trióxido de molibdênio é obtida utilizando o AHM (heptamolibdato de amônio tetra-hidratado) como precursor de síntese, geralmente ocorre a orientação dos microcristais pela interação dos grupos -OH dispostos nos cantos dos clusters com os íons de amônio (NH_4^+) presentes no meio reacional. Assim, os resultados obtidos por difração de raios X corroboraram as informações extraídas na espectroscopia IVFT, uma vez identificados os modos vibracionais ativos nos números de onda 1398, 3143 e 3324 cm^{-1}, referentes às vibrações moleculares das ligações N-H provenientes dos íons de amônio intercalados no *bulk* dos microcristais [40]. As vibrações moleculares pertinentes às moléculas de água adsorvidas na estrutura dos microcristais de h-MoO_3 também foram identificadas nos números de onda 1618, 3413 e 3480 cm^{-1}, mais precisamente associadas com as deformações e estiramentos simétricos e assimétricos das ligações O-H [41]. Os modos ativos identificados no intervalo de 400 a 1100 cm^{-1} são considerados assinaturas dos trióxido de molibdênio [30, 34]. Em adição, os modos em 912 e 973 cm^{-1} são descritos como sendo característico dos estiramentos das ligações Mo=O [38, 40], enquanto em 515 cm^{-1} é geralmente relacionado com as vibrações das ligações do esqueleto da rede cristalina, em geral, promovido pelas vibrações das ligações Mo-O-Mo [42].

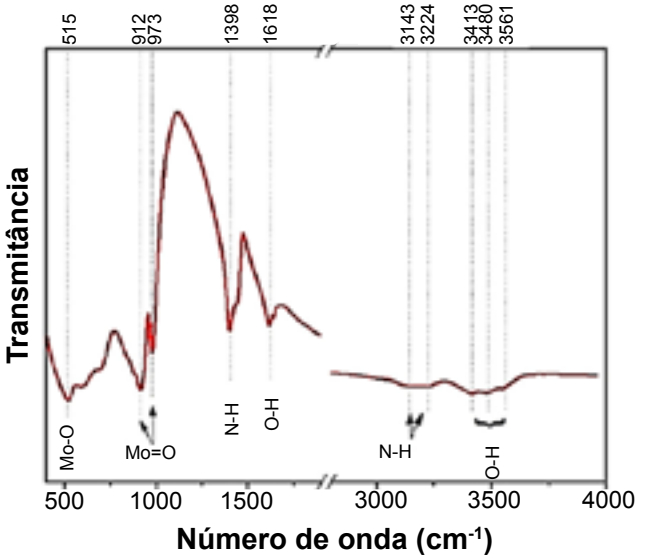

Figura 5: Espectro de IVFT dos microcristais de h-MoO_3 obtidos pelo método MH.
[Figure 5: FTIR spectrum of h-MoO_3 microcrystals obtained from MH method.]

Morfologia de h-MoO_3 por microscopia eletrônica de varredura (MEV): a morfologia dos microcristais de h-MoO_3 sintetizados por micro-ondas hidrotermal foi investigada por MEV (Fig. 6). Observou-se que os microcristais possuíram estruturas com faces hexagonais em forma de bastões alongados com elevada densidade de defeitos superficiais, semelhantes a poros na superfície, porém, característicos da fase hexagonal para o trióxido de molibdênio; devido à forte influência da pressão e temperatura no método MH, sugere-se que os microcristais cresceram pelo processo de maturação (*ripening*) de Ostwald [30, 39]. O resultado da análise de adsorção e dessorção de N_2 usando o método de BET, graficamente apresentado na Fig. 7, revelou que os microcristais exibiram valor de área superficial de 0,36(5) $m^2.g^{-1}$, semelhante aos

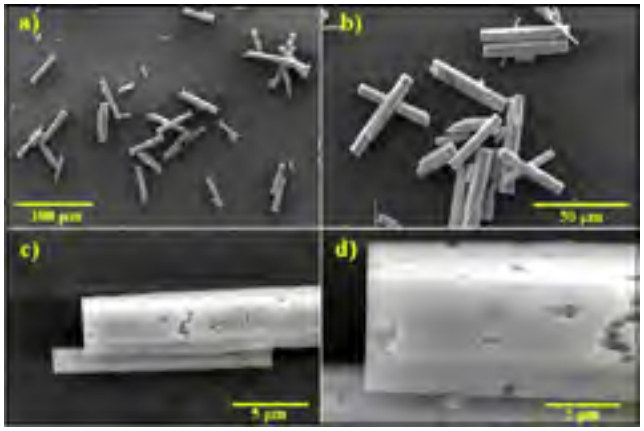

Figura 6: Micrografias de MEV dos microcristais hexagonais de h-MoO_3 em diferentes magnificações.
[Figure 6: SEM micrography of hexagonal h-MoO_3 rod-like microcrystals at different magnifications.]

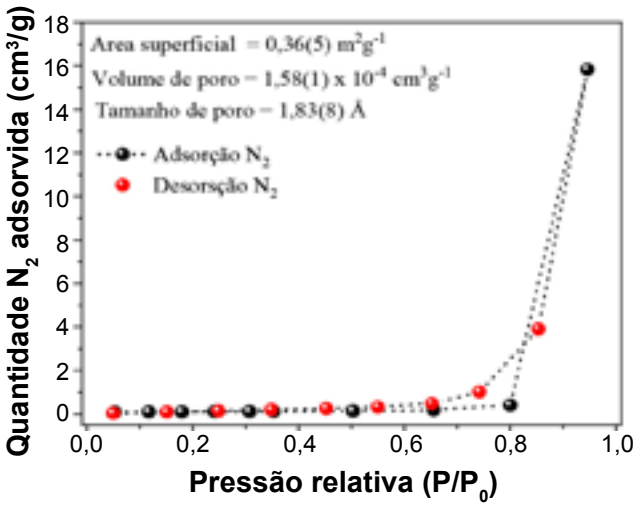

Figura 7: Isoterma de adsorção-dessorção de N_2 pelo método BET para os microcristais de h-MoO_3.
[Figure 7: Adsorption-desorption isotherm of N_2 by BET method for h-MoO_3 microcrystals.]

valores reportados de 0,43 $m^2.g^{-1}$ [43] e <1 $m^2.g^{-1}$ [44].

Estudo de adsorção

Efeito da dosagem do adsorvente: com intuito de averiguar a menor massa de adsorvente que seria capaz de proporcionar o maior percentual de remoção de adsorção do AMe em solução aquosa, foi analisado o efeito da dosagem de microcristais h-MoO_3. Através da Fig. 8a, pode-se observar que o percentual de remoção (entre 40% a 64%) do AMe aumentou com o aumento da massa dos microcristais de h-MoO_3 ocasionado pelo aumento dos sítios de adsorção, conforme observado em estudos similares [5, 45]. No entanto, notou-se que para a amostra obtida no tempo de 60 min (h-MoO_3-1h) o equilíbrio de adsorção foi iniciado com maior capacidade de adsorção (56,9 $mg.g^{-1}$) e percentual de remoção (58,1%) do corante AMe, quando foi utilizada uma massa de 20,0 mg do adsorvente. Assim, a massa de 20,0

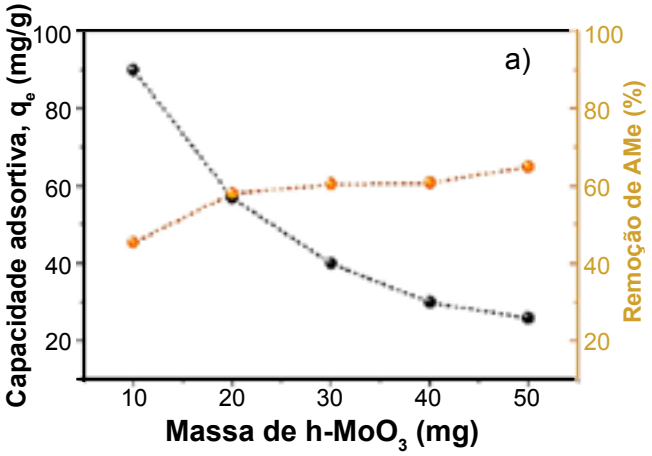

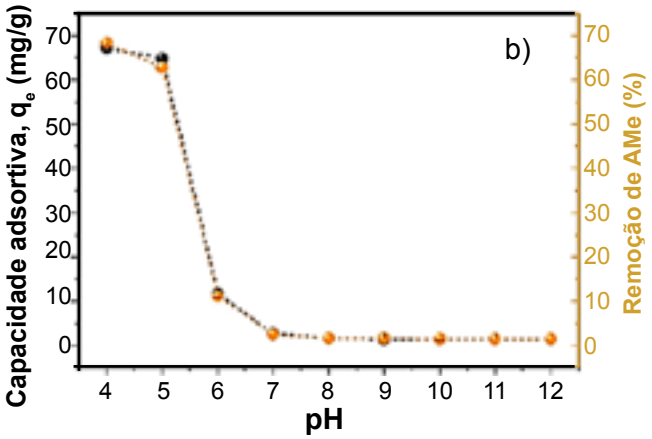

Figura 8: Efeito da dosagem do adsorvente (a) e do pH (b) na adsorção do AMe por microcristais de h-MoO_3 em forma de bastão.
[Figure 8: Effect of adsorbent dosage (a) and pH (b) on the adsorption of MO by h-MoO_3 rod-like microcrystals.]

mg e a matriz h-MoO_3-1h foram utilizadas nos ensaios de adsorção posteriores.

Efeito do pH: a Fig. 8b mostra o percentual de remoção e a capacidade de adsorção do AMe utilizando os microcristais h-MoO_3 em diferentes valores de pH da solução do corante. Observou-se que a maior capacidade de adsorção ocorreu em pH 4,0, sendo este pH considerado para estudos posteriores, pois pode ter provocado uma maior protonação da superfície do adsorvente proporcionando um aumento na adsorção de espécies aniônicas do AMe por interações eletrostáticas. No entanto, o aumento do pH proporcionou diminuição na adsorção do corante AMe devido à diminuição destas interações e aumento das ligações de hidrogênio e interações de van der Waals [46]. Estas evidências foram suportadas pela análise do ponto de carga zero (pH_{pzc}) dos microcristais de h-MoO_3; como pode ser visualizado na Fig. 9, a carga superficial dos microcristais em valores de pH acima de 4 resultaram nos valores de pH>pH_{pzc}, o que implicou na presença de cargas superficiais negativas. Assim, justificou-se a ausência de adsorção efetiva em valores de pH superior a 5 devido à repulsão das moléculas do corante AMe, aniônicas, pelos microcristais de h-MoO_3, enquanto em valores de pH≈4 houve uma melhor performance na adsorção do corante AMe. Resultados similares foram

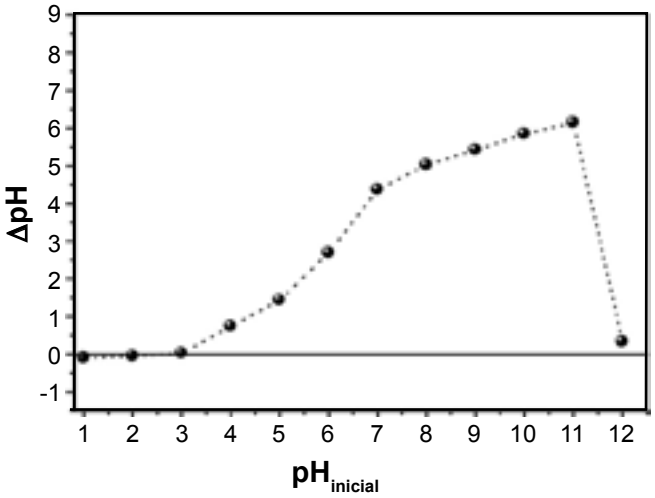

Figura 9: Gráfico de potencial de carga zero (pH_{pzc}) para os microcristais de h-MoO_3.
[Figure 9: Graph of point of zero charge (pH_{pzc}) of h-MoO_3 microcrystals.]

observados nos estudos de Mohammad et al. [5] e Li et al. [47], que relataram a atração eletrostática entre o corante AMe e nanocompósito de quitosana/TiO_2 ou nanoestrutura de Cu_3SnS_4@C em pH 4,0 e 5,0, respectivamente. Outros estudos [48, 49] relatam que em pH baixo é favorável a protonação da superfície do adsorvente, no qual pode aumentar a atração eletrostática existente entre a superfície do adsorvente carregado positivamente e o corante aniônico (por exemplo, AMe), consequentemente tendo uma maior eficiência na remoção deste tipo de corante. Com o aumento do pH há uma diminuição na capacidade adsortiva devido à repulsão eletrostática entre a matriz e o corante aniônico ou uma competição de OH^- e o corante pelos sítios ativos do adsorvente; comportamento parecido pode ter ocorrido neste estudo.

Efeito do tempo de contato: através do estudo do tempo mostrado na Fig. 10, pode-se observar que o equilíbrio entre o adsorvente e adsorvato foi atingido em torno de 960 min, pois a quantidade adsorvida de AMe permaneceu praticamente constante a partir deste tempo, que foi considerado para estudos posteriores. Com intuito de investigar a cinética e mecanismo de adsorção que determinaram o processo de adsorção, os dados obtidos experimentalmente através deste estudo foram submetidos a cálculos matemáticos utilizando diferentes modelos cinéticos [46]. Com base na Tabela V, que mostra os parâmetros obtidos com o ajuste aos diferentes modelos cinéticos para o sistema em estudo, observou-se que o maior valor do coeficiente de correlação (R^2=0,9997) foi obtido utilizando o modelo de pseudossegunda ordem quando comparado com os outros modelos. Além disso, o valor da quantidade de adsorção calculada ($q_{e,cal}$) para este modelo cinético foi o que mais se aproximou da quantidade de adsorção obtida experimentalmente ($q_{e,exp}$). Assim, este modelo que determina a quimissorção como etapa determinante do processo de adsorção foi o mais apropriado para descrever o processo de adsorção do AMe utilizando h-MoO_3, como foi observado em trabalhos semelhantes [47-50]. Além disso, a performance dos microcristais na adsorção do corante AMe ao longo de quatro ciclos consecutivos, como mostra a Fig. 11, resultou no decréscimo de 14% no percentual de adsorção ao fim do 4º ciclo de adsorção, comparado com o primeiro ciclo; portanto, os microcristais podem ser amplamente reutilizados nos processos de adsorção.

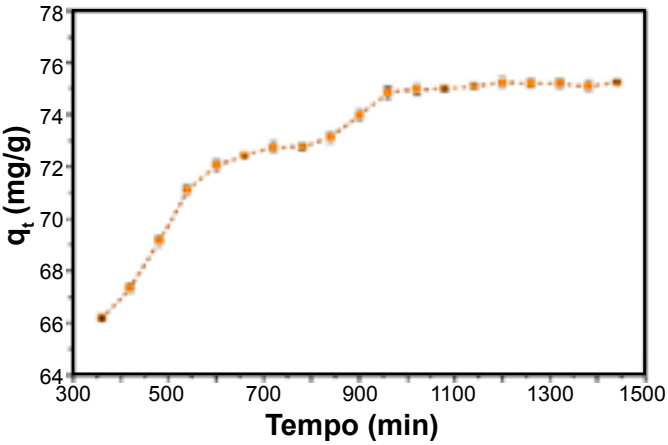

Figura 10: Efeito do tempo de contato na adsorção do AMe por microcristais de h-MoO_3 em forma de bastão.
[Figure 10: Effect of contact time on the adsorption of MO by h-MoO_3 rod-like microcrystals.]

Efeito da concentração e temperatura do corante: a Fig. 12 mostra as curvas de adsorção do corante AMe obtidos experimentalmente utilizando a matriz adsorvente h-MoO_3 realizadas a 298, 308 e 318 K. Os dados obtidos experimentalmente foram ajustados com diferentes modelos de isotermas; apesar dos modelos empíricos não refletirem nas questões relacionadas com o mecanismo da adsorção, fornecem informações úteis sobre interpretação do processo de adsorção em estudo [28, 46]. A Tabela VI mostra os valores dos parâmetros dos modelos de isotermas para adsorção do corante AMe em meio aquoso. Pode-se observar que os coeficientes de correlação (R^2) obtidos a partir de ajustes lineares dos dados experimentais apresentaram os maiores valores para o modelo de Temkin, sendo 0,9903 a

Tabela V - Parâmetros dos modelos cinéticos para a adsorção de AMe por microcristais de h-MoO_3 em forma de bastão.
[Table V - Modeled kinetic parameters for the adsorption of MO on h-MoO_3 rod-like microcrystals.]

	Pseudoprimeira ordem			Pseudossegunda ordem				Elovich		
$q_{e,exp}$	k_1 (min^{-1})	$q_{e,cal}$ ($mg.g^{-1}$)	R^2	k_2 ($g.mg^{-1}.min^{-1}$)	$q_{e,cal}$ ($mg.g^{-1}$)	h ($mg.g^{-1}.min^{-1}$)	R^2	α ($mg.g^{-1}.min^{-1}$)	β ($g.mg^{-1}$)	R^2
75,25	0,0057	114,2	0,9048	0,0002	79,05	1,250	0,9997	766,5	0,1578	0,9031

298 K, 0,9925 a 308 K e 0,9861 a 318 K. Silva et al. [46] relatam que o modelo de Temkin é o mais próximo do

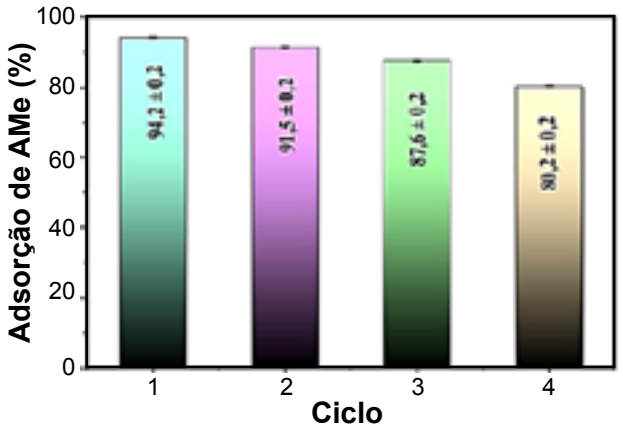

Figura 11: Ensaios de reuso dos microcristais de h-MoO_3 em 4 ensaios consecutivos. Condições experimentais: massa de microcristais=20 mg, pH=4,0, tempo de contato=960 min, concentração inicial do corante AMe=700 mg.L^{-1} e volume da solução=20 mL.

[Figure 11: Reusability tests of h-MoO_3 microcrystals for 4 consecutive cycles. Experimental conditions: adsorbent load=20 mg, pH=4.0, contact time=960 min, initial concentration of MO dye=700 mg.L^{-1}, and volume of solution=20 mL.]

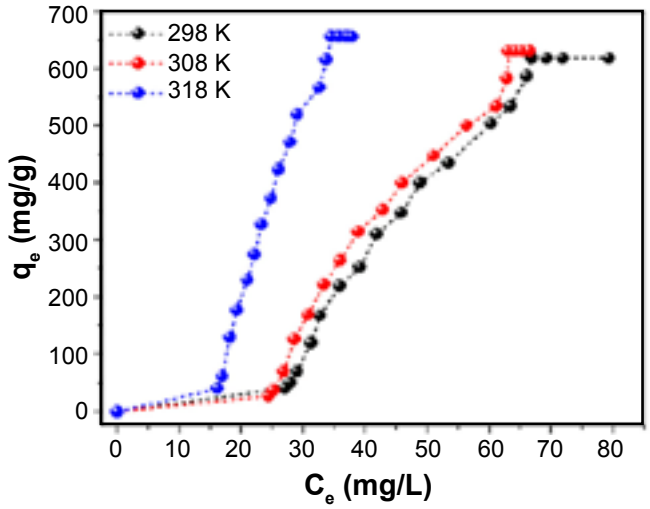

Figura 12: Efeito da concentração do AMe no processo de adsorção pelos microcristais de h-MoO_3 a 298, 308 e 318 K.

[Figure 12: Effect of MO concentration on the adsorption process by h-MoO_3 rod-like microcrystals at 298, 308, and 318 K.]

Tabela VII - Parâmetros termodinâmicos para a adsorção de corante AMe por microcristais de h-MoO_3 em forma de bastão.

[Table VII - Thermodynamic parameters for the adsorption of MO dye on h-MoO_3 rod-like microcrystals.]

Temperatura (K)	ΔG° (kJ.mol^{-1})	ΔH° (kJ.mol^{-1})	ΔS° (J.mol^{-1}.K^{-1})
298	-5,277		
308	-6,400	28,18	112,3
318	-7,522		

modelo de Langmuir [51], considerando que o processo de adsorção ocorre em monocamada, o que pode ter acontecido no sistema em estudo, conforme observado na adsorção do corante AMe em nanotubos de carbono [52]. O modelo de Temkin relata que o calor de adsorção de todas as moléculas que recobrem o adsorvente diminui linearmente em função do recobrimento, devido às interações adsorbato-adsorbato, e a adsorção é caracterizada por uma distribuição uniforme de energia [5, 53].

Os parâmetros termodinâmicos para adsorção do AMe em h-MoO_3 são mostrados na Tabela VII. Os valores de entalpia (ΔH°) e entropia (ΔS°) positivos conferem que o processo de adsorção é de natureza endotérmica e que ocorre um aumento na aleatoriedade sólido/solução durante o processo de adsorção, respectivamente. Já os valores negativos de ΔG° indicaram que o processo de adsorção é favorável e espontâneo termodinamicamente. Além disso, observou-se que o valor de ΔG° reduziu com o aumento da temperatura, indicando que em temperaturas mais altas o processo de adsorção é mais favorável energeticamente. Geralmente um valor de ΔG° entre -20 e 0 kJ.mol^{-1} indica processo de adsorção de natureza física [54]. Com isso, a remoção do corante AMe pode ter sido influenciado por processo de adsorção física, conforme relatado no estudo do pH, porém, a etapa determinante do processo de adsorção foi a quimissorção, como discutido no estudo do tempo; resultados similares aos discutidos podem ser observados em outros trabalhos [45, 48, 55].

CONCLUSÕES

Microcristais de h-MoO_3 foram sintetizados utilizando o método micro-ondas hidrotérmico, evidenciados a partir

Tabela VI - Parâmetros dos modelos isotérmicos para a adsorção de corante AMe por microcristais de h-MoO_3 em forma de bastão.

[Table VI - Isotherm model parameters for the adsorption of MO dye on h-MoO_3 rod-like microcrystals.]

Temperatura (K)	Freundlich			Temkin		
	n_f	K_f (L.g^{-1})	R^2	A_T (L.mg^{-1})	b_T (J.mol^{-1})	R^2
298	0,4306	0,0367	0,8748	0,0397	4,2026	0,9903
308	0,3980	0,0209	0,8547	0,0427	4,2686	0,9925
318	0,3680	0,0452	0,8580	0,0663	3,5221	0,9861

das análises de DRX, Raman, IVFT e MEV. Nos ensaios de adsorção, os microcristais de h-MoO_3 foram eficientes na adsorção do corante alaranjando de metila (AMe) em meio aquoso. O modelo de pseudossegunda ordem foi o que teve o melhor ajuste para os dados obtidos experimentalmente no estudo de tempo de adsorção. As isotermas de concentração obtidas tiveram melhores ajustes ao modelo proposto por Temkin. A capacidade de adsorção frente ao AMe utilizando microcristais de h-MoO_3 foi de 656,9 mg.g^{-1} a 318 K em pH 4,0. Além disso, o adsorvente preparado neste trabalho foi eficiente no processo de adsorção de efluente têxtil e as interações eletrostáticas foram as que mais favoreceram o processo de adsorção. Portanto, microcristais de h-MoO_3 podem ser utilizados na remoção de corante AMe no ambiente, uma vez que esses materiais possuem boa capacidade de adsorção e podem servir como um adsorvente promissor para purificação de água.

AGRADECIMENTO

Os autores gostariam de agradecer ao Conselho Coordenação de Aperfeiçoamento de Pessoal de Nível Superior - CAPES pelo suporte financeiro no desenvolvimento desta pesquisa.

REFERÊNCIAS

[1] M. Vakili, S. Deng, G. Cagnetta, W. Wang, P. Meng, D. Liu, G. Yu, Sep. Purif. Technol. **224** (2019) 373.
[2] Y. Zheng, J. Liu, B. Cheng, W. You, W. Ho, H. Tang, Appl. Surf. Sci. **473** (2019) 251.
[3] O.M.L. Alharbi, A.A. Basheer, R.A. Khattab, I. Ali, J. Mol. Liq. **263** (2018) 442.
[4] Y. Wu, M. Su, J. Chen, Z. Xu, J. Tang, X. Chang, D. Chen, Dyes Pigm. **170** (2019) 1.
[5] A.K.T. Mohammad, A.S. Abdulhameed, A.H. Jawad, Int. J. Biol. Macromol. **129** (2019) 98.
[6] B. Tanhaei, A. Ayati, M. Sillanpää, Int. J. Biol. Macromol. **121** (2019) 1126.
[7] A.M. Zayed, M.S.M. Abdel Wahed, E.A. Mohamed, M. Sillanpää, Appl. Clay Sci. **166** (2018) 49.
[8] S. Hosseini, M.A. Khan, M.R. Malekbala, W. Cheah, T.S.Y. Choong, Chem. Eng. J. **171** (2011) 1124.
[9] J. Dotto, M.R. Fagundes-Klen, M.T. Veit, S.M. Palácio, R. Bergamasco, J. Clean. Prod. **208** (2019) 656.
[10] J. Paul Guin, Y.K. Bhardwaj, L. Varshney, Appl. Radiat. Isot. **122** (2017) 153.
[11] X. Li, J.L. Shi, H. Hao, X. Lang, Appl. Catal. B Environ. **232** (2018) 260.
[12] A.H. Jawad, S. Sabar, M.A.M. Ishak, L.D. Wilson, S.S. Ahmad Norrahma, M.K. Talari, A.M. Farhan, Chem. Eng. Commun. **204** (2017) 1143.
[13] A.M. Awad, S.M.R. Shaikh, R. Jalab, M.H. Gulied, M.S. Nasser, A. Benamor, S. Adham, Sep. Purif. Technol. **228** (2019) 115719.
[14] F. Falaki, A. Fakhri, J. Phys. Theor. Chem. **10** (2014) 117.
[15] F. Zhang, X. Chen, F. Wu, Y. Ji, Colloids Surf. A Physicochem. Eng. Asp. **509** (2016) 474.
[16] Y. Liu, C. Luo, J. Sun, H. Li, Z. Sun, S. Yan, J. Mater. Chem. A **3** (2015) 5674.
[17] A. Santos-Beltrán, M. Santos-Beltrán, F. Paraguay-Delgado, L. Fuentes, R. García, V.G. Orozco, J. Phys. Chem. Solids **121** (2018) 266.
[18] E. Pargoletti, V. Pifferi, L. Falciola, G. Facchinetti, A. Re Depaolini, E. Davoli, M. Marelli, G. Cappelletti, Appl. Surf. Sci. **472** (2019) 118.
[19] G.P. Nagabhushana, D. Samrat, G.T. Chandrappa, RSC Adv. **4** (2014) 56784.
[20] Y. Wang, X. Du, J. Wang, M. Su, X. Wan, H. Meng, W. Xie, J. Xu, P. Liu, ACS Appl. Mater. Interfaces **9** (2017) 5543.
[21] L. Wang, G.H. Zhang, Y.J. Sun, X.W. Zhou, K.C. Chou, J. Phys. Chem. C **120** (2016) 19821.
[22] S. Huang, Y. Long, H. Yi, Z. Yang, L. Pang, Z. Jin, Q. Liao, L. Zhang, Y. Zhang, Y. Chen, H. Cui, J. Lu, X. Peng, H. Liang, S. Ruan, Y.J. Zeng, Appl. Surf. Sci. **491** (2019) 328.
[23] K. Lu, T. Wang, L. Zhai, W. Wu, S. Dong, S. Gao, L. Mao, J. Colloid Interf. Sci. **539** (2019) 553.
[24] R. Ni, Y. Wang, X. Wei, J. Chen, P. Xu, W. Xu, J. Meng, Y. Zhou, Anal. Chim. Acta **1054** (2019) 47.
[25] M. Mincea, V. Patrulea, A. Negrulescu, R. Szabo, V. Ostafe, J. Water Resour. Prot. **5** (2013) 446.
[26] H.M.F. Freundlich, Z. Phys. Chem. **57** (1906) 385.
[27] A.O. Dada, A.P. Olalekan, A.M. Olatunya, O. Dada, IOSR J. Appl. Chem. **3** (2012) 38.
[28] L.S. Silva, M.S. Silva, F.J.L. Ferreira, L.C.B. Lima, R.D.S. Bezerra, A.M.G.L. Citó, J.A. Osajima, E.C. Silva Filho, Water Air Soil Pollut. **229** (2018) 218.
[29] L.S. Silva, L.C.B. Lima, F.J.L. Ferreira, M.S. Silva, J.A. Osajima, R.D.S. Bezerra, E.C. Silva Filho, Open Chem. **13** (2015) 801.
[30] Y. Song, Y. Zhao, Z. Huang, J. Zhao, J. Alloys Compd. **693** (2017) 1290.
[31] H.J. Lunk, H. Hartl, M.A. Hartl, M.J.G. Fait, I.G. Shenderovich, M. Feist, T.A. Frisk, L.L. Daemen, D. Mauder, R. Eckelt, A.A. Gurinov, Inorg. Chem. **49** (2010) 9400.
[32] Z. Wu, D. Wang, X. Liang, A. Sun, Ultrason. Sonochem. **18** (2011) 288.
[33] J. Song, X. Wang, X. Ni, H. Zheng, Z. Zhang, M. Ji, T. Shen, X. Wang, Mater. Res. Bull. **40** (2005) 1751.
[34] A. Chithambararaj, A.C. Bose, Beilstein J. Nanotechnol. **2** (2011) 585.
[35] C.I. Vargas-Consuelos, M. Camacho-López, Superf. Vacío **27** (2014) 123.
[36] V.V. Atuchin, T.A. Gavrilova, V.G. Kostrovsky, L.D. Pokrovsky, I.B. Troitskaia, Inorg. Mater. **44** (2008) 622.
[37] A. Chithambararaj, N.S. Sanjini, S. Velmathi, A. Chandra Bose, Phys. Chem. Chem. Phys. **15** (2013) 14761.
[38] A. Chithambararaj, N. Rajeswari Yogamalar, A.C. Bose, Cryst. Growth Des. **16** (2016) 1984.
[39] A. Chithambararaj, N.S. Sanjini, A.C. Bose, S. Velmathi,

Catal. Sci. Technol. **3** (2013) 1405.
[40] S. Saravanamoorthy, A. Chandra Bose, S. Velmathi, RSC Adv. **5** (2015) 99074.
[41] H. Hu, C. Deng, J. Xu, K. Zhang, M. Sun, J. Exp. Nanosci. **10** (2015) 1336.
[42] P. Wongkrua, T. Thongtem, S. Thongtem, J. Nanomater. **2013** (2013) 702679.
[43] A. Manivel, G.J. Lee, C.Y. Chen, J.H. Chen, S.H. Ma, T.L. Horng, J.J. Wu, Mater. Res. Bull. **62** (2015) 184.
[44] K. Schuh, W. Kleist, M. Hoj, A.D. Jensen, P. Beato, G.R. Patzke, J.D. Grunwaldt, J. Solid State Chem. **228** (2015) 42.
[45] A. Labidi, A.M. Salaberria, S.C.M. Fernandes, J. Labidi, M. Abderrabba, Materials **12** (2019) 361.
[46] L.S. Silva, F.J.L. Ferreira, M.S. Silva, A.M.G.L. Citó, A.B. Meneguin, R.M. Sábio, H.S. Barud, R.D.S. Bezerra, J.A. Osajima, E.C. Silva Filho, Int. J. Biol. Macromol. **116** (2018) 1282.
[47] Y. Li, F. Liu, H. Zhang, X. Li, X. Dong, G. Lu, C. Wang, Mater. Lett. **238** (2019) 183.
[48] D. Kang, X. Yu, M. Ge, F. Xiao, H. Xu, J. Environ. Sci. **54** (2017) 1.
[49] T.H. Tu, P.T.N. Cam, L.V.T. Huy, M.T. Phong, H.M. Nam, N.H. Hieu, Mater. Lett. **238** (2019) 134.
[50] M.K. Uddin, U. Baig, J. Clean. Prod. **211** (2019) 1141.
[51] I. Langmuir, J. Am. Chem. Soc. **38** (1916) 2221.
[52] R.K. Ibrahim, A. El-Shafie, L.S. Hin, N.S.B. Mohd, M.M. Aljumaily, S. Ibraim, M.A. AlSaadi, J. Environ. Manage. **235** (2019) 521.
[53] M. Ghaedi, A. Hassanzadeh, S.N. Kokhdan, J. Chem. Eng. Data **56** (2011) 2511.
[54] Y. Tian, Y. Liu, Z. Sun, H. Li, G. Cui, S. Yan, RSC Adv. **5** (2015) 106068.
[55] B. Chen, S. Chen, H. Zhao, Y. Liu, F. Long, X. Pan, Chemosphere **216** (2019) 605.
(Rec. 03/12/2019, Rev. 26/01/2020, Ac. 27/01/2020)

CC BY-NC

Preparation and characterization of porous alumina ceramics using sunflower seed shells as fugitive material

(Preparação e caracterização de cerâmica de alumina porosa utilizando casca de semente de girassol como material fugitivo)

J. Alzukaimi[1]*, R. Jabrah[1]
[1]Higher Institute for Applied Sciences and Technology, Damascus, Syria

Abstract

Porous alumina ceramics were prepared through the space holder technique, using ground sunflower seed shells as a fugitive material and uniaxial pressing for forming the green ceramics. Influences of the sunflower seed shell content on the shrinkage of the green bodies and porosity of sintered products were evaluated. The prepared ceramics were characterized for mechanical properties using the Brazilian disk test, and the porosity effect on the measured strength was determined. The microstructure was characterized by SEM. The sunflower seed shell content was varied from 0 to 60 wt%. Porosities within 29.9-71.0 vol% were achieved, and the strength of the obtained alumina ceramics decreased accordingly from 59.7 to 4.0 MPa. Additional samples, prepared with different compaction pressure, were characterized for electrical properties and showed high electrical insulation capability, which increased with porosity. Mechanical and electrical data were discussed based on theoretical models, namely the Gibson-Ashby model and/or the minimum solid area model.
Keywords: alumina, porous materials, fugitive material, mechanical properties, solid-state synthesis.

Resumo

Cerâmica porosa de alumina foi preparada pela técnica de queima de orgânico, usando cascas de sementes de girassol moídas como material fugitivo e prensagem uniaxial para conformação do corpo verde. Foram avaliadas as influências do teor de casca de semente de girassol na retração do corpo verde e na porosidade das peças sinterizadas. As cerâmicas preparadas foram caracterizadas quanto às propriedades mecânicas usando o ensaio de compressão diametral e o efeito da porosidade na resistência mecânica foi determinado. A microestrutura foi caracterizada por MEV. O teor de casca de semente de girassol variou de 0 a 60% em massa. Porosidades de 29,9-71,0% em volume foram alcançadas, e a resistência das cerâmicas de alumina obtidas diminuiu de 59,7 para 4,0 MPa. Amostras adicionais, preparadas com diferente pressão de compactação, foram caracterizadas quanto às propriedades elétricas e apresentaram alta capacidade de isolamento elétrico que aumentou com a porosidade. Os dados mecânicos e elétricos foram discutidos com base nos modelos teóricos de Gibson-Ashby e/ou área sólida mínima.
***Palavras-chave**: alumina, materiais porosos, material fugitivo, propriedades mecânicas, síntese em estado sólido.*

INTRODUCTION

Porous ceramics combine two types of properties: the first is inherited from the solid ceramic phase, such as high melting temperature, chemical and thermal stability, high corrosion resistance, high mechanical strength, and biocompatibility, and the second is associated with the features gained from the addition of the pores, such as reduced density, increased surface area, high fluid permeability, reduced thermal conductivity, reduced dielectric constant, and increased specific strength [1-3]. As a result, these materials find an increasing demand for use in relevant applications where such a combination of properties is mandatory or more efficient than other alternatives. Examples include high-temperature insulation, molten metal and hot corrosive gas and liquid filtration, catalyst supports, biomaterials, metal and polymer matrix composites, absorbents, chemical sensors, electrodes for fuel cells, lightweight structural materials, and gas combustion burners [1-5]. Several routes for the creation of pores inside ceramics can be found in the literature. While partial sintering of powder compacts being the simplest [1], the replica technique is considered the most conventional processing method for the fabrication of porous ceramics [3, 6, 7], where a polymeric sponge is immersed in a ceramic slurry, followed by squeezing, drying, heat treatment for removing the sponge template, and sintering of the ceramic coating [1, 3, 5, 8, 9]. However, since the obtained structure is a positive copy of the original sponge template, the removal of the template usually leaves flaws that lead to poor mechanical properties. As opposed to this method, the sacrificial phase method produces a porous structure that is a negative copy of the used template (i.e., the sacrificial phase), and therefore, no

**julianzukaimi@yahoo.com*
https://orcid.org/0000-0002-4376-9456

flaws are caused by template removal [8, 9]. This method is based on the mixing of the ceramic powder, or its precursors, with a fugitive material which acts as a pore-forming agent (space holder or pore former, abbreviated PF henceforth), followed by the formation of a green body, extraction of the PF, and sintering of the ceramic phase. A variety of PFs has been used: 1) solid organics (natural and synthetic), such as cellulose, wax, carbon black, sawdust, beads (PVC, PMMA, PS) and nylon, which are removed by pyrolysis [1, 7, 10]; 2) liquids, such as water and volatile oils, the removal of which is done by sublimation [1, 9]; 3) salts, being removed by washing with water [1, 11]; and 4) metals, which are leached with acids [1, 10, 11]. Further uncommon biopolymeric PFs, such as yeast, fine flour, coffee, and poppy seeds, were tried by other researchers [11, 12]. Ali et al. [12] used commercial rice husk ash and Ribeiro et al. [13] used commercial rice husk as PFs for the fabrication of porous alumina ceramics. Waste materials such as paper pulp waste and primary battery graphite waste were tried as well [12]. The use of waste material is a promising choice for obvious economic and ecological reasons, and the search for new sources is still in progress [12].

In this study, a new waste material of biological origin, namely sunflower seed shells (hulls or husks), is suggested. Sunflower seed shells are composed mostly of cellulose and other organic materials, with sufficiently little ash content (up to 2.1-2.7 wt%) [14, 15]. After consumption of the kernels, the shells are either burned as a biomass fuel [16] or thrown away as a by-product or waste. Other possible uses are reported [17, 18]. In 2018/2019, global production of sunflower seeds was 51.46 million tons, led by Ukraine with 29% and Russia with 25% of the world total. European Union, Argentina, and Turkey also contributed significant volumes [19]. Therefore, being abundant and low in both ash and cost, sunflower seed shells constitute a direct solid and cheap candidate as a pore-forming agent for the fabrication of porous ceramic materials using the sacrificial phase route and the solid-state processing.

Among other ceramic materials, alumina has major importance as raw material and is widely used for the production of traditional and advanced ceramics, both dense and porous, that fulfill the needs of a variety of applications [20-22]. The aim of the present work was to study the potential use of sunflower seed hulls as a solid PF for the fabrication of porous alumina ceramics by the sacrificial phase method and the solid-state processing route, and to characterize the obtained alumina ceramics for physical, mechanical, and electrical properties. The use of sunflower seed hulls as a pore-forming agent preserves the ceramic solid-state processing without any further complication and benefits from its abundance and low cost. So far, no report on the use of this material (i.e., sunflower seed hulls) as a pore-forming agent for the fabrication of porous alumina ceramics appears to have been published yet.

EXPERIMENTAL PROCEDURE

Materials: aluminum oxide G, neutral, for thin-layer chromatography (TLC, with maximum limits of impurities of 0.02% iron and 0.012% chloride) from Himedia, was heat-treated at 1300 °C for 1.5 h and the obtained powder was used as the starting ceramic raw material. Sunflower seeds were purchased from the domestic market and handpicked to remove the kernels. The obtained shells were collected and soaked in hot distilled water for 2 h to dissolve the remaining salt. After several soaking and washing cycles, they were left to air dry for 3 days, then dried at 150 °C for 24 h, and subsequently ground using an ordinary coffee grinder, and finally sieved to a particle size ≤250 μm in a 60 mesh screen. Polyvinyl alcohol, fully hydrolyzed (MW approx. 60000) for synthesis, from Merck, was dissolved in hot distilled water for the preparation of an 8 wt% polyvinyl alcohol (PVA) binder in the form of an aqueous solution.

Sample preparation: the PF ground sunflower seed shells (SSS) were mixed with the alumina powder at contents of 0, 20, 40 and 60 wt%. Then, proper amounts of the binder were added stepwise (5-15 drops a time) and thoroughly blended in an agate mortar and pestle for the 4 alumina/SSS mixtures to obtain 4 pastes. Drying the pastes was conducted at 100 °C in a dryer (Memmert) for 24 h. It was found that the binder amount required for obtaining a paste increased with the increase in the SSS content, and the PVA content varied accordingly as 3.4, 6.5, 8.5 and 10.5 wt% in the dry pastes. Next, the dry pastes were ground in the agate mortar and sieved to a particle size <250 μm, using a 60-mesh screen. To make pellets, the resulting ground powders were pressed in hardened stainless steel die (10 mm in diameter), at a pressure of 125 MPa, using a manually operated hydraulic press (Graseby Specac, maximum load of 15 tons). Ejection was done without lubrication, and the die was cleaned with acetone. For each SSS content, 7 disks, 5 mm thick, were prepared. After drying for 24 h at 100 °C, the disks were sintered in a programmable electrical resistance heating furnace (Lenton Furnaces) according to a predefined thermal cycle up to 1500 °C for 2 h. Cooling was performed by switching off the furnace. A sintering temperature of 1500 °C was chosen in order to minimize grain growth and to avoid significant elimination of pores. In order to allow for a volume electrical resistivity measurement using available equipment, additional bigger size alumina disks were prepared by the same procedure, but with the following settings: SSS contents of 0, 5, 10 and 15 wt%, a 70 mm diameter die, and a pressing load of 15 tons (i.e., a pressure of about 38 MPa).

Characterization. X-ray diffraction (XRD) test: the crystalline structures of the as-received alumina powder, before and after the heat treatment, and some of the obtained alumina ceramic samples were characterized by XRD using a diffractometer (Philips, PW3710, Bragg-Brentano θ-2θ), having a negligible instrumental broadening, operating at 40 kV, and 30 mA with a CuKα radiation (λ=1.5406 Å); a range of 2θ=20-70° was scanned at a rate of 0.02 °/s. *Thermogravimetry and differential scanning calorimetry (TGA/DSC) analysis*: in order to design the thermal cycle for the sintering of the prepared green alumina ceramic

disks, the thermal behavior of the used SSS was studied by TGA/DSC analysis using a thermal analyzer (Setaram Instr., France) at a heating rate of 5 °C/min up to 950 °C in ambient air. The untreated alumina was also studied by thermogravimetry at the rate of 10 °C/min up to 1300 °C to account for its mass and phase change during heat treatment. *Particle size measurement of SSS powder*: the SSS powder, sieved to a particle size ≤250 μm, was dispersed in distilled water and characterized for its particle size distribution using a Mastersizer 2000E instrument (Malvern, UK). *Optical microscopy examination of SSS powder*: transmission and reflection metallurgical microscope equipped with a camera (XJZ-6 Upright, China) was used to examine the morphology of the SSS powder, which was sieved with a 60 mesh screen and manually dispersed over a flat glass slide without any additional treatment. *Shrinkage and porosity measurements*: linear and volumetric shrinkages of the prepared disk samples were calculated by:

$$\text{Shrinkage}(\%) = \frac{G_{AS} - G_{BS}}{G_{BS}} .100 \qquad (A)$$

where G refers to the sample diameter (for the radial shrinkage), thickness (for the vertical shrinkage), or volume (for the volumetric shrinkage) and subscript BS and AS refer to the sample before and after sintering, respectively. The overall porosity (P) was calculated by:

$$P = 1 - \frac{\rho_b}{\rho_s} \qquad (B)$$

where ρ_b is the bulk density, and ρ_s is the density of the solid ceramic phase. Dimensions and mass of the prepared disks (after sintering) were used to determine ρ_b, and a value of 3.96 g/cm^3 was taken for ρ_s [23, 24] since the solid phase of the prepared porous alumina samples was composed of α-Al_2O_3, as shown later by the XRD result and the very little residual ash content confirmed by TGA test. Open porosity was measured using the Archimedes principle, following the ASTM C20 procedure [25]. The closed porosity is the difference between the total and open porosities. *Microstructure evaluation*: the obtained porous alumina ceramic disks were observed by the scanning electron microscopy (SEM), in order to characterize the morphology of the pores. An SEM instrument (Tescan, Vega-II XMU5136, USA) was used, and the micrographs were taken by examining the cross-sectional areas (12 mm^2 on average) of 4 specimens, each representing one SSS content. Fresh surfaces were prepared by breaking the disks immediately before the test. *Mechanical property characterization*: indirect tensile strength of the sintered porous alumina ceramic samples, designed for mechanical characterization, was determined through the Brazilian disk test method. This method is suited for brittle materials like rocks and ceramics. It is based on the diametrical compression (until fracture) of a cylindrically shaped test sample, which creates a tensile stress field indirectly applied across the diametrical plane [26-28]. The mechanical property provided is the indirect tensile strength (also called the splitting tensile strength, because of the fracture shape) given by:

$$\sigma_s = \frac{2.P_m}{\pi.D.t} \qquad (C)$$

where P_m is the maximum force at fracture, and D and t are the diameter and thickness of the cylinder, respectively. Breaking of the prepared disks (7 samples for each of the 4 SSS compositions, a total of 28 samples) was conducted using universal materials testing machine (Adamel Lhomargy, DY34; capacity of 10 kN) with a displacement rate of 0.5 mm/min. The obtained data were analyzed by the Weibull statistics, based on a linear fitting of $\ln[\ln(1/P_s)]$ versus $\ln\sigma_s$, where P_s is the survival probability. To calculate this probability for a given series of N equivalent samples, the samples were first ranked in order of increasing strength, then the relation P_s=1-n/(N+1) was applied, where n=1, 2, …, N is the sample rank. The Weibull statistics entails two parameters: characteristic strength and Weibull modulus. The characteristic strength (σ_0) corresponds to a probability of survival P_s=1/e (≈0.37). The Weibull modulus (m) is the slope of the fitted straight line of $\ln[\ln(1/P_s)]$ as a function of $\ln\sigma_s$. It indicates how rapidly the strength falls when approaching σ_0 (the higher the m value, the lower is the variability of strength). In terms of the flaws within the material under test, it provides an estimation of the narrowness of their size distribution: a high m corresponds to a narrow flaw size distribution and, therefore a low scattering of the strength [29-31]. In all the measurements concerning the splitting tensile strength, shrinkage, and porosity, the average of 7 results was taken and their standard deviation was used to estimate the experimental error. *Electrical property characterization*: DC resistance of 4 disk samples was indirectly measured, using a circular electrode for the measurement of the surface and volume resistivity of solid electrical insulators connected to a high resistance meter (megohmmeter, HP, 4329A). DC voltages of 500 and 1000 V were applied. Dimensions of the electrode and thickness of each sample were used to determine the volume electrical resistivity according to the ASTM-D257-07 standard [32].

RESULTS AND DISCUSSION

Characterization of the starting alumina: the XRD pattern of the as-received alumina (before heat treatment) is given in Fig. 1a. Comparison with the XRD pattern of boehmite (γ-AlOOH, JCPDS 21-1307) indicated a matching of 10 diffraction peaks [20]. Three peaks at 2θ= 31.38°, 45.58°, and 67° were related to γ-Al_2O_3 (JCPDS 10-0425) [33], although the last two peaks (2θ= 45.58° and 67°) are shared with boehmite. The peak at 2θ=25.44° might be attributed to α-Al_2O_3 (JCPDS 42-1468) [20, 23, 33]. These results suggested that the as-received alumina (untreated) was possibly constituted of a mixture of an aluminum oxyhydroxide, boehmite, and some additional transition alumina phases. The identified boehmite structure of the untreated alumina was not well crystallized, as indicated by the wideness and low intensity of the matched peaks,

especially for 2θ≥35°. This alumina was found to have lost a significant amount of its weight (about 14%) by heat treatment, as demonstrated later by the TGA result, meaning that it could not be composed purely of transition aluminas. The dehydration of boehmite is described by:

$$2AlOOH \rightarrow Al_2O_3 + H_2O \quad (D)$$

corresponding to a weight loss of 15 wt%. This is consistent with the XRD result detailed above. Fig. 1b shows the XRD pattern of the as-received alumina after heat treatment at 1300 °C. The α-Al_2O_3 phase peaks were well recognized (JCPDS 42-1468) [20, 23, 33]. However, additional peaks were present as well. These were associated with non-alpha alumina phases that remained due to incomplete transformation after the above-mentioned heat treatment. For instance, the peaks at 2θ= 21.98°, 23.66°, 24.52°, 27.26°, 27.92°, 29.02°, 36.16°, and 58.64° were associated with δ-Al_2O_3 (ICDD 16-0394) [33], while those at 2θ= 31.4° and 36.9° were related to θ-Al_2O_3 (JCPDS 35-0121) [33]. The peaks at 2θ= 32.16°, 34.12°, 39.34°, 44.98°, 46.14°, and 67.28° seem common to these two transition alumina phases. After sintering of this 1300 °C heat-treated alumina at 1500 °C, all these peaks related to the transition alumina phases disappeared completely, and a mass change of 1-2 wt% was observed. This confirmed that the heat treatment of the starting raw alumina up to 1300 °C was not sufficient to achieve complete conversion to α-Al_2O_3. Fig. 1c corresponds to the XRD pattern of the sintered pellets, prepared with an SSS content of 60 wt%. The corundum (α-Al_2O_3) crystalline structure was well identified (JCPDS 42-1468) [20, 23, 33]. No additional peaks other than the α-Al_2O_3 phase peaks were present. This proved that the phase transformation into α-Al_2O_3 was completed during the sintering process and justified the later use of the value of 3.96 g/cm^3 as the density ρ_s (theoretical density) of the solid phase in the prepared porous alumina samples [23, 24], required for the calculation of the total porosity P.

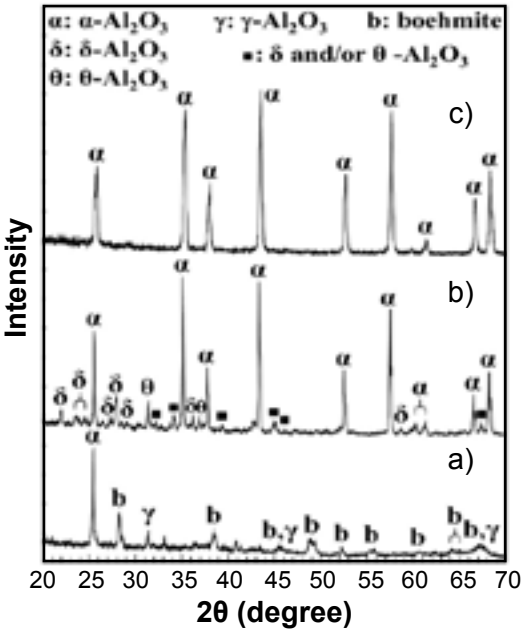

Figure 1: XRD patterns of: a) as received untreated alumina powder; b) raw alumina after heat treatment of the as-received alumina (heating rate of 10 °C/min, in ambient air, at 1300 °C for 90 min), used for the preparation of the porous alumina ceramic samples; and c) sintered product obtained using 60 wt% of ground sunflower seed shells (SSS).
[Figura 1: Padrões de DRX de: a) pó de alumina como recebido, não tratado; b) alumina de partida após tratamento térmico da alumina recebida (taxa de aquecimento de 10 °C/min, ao ar, a 1300 °C por 90 min), utilizada na preparação das amostras de cerâmica de alumina porosa; e c) produto sinterizado obtido utilizando 60% em massa de cascas de sementes de girassol moídas (SSS).]

Heat treatment and thermal cycle selection: the thermogravimetric analysis of the as-received alumina (before heat treatment) is given in Fig. 2a; a weight loss of 14 wt% was measured, which is expected to be associated with the removal of adsorbed and structural water (i.e., moisture removal and dehydration of boehmite [20]). The thermal analysis results, TGA and DSC, for the used SSS are shown in Figs. 2b and 2c, respectively. The SSS lost more than 98% of its weight at 950 °C. The main loss occurred between 250 and 450 °C, as revealed by the large exothermal DSC peak, which was related to the burning of organic material. Although more than 70% of this weight was lost at around 450 °C, weight loss continued up to 950 °C. This was somewhat in agreement with the findings of Haykiri-Acma et al. [15], who obtained a completion of the weight loss by about 900 °C for the SSS they used. Based on the obtained SSS thermal analysis result, it was suggested that a burn-off temperature of 950 °C would be sufficient for the removal of all organic material, whether from the SSS or the binder since the PVA binder should burn much earlier. Therefore, the thermal cycle adopted for the sintering of the prepared alumina green bodies was as follows: heating at a rate of 5 °C/min from room temperature to 950 °C, with

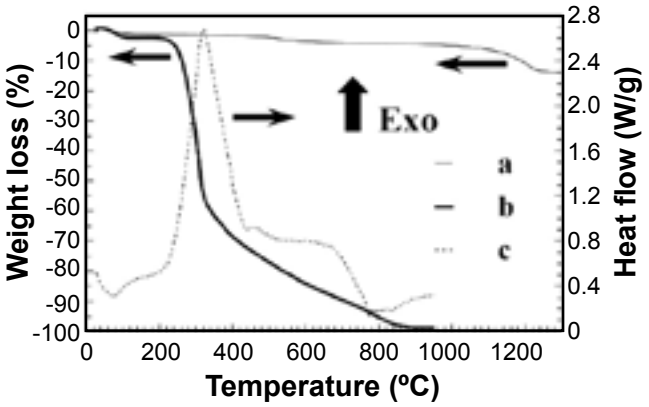

Figure 2: TGA curve (a) of the as-received untreated alumina powder (heating rate of 10 °C/min, in ambient air); and TGA (b) and DSC (c) curves of the used SSS (heating rate of 5 °C/min, in ambient air).
[Figura 2: Curva de TGA (a) do pó de alumina como recebido, não tratado (taxa de aquecimento de 10 °C/min, ao ar); e curvas de TGA (b) e DSC (c) de SSS usado (taxa de aquecimento de 5 °C/min, ao ar).]

a dwell time of 1 h for organics removal, followed by a heating at a rate of 10 °C/min up to the sintering temperature of 1500 °C, with a dwell time of 2 h; then, the furnace was switched off for cooling. According to the TGA result of the SSS, a total of 1.42 wt% residual ash was observed. Since the alumina in the green samples lost no more than 2 wt% during the sintering, it may be estimated that the samples prepared using the highest SSS content of 60 wt% contained no more than 2.2 wt% of residual ashes.

Particle size distribution of sunflower seed shell powder: the particle size distribution curve of the used SSS is shown in Fig. 3a. Usual percentile readings of d10=15 μm, d50=89 μm, and d90=275 μm were observed, with a residual weight of 0.35%. 9.6 vol% of the analyzed sample was found to be above 250 μm, which may be explained by a swelling effect of the SSS with the dispersant water and/or agglomeration of its particles since it was sieved to a particle size less than 250 μm, or could suggest that the measured sizes of the SSS particles were overestimated. The wide size distribution curve shown in Fig. 3a suggested that the used ground SSS was composed of particles with a wide size range. *Microscopy evaluation of sunflower seed shells powder*: the particle shape of the used SSS powder was analyzed by optical microscopy (Fig. 3b). Randomly shaped SSS particles with size up to about 400 μm were seen. The large lumps corresponded to agglomerates of individual particles since the SSS powder was sieved using a 60 mesh screen. Large grains, as well as small ones, were seen, and the used SSS particle size varied over a wide range.

Linear and volumetric shrinkage: Fig. 4 shows the linear and volumetric shrinkages of the prepared alumina ceramic samples. Shrinkage of fired ceramic bodies is the sum of several contributions: 1) weight loss due to water removal and organic material burnout; 2) change in the density of the ceramic powder material caused by a phase transformation, if any; and 3) sintering process if at least one densifying mechanism is active. Shrinkage increased with the increase in the SSS content, which was in line with other studies [4, 12]. It was noted that the vertical and radial shrinkages (i.e., shrinkage of the thickness and diameter of the pellet, respectively) were equal for an SSS content ≤40 wt%, whereas the former was somewhat lower for a SSS content of 60 wt%. Although this effect was not clearly observed until a high SSS content was attained, a possible qualitative explanation is suggested: the uniaxial pressure used for the compaction of the pellets was vertically applied, thereby bringing the alumina and the SSS particles closer to each other more in the direction of the pressure than in the transversal one. Therefore, after removal of the SSS, more empty space was available along the radius for the alumina particles to contact each other, leading to an increase in the radial shrinkage. The increase in shrinkage as the SSS content increased is expected to be caused by the removal of more organics introduced by the SSS material and by the binder. The moderately high volumetric shrinkage value of 31% for the sample prepared with no SSS and with a small binder amount of 3.4 wt% may indicate a slight increase in

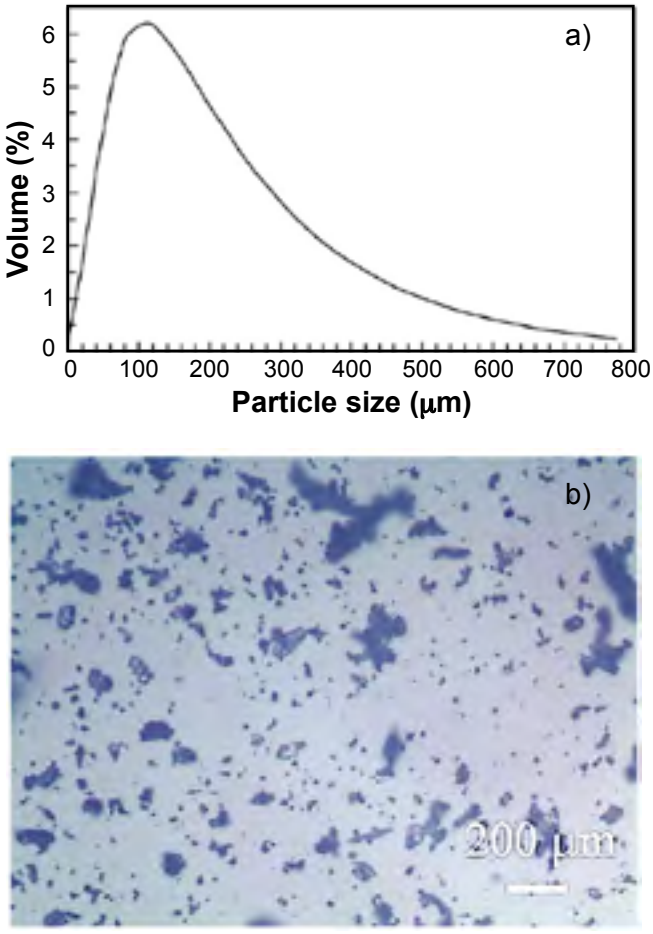

Figure 3: Particle size distribution curve (a) and optical micrograph (b) of the used SSS.
[Figura 3: Curva de distribuição do tamanho de partícula (a) e micrografia óptica (b) de SSS usado.]

the density of the alumina phase, since its transformation into α-Al_2O_3 was not complete after heat treatment at 1300 °C, as shown by Figs. 1b and 1c. The densification role of the SSS-free alumina sample was not expected to be significant since, in this case, the sintered alumina was highly pure, and the sintering temperature of 1500 °C was rather low. The former argument would apply to all the other non-zero SSS alumina samples since the same alumina was used in their preparation, whereas the latter may not be true as the residual ashes (i.e., impurities) from the SSS material (2.2 wt%) could activate some densifying mechanisms, thereby adding another contribution to the shrinkage. For instance, it is interesting to report that SSS usually includes a high content of silica [18].

Porosity measurement: total porosity, along with the open porosity, increased with the increase in the SSS content, as shown in Figs. 5a and 5b. Porosity may correspond to the space left by the imperfect packing of the randomly-shaped alumina particles in the green compact, as well as to the pores possibly contained inside these particles, or could be created by the burnout of the organic matter from the PF (pore former) and/or the binder, or by the removal of the remaining hydroxyl groups in the incompletely transformed heat-

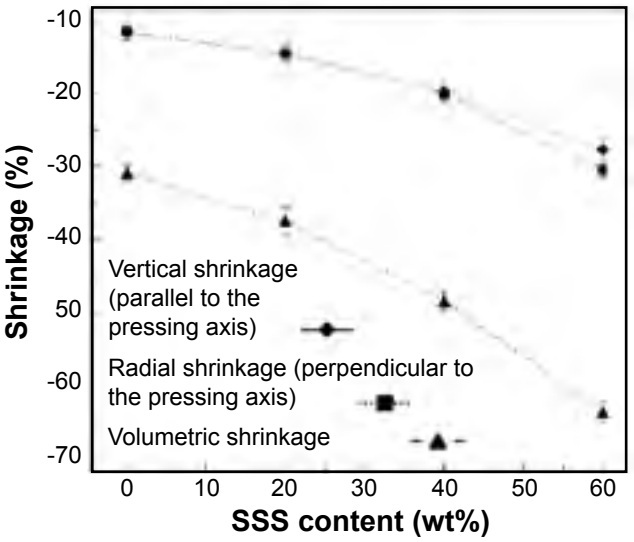

Figure 4: Linear shrinkage (along radius and thickness) and volume shrinkage of the alumina ceramic pellets versus SSS content in the green body.

[Figura 4: Retração linear (ao longo do raio e da espessura) e retração do volume dos discos de alumina versus teor de SSS no corpo verde.]

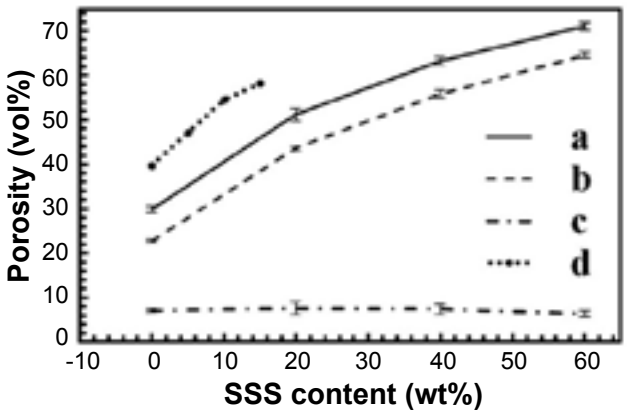

Figure 5: Total (a), open (b), and closed (c) porosity of small alumina ceramic pellets (compacted at 125 MPa), and total porosity (d) of large disks (compacted at 38 MPa) versus the SSS content in the green bodies.

[Figura 5: Porosidade total (a), aberta (b) e fechada (c) de pequenos discos de alumina (compactados a 125 MPa) e porosidade total (d) de discos grandes (compactados a 38 MPa) versus o teor de SSS nos corpos verdes.]

treated alumina. Since the increase in the SSS content led to an increase in its volume, the porosity increased. However, porosity and SSS content were not linearly proportional due to the concurrent shrinkage, as can be seen in Fig. 4. This effect can be viewed by noting that an increase of 20 wt% in the SSS content, from 0 to 20%, yielded an increase of 21.3 vol% in the total porosity, whereas the same increase from 40 to 60 wt% in the SSS content yielded an increase of only 7.8 vol% in the total porosity. The closed porosity (i.e., the difference between the total and open porosities) ranged from 6.4 to 7.5 vol%, which was small compared with the total porosity, and was basically independent from the SSS content (Fig. 5c), suggesting that it might be associated with pores inside the alumina particles (or created by its dehydration), and the resulting overall porosity was mainly open. Another possibility is an underestimated value for the open porosity provided by the ASTM C20 procedure. Regarding the large porous alumina disk samples (prepared for the electrical resistivity measurement under the same conditions except for the smaller compaction pressure of 38 MPa), it was observed that only decreasing the compaction pressure allowed the achievement of 58.3 vol% porosity with only 15 wt% SSS content, which was nearly equivalent to 40 wt% SSS content at a compaction pressure of 125 MPa, as can be verified by Figs. 5d and 5a, respectively.

Microstructure characterization: Fig. 6 shows the SEM micrographs of the cross-sectional surfaces of 4 porous alumina samples, prepared by breaking the pellets immediately before the examination. The obtained microstructure was rather simple to describe. For all SSS contents, Figs. 6A1, 6B1, 6C1, and 6D1 show a distribution of randomly shaped pores within a partially sintered solid alumina matrix. Figs. 6A3, 6B3, 6C3, and 6D3 demonstrate the randomly shaped alumina particles, of sizes ranging from less than 1 μm and up to about 5 μm. For the sample prepared with 0% SSS, the macropores observed in Figs. 6A2 and 6A3, with sizes of up to about 13 μm, were related to the poor packing or the aggregates of the irregularly shaped alumina particles in the green body or may result from the burnout of the PVA binder, although its content was small, only 3.4 wt% in this case. Once the SSS content was raised (Figs. 6B2, 6C2, and 6D2), additional pores appeared, associated with the burnout of the SSS, which left voids or cavities behind and created pores with size that depended upon the SSS particle size, content, and packing inside the green body, in addition to the final shrinkage (Fig. 4). Figs. 6A2, 6B2, 6C2, and 6D2 show that larger pores were produced as the SSS content was increased, which is in line with other works [4, 8, 12, 21]. The PVA content increased as well, adding another contribution to this effect. Also, channel-like pores and/or other small pores around 1-4 μm in width can be seen in Figs. 6A3, 6B3, 6C3, and 6D3, mostly resulting from the imperfect packing of the alumina particles or the burnout of small amounts of SSS or PVA materials. Thus, small pores (down to about 1 μm) and large pores (up to about 102 μm, depending on the SSS content) coexisted in the samples with a non-zero SSS content, resulting in a wider pore size distribution compared with the 0% SSS sample, whose porous structure consisted of only small pores up to about 13 μm (Fig. 6A2). Hence, larger pores seem to result only from the SSS addition, whereas smaller pores might be produced either by the non-ideal packing of the alumina particles or the burnout of small contents of SSS or organic binder. The increased shrinkage with the increase in the SSS content (Fig. 4), in addition to the SSS agglomeration inside the green bodies, make it difficult to relate the size of the large pores to the size of the SSS particles. However, the depicted morphology of the porous alumina product obtained through the sacrificial phase technique was consistent with the microstructural

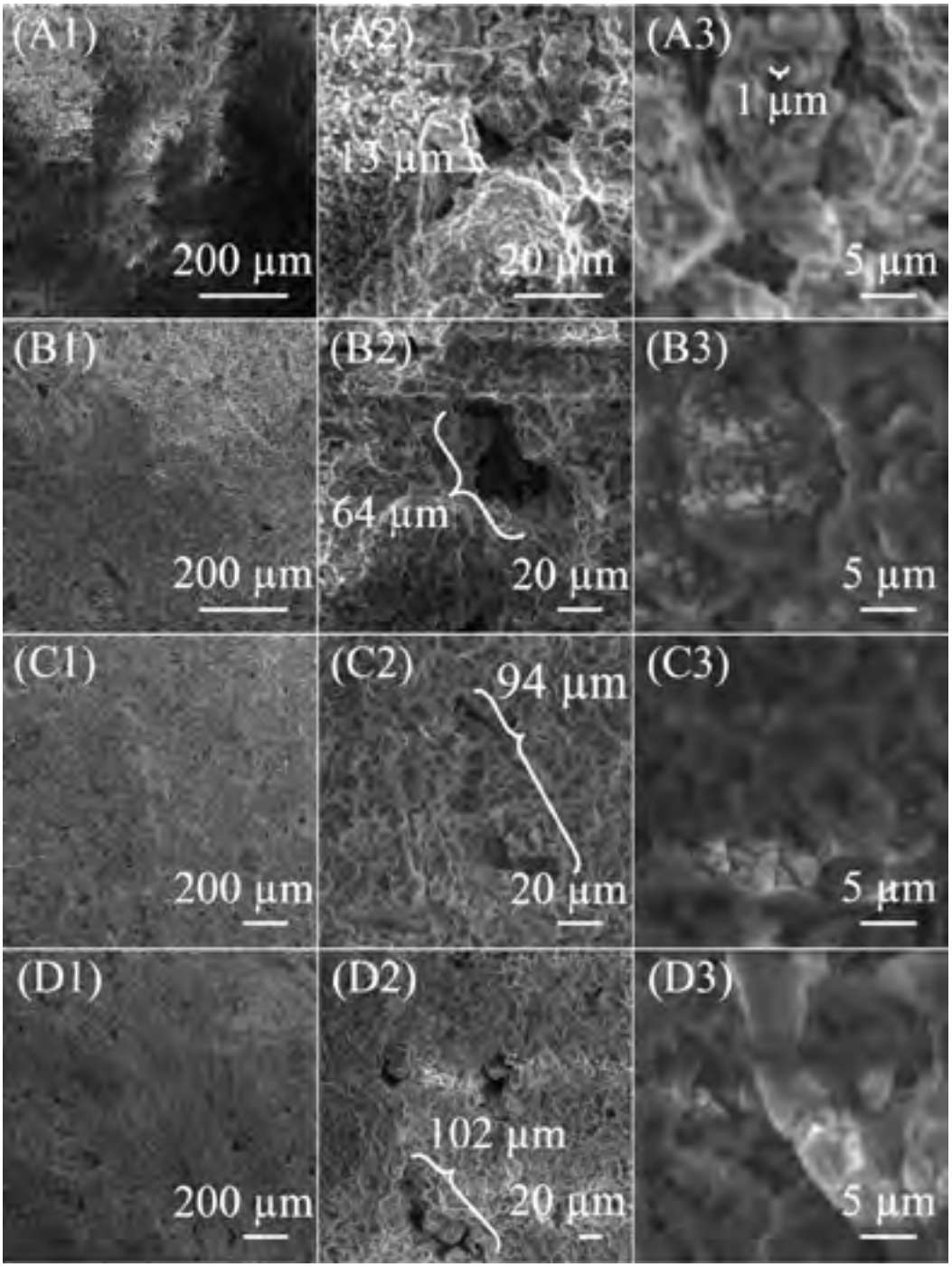

Figure 6: SEM micrographs of porous alumina ceramic samples prepared with SSS content of 0 wt% (A), 20 wt% (B), 40 wt% (C), and 60 wt% (D).
[Figura 6: Micrografias de MEV de amostras de alumina porosa preparadas com teor de SSS de 0 wt% (A), 20 wt% (B), 40 wt% (C) e 60 wt% (D).]

characteristic for a negative copy of the PF material.

Indirect tensile strength: Fig. 7 demonstrates typical examples of the diametrical fracture during the Brazilian disk test for samples prepared with different SSS contents. Fig. 8 shows the results of the indirect tensile strength measurement for the prepared alumina ceramic disks. The Weibull statistics for the strengths of the alumina ceramic samples obtained from each SSS content are given in Fig. 9. Parameters of the Weibull statistics obtained for each type of the prepared porous alumina ceramics are given in Table I. The Weibull moduli given in Table I are in the range 9-46. Although these values might be overestimated (due to the small number of tested samples), especially for the case of 0 wt% SSS content, a mutual comparison (the general trend) suggested that the reliability of the obtained product decreased with the increase in its porosity. This was in accordance with the microstructural evaluation since pores can be considered flaws, whose size was found to increase with the increase in porosity (Figs. 5, 6A2, 6B2, 6C2, and 6D2). The samples prepared with a non-zero SSS

content had low values of Weibull modulus (m) in the range 9-13, which reflected a high scattering of the indirect tensile strengths (i.e., wide distribution of flaw sizes), as opposed to the samples prepared with no SSS, which showed a very high value of 45.65 for the Weibull modulus and therefore a low scattering of the indirect tensile strength values. The mechanical strength decreased with the increase in porosity, i.e., with the decrease in bulk density, as shown in Table I and Fig. 8. This result agreed with many literature data, and it is a general trend in all porous materials, where the application of a mechanical load causes the pores to coalesce, meaning that the higher the porosity, the higher the probability of this coalescence and the larger is the resulting flaw size [4, 8, 34]. Another explanation is that the pores play the role of stress concentration sites, and they reduce the cross-sectional area of the solid phase subject to load [10, 12, 27]. Therefore, the increase in porosity usually leads to a reduction in strength. According to a model developed by Gibson and Ashby [8, 23, 35], the so-called GA model, the compressive strength (σ_c) of a porous material is related to its relative density (ρ_b/ρ_s=1-P), with P being the total porosity, according to:

$$\frac{\sigma_c}{\sigma_f} = C.\left(\frac{\rho_b}{\rho_s}\right)^n \qquad (E)$$

where σ_f is the bending strength of the solid phase, c a geometric constant, and n equals 1.5 for an open-cell porous structure or ranges from 1 to 1.5 for closed-cell structures. A linear regression of the obtained data with respect to Eq. E, using a double log plot, yields n=3.04 and c=0.444, with R^2=0.999, where a value of 400 MPa was assumed for the modulus of rupture (σ_f) of the alumina composing the solid skeleton of the prepared porous samples [1, 23]. The calculated value of n was larger than the exponent 1.5 predicted by the GA model for open-cell foams, a result

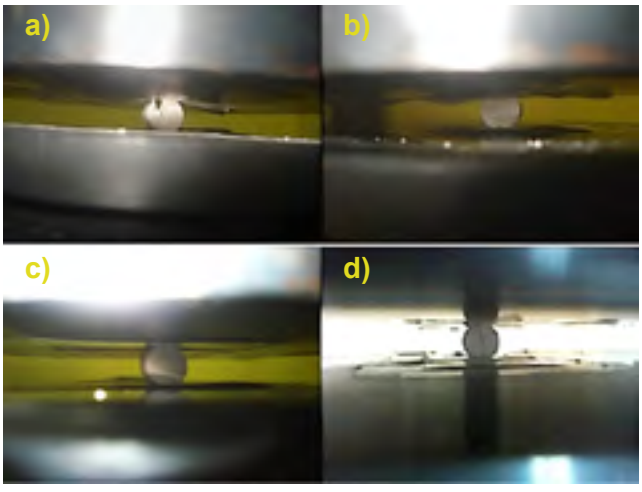

Figure 7: Images of diametrical fracture during the Brazilian disk test of porous alumina disk samples prepared with different SSS contents: a) 0 wt%; b) 20 wt%; c) 40 wt%; and d) 60 wt%.
[Figura 7: Imagens de fratura diametral durante ensaio de compressão diametral de amostras de disco de alumina porosa preparadas com diferentes teores de SSS: a) 0 wt%; b) 20 wt%; c) 40 wt%; e d) 60 wt%.]

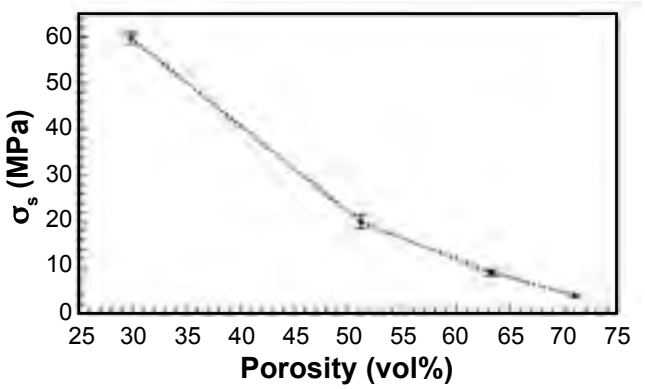

Figure 8: Brazilian disk tensile strength versus total porosity of the prepared alumina ceramics.
[Figura 8: Resistência à tração por compressão diametral versus porosidade total das cerâmicas de alumina.]

that pointed toward a rather open structure for the prepared samples. The small value of the closed porosity relative to the total porosity (Fig. 5) is in line with this result. A comparison between the theory and the experiment is presented in Table II, where the determined indirect tensile strengths of the prepared porous alumina pellets, along with the compressive strengths predicted by the GA model for porous alumina ceramics (with both open and closed cell structures [1, 36]) are given in terms of the relative density.

Again, this comparison was consistent with the fact that the obtained porous structure of the prepared alumina ceramics was an open-cell structure, as explained earlier in Fig. 5. However, the compared data was the splitting tensile strength, measured using the Brazilian disk test, and not the compressive strength, considered by the GA model in Eq. E. A fracture mechanics analysis was applied to the GA model, which allowed to obtain the following expression for the tensile strength (σ_t) of a cellular structure or foam:

$$\frac{\sigma_t}{\sigma_f} = c'.\sqrt{\frac{L}{R}}.\left(\frac{\rho_b}{\rho_s}\right)^{1.5} \qquad (F)$$

where c' is a dimensionless geometric constant, L is the foam cell size, and R is the critical or macroscopic flaw size. Eq. F is valid only when L≤R, with equality, if the foam is intact (i.e., flaw-free). The values of c and c' are approximately the same (about 0.2) [1, 23, 37]. This means that the tensile and compressive strengths are equal for an intact open-cell foam (i.e., when L=R and n=1.5). In light of this argument, and due to the comparable values of the experimental results of the splitting tensile strength and the theoretical compressive strength expected by the GA model for an open-cell porous structure, as revealed by Table II, it seems reasonable to deduce that the prepared alumina samples may be intact. This is consistent with the general aspect of porous ceramics produced by the sacrificial phase method, i.e., constituting a negative copy of the PF with no flaws being caused by its removal. However, due to the absence of a well-defined cell (i.e., a cellular structure, in a sense dealt in the GA model) as the SEM micrographs in Fig. 6 showed, it became difficult to interpret these results with the aid of this model. In fact, this

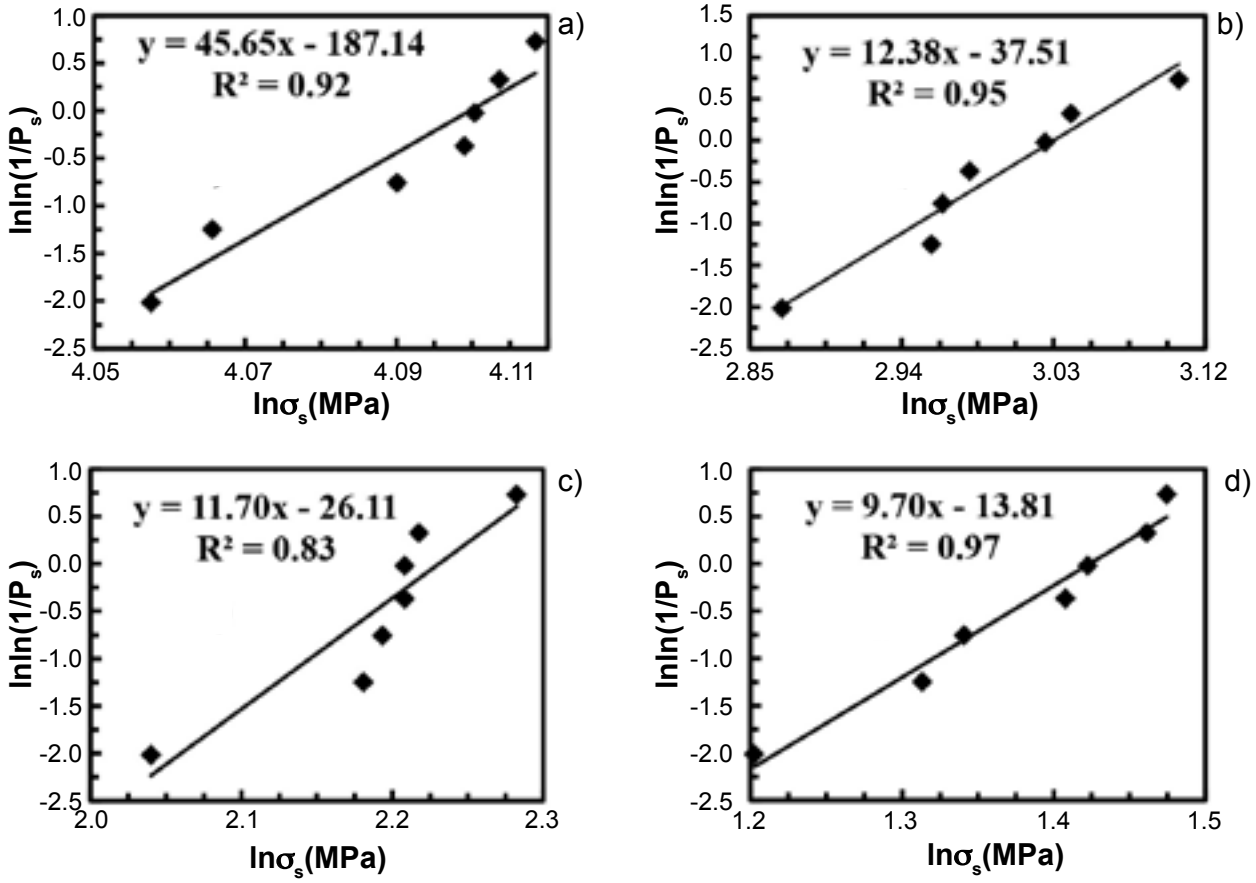

Figure 9: Weibull plots for the tensile strength data of the porous alumina samples prepared with SSS content of 0 wt% (a), 20 wt% (b), 40 wt% (c), and 60 wt% (d).
[Figura 9: Gráficos de Weibull para os dados de resistência à tração das amostras de alumina porosas preparadas com teor de SSS de 0 wt% (a), 20 wt% (b), 40 wt% (c) e 60 wt% (d).]

morphology might be the reason behind the largeness of the obtained value of n. Furthermore, it must be noticed that the mechanical property involved in the previous discussion is the 'indirect tensile' rather than the 'tensile' strength. The relatively small difference between the indirect tensile strength of the prepared alumina samples and the theoretical compressive strength predicted by the GA model was exceptional to the accepted rule stating that the latter is at least one order of magnitude higher than the former [37-39], but it revealed the higher mechanical properties achievable by the sacrificial phase route, as compared to other methods used for the preparation of porous ceramics. A more generalized formula of Eqs. E and F is based on expressing the dependence of some properties of porous materials, including mechanical, thermal, and electrical, on their fractional (or relative) density ratio ρ_b/ρ_s, as a power-law function of the form: property=f[$(\rho_b/\rho_s)^k$], where k is between 1 and 3 [40]. Another modeling for the relation between porosity and several properties of porous materials is described by what is called 'minimum solid area' or MSA model. This model predicts an exponential dependence of property on porosity. In particular, the MSA model gives the following expression for mechanical properties, known as Rice's formula:

$$\sigma = \sigma_d.e^{-b.P} \quad (G)$$

where P is the porosity, σ is the strength of the material with porosity P, σ_d is the strength of the dense material (i.e., with zero porosity), and b is a parameter characterizing the porous structure of the material [9, 34, 41]. The approach adopted by the MSA model is based on equating the fraction of the property at zero porosity, as a function of the porosity P, with the minimum solid area fraction of the total area of the porous material normal to a given reference axis, such as stress. The underlying assumption is that porous materials (or bodies) may be ideally constructed by stacking of 2 basic types of identical features: partially bonded solid spheres (i.e., particles), and spherical bubbles or pores within a solid matrix. The model expects that most real porous structures may be represented by a combination of these two types of geometry [41]. The value of factor b in Rice's formula (Eq. G) depends on this combination, i.e., the contribution of each feature type and its stacking. For instance, b=3 if the pore structure may be represented by cubic stacking of bubbles (i.e., spherical pores), b=5 corresponds to cubic stacking of solid spheres, whereas a value between 3 and 5 would characterize a mixture of bubbles and solid spheres, both cubically stacked. Treatment of the present data with respect

Table I - Porosity, average splitting tensile strength (σ_s), and Weibull statistics parameters (m - Weibull modulus, σ_0 - characteristic strength) of the prepared alumina ceramics.
[Tabela I - Porosidade, resistência à tração média por compressão diametral (σ_s) e parâmetros de Weibull (m - módulo de Weibull, σ_0 - resistência característica) das cerâmicas de alumina.]

SSS content (wt%)	No. of samples	Porosity (vol%)	σ_s (MPa)	m	σ_0 (MPa)
0	7	29.9±0.7	59.7±1.2	45.6	60.3
20	7	51.2±1.4	20.0±1.5	12.4	20.7
40	7	63.2±0.9	9.0±0.6	11.7	9.3
60	7	71.0±0.9	4.0±0.4	9.7	4.2

Table II - Indirect tensile strengths of the prepared alumina samples and compressive strengths predicted by the GA model for open and closed cell porous alumina ceramics for the same values of relative density.
[Tabela II - Resistências à tração indiretas das amostras de alumina e resistências à compressão previstas pelo modelo GA para cerâmicas de alumina porosas de células abertas e fechadas para os mesmos valores de densidade relativa.]

SSS ratio (wt%)	Relative density	Splitting tensile strength - measured (MPa)	Compressive strength - GA model (MPa)	
			Open-cell foam	Closed-cell foam
0	0.70±0.01	59.7±1.2	47.0	280.4
20	0.49±0.01	20.0±1.5	27.3	195.4
40	0.37±0.01	9.0±0.6	17.8	147.1
60	0.29±0.01	4.0±0.4	12.5	115.9

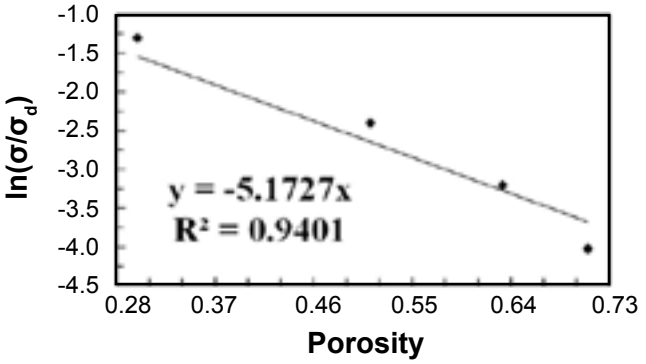

Figure 10: Relative splitting tensile strength curve of the prepared alumina pellets fitted with Rice's formula.
[Figura 10: Curva de resistência à tração relativa das pastilhas de alumina ajustada com a fórmula de Rice.]

to Eq. G, using linear regression in a semi-log plot, as shown in Fig. 10, yielded b=5.17, with R^2=0.94, where a value of 220 MPa for the tensile strength of dense alumina (σ_d) was utilized [24]. The obtained value for b suggested that the pore structure of the prepared samples might be represented by one type of geometry, namely solid spheres or particles, which are partially bonded by a combination or mixture of two kinds of stacking: the first being cubic and comprising the main component, and the second is a rhombic stacking making up only a little portion of the mixed stacking. According to the MSA model, it seems that no spherical pores were needed for the description of the obtained porous structure, although this is somewhat inconsistent with the range of porosities obtained, especially for P>50 vol% [41]. This might be attributed to the strict constraint of the model concerning the assumption of a uniform cell size, which is not satisfied in reality, as confirmed, for instance, by the microstructures shown in Fig. 6.

Fig. 11 presents a comparison between the splitting tensile strengths of porous alumina ceramic pellets prepared by uniaxial pressing and space holder method but using 5 different types of PFs: primary batteries graphite waste, active yeast, commercial rice husk ash [12], naphthalene

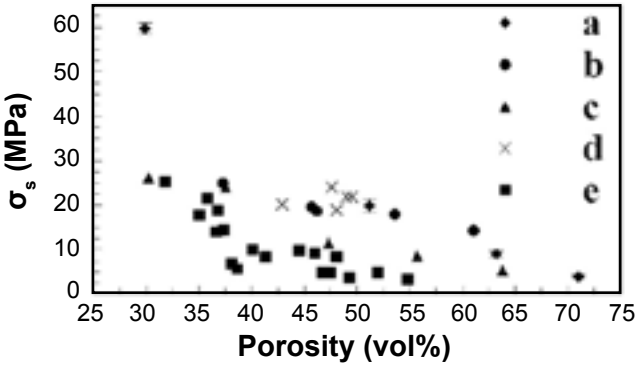

Figure 11: Indirect tensile strength measured by the Brazilian disk test for porous alumina ceramics prepared by the sacrificial phase method with different pore formers (PFs): a) sunflower seed shells (this study); b) graphite waste [12]; c) active yeast [12]; d) commercial rice husk ash [12]; and e) naphthalene [21].
[Figura 11: Resistência à tração indireta medida pelo ensaio de compressão diametral para cerâmicas porosas de alumina preparadas pelo método da fase de sacrifício com diferentes formadores de poros: a) cascas de sementes de girassol (este estudo); b) resíduo de grafita [12]; c) levedura ativa [12]; d) cinza comercial de casca de arroz [12]; e e) naftaleno [21].]

[21], and sunflower seed shells (this study). It was clear that a wide range of porosity, with high levels of mechanical properties, was achieved for the porous alumina ceramics prepared with sunflower seed shells as the pore-forming agent. Furthermore, it might be useful to report that this result holds even though the alumina samples prepared in this study were sintered at 1500 °C, which was lower than the 1550 and 1600 °C used in the mentioned studies [12, 21].

Volume electrical resistivity: the results of the volume resistivity measurement of 4 selected samples as a function of their porosity are shown in Table III. The increase in the volume electrical resistivity as the porosity increased was in accordance with the literature [4, 35]. Resistivity is the reciprocal of electrical conductivity. Many models describing the relationship between porosity and electrical conductivity of porous materials may be found in the literature [41-46]. Although some of them focus mainly on porous metals, they all indicate that the electrical conductivity of porous materials decreases as the relative density decreases (i.e., the resistivity would increase by increasing porosity). Two models were chosen and found useful to draw meaningful conclusions when applied to the data presented in Table III, the MSA model and the model used in [42], which gives the following expression for the effective electrical conductivity of a porous material versus porosity:

$$K=K_d.(1-w.P) \quad (H)$$

where K denotes the conductivity, and the subscript d corresponds to dense material. The w term is expected to vary between 1 and 2, provided that the pores inside the material are spherical. Table III shows the calculated value of this w term, for each of the 4 porous alumina ceramic samples tested for the electrical resistivity, where a value of 10^{14} Ω.cm for the resistivity of dense alumina was adopted [4]. Clearly, the two samples prepared with a PF content of 10 and 15 wt% yielded a w value between 1 and 2, as predicted by the theoretical model. However, in the case of the samples prepared with 0 and 5 wt% PF content, the w value was outside the indicated range. A possible explanation is related to the fact that the model described by Eq. H assumes a spherical pore structure (after the solid skeleton attaining full density). This condition is expected to be difficult to achieve for the high open porosity alumina ceramic sample prepared with 0 wt% PF and sintered at a moderately low temperature of 1500 °C. Similarly, it seems that full density was not attained in the case of the sample prepared with a 5 wt% PF content, as opposed to the remaining two samples prepared with 10 and 15 wt% PF, where the amounts of impurities introduced by the SSS material were sufficient to promote densification of the solid skeleton. Fig. 12 shows the measured results of electrical conductivity and the curve fitted with the exponential relationship of the MSA model (Eq. I), which is Rice's formula of Eq. G with

Table III - Volume electrical resistivity measured at room temperature and porosity of sintered alumina ceramic disks prepared with different SSS content at a compaction pressure of 38 MPa.

[Tabela III - Resistividade elétrica volumétrica medida à temperatura ambiente e porosidade de discos sinterizados de alumina preparados com diferentes teores de SSS a uma pressão de compactação de 38 MPa.]

SSS content (wt%)	Porosity (vol%)	Volume resistivity (x10^{15} Ω.cm)	w
0	39.7	1.4	2.34
5	47.2	4	2.06
10	54.5	10	1.82
15	58.3	15	1.70

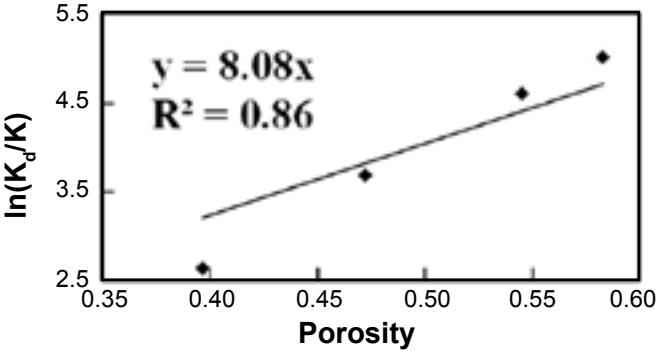

Figure 12: Relative electrical conductivity curve of alumina ceramic disks fitted with Rice's formula.

[Figura 12: Curva de resistividade volumétrica relativa de discos de alumina ajustada com a fórmula de Rice.]

σ being replaced with K (volume electrical conductivity) and b with b':

$$K=K_d.e^{-b'.P} \quad (I)$$

From Fig. 12, a characteristic coefficient of b'=8.08 was obtained, with a coefficient of determination of R^2=0.86. According to [41], the obtained value of b' would correspond to an array of pores, which may be reasonably represented by the solid spherical particle geometry, partially bonded together through a combination of cubic and rhombohedral stacking. This is interesting since it is nearly the same porous structure obtained when interpreting the mechanical properties with the MSA model (Fig. 10). The larger value of b' compared to b may be related to a larger portion of the solid spheres being rhombohedrally stacked, and this may be connected to the difference in the conditions under which the two groups of samples were prepared, especially the compaction pressure. The model developed in [43] could not be fully used, as it requires a sufficiently accurate measurement of the tap porosity of the starting powder, which in the present study was a mixture of transformed and non-transformed alumina phases, and SSS residues.

CONCLUSIONS

Macroporous alumina ceramics have been successfully prepared by the space holder technique, using sunflower seed shells as the fugitive template material, which is a natural, cheap, and widely available waste material. The green bodies were formed by uniaxial dry pressing. Physical and mechanical properties of the sintered porous alumina ceramics, along with its microstructure, were studied in the function of the sunflower seed shells content in the green bodies. Electrical properties were investigated as well. Sunflower seed shells proved to be a promising pore-forming agent, compared to other types of fugitive materials, in terms of the wide range of porosity produced (extending from 30 up to 71 vol%) and the corresponding high mechanical strengths attained (splitting tensile strength within 4-60 MPa). Volume electrical resistivity as high as $15x10^{15}$ Ω.cm was obtained for the sample with 58.3 vol% porosity. Experimental mechanical results were consistent with the Gibson-Ashby model. Electrical resistivity results were consistent with literature data for porous alumina ceramics. Porosity could be increased by increasing the SSS content up to 60 wt%, and a further increase seems to be possible since no limiting effect due to the shrinkage was observed. The porosity of the prepared porous alumina ceramics is mainly open. Hence, the specific potential applications are in the field of filtration of hot and corrosive liquids and gases, as well as catalyst supports. Also, the samples with high mechanical strength may be useful as lightweight structural materials and grinding tools, whereas those with good insulating properties are typical for electrical applications. Another potential application is in the field of thermal insulation. The use of solid pore formers complies well with the conventional solid-state processing of ceramic materials without any further complication.

ACKNOWLEDGMENTS

The authors would like to acknowledge the Higher Institute for Applied Sciences and Technology (HIAST) and the Department of Physics for their financial support and facilities.

REFERENCES

[1] A.R. Studart, U.T. Gonzenbach, E. Tervoort, L.J. Gauckler, J. Am. Ceram. Soc. **89**, 6 (2006) 1771.
[2] K. Ishizaki, S. Komarneni, M. Nanko, *Porous materials: process technology and applications*, Springer, USA (1998).
[3] M.A.A.M. Nor, L.C. Hong, Z.A. Ahmad, H.M. Akil, J. Mater. Process. Technol. **207**, 1-3 (2008) 235.
[4] R.M. Khattab, M.M.S. Wahsh, N.M. Khalil, Ceram. Int. **38**, 6 (2012) 4723.
[5] K. Huang, Y. Li, Y. Zhao, S. Li, Y. Li, S. Sang, Mater. Lett. **165** (2016) 19.
[6] J. Luyten, S. Mullens, J. Cooymans, A.M.D. Wilde, I. Thijs, R. Kemps, J. Eur. Ceram. Soc. **29**, 5 (2009) 829.
[7] P. Colombo, Philos. Trans. R. Soc. A **364** (2006) 109.
[8] B.V.M. Kumar, Y.W. Kim, Sci. Technol. Adv. Mater. **11**, 4 (2010) 44303.
[9] G. Liu, "Fabrication of porous ceramics and composites by a novel freeze casting process", PhD Thesis, Un. Birmingham (2011) 3.
[10] R. Ahmad, J.H. Ha, I.H. Song, J. Kor. Powd. Met. Inst. **21**, 5 (2014) 389.
[11] Z. Živcová, E. Gregorová, W. Pabst, Process. Appl. Ceram. **2**, 1 (2008) 1.
[12] M.S. Ali, M.A.A. Hanim, S.M. Tahir, C.N.A. Jaafar, M. Norkhairunnisa, K.A. Matori, J. Ceram. Soc. Jpn. **125**, 5 (2017) 402.
[13] G.C. Ribeiro, B.A. Fortes, L. da Silva, J.A. Castro, S. Ribeiro, Cerâmica **65**, Suppl 1 (2019) 70.
[14] P.F. Cancalon, J. Am. Oil Chem. Soc. **48**, 10 (1971) 629.
[15] H. Haykiri-Acma, A.Z. Turan, S. Yaman, S. Kucukbayrak, Fuel Process. Technol. **91**, 11 (2010) 1569.
[16] H. Haykiri-Acma, S. Yaman, in Proc. World Renew. Energy Cong. Bioenergy Technol., Linköping (2011) 251.
[17] K. Salasinska, M. Polka, M. Gloc, J. Ryszkowska, Polymer **61**, 4 (2016) 255.
[18] C. Cosereanu, L.M. Brenci, O. Zeleniuc, A. Fotin, BioResources **10**, 1 (2015) 1127.
[19] M. Shahbandeh, "Sunflower seed production in major countries 2018/19", Statista, New York (2020), https://www.statista.com.
[20] A. Boumaza, L. Favaro, J. Lédion, G. Sattonnay, J.B. Brubach, P. Berthet, A.M. Huntz, P. Roy, R. Tétot, J. Solid State Chem. **182**, 5 (2009) 1171.
[21] S. Surabhi, "Production of alumina based porous ceramics using naphthalene as the pore former", Bach. Thesis, Nat. Inst. Technol., Rourkela (2012).
[22] J. Yu, X. Sun, Q. Li, X. Li, Y. Liu, K. Duan, Adv. Mater. Res. **42** (2008) 265.
[23] A.R. Jamaludin, S.R. Kasim, A.K. Ismail, M.Z. Abdullah, Z.A. Ahmad, J. Eur. Ceram. Soc. **35**, 6 (2015) 1905.
[24] K. Davis, School Dr. Stud. European Union J. **2** (2010) 109.
[25] ASTM C20-00, "Standard test methods for apparent porosity, water absorption, apparent specific gravity, and bulk density of burned refractory brick and shapes by boiling water", ASTM (2010).
[26] D. Li, L.N.Y. Wong, Rock. Mech. Rock. Eng. **46**, 2 (2013) 269.
[27] B.S.M. Seeber, U.T. Gonzenbach, L.J. Gauckler, J. Mater. Res. **28**, 17 (2013) 2281.
[28] ASTM D 3967-95a, "Standard test method for splitting tensile strength of intact rock core specimens", ASTM (2001).
[29] M.V. Silva, D. Stainer, H.A. Al-Qureshi, O.R.K. Montedo, D. Hotza, J. Ceram. **2014** (2014) 618154.
[30] D.W. Richerson, *Modern ceramic engineering: properties, processing, and use in design*, 2nd ed., Marcel Dekker, New York (1992).

[31] V. Sciamanna, B.N. Ali, M. Gonon, Ceram. Int. **41**, 2 (2015) 2599.
[32] ASTM D257-07, "Standard test methods for dc resistance or conductance of insulating materials", ASTM (2007).
[33] P.S. Santos, H.S. Santos, S.P. Toledo, Mater. Res. **3**, 4 (2000) 104.
[34] J.H. Eom, Y.W. Kim, S. Raju, J. Asian. Ceram. Soc. **1**, 3 (2013) 220.
[35] L.J. Gibson, M.F. Ashby, *Cellular solids: structure and properties*, 2nd ed., Cambridge Un. Press, UK (1997).
[36] C. Tallon, C. Chuanuwatanakul, D.E. Dunstan, G.V. Franks, Ceram. Int. **42**, 7 (2016) 8478.
[37] R. Brezny, D.J. Green, J. Am. Ceram. Soc. **76**, 9 (1993) 2185.
[38] L. Montanaro, Y. Jorand, G. Fantozzi, A. Negro, J. Eur. Ceram. Soc. **18**, 9 (1998) 1339.
[39] R.W. Rice, J. Mater. Sci. **32**, 17 (1997) 4731.
[40] B.C. Nicolat, T. Fey, P. Greil, Adv. Eng. Mater. **12**, 9 (2010) 884.
[41] R.W. Rice, J. Mater. Sci. **31**, 1 (1996) 102.
[42] R.M. German, *Sintering: from empirical observations to scientific principles*, Elsevier, USA (2014).
[43] J.M. Montes, F.G. Cuevas, J. Cintas, Appl. Phys. A **92**, 2 (2008) 375.
[44] P.S. Liu, T.F. Li, C. Fu, Mater. Sci. Eng. A **268**, 1-2 (1999) 208.
[45] F.G. Cuevas, J.M. Montes, J. Cintas, P. Urban, J. Porous Mater. **16**, 6 (2009) 675.
[46] M. Hakamada, T. Kuromura, Y. Chen, H. Kusuda, M. Mabuchi, Mater. Trans. **48**, 1 (2007) 32.
(Rec. 12/09/2019, Rev. 17/12/2019, Ac. 31/01/2020)

BY-NC

A ENGENHARIA TRANSFORMA
DO TIJOLO AOS EDIFÍCIOS

A capacidade de transformar os elementos e modificar a natureza é o que nos faz humanos. Da terra, da água ou do ar, a engenharia é capaz de criar mais alimentos, mais segurança, mais conforto e mais energia, transformando as nossas vidas para melhor. Todas as descobertas, máquinas, equipamentos que facilitam e enriquecem o nosso dia a dia são conquistas da engenharia.

Para qualquer obra ou serviço, conte sempre com um engenheiro.

www.confea.org.br

CONFEA
Conselho Federal de Engenharia e Agronomia

CREA
Conselhos Regionais de Engenharia e Agronomia

MÚTUA
CAIXA DE ASSISTÊNCIA DOS PROFISSIONAIS DO CREA

Instruções para Autores
(Instructions for Authors)

Encaminhamento de Contribuições

As contribuições devem ser submetidas por meio da URL: https://mc04.manuscriptcentral.com/ce-scielo.

Tipos de contribuição

Trabalhos técnico-científicos originais e artigos revisão. Todas as contribuições serão submetidas à análise por relatores. Toda submissão deve conter pelo menos dois nomes e endereços eletrônicos de relatores (que não sejam da instituição dos autores), e e-mails de todos os autores.

Preparação da contribuição

As contribuições devem:

A- Ser redigidas com editor de texto MSWORD (.doc ou .docx) em português ou inglês, em formato A4, em uma coluna com margens 1,5 cm acima e abaixo, 2,5 cm à esquerda e 1,5 cm à direita, espaço simples, com fonte Times New Roman 10, sem formatação especial.

B- Ser submetidas por meio da URL: https://mc04.manuscriptcentral.com/ce-scielo.

C- Conter

título em português
título em inglês
nomes dos autores
afiliação, endereço, e-mail
resumo (máximo 300 palavras)
palavras-chave (pelo menos duas)
abstract (máximo 300 palavras)
keywords (pelo menos duas)
texto em português na seguinte ordem:

- INTRODUÇÃO
- EXPERIMENTAL (ou **MATERIAIS E MÉTODOS**)
- RESULTADOS E DISCUSSÃO
- CONCLUSÕES
- AGRADECIMENTOS (se necessário)
- APÊNDICE (se necessário)
- REFERÊNCIAS

- Tabelas, numeradas sequencialmente com algarismos romanos, com legendas na parte superior em português e em inglês. *As tabelas devem ser inseridas no texto.*
(Tabelas não devem ter formatação especial, como cores e sombreamento. As tabelas devem ter preferencialmente três linhas horizontais, como no exemplo:

Tabela I - Limites de Atterberg das amostras.
[Table I - Atterberg limits of the samples.]

Amostra	Limite de liquidez (%)	Limite de plasticidade (%)	Índice de plasticidade (%)
A	38,5	20,5	18,0
B	40,0	19,0	21,0
C	37,5	19,8	17,7
D	38,9	18,8	20,1
E	34,8	17,8	17,0

- Figuras numeradas sequencialmente com algarismos arábicos, com legendas na parte inferior *em português e em inglês***.** *As figuras devem ser preferencialmente inseridas no texto.*

As figuras (incluindo gráficos, desenhos, fotos e micrografias) devem ter bom contraste e dimensões que permitam a leitura após redução (recomenda-se dimensões de 12 cm x 8 cm ou 12 cm x 12 cm).

Gráficos feitos no software Origin devem ter traço de eixos 4, números com font 30 negrito, nomes nos eixos com font 36 negrito, símbolos tamanho 12, e devem ser colados no MSWORD com colar especial.

As equações devem ser indicadas sequencialmente no texto com letras maiúsculas.
Exemplo de equação:

$$\Theta(t, T) = \int_{t_0}^{t} \frac{1}{T} \exp\left(-\frac{Q}{kT}\right) dt \qquad (A)$$

D - Ter as referências assinaladas sequencialmente no texto com algarismos arábicos, entre colchetes, e apresentadas no final da contribuição. *As referências não devem ser linkadas (referência cruzada) ao texto. Expressões do tipo et al., e cols., e similares, não devem ser empregadas nas referências. Evitar referenciar sites, dissertações de mestrado e teses de doutorado. Referenciar os periódicos em que os trabalhos de dissertação e tese foram publicados.*

Como formatar as referências:

Artigos em periódicos
(Nomes dos autores separados por vírgulas, nome do periódico, volume em negrito, número (opcional), ano entre parênteses, página inicial-página final.)

Exemplos:

[1] A.H.A. Pereira, D.Y. Miyaji, M.D. Cabrelon, J. Medeiros, J.A. Rodrigues, Cerâmica **60**, 355 (2014) 449-456.
[2] R. Muccillo, E.N.S. Muccillo, J. Eur. Ceram. Soc. **34**, 4 (2014) 915-923.

Livros
(Nomes dos autores separados por vírgulas, título do livro, edição, nome da editora, local da edição, ano entre parêntesis, número da página referenciada.)

Exemplos:

[1] I.R. de Oliveira, A.R. Studart, R.G. Pileggi, V.C. Pandolfelli, Dispersão e empacotamento de partículas - princípios e aplicações em processamento cerâmico, Fazendo Arte Editorial, S. Paulo, Brasil (2000) 25.
[2] P. Souza Santos, Ciência e Tecnologia de Argilas, 3ª ed., Vol. 1, Edgard Blücher, S. Paulo, SP (1992) 397.
[3] J.S. Reed, Principles of ceramics processing, John Wiley, New York, EUA (1995) 254.

Artigos em anais de congressos
(Nomes dos autores separados por vírgulas, nome do congresso, nomes do(s) editor(es), editora, local do congresso, volume, ano entre parêntesis, número da página referenciada.)

Exemplos:

[1] E.C.F. Souza, S.R.M. Antunes, S.A. Pianaro, A.J. Zara, A.C. Antunes, Anais XIII CBECIMAT, Curitiba, PR (1998) 2437.
[2] M.A. Quintela, F.D. Santos, C.A. Pessoa, J.A. Rodrigues, V.C. Pandolfelli, Proc. Unified Int. Tech. Conf. Refractories, UNITECR'05, Orlando, EUA (2005) 380.
[3] M. Kleitz, L. Dessemond, M.C. Steil, F. Thevenot, Proc. Materials Research Society Symposium, Eds.: R.A. Gerhardt, S.R. Taylor, E.J. Garboczi, Materials Research Society, Pittsburgh, EUA, **411** (1996) 269.

Custo e separatas

Não há cobrança aos autores. Um arquivo pdf contendo a forma final do artigo será enviado ao autor responsável pela submissão.

Processo de publicação

1- o artigo é encaminhado para análise de relatores, membros ou não do Conselho de Editores (sistema de avaliação cego-simples - anonimato dos nomes dos relatores aos autores);
2- os pareceres dos relatores são encaminhados ao autor com **"aceito para publicação"** (o artigo aprovado pelos relatores é agendado para publicação), com **"sugestão de revisão"** (o artigo é encaminhado ao autor para revisão e quando providenciada, encaminhado aos relatores para nova análise), com **"não aceito para publicação"** (o artigo não é publicado; se houver pedido de reconsideração, esta é enviada aos relatores e o artigo pode, posteriormente, ser enviado a novos relatores).
3- artigos aprovados são editados graficamente no layout da revista Cerâmica. ***Artigos submetidos nos padrões da revista (contidas nas Instruções para Autores)*** são agendados preferencialmente.
4- visando aumentar a internacionalização da revista, ***artigos submetidos em inglês terão prioridade de publicação***.

Submission of papers

Contributors should submit their papers (**.doc** or **.docx MSWord files**) at: https://mc04.manuscriptcentral.com/ce-scielo.

Types of contributions

Original papers and state-of-the art review articles. All papers will be blind peer reviewed.

Manuscript preparation

- All manuscripts should be written in English. A Portuguese version of the abstract and captions of **foreign** contributions in English will be provided by the Editors.
- The manuscript should follow the instructions:

a) single-space typing, font Times New Roman, font size 10, one column without any special formatting, on A4-size (210 mm x 297 mm) pages, margins 1.5 cm top, right and bottom, 2.5 cm left;
b) the manuscript should contain title, name, affiliation(s) and **e-mail address(es) of all author(s)**, an abstract with no more than 300 words, and at least two keywords.
c) the standard sequence for papers should be followed: Title, Authors names, Affiliations, Abstract, Keywords, Introduction, Experimental (or Materials and Methods), Results and Discussion (or Results), Discussion, Conclusions, Acknowledgements (if pertinent), References. Footnotes should be avoided.
d) tables should be inserted in the text.
e) illustrations: 9 or 18 cm wide and 18 cm maximum height. The line drawings should be large enough (3 - 5 mm) to remain legible after reduction for printing. Any scale markers should be inserted on micrographs.
f) figures should be preferentially inserted in the text.
g) equations, indicated in the text by capital letters, should be represented as shown below:

$$\Theta(t, T) = \int_{t_0}^{t} \frac{1}{T} \exp\left(-\frac{Q}{kT}\right) dt \qquad (A)$$

h) references should be non-linked and consecutively numbered in the text using square brackets and listed by number in the Reference list. Examples:
[1] I.R. Oliveira, V.C. Pandolfelli, Ceram. Int. **36**, 1 (2010) 79-85.
[2] W.D. Kingery, H.K. Bowen, D.R. Uhlmann, Introduction to Ceramics, 2nd ed., John Wiley & Sons, New York, USA (1975) p. 293.
[3] M. Kleitz, L. Dessemond, M.C. Steil, F. Thevenot, *in* Proc. Mat. Res. Soc. Symp., Vol. 411, Eds. R.A. Gerhardt, S.R. Taylor, E.J. Garboczi, Materials Research Society, Pittsburgh, USA (1996) pp. 269-275.

Page charges and offprints

There will be no page charges. A pdf file of the paper will be sent to the corresponding author.

Cerâmica

Ano LXVI - Vol 66, 378 ABR/MAI/JUN 2020 - ISSN-0366-6913

Intercalation experiments for morphological alteration of kaolinite present in iron ore tailings
(Experimentos de intercalação para alteração morfológica da caulinita presente em rejeitos de mineração de ferro)
M. V. B. Gonçalves, A. V. Cardoso, F. V. Parreira *93*

Reuso de resíduo de lama de papel na produção de suporte cerâmico poroso de baixo custo
(Reuse of paper sludge waste in the production of low-cost porous ceramic support)
R. A. Bou-Issa, R. L. Loiola, J. N. F. Holanda *106*

Structural transition and magnetic properties of high Cr-doped $BiFeO_3$ ceramic
(Transição estrutural e propriedades magnéticas da cerâmica $BiFeO_3$ dopada com Cr)
S. S. Arafat *114*

Regeneração de defeito ósseo crítico após implantação de fosfato de cálcio bifásico (β-fosfato tricálcico/pirofosfato de cálcio) e vidro bioativo fosfatado
(Regeneration of a critical bone defect after implantation of biphasic calcium phosphate - β-tricalcium phosphate/calcium pyrophosphate - and phosphate bioactive glass)
R. S. Almeida, M. H. Prado da Silva, D. Navarro da Rocha, I. I. A. Ribeiro, A. A. Barbosa Júnior, F. B. Miguel, F. P. Rosa *119*

Electron paramagnetic resonance of manganese-doped strontium titanate
(Ressonância paramagnética eletrônica de titanato de estrôncio dopado com manganês)
R. S. de Biasi, M. L. N. Grillo *126*

Clarification of used lubricating oils by application of chemically-modified clays
(Clarificação de óleo lubrificante usado por aplicação de argilas quimicamente modificadas)
M. S. L. Rosa, T. Knoerzer, F. C. Figueiredo, J. R. dos Santos Júnior *130*

Synthesis and application of a composite NaA zeolite/gamma-alumina membrane for oil-water separation process
(Síntese e aplicação de uma membrana compósita zeólita NaA/ gama -alumina para o processo de separação de óleo/água)
T. L. A. Barbosa, F. M. N. Silva, A. S. Barbosa, E. G. Lima, M. G. F. Rodrigues *137*

Effect of temperature on the photocatalytic properties of TiO_2-CeO_2 multilayer thin films obtained by spin coating method
(Efeito da temperatura nas propriedades fotocatalíticas de filmes finos multicamadas de TiO_2-CeO_2 obtidos por spin coating)
T. B. O. Nunes, N. F. Andrade Neto, L. M. P. Garcia, R. M. Nascimento, M. R. D. Bomio, F. V. Motta *145*

Influence of microstructural and morphological properties of raw natural clays on the reactivity of clay brick wastes in a cementitious blend matrix
(Influência das propriedades microestruturais e morfológicas de argilas in natura na reatividade de resíduos de tijolos em uma matriz cimentícia)
A. Schackow, S. L. Correia, C. Effting *154*

Artificial stone production using iron ore tailing (IOT)
(Produção de rocha artificial utilizando rejeito de minério de ferro)
C. B. da Silva, P. R. P. de Paiva *164*

Produção de geopolímeros utilizando cinza da casca de arroz como fonte complementar de sílica
(Production of geopolymers using rice husk ash as supplementary source of silica)
P. H. Apolonio, J. S. Lima, E. P. Marinho, A. C. V. Nobrega, J. C. O. Freitas, A. E. Martinelli *172*

Utilization of diverse cheap materials as pore generating agent to manufacture low-cost porous ceramic
(Utilização de diversos materiais baratos como agente gerador de poros na fabricação de cerâmica porosa de baixo custo)
M. M. Salman, N. S. Radhi, O. H. Sabr, H. T. Nhabih *179*

Investigation of mechanical, thermal and electrical parameters of gel combustion-derived cubic zirconia/epoxy resin composites for high-voltage insulation
(Investigação de parâmetros mecânicos, térmicos e elétricos de compósitos zircônia cúbica derivada de gel-combustão/resina epóxi para isolamento de alta tensão)
J. S. Sagar, S. J. Kashyap, G. M. Madhu, Pradipkumar Dixit *186*

Remoção do alaranjado de metila em meio aquoso por microcristais de h-MoO_3 obtidos pelo método micro-ondas hidrotérmico
(Removal of methyl orange in aqueous medium by h-MoO_3 microcrystals obtained by hydrothermal microwave method)
M. L. de Sá, F. X. Nobre, J. M. E. de Matos, M. R. M. C. Santos *197*

Preparation and characterization of porous alumina ceramics using sunflower seed shells as fugitive material
(Preparação e caracterização de cerâmica de alumina porosa utilizando casca de semente de girassol como material fugitivo)
J. Alzukaimi, R. Jabrah *208*

PATROCINADOR